THE UNIVERSITY OF CHICAGO

A MEASUREMENT OF D^* PRODUCTION IN JETS FROM

$\bar{P}P$ COLLISIONS AT $\sqrt{S} = 1.8$ TEV

A DISSERTATION SUBMITTED TO

THE FACULTY OF THE DIVISION OF THE PHYSICAL SCIENCES

IN CANDIDACY FOR THE DEGREE OF

DOCTOR OF PHILOSOPHY

DEPARTMENT OF PHYSICS

BY

GEORGE REDLINGER

CHICAGO, ILLINOIS

DECEMBER, 1989

ACKNOWLEDGEMENTS

TABLE OF CONTENTS

LIST OF TABLES

LIST OF ILLUSTRATIONS

xi

ABSTRACT

The production rate of charged D^* mesons in jets has been measured in 1.8 TeV $\bar{p}p$ collisions at the Fermilab Tevatron Collider with the CDF detector. In a sample of approximately 32,300 jets with a mean transverse energy of 47 GeV obtained from a 1987 exposure of 21.1 nb^{-1}, a signal corresponding to 25.0 ± 7.5(stat) ± 2.0(sys) $D^{*\pm} \rightarrow K^{\mp}\pi^{\pm}\pi^{\pm}$ events is seen above background. This corresponds to a ratio $N(D^{*+} + D^{*-})/N(jet) = 0.10 \pm 0.03 \pm 0.03$ for D^* mesons with fractional momentum z greater than 0.1. The z distribution is soft with approximately 70% of the observed D^*s produced with z between 0.1 and 0.2.

CHAPTER 1

INTRODUCTION

Strongly interacting matter is made of quarks, which currently come in five different "flavors" - u,d,s,c, and b - although there are both theoretical and experimental reasons[1] to believe that a sixth flavor, t, must exist. The first three quarks in the list are known as the "light" quarks since their masses are either comparable or less than the hadronic mass scale of around 300 MeV/c^2. The remaining two known quarks, c and b, have masses around 1.5 GeV/c^2 and 5 GeV/c^2 respectively and are placed in the category of "heavy" quarks. The t ("top") quark is known to have a mass greater than 77 GeV/c^2 at a 95% confidence level.[2] The production of heavy quarks in hadronic interactions is a subject of considerable theoretical and experimental interest.

The basis of the theoretical interest is that heavy quark production rates in hadronic interactions can be calculated by applying perturbative techniques to Quantum Chromodynamics (QCD), the theory of the strong interaction. The argument[3] is that heavy quark production involves momentum transfers on the order of the heavy quark mass and thus occurs on a very short time-scale. This makes the problem tractable as it allows one to treat the production process in terms of three temporally well-separated processes: the evolution of the initial state of quarks and gluons (collectively known as partons) inside the hadron, the hard collision between the partons which produces the heavy quark, and the fragmentation of the final-state partons into color-neutral hadrons.

Recently, radiative corrections to the heavy quark production cross section have been calculated[4] at third-order in the QCD coupling

constant, a_s. The behavior of these higher-order corrections has confirmed the applicability of a perturbative calculation.

The experimental interest stems from two broad areas. The first is to test the predictions of QCD for the production rates, and to this end, there have been several experiments to measure the production rates for the charm[5] and bottom[6] quarks. It is important to verify the QCD predictions for these quarks if we are to have any confidence in the predictions for the production rates for as yet undiscovered heavy strongly interacting particles (such as the top quark). These measurements are also important for an understanding of backgrounds to new or rare processes whose signatures are often multilepton final states (which can be mimicked by semileptonic decays of heavy quarks).

The second source of experimental interest is the hope of utilizing the high production rates in hadronic interactions to make precise measurements of the lifetimes, branching ratios, and other properties of heavy quark bound states; CP violation in the b system is an example of the last category. The rates are large compared to those achievable in e^+e^- collisions. For example, the highest rate in the next few years for b quark production in e^+e^- collisions is expected to be at the Cornell Electron Storage Ring (CESR) where a peak rate of approximately 0.6 $b\bar{b}$ pairs per second is anticipated;[7] by contrast the Fermilab $\bar{p}p$ collider, for example, is already producing on the order of 10 $b\bar{b}$ pairs per second.[8] Unfortunately, the detection of these particles in hadronic interactions is tremendously difficult due to the enormous flux of background particles accompanying the breakup of the projectiles. Nevertheless, several groups have taken advantage of the large production rate in hadronic interactions to produce competitive measurements of B^0-$\bar{B}^0$ mixing[9] and some of the most sensitive measurements of the lifetimes of charmed mesons[10] and of D^0-$\bar{D}^0$ mixing.[11]

This thesis deals with one part of this rich area of heavy quark physics. It is a report on a measurement of the multiplicity of charged D^* mesons[12] in jets produced in $\bar{p}p$ collisions at a center-of-

mass energy ($\sqrt{s}$) of 1.8 TeV using the CDF detector at Fermilab.[13] Indirectly this serves as a measurement of the charm quark multiplicity in jets (averaged over jet type, e.g. gluon initiated jets, b quark jets and so forth) since the probability that a charm quark materializes as a D^* meson has been measured.[14]

1.1 Heavy Quark Multiplicity in Jets

The multiplicity of heavy quarks in gluon jets has been calculated in perturbative QCD to be[15]

$$\frac{\text{\# of quarks}}{\text{\# of gluon jets}} = \frac{2}{3\pi} \int_{4M^2}^{Q^2} \frac{dK^2}{K^2} \, \alpha_s(K^2) \left[1 + \frac{2M^2}{K^2} \right]$$
$$\cdot \left[\frac{1}{4} - \frac{M^2}{K^2} \right]^{1/2} n_g(Q^2, K^2).$$

Note that this expression differs from the one in the literature by a factor of two since we are expressing the number of quarks per jet rather than the number of quark pairs. The quantity $n_g(Q^2, K^2)$ is the "gluon multiplicity", which is the number of (spacelike) gluons with 4-momentum squared k^2 (where $K^2 = -k^2$) in a jet initiated by a gluon of 4-momentum squared q^2 (again, where $Q^2 = -q^2$). The gluon multiplicity is given by

$$n_g(Q^2, K^2) = \left[\frac{\ln(Q^2/\Lambda_{QCD}^2)}{\ln(K^2/\Lambda_{QCD}^2)} \right]^a \frac{\exp\sqrt{6/(\pi b)\,\ln(Q^2/\Lambda_{QCD}^2)}}{\exp\sqrt{6/(\pi b)\,\ln(K^2/\Lambda_{QCD}^2)}}$$

where

$$a = -\frac{1}{4}\left[1 + \frac{10N_f}{27\pi b}\right] \qquad\qquad b = \frac{33 - 2N_f}{12\pi}$$

N_f = the number of participating flavors (i.e. 4)

M = the mass of the heavy quark.

Λ_{QCD} is a parameter of the theory and has to be determined experimentally. The current world average value[10] is $200 \, ^{+\,150}_{-\,80}$ MeV for four flavors. The number of charm quarks per jet is plotted in Figure 1 for two extreme values of the charm quark mass and Λ_{QCD}; note that the gluon multiplicity factor can change the result by a factor of two or more once Q^2 gets greater than about $(30 \text{ GeV})^2$. Taking Q^2 to be the square of the jet energy, the number of charm quarks per jet ranges from 0.12 to 0.27 for 30 GeV jets. This corresponds approximately to a range of 0.05 to 0.10 for the number of charged D^* mesons per jet since the probability that a charm quark materializes as a D^{*+} or D^{*-} is approximately 3/8. (We will describe this in more detail in Chapter 8.)

The process is schematically illustrated in Figure 2 where a highly virtual gluon radiates quarks and gluons to reduce its Q^2, and the radiated quanta eventually materialize into color-neutral hadrons. (From here on, we will use the term Q^2 to refer generically to minus the 4-momentum squared.) The calculation can be thought of as consisting of two pieces. One is the behavior of the multiplicity of partons in the cascade down to some cutoff in Q^2. This process is now believed to be rather well understood,[16] and is quantified by the gluon multiplicity factor. The second stage is the production of hadrons beyond the cutoff point. For light hadron production, this is incalculable in perturbation theory because the QCD coupling becomes large.[17] The difference with heavy quarks is that the Q^2 of the gluon has to be at least of order M_q^2 where M_q is the mass of the heavy quark. If $M_q^2 \gg \Lambda_{QCD}^2$, then the final stage of the cascade can also
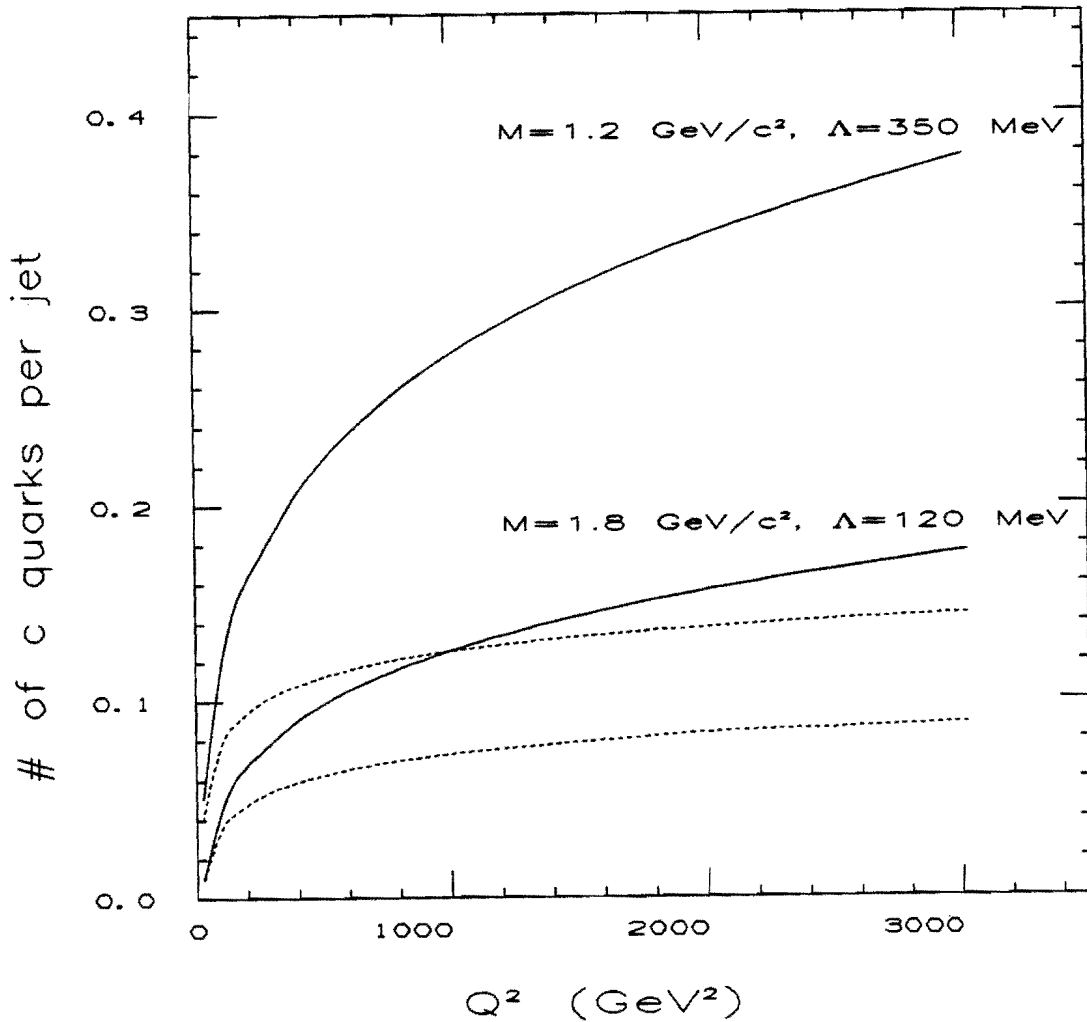
Figure 1. The number of charm quarks per gluon jet as a function of the Q^2 of the gluon. The formulae of Reference 15 have been used. The two solid lines show the charm quark multiplicity for two extreme values of the charm quark mass and Λ_{QCD}. The two dotted lines show the corresponding multiplicity when the gluon multiplicity factor (see text) is neglected.
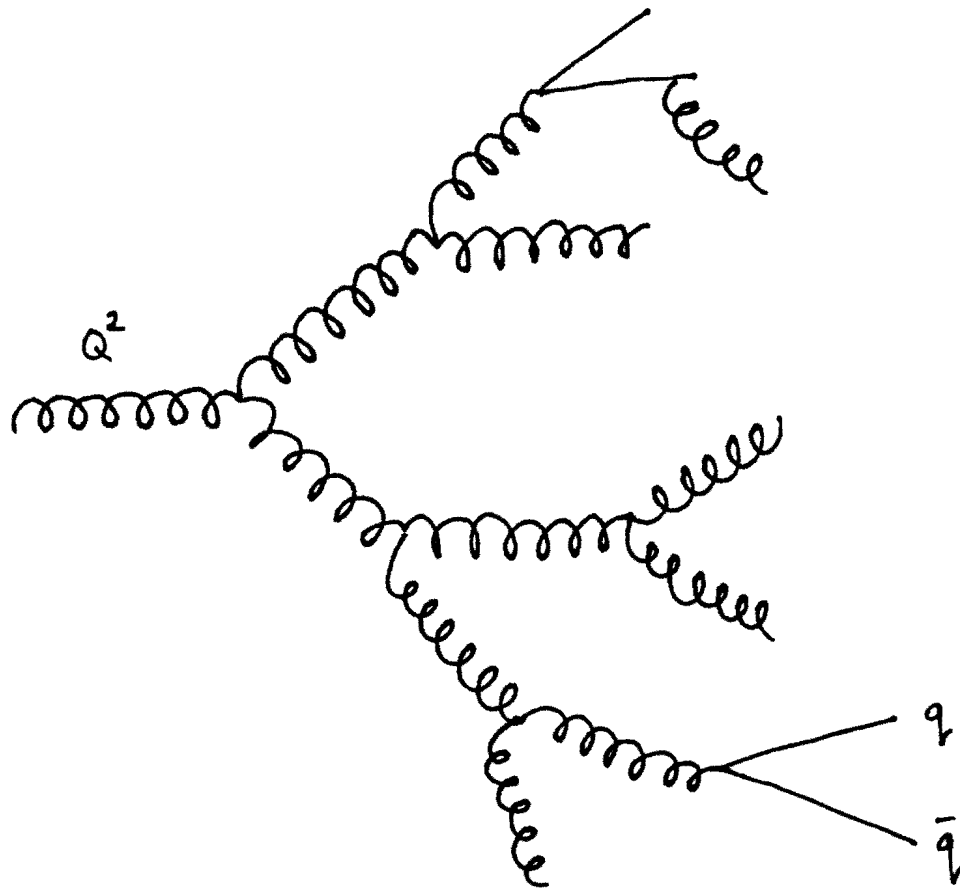
Figure 2. One way to visualize the production of heavy quarks in gluon jets.

be calculated perturbatively via the Altarelli-Parisi splitting functions.[18]

One of the big questions in heavy quark calculations is how heavy the quark must be in order for perturbative methods to be valid. This is particularly significant for the charm quark whose mass is approximately 1.5 GeV/c^2 to be compared with Λ_{QCD} of about 0.2 GeV/c^2. Many of the earlier measurements of the charm production total cross section, for example, were an order of magnitude higher than the predictions[19] and have led to speculation about alternative mechanisms for charm production.[20] More recent data, however, seem to indicate reasonable agreement between QCD and the data.[5] The nice feature of heavy quark pair production in gluon jets is that the non-perturbative contributions can actually be calculated,[15] and in the case of charm, the leading non-perturbative correction is found to be five orders of magnitude smaller than the perturbative contribution.[21]

Prior to this calculation, the UA1 Collaboration generated some excitement when their measurement[22] of the D* multiplicity in jets suggested that the charm content in gluon jets was much higher than predicted by QCD.[23] As with the charm total cross section, it appeared that non-perturbative effects would have to be invoked to explain the discrepancy. The measured rate was N(D^{*+} + D^{*-})/N(jet) = 0.65 ± 0.19(stat) ± 0.33(sys) for D*s with fractional momentum z greater than 0.1. The variable z, commonly used in jet fragmentation studies, is defined as $\vec{p}_{D*} \cdot \vec{p}_{jet}/|\vec{p}_{jet}|^2$. This measurement was based on a sample of jets with an average transverse energy[24] of 28 GeV. The systematic uncertainties were large so that the measured value could be interpreted as being consistent with QCD predictions; nevertheless the central value was tantalizing.

The measurement was performed by looking for the decay D^{*+} → D$^0 \pi^+$ followed by D^0 → K$^- \pi^+$ as well as the charge conjugate mode.[25] K-π and K-π-π mass combinations were formed using the charged particle tracks in the central detector. No particle identification was used so that both K and π assignments had to be tried for all tracks. A D* signal would show up as a statistically significant enhancement in the

number of mass combinations with a K-π mass equal to the D^0 mass and a K-π-π mass equal to the D^* mass. Figure 3 shows the UA1 result; the mass difference $\Delta M \equiv M_{K\pi\pi} - M_{K\pi}$ is shown for track combinations where the K,π mass was close to the D^0 mass. There appears to be a nice signal of an estimated 20 events on a background of 8.

In a subsequent UA1 measurement[26] the sample of jets was enlarged but the signal was much weaker (15 events on a background of 12),[27] leading to a much lower multiplicity, $N(D^{*+} + D^{*-})/N(jet) = 0.08 \pm 0.02 \pm 0.04$, where the central value is now more in line with QCD estimates. The two measurements differ by about 1.5 standard deviations; it has been suggested that different trigger conditions in the two measurements could have contributed to the difference.

The CDF detector enjoys better charged tracking resolution than UA1. This is essential for the measurement of D^* production because the mass resolution provides the main handle on rejecting the background from random track combinations. Monte Carlo estimates for the resolution, using the nominal values for the spatial resolution of the tracking chambers, are:[28]

	CDF	UA1
$\sigma(M_{K\pi})$	14 MeV/c^2	34 MeV/c^2
$\sigma(\Delta M)$	0.5 MeV/c^2	0.8 MeV/c^2

Since the signal-to-noise ratio (SNR) is inversely proportional to the product of the two values for the mass resolution, CDF has an advantage of close to a factor of four. This can make a big difference especially when the SNR is less than one.

1.2 B physics

UA1 measurements of b quark production[29] have been primarily extracted from measurements of muon production, utilizing the semileptonic decays of b quarks, b $\rightarrow$ c$\mu\nu$. One of the difficulties of
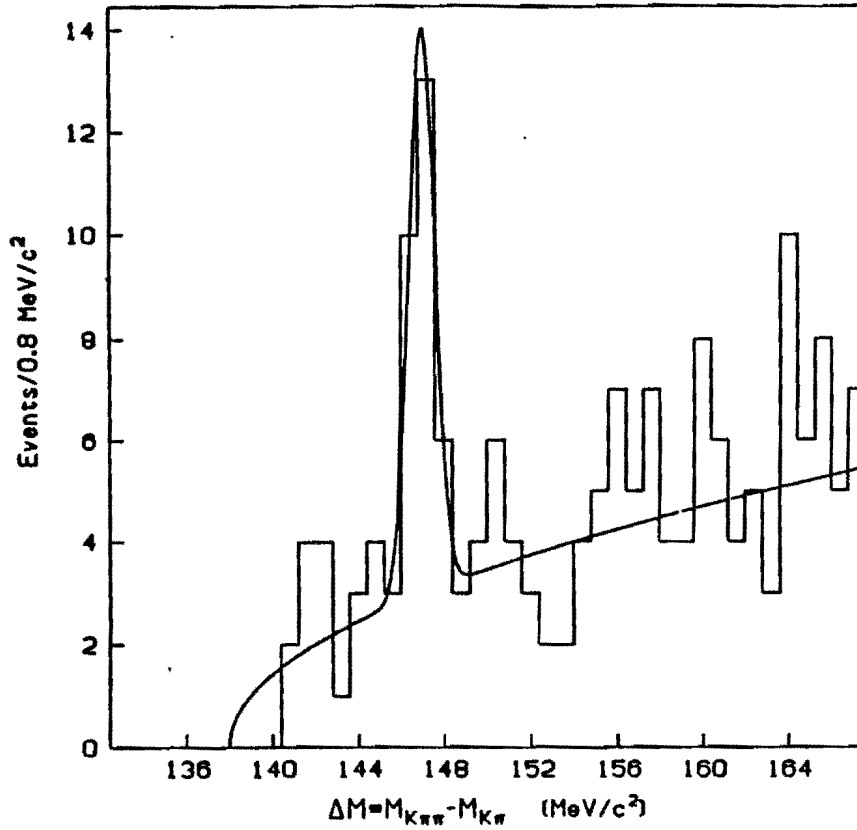
Figure 3. The original UA1 evidence for D^* production in jets. The figure is taken from Reference 22. The mass difference $\Delta M \equiv M_{K\pi\pi} - M_{K\pi}$ is shown for track combinations with $1.83 < M_{K\pi} < 1.92$ GeV/c^2. The peak near the D^*-D^0 mass difference is evidence for the decay chain $D^{*+} \to D^0\pi^+$, $D^0 \to K^-\pi^+$ and the charge conjugate mode.

this measurement is that several other processes contribute to the muon rate: π and K decays, muons produced by the Drell-Yan mechanism,[30] decays of charm mesons, and decays of the J/ψ and Υ resonances. The contribution of these processes is typically 40% of the total rate and the subtraction is not straightforward. The observation of both the charm meson and the lepton from the semileptonic decay of the b would provide further evidence that b decays are being observed. In this context, the search for D^*s in jets serves as a training ground for bottom meson identification. Depending on how well charm can be identified, one can even imagine distinguishing semileptonic b decays on an event by event basis.[31]

1.3 Outline of the Thesis

The remainder of this thesis is organized as follows. Chapter 2 outlines those parts of the CDF detector relevant to this analysis and points the reader to detailed documentation in the literature. Chapter 3 discusses the data collection and reconstruction. Chapter 4 then describes how the D^* signal was extracted from the data, and Chapters 5-7 discuss the treatment of systematic corrections for the effects of D^* detection efficiency and detector resolution. The thesis concludes in Chapter 8 with a presentation of the results of this work and a discussion of possibilities for related measurements in the future.

This is followed by a series of appendices containing more detailed information about items discussed above. Appendix A contains a list of the collaborators on this experiment. Appendix B discusses the sources of tracking inefficiency in more detail. Appendix C discusses the determination of the jet energy scale and the associated uncertainty. Appendix D describes the measurement of the jet energy resolution. Appendix E then describes the details of a Monte Carlo which was used to estimate the effect of the uncertainty in the jet energy measurement on our analysis. Finally in Appendix F we describe

a quick search that we performed on a more recent (and larger) data sample for correlated electron-D^* production.

CHAPTER 2

THE CDF DETECTOR

Our description of the Collider Detector at Fermilab (also known as the CDF detector), will be brief since there exists extensive documentation in the literature.[32] We begin with a brief overview of the detector followed by more detailed descriptions of those parts of the detector most relevant to this analysis.

2.1 Overview

The CDF detector was designed to study proton-antiproton collisions at the Fermilab Tevatron Collider[33] which ran at a center-of-mass energy ($\sqrt{s}$) of 1.8 TeV and a "luminosity" as high as 10^{29} cm^{-2} sec^{-1} for the data taken for this analysis. The luminosity (which at the time of this writing had already reached as high as $2*10^{30}$ cm^{-2} sec^{-1}) is a quantity which is used to measure the performance of a colliding beam machine and represents the number of particles crossing a given area per unit time. It can also be written as

$$\text{Luminosity (L)} \equiv \frac{\text{interaction rate}}{\sigma}$$

where σ is the cross section for a $\bar{p}p$ interaction. To give the reader some feeling for the numbers, the inelastic cross section for a $\bar{p}p$ interaction at $\sqrt{s}$=1.8 TeV is estimated[34] to be around 60 mb (where 1 mb $\equiv 10^{-27}$ cm^2) based on extrapolations from measurements at lower energies. Therefore, at a luminosity of 10^{29} cm^{-2} sec^{-1}, the accelerator was producing inelastic interactions at a rate of around 6

12

kHz.[35] The p and $\bar{\text{p}}$ "bunches" crossed each other every 7 μs so there was roughly one interaction for every 24 crossings.

Since collisions at this energy had never been observed in any accelerator, the CDF detector was designed as a general-purpose detector capable of observing unexpected "new" physics as well as providing solid measurements of "known" physics. To quote from the literature, the strategy was to "measure the energy, momentum and, where possible, the identity of the particles produced at the Tevatron over as much of the solid angle as practical".[36] This was achieved with the now-standard design of surrounding the interaction region with charged particle tracking in a magnetic field, followed by finely-segmented electromagnetic and hadronic calorimeters to measure the energies of individual particles. Drift chambers outside the calorimeters are sensitive to muons. This is illustrated in Figure 4 which shows a cut-away view of one half of the detector. The detector is forward-backward symmetric about the interaction point as well as cylindrically symmetric about the beam axis. Coverage extends down to within two degrees of the beam line so that essentially all the particles produced with significant momentum transverse to the beam axis are intercepted. The measurement of the vector sum of the transverse momenta of these particles allows inferences to be made about the production of neutrinos by using the apparent momentum imbalance in the transverse plane, a powerful technique previously exploited by the UA1 Collaboration.

The coordinate system we will use has the x-axis coming out of the page in Figure 4 (away from the center of the accelerator ring), the y-axis pointing up, and the z-axis pointing to the left (along the proton direction); the origin is at the center of the detector. Due to the cylindrical symmetry of the detector, we will often use the cylindrical coordinates r,ϕ and z. We will also refer to the polar angle θ which is measured in the usual way with respect to the z-axis. In addition to the polar angle θ, a useful variable in this dimension for $\bar{\text{p}}$p interactions is the pseudorapidity (η), which is defined as

Figure 4. A cut-away view through the forward half of the CDF detector. From Reference 36.
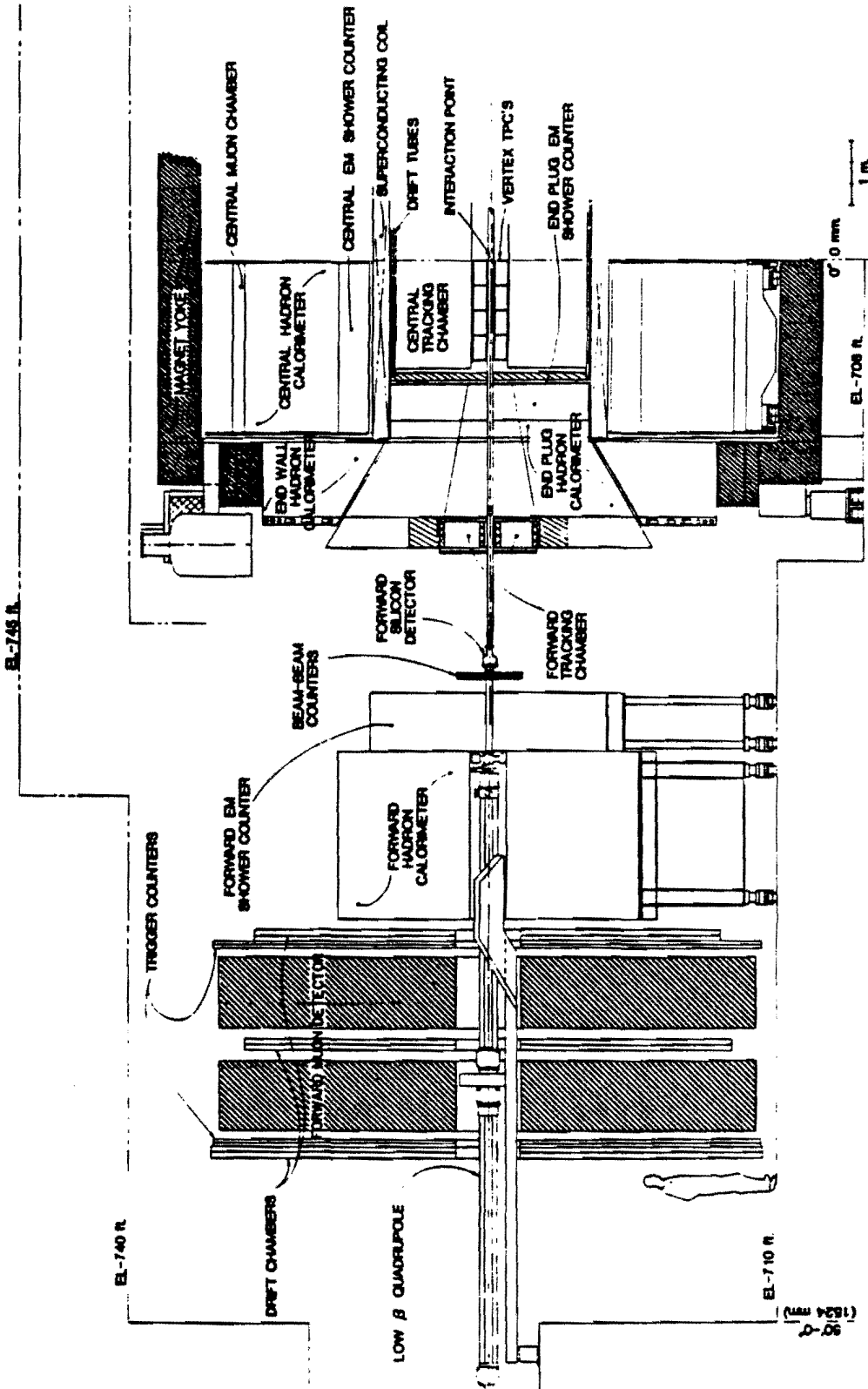
ELEVATION VIEW LOOKING SOUTH

$$\eta \equiv -\ln(\tan \frac{\theta}{2}).$$

This variable is chosen because of its near equivalence to the Lorentz-boost variable rapidity (y), defined as

$$y \equiv \frac{1}{2} \ln \frac{E + p_z}{E - p_z},$$

which in turn is useful because in $\bar{p}p$ collisions, the center-of-mass system of the partons are boosted along the z direction in the lab frame. The rapidity and pseudorapidity are equal for particles whose masses are negligible compared to their momenta transverse to the z-axis. The detector is segmented uniformly in η and ϕ since the average particle density is expected to be approximately uniform in these variables.

This thesis is based on data from the following detector components: 1) Vertex Time-Projection Chamber (VTPC), 2) Central Tracking Chamber (CTC), and 3) the calorimeters. We now briefly describe each of these in turn. In addition, we describe the trigger system which was used to select the events to be recorded on tape.

2.2 Vertex Time-Projection Chamber[37]

The VTPC was used in this analysis to determine the z position of the $\bar{p}p$ interaction point. It is located immediately outside the beam pipe, and provides information on the $r-z$ projection of the trajectories of charged particles produced at polar angles greater than 3.5°. Approximately 2.8m long, the VTPC consists of eight octagonal modules mounted end-to-end along the beam direction. Each module has a central high-voltage grid dividing it into two drift regions. These drift regions were kept fairly short (15.25 cm) in order for the maximum drift time to be less than the time between beam crossings (designed to be 3.5 μs). The use of many short TPC's is different from the implementation in e^+e^- experiments where the

interaction region can be covered with one module[38] due to the longer time between beam crossings.

The TPC records the ionization trail left by the passage of a charged particle by drifting the ionization electrons away from the center grid, through a cathode grid, and into one of the two proportional chamber endcaps. Each endcap is divided into octants with 24 sense wires and 24 cathode pads per octant. The arrival times of ionization electrons at the sense wires give the z-coordinates of the track and the positions of the sense wires give the radial coordinates. Adjacent modules are rotated azimuthally relative to one another by roughly 11° to eliminate inefficiencies near octant boundaries and to provide ϕ information from small-angle stereo. At polar angles between 5° and 25°, the wires and pads are instrumented to encode digitally the pulse shapes, thereby giving another handle on the ϕ coordinate as well as providing dE/dx information.

Considerable effort was put into minimizing the amount of material in the VTPC so as to minimize the number of secondary interactions and the amount of multiple Coulomb scattering. This is shown in Figure 5. The tracks used in this thesis were required to be in the region ~34° < θ < ~124°; the amount of material traversed by particles before entering the active volume of the CTC is therefore less than 5% of a radiation length.

2.3 Central Tracking Chamber[39]

The CTC is located immediately outside the VTPC and provides precise momentum determination for charged particles in the angular region 40° < θ < 140°. The momentum is determined by measuring the particle trajectories in a uniform 1.5T magnetic field produced along the z-direction by a superconducting solenoid surrounding the chamber. The CTC is a 1.3m radius, 3.2m long cylindrical drift chamber measuring up to 84 points per track (depending on the polar angle). The sense wires are grouped into 9 "superlayers". Five of these superlayers (known as the "axial" superlayers) each consist of 12

Figure 5. Material traversed versus polar angle. The dots
indicate material traversed before entering the active volume of the
VTPC. The crosses indicate the total amount of material crossed by a
particle as it exits the VTPC system. The triangles indicate the
average total material traversed before entering the active volume of
the CTC or FTC (Forward Tracking Chamber). The figure is from
Reference 39.
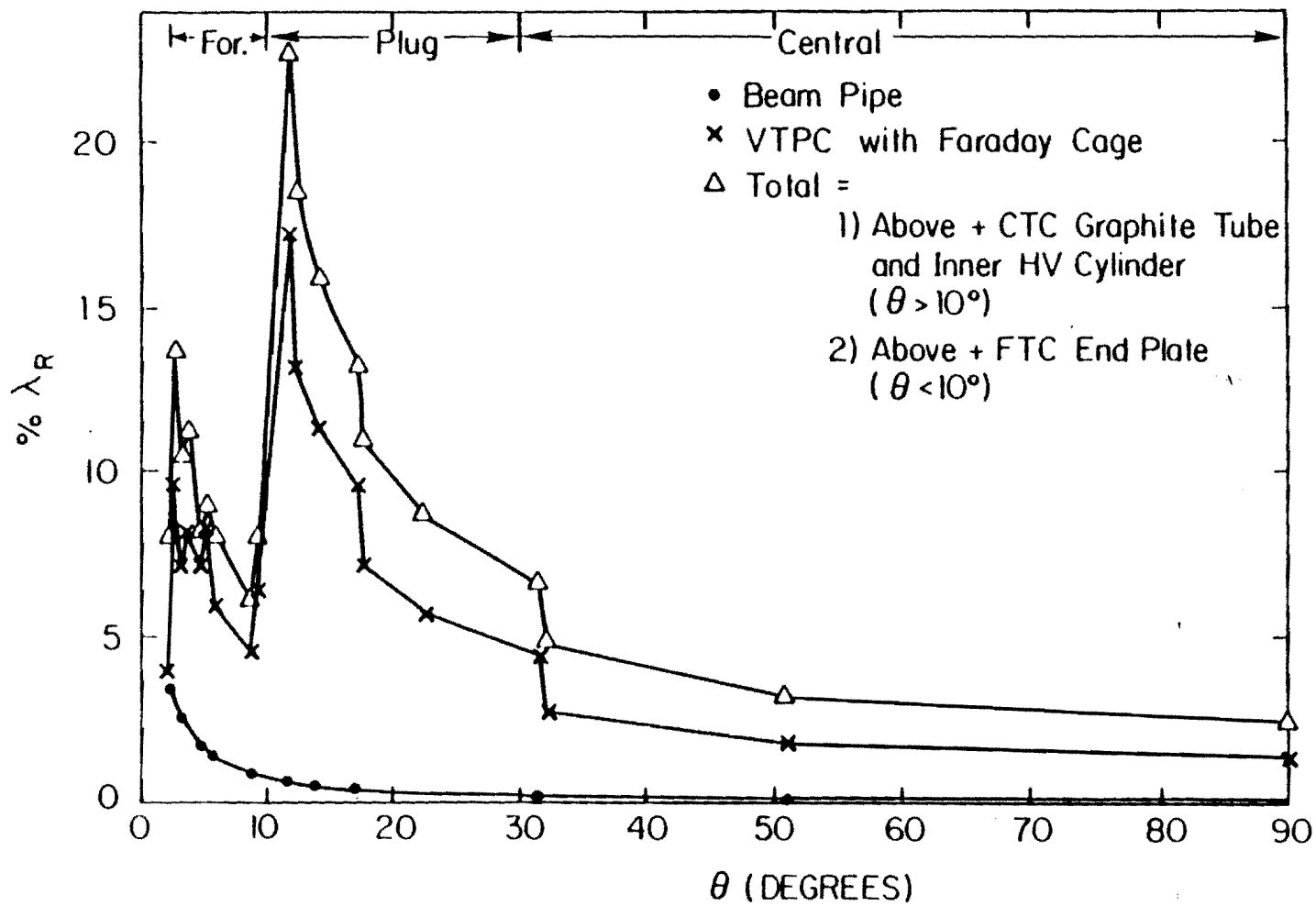
sense wires strung parallel to the beam axis that provide information on the coordinates of the particles in the r-ϕ plane, again by measuring the drift time of the ionization electrons. These axial superlayers are interleaved with four "stereo" superlayers each of which consist of 6 wires tilted by $\pm 3°$ with respect to the beam axis and which, through their tilt, provide information on the z-coordinate of the tracks. The superlayers are divided into cells with a maximum drift distance of $\leq$ 40 mm, corresponding to a drift time of about 800 ns. Each wire is instrumented with multi-hit TDC's (Time-to-Digital Converters, where multiple times can be recorded before the device needs to be reset).

Figure 6 shows the endplate of the chamber, illustrating how the drift cells are tilted by 45° with respect to the radial direction. This was done to reduce dead space and to keep the drift-time drift-distance relationship linear near the ends of the cells when the chamber is immersed in the 1.5T magnetic field. The tilted configuration causes the drift trajectories to be approximately azimuthal when the magnet is on. There are added advantages of having the cells tilted at a large angle, and these are as follows:

1) The cells overlap in azimuth so that every track above roughly 700 MeV/c passes close to at least one sense wire in every superlayer. This is nice for two reasons. First, it allows one to fit for "t_0" of every track, where by "t_0" we mean the following. The position of the charged particle is obtained by measuring the arrival time of ionization electrons onto the sense wires and multiplying by the drift velocity of these electrons. The arrival times have offsets associated with them due to signal propagation delays and time of flight of the charged particles. These offsets are known as t_0's. Improved knowledge of the t_0's leads to improved resolution of closely spaced tracks. The other advantage of having particles crossing the sense wire planes is that the resulting "prompt" hits can be used in a hardware processor to trigger on high transverse momentum (p_t) tracks.[40]

Figure 6. An end view of the CTC showing the location of the slots in the aluminum endplates. This figure is from Reference 39.

554.00mm I.D.

2760.00mm O.D.
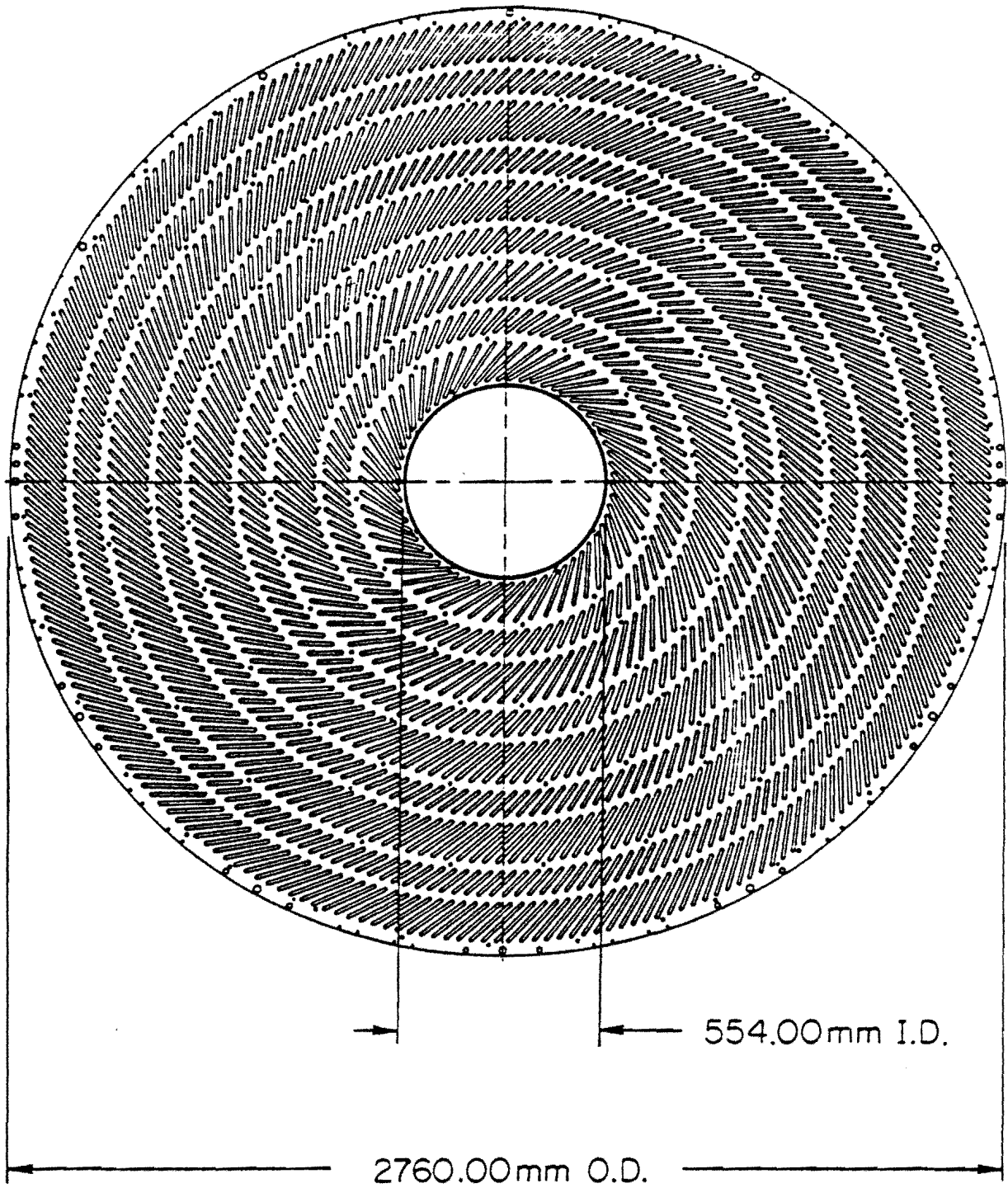
2) The pattern recognition problem of resolving the "left-right ambiguity" is simplified. "Left-right" ambiguity refers to the fact that the drift-time measurement does not tell us on which side of the sense wire the particle passed. The rotation of the cell causes the track segment defined by the improper assignment to be rotated by a large angle (approximately 70°) so that it fails to match up with any other segments.

3) Single high-p_t tracks sample the full range of drift distances in the cell; this is useful for the in-situ calibration of the drift velocity.

The chamber was designed to have a spatial resolution of 200 μm in the r-ϕ plane. This translates to a resolution in the z-direction for the stereo wires of 200μm/sin 3° or approximately 4mm. This is superior to the resolution one can achieve by the technique of charge division (where one determines the z-coordinate by comparing the charge collected at each end of the sense wire) and is furthermore cheaper to implement since only the drift time (and not the total charge collected) needs to be recorded.[41] The price one has to pay is in the track reconstruction software where the matching of z information with tracks reconstructed in the r-ϕ plane is more complicated. The double-track resolution was expected to be less than 5mm, corresponding to a drift time difference of approximately 100 ns. We will see in Chapter 5 that this is borne out by the data where the typical widths of the sense wire pulses are around 60 ns.

2.4 Calorimeters[42]

The calorimeters cover almost the entire solid angle (to within 2° of the beam). They are arranged in a projective "tower" geometry in which the calorimeter elements are arranged to point back to the nominal interaction point. The size of the towers is 0.1 units in η by either 15° or 5° in ϕ depending on the location. The towers in the central calorimeter ($|\eta|<\sim1.1$) are 15° wide while those in the "plug" ($\sim1.1<|\eta|<\sim2.4$) and the "forward" ($\sim2.4<|\eta|<4.2$) regions cover

5° in azimuth. Figure 7 shows the segmentation. Each tower consists of an electromagnetic (EM) shower counter followed by a hadron calorimeter. The EM calorimeters use lead sheets interleaved with an active medium consisting of scintillator in the central region and proportional chambers with "cathode pad readout"[43] elsewhere; the hadronic calorimeters use steel sheets instead of lead. Proportional chambers were selected outside the central region for the following reasons: 1) Since the towers are of uniform size in η, the actual solid angle coverage decreases considerably as $|\eta|$ increases. The introduction of numerous light guides to bring the light out from all the small pieces of scintillator would introduce significant dead areas and non-uniformities in the coverage. 2) In the forward regions, radiation resistance of the detector is of considerable concern. Gas systems allow the active medium to be replaced with very little effort compared to replacing scintillator planes. The price one has to pay is that the proportional chambers are quite sensitive to the air pressure which can change quite rapidly depending on the weather. Careful monitoring of the pressure is therefore required.

Each tower of the central EM calorimeter ($|\eta| < 1.1$) is viewed by two phototubes, one on each of the ϕ boundaries. These phototubes integrate the light output from all layers in the calorimeter. To provide additional depth information and higher spatial resolution, a proportional chamber with a resolution of about 2mm is embedded at a depth of about 6 radiation lengths. Each tower consists of about 18 radiation lengths of material; the magnet coil provides approximately one additional radiation length. In the plug EM calorimeter ($1.1 < |\eta| < 2.4$) there are three channels in depth, integrating over 3.8, 14.2 and 3.0 radiation lengths. Each of the 24 wire planes in depth is also digitized by quadrant so that one obtains a detailed longitudinal shower profile in addition to the three depth samples for isolated electrons or photons. The forward EM calorimeter ($2.2 < |\eta| < 4.2$) has two depth segments each of which integrate over 12 radiation lengths. As in the plug, the wire planes at each layer are read out to provide
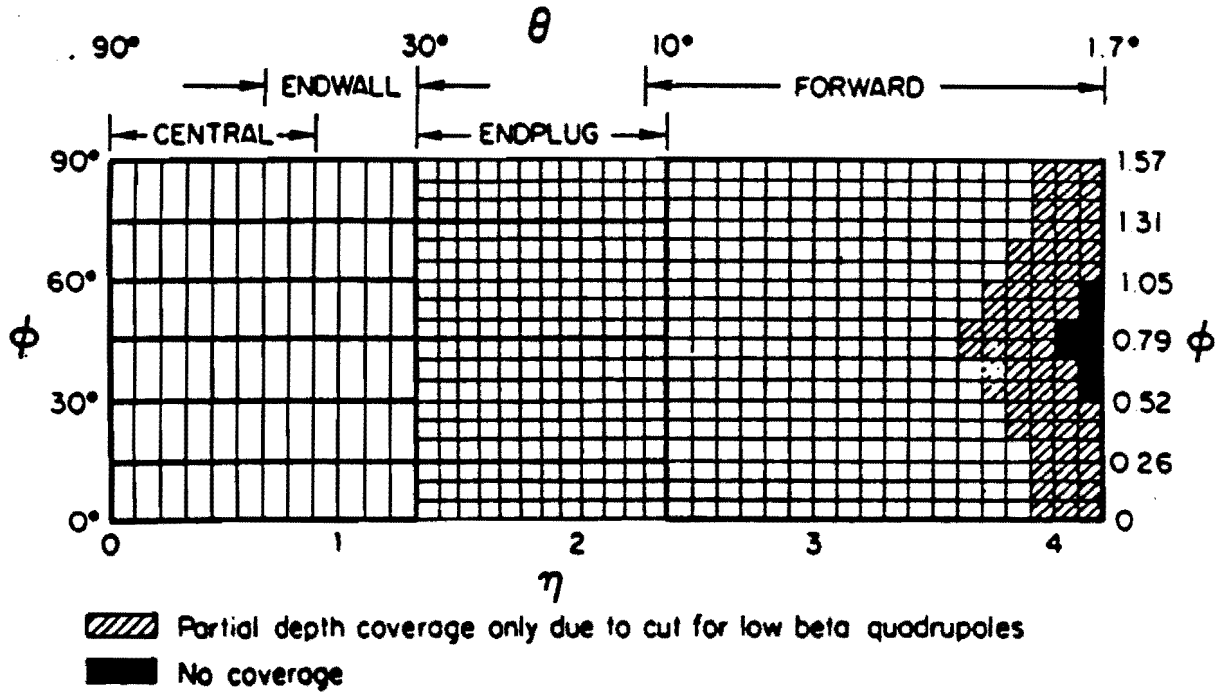
Figure 7. Hadron calorimeter towers in one of eight identical η-ϕ quadrants ($\Delta\phi$=90°, η>0). The heavy lines indicate module or chamber boundaries. The EM calorimeters have complete ϕ coverage out to η=4.2. This figure is from Reference 36.

longitudinal shower profile information, but the planes are divided into five separate regions per quadrant.

In the hadron calorimeters the sharing of the rapidity coverage between "central", "plug" and "forward" is different from the EM calorimeters because of the presence of the magnet coil. In the central detector there are hadronic towers attached to the back of the EM towers in the region $|\eta|<0.9$ and additional towers in the "endwalls" covering the region $0.9<|\eta|<1.3$ as shown in Figure 4. As in the central EM calorimeter, each tower is viewed by two phototubes. The plug hadron calorimeters cover the region $1.3<|\eta|<2.4$ and the forward calorimeters cover $2.3<|\eta|<4.2$. All the hadron calorimeters have only one channel, integrating over the entire depth of the calorimeter. In the plug and forward calorimeters, however, the wires of each wire plane are digitized (by quadrant, again) to provide shower profile information. The central and endwall hadron calorimeters are instrumented to measure the time of the shower relative to the beam crossing time. We will see in Chapter 3 that this information is very useful for rejecting cosmic rays which deposit large amounts of energy in the calorimeters via bremsstrahlung.

Systematic effects associated with the jet energy scale are discussed in Appendix C. The jet energy resolution is discussed in Appendix D.

2.5 Trigger

The purpose of the trigger is to select "interesting" events from the overwhelming barrage of inelastic interactions which occur at a rate of approximately 60 kHz at the design luminosity of 10^{30} cm^{-2} sec^{-1}. Data is written to tape at approximately 1 Hz, a rate determined largely by the rate at which data can be analyzed. This reduction of rate is achieved by a three-level trigger, the first two of which were built largely at the University of Chicago[44] and consist of specially designed hardware to calculate the topology of transverse energy flow and to identify electrons, muons and jets. The third-

level trigger[45] is based on a microprocessor farm, enabling event selection algorithms to be implemented by software. The multi-level structure of the trigger was motivated by the desire to introduce as little bias as possible at the lower levels while reducing the rate sufficiently so that the next level can do a more sophisticated analysis without incurring significant deadtime. We will restrict our discussion to the Level 1 trigger since the other levels were not used to collect the data for this thesis.

For this data-taking run, the Level 1 decision was based on the following information:

1) Electromagnetic, hadronic and total E_t summed over those calorimeter trigger towers which are above programmable thresholds.

2) The existence of high-p_t tracks in the CTC.

3) The existence of muon candidates in the central and forward muon chambers.

4) The presence of a beam-beam interaction and/or the presence of a beam-gas interaction.

The decision was made in the time between beam crossings so that no deadtime was incurred. As this thesis is based only on the data taken with the calorimeter and beam-beam triggers, we will restrict our discussion only to these.

The projective geometry of the calorimeters is preserved in the trigger but with coarser segmentation: 0.2 units in η and 15° in ϕ for all η. Outputs from all phototubes are brought to the counting room and summed into trigger towers. The gas calorimeter signals are summed into trigger towers at the detector and then brought up to the counting room. All the signals are then weighted by $\sin\theta$ of the corresponding tower to form the transverse energy deposited in the tower. To get away from electronic noise, the towers are then required to have E_t above a programmable threshold, typically 1 GeV. The signals from those towers above threshold are then summed together by detector component[46] and digitized. Digital sums are then made of the EM, hadronic and total E_t.

The presence of an inelastic $\bar{p}p$ interaction was identified by looking for hits in the beam-beam counters (BBC) which cover the angular region $0.32°<\theta<4.47°$ on each side of the interaction region. The BBC consist of two planes each with 16 time-of-flight scintillation counters, located in front (as viewed from the interaction point) of the forward and backward EM calorimeters. The counters are arranged in four quadrants of four counters each, with each counter covering approximately 0.7 units in η. The BBC system as a whole covers the region $3.2<|\eta|<5.9$. Each counter is viewed by two phototubes. A coincidence of hits in both planes was used to flag beam-beam interactions.

We will discuss the trigger threshold settings in Chapter 3.

CHAPTER 3

DATA COLLECTION, EVENT SELECTION AND RECONSTRUCTION

In this chapter we provide some of the details on how the data were collected, reconstructed, and selected for analysis. This is followed by a sampling of plots to provide some idea of the general quality of the data.

3.1 Data Collection

The data were collected at the Fermilab Tevatron during the "1987 Collider Run" which nominally began in January of 1987 and ended in mid-May of the same year. As this was an engineering run for both the accelerator and for the CDF detector, the first few months of the run were spent preparing both for serious data-taking. The data for actual physics analysis were accumulated starting around the beginning of March.

As mentioned in the previous chapter, the performance of a colliding beam machine is usually measured in terms of the luminosity, L, which is defined as follows:

$$L \equiv \frac{\text{observed event rate}}{\sigma}$$

where σ is the cross section for a $\bar{p}p$ interaction. Integrated over the course of the entire run, one obtains the "integrated luminosity" which is a measure of the number of events of a given cross section which one expects to be contained in the data collected. The integrated luminosity delivered by the accelerator during the 1987 run was 72 nb^{-1} of which approximately 33 nb^{-1} was recorded on tape.[47]

Just to be clear on this concept of integrated luminosity, 33 nb^{-1} means that if there were a process with a cross section of 1 nb ($\equiv 10^{-33}$ cm^{-2}), one would have 33 such events in the data sample. The average data-taking efficiency for the entire run was 46% (33 nb^{-1}/72 nb^{-1}) although by the end of the run, the efficiency had grown as high as 83%.[48] The sources of deadtime are as follows:

1) Approximately 15% of the collision time was lost by the need to disable data-taking during certain parts of the Main Ring cycle. The Main Ring continued to operate, even after the proton and antiproton beams were stored in the Tevatron, in order to produce antiprotons which were then collected and stored for future use. Stray particles from the Main Ring, which passed approximately five feet above the detector, caused large depositions of energy in the detector, making it impossible to measure the energy from the $\bar{p}p$ collisions when the Main Ring beam was present in the collision hall.

2) Deadtime from reading out the detector amounted to a few percent.

3) The remainder of the deadtime was caused by time to start new runs, load new gas calorimeter gains into the front-end electronics, and to change tapes. Early in the run, the time to start new runs could get quite long since the detector was still being checked out.

An event was accepted onto tape if it passed any one of the triggers described below. All the trigger threshold settings depended on the luminosity and were chosen so that the rate at which data were written to tape was approximately 1 Hz. The triggers were:

1) A "jet" trigger requiring either

    a) A transverse energy (E_t) deposition greater than 20,30,40 or 45 GeV (depending on the luminosity) summed over the entire detector, excluding the plug and forward hadron calorimeters, OR

    b) E_t > 10,15, or 20 GeV (again depending on the luminosity) in the plug and forward EM calorimeters.

Only towers with $E_t > 1$ GeV were included in the sum. The hadronic part of the plug and forward calorimeters was not included in the trigger because of problems with noise on the front-end electronics and because of the so-called "Texas towers". These were clumps of energy caused by knock-on protons traversing the sampling volume of the calorimeters at very low velocity ($p\sim1$ MeV/c), depositing much more energy than a minimum ionizing particle. Due to the relatively low sampling fraction in these calorimeters, the sensitivity to low energy particles in the hadronic cascade was magnified.[49]

2) A "central electron/muon" trigger requiring either

   a) $E_t > 7.4$, 9, 10, or 12 GeV (once again depending on the luminosity) in a single tower of the central EM calorimetry, OR

   b) A track segment in the central muon chambers with transverse momentum (p_t) greater than 5 or 10 GeV/c together with a track anywhere in the CTC with p_t greater than 3, 5.5, or 7 GeV/c.

3) A "forward muon" trigger requiring a certain pattern of hits in the forward muon drift chamber system. This trigger was rate limited to 0.05 Hz, i.e. events satisfying this trigger were accepted at the rate of only 0.05 Hz, although the rate at which this trigger requirement was satisfied was larger than that. The rate was high due to spurious hits in the chambers from beam fragments interacting in the "low-β" quadrupole magnets situated around the beam pipe in the forward region. (See Figure 4.)

4) A "minimum bias" trigger requiring one hit on each side of the interaction region in the beam-beam counters within a 15ns window centered on the beam-crossing time. This trigger was also rate limited to 0.05 Hz.

Triggers 1 through 3 required, in addition, the "minimum bias" trigger to have been satisfied. Only Trigger 1 was used in this analysis.

3.2 Event Reconstruction

The first pass through the data for the D^* analysis was to go through all the data tapes, selecting those events which passed the "jet" trigger described above. Good runs were selected on the basis of the number of "Main Ring events" per run, the average number of jets per event, problems with the monitoring of the luminosity, trigger problems, and high voltage problems. More specifically, the cuts required good runs to have $\lesssim$ 10% of the events to be Main-Ring-induced and an average number of jets (with E_t > 25 GeV) per event greater than 0.02. Approximately $1.5*10^5$ events were selected, corresponding to about 90% of the events passing the jet trigger.

3.2.1 Data "cleanup"

The events were then subjected to a series of software filters which either fixed known problems in the calorimetry data or discarded events which were not worth repairing. We should emphasize that only a small fraction of the events were affected. We will describe only those filters which affect the data in the central detector since this analysis is concerned only with jets in the central region (for which full tracking coverage exists).

1) First event after a pause in the data-taking
   This filter rejected the first event in each run as well as the first event after a long pause (> 20 sec.) in the data-taking. The reason for this was that during long pauses the voltage levels on the output of the front-end electronics drifted up to (and were pinned at) the power supply voltage, equivalent to an unphysical amount of energy deposited in the calorimeter. Approximately 0.5% of the events were rejected in this way.[48]

2) Pedestal correction[50]

The average DC offset on the front-end electronics when no
energy was deposited in the calorimeter is known as a
"pedestal". For each calorimeter tower, the pedestal value
was obtained during calibration runs taken while the beam
was off. For some channels, however, this procedure gave
unsatisfactory pedestal calibrations due to differences in
noise conditions between calibration runs and actual data-
taking. The minimum bias data (in which there is relatively
little beam-related activity in the calorimeters) were
therefore used to identify channels with significant shifts
in the pedestal value. Only two of the approximately 2300
channels in the central calorimeters had their pedestal
values corrected.[48]

3) "Hot" phototube suppression[51]

The photomultiplier tubes in the central calorimeters
experienced electric discharges at a low rate between the
photocathode and the mu-metal shielding. Since essentially
all the towers in the central calorimeters are viewed by
two phototubes, these discharges were identified by
comparing the signals in the two tubes. Using the pulse
heights in the two tubes, the width of the calorimeter
tower, and the attenuation length of the scintillator, a
shower center relative to the center of the tower was
calculated. The uncertainty in the shower position was
calculated using Poisson statistics on the total number of
photoelectrons. A signal was declared to be spurious when
the shower center was more than three sigma outside the
physical boundary of the tower. The energy in the tower was
then set to the energy seen by the other phototube. Again,
this was a small effect ($\lesssim$ 1%), although unfortunately we
have not been able to find the exact number of events which
had hot phototubes.

4) Main Ring and Cosmic Ray Induced Showers[52]

We have described earlier how the detector was gated off
during certain parts of the Main Ring cycle to veto events
caused by stray particles from the Main Ring. Some
particles, however, still managed to enter the detector
outside the veto gates. In addition, the calorimeters are
subjected to constant bombardment from cosmic ray muons,
some of which deposit significant amounts of energy via
bremsstrahlung in the calorimeter material. Both of these
types of events were identified by their timing relative to
the beam crossing time using the TDC's (Time-to-Digital
Converters) in the central and endwall hadron calorimeters.
Energy deposited outside a time window ranging from -10 to
+25 ns in the central calorimeters and between -10 and +55
ns in the endwall with respect to the beam-crossing time
was declared to be "out-of-time". Only towers with energy
greater than 1 GeV were used due to the degradation of the
timing accuracy at lower energies. Towers with times equal
to exactly 0 (again with energy greater than 1 GeV) were
also flagged as anomalous. Since the TDC's are very
efficient for energies above 800 MeV, the absence of a TDC
hit indicated that either the channel was dead or that
energy was deposited during the 150 ns interval (occurring
~200 ns before beam crossing) during which the ADC's are
enabled but the TDC's are not. The following criteria were
then used to reject events:

1) > 8 GeV in the out-of-time towers, OR

2) > 8 GeV in the towers with t=0.0.

Less than approximately 0.5% of the events were rejected.
The filter was essentially 100% efficient in rejecting Main
Ring splashes since the extent in time of the splashes was
long enough that there were always enough towers out-of-
time. For cosmic ray bremsstrahlung, it has been estimated
that the filter is around 90% efficient. The remainder of

the cosmic rays either fall within the in-time window or
shower in the EM calorimeter which was not equipped with
TDC's. We will come back to these later.

5) CTC Noise

The CTC occasionally experienced "bursts" of noise in which
noise from a few wires spread through large regions of the
chamber by electronic crosstalk between wires. The noise
was from low-energy electrons (p ~ 100 keV/c to 1 MeV/c)
from the uranium absorber in the crack detectors which are
located at 15° intervals in ϕ outside the CTC. These
detectors cover the cracks in the central calorimeter
coverage where the light guides are brought out. The
signals from such electrons are large (approximately 100
times minimum ionizing) because the electrons tend to
spiral around a single wire, causing the amplifiers on the
pulse-shaping electronics to ring. These bursts were
flagged by looking for contiguous sets of drift cells in
which all wires were hit within a narrow time window.
Approximately 1% of the events were rejected in this way.
Since 1987 the uranium has been replaced by tungsten, and
the grounding on the front-end electronics has been
fortified.

3.2.2 Jet Reconstruction

After the calorimeter energies were determined to the best of
our knowledge, jets were reconstructed, where jets are defined
operationally as localized depositions of energy in the calorimeter.
To make contact with theoretical calculations, jets are identified
with the hadronized end-product of a scattered quark or gluon. This
definition is reasonable since most of the physical particles into
which the parton materializes are observed to have a fairly limited
momentum (on the order of 400 MeV/c) transverse to the direction of

the parton. The direction of the original parton is thus fairly well preserved (at least for jets with E_t greater than approximately 15 GeV).

The jet-finding program proceeded as follows. Calorimeter towers with E_t greater than 1 GeV were selected as starting points, or "seeds", for cluster finding. The remaining towers with $E_t > 200$ MeV were then considered as candidates for clustering. "Preclusters" were formed around each seed tower by looking for an unbroken chain of adjacent towers with E_t continuously decreasing as one got further from the seed tower. Preclusters with total E_t greater than 2 GeV were then used as starting points for further clustering. The centroid of the precluster was defined by the energy-weighted mean

$$\langle \eta \rangle \equiv \frac{\sum_{towers} E_{ti} \cdot \eta_i}{\sum_{towers} E_{ti}}$$

$$\langle \phi \rangle \equiv \frac{\sum_{towers} E_{ti} \cdot \phi_i}{\sum_{towers} E_{ti}}$$

All towers above 200 MeV inside a fixed cone in η-ϕ space with a radius[53] of 1.0 with respect to the precluster centroid were then added to the precluster to form a cluster. A new centroid was calculated for this newly formed cluster and again all towers within a cone around the new centroid were merged into the cluster. For each precluster, the process was repeated until no more towers were added to the cluster.

Overlapping clusters were treated as follows. An "overlap fraction" was computed as the sum of the E_t of the common towers divided by the E_t of the smaller cluster. Two clusters were combined when the overlap fraction was greater than 0.75. This number should be treated as part of our experimental definition of a jet. In cases where the overlap fraction was less than 0.75, the clusters were kept separate and the energy in the overlapping towers was assigned to one

or the other cluster depending on the distance of the tower to the cluster centroid. After all the overlapping towers were assigned to a cluster, the centroids were recomputed and the original overlapping towers were reassigned depending on the distance to the new centroids. The process was then repeated until no towers needed to be reassigned.

Several different clustering algorithms were tried and their performance was compared with the fixed-cone algorithm described above.[54] The main tests were to compare the ability of the algorithms to resolve closely spaced jets and to see how much energy was misassigned between two nearby clusters which had not been merged. This was done with a sample of clean two jet events in which there were no other jets above 5 GeV. The calorimeter information from pairs of such events were combined, and the clustering algorithms were run on the merged event. For the first test, the fraction of time that separate clusters were merged was examined as a function of the η-ϕ separation between clusters. The fixed-cone algorithm was found to have the sharpest cutoff in η-ϕ space beyond which two separate clusters could be resolved. In the second test, the E_t of the clusters in the unmerged events was compared to those in the merged events. Again the fixed-cone algorithm was found to be the most stable with the smallest difference. In addition, the fixed-cone algorithm is thought to lend itself more naturally to theoretical calculations since it is most closely related to the way in which collinear singularities are regulated in calculations of gluon bremsstrahlung.[55] Based on these features, the fixed-cone algorithm was crowned the algorithm of choice for CDF.

Jets were reconstructed over all of the calorimeters. The E_t of the jet was computed by taking the sum of the EM and hadronic energies of the towers in the jet and multiplying by the sine of the polar angle defined by the jet energy centroid. The UA2 Collaboration has used a weighted sum of EM and hadronic energies to define the jet energy.[56] Studies with CDF jet data[57] seem to indicate, however, that in the CDF detector a simple sum provides the same jet energy resolution as a separately weighted sum.

3.2.3 Event Vertex Determination

The position of the event vertex along the beam axis was determined by finding tracks in the r-z projection in octants of the VTPC, fitting them to straight lines, extrapolating them to the beam (r=0) and then searching along the beam axis for clusters of points where the track segments intersected the beam axis. The event vertex was determined from the position of the cluster with the largest number of tracks. The precise details of this procedure are described elsewhere.[58] The vertex distribution is well described by a Gaussian with a sigma of approximately 35 cm and a mean of +3.6 cm from the nominal center of the detector. On an event-by-event basis, the vertex is determined with an accuracy of approximately 1mm where the uncertainty is dominated by systematics and comes from the lack of knowledge of the position of the VTPC relative to the rest of the detector.[59]

3.2.4 CTC Track Reconstruction

Before getting into the CTC track reconstruction program, let us briefly recall some of the features of the chamber. As we mentioned in Chapter 2, the CTC is a cylindrical drift chamber immersed in a 1.5T axial magnetic field. The sense wires are grouped into superlayers, five of which ("axial" superlayers) are strung parallel to the z-axis and the remaining four ("stereo" superlayers) which are tilted by $\pm 3°$ with respect to the z-axis. Axial and stereo superlayers alternate as one goes along the r-direction. The axial layers measure the r and ϕ coordinates of charged particles, and the stereo layers measure the z coordinate. Momentum information for charged particles is obtained by measuring the curvature of the helical trajectory of the particle in the magnetic field.

The CTC track reconstruction program is divided naturally into two parts: reconstruction of tracks in the r-ϕ projection using the axial wires, followed by full 3-dimensional reconstruction combining

the r-ϕ view with z information from the stereo wires. The r-ϕ reconstruction begins by looking in the outermost axial superlayer for a set of hits which is consistent with a line segment crossing the sense wire plane. Once such a segment is found, the search for other hits from this potential track is conducted both inward and, when possible, outward in a circular road passing through the segment and the z-axis. The search is repeated, using a better starting approximation of the trajectory on each iteration, until no more acceptable hits are found. The search for "seed" segments not already associated with tracks continues inward through all the axial superlayers.

The z reconstruction uses the track parameters determined in the r-ϕ reconstruction to look for line segments in each of the stereo superlayers whose slopes relative to the predicted position of the track (at z=0) are small. The z position of each segment is determined from the r-ϕ distance between the segment and the location of the track at z=0. Once line segments have been selected as candidates for the track, the segments which best match the track are found by fitting all combinations of segments (there can be several segments per stereo superlayer) to a linear function in z and ϕ. The set of segments with the smallest χ^2 is then used to get a first approximation of the polar angle of the track. The search for stereo hits is then repeated from scratch, this time using the approximate polar angle to restrict the search region.

A fit to a helix is then performed. The helix is described by five parameters:

1) Half-curvature, C. This is the inverse of the diameter of the circle traced out by the particle in the r-ϕ plane. It is a signed quantity, where the sign depends on the charge of the particle.

2) Distance of closest approach, D, also known as the impact parameter. This is the shortest distance in the r-ϕ plane between the track and the origin. It is easy to show that this is the distance between the track circle and the origin measured along a line passing through the center of the circle and the origin. The impact parameter is also a signed quantity where the sign depends on the charge of the

particle and whether or not the origin is enclosed by the track circle.

3) Azimuthal angle, ϕ_0. This is the azimuthal angle of the tangent to the track at the point of closest approach.

4) $\cot\theta$, where θ is the polar angle of the track at the point of closest approach.

5) Z_0, the z position of the track at the point of closest approach.

3.2.5 Vertex Constrained Track Fitting

Tracks with an impact parameter less than 0.5 cm were refit with the added constraint that they pass through the event vertex, the position of which is measured with the VTPC to higher precision than the pointing accuracy of the CTC itself. The method used to constrain the tracks to the vertex is described in detail in the literature.[60] We give a brief summary here. The functional dependence of the five track parameters (denoted by the vector $\vec{p}$) on the position of the event vertex ($\vec{x}$) and the track momentum ($\vec{q}$) at the vertex is written as a linear expansion about approximate values of $\vec{x}$ and $\vec{q}$ (denoted by $\vec{x}_0$ and $\vec{q}_0$) as follows:

$$\vec{p} = \vec{p}_0 + A \cdot (\vec{x} - \vec{x}_0) + B \cdot (\vec{q} - \vec{q}_0) \qquad [3.1]$$

where A and B are the following 5-by-3 matrices

$$A = \begin{bmatrix} \dfrac{\partial p_1}{\partial x} & \dfrac{\partial p_1}{\partial y} & \dfrac{\partial p_1}{\partial z} \\ \vdots & & \vdots \\ \dfrac{\partial p_5}{\partial x} & \cdots & \dfrac{\partial p_5}{\partial z} \end{bmatrix} \qquad B = \begin{bmatrix} \dfrac{\partial p_1}{\partial q_x} & \dfrac{\partial p_1}{\partial q_y} & \dfrac{\partial p_1}{\partial q_z} \\ \vdots & & \\ \dfrac{\partial p_5}{\partial q_x} & \cdots & \dfrac{\partial p_5}{\partial q_z} \end{bmatrix}$$

and where p_1 through p_5 denote the five track parameters. Both matrices are evaluated at $(\vec{x}_0, \vec{q}_0)$. The vectors $\vec{x}$ and $\vec{q}$ are determined by minimizing a chi-square which is formed between the measured track parameters $\vec{p}_{obs}$ and the track parameters, $\vec{p}_{exp}$, calculated with equation 3.1, i.e.

$$\chi^2 = (\vec{p}_{obs} - \vec{p}_{exp})^T \cdot G \cdot (\vec{p}_{obs} - \vec{p}_{exp})$$

where G is the inverse of the 5-by-5 covariance matrix of the measured track parameters. The values of $\vec{x}$ and $\vec{q}$ determined in this way are then plugged into equation 3.1 to obtain the vertex constrained track parameters.

Multiple scattering in the material before the sensitive volume of the CTC (< 5% of a radiation length) was neglected. There was a provision in the fitting routine to take multiple scattering into account by appropriately incrementing the covariance matrix of the track parameters, but this was found to have only a small effect on the results of the vertex constrained fit.[61]

3.2.5.1 The Beam Position

We have described earlier how the position of the z-component of the event vertex was determined from the r-z projections of tracks in the VTPC. We now describe how the x,y components of the vertex, namely the beam position, were determined with respect to the CTC. In the approximation that the radius of curvature of the track is much larger than the impact parameter (a condition that is met by all observed tracks), one can show that the dependence of the impact parameter, D, for primary tracks on ϕ_0 is given by

$$D = -x_{Beam} \sin\phi_0 + y_{Beam} \cos\phi_0 . \qquad [3.2]$$

Writing the beam position as a linear function of z, i.e.

$$x_{Beam} = a_x + b_x z$$
$$y_{Beam} = a_y + b_y z$$

the parameters a_x, b_x, a_y, and b_y were determined by fitting the impact parameter of 3-dimensional tracks versus the z-intercept and ϕ_0 according to the form given by equation 3.2. If the χ^2 contribution of a track was greater than 10 (where the σ on the impact parameter was set to 500 μm), it was set to 10 so as to keep the fit from getting pulled by poorly measured or non-primary tracks.

The beam position constants which we used were derived from the minimum bias data and are as follows:

$$a_x = -550 \ \mu m \qquad\qquad a_y = -130 \ \mu m$$
$$b_x = \ \ 2.8 \ \mu m/cm \qquad\qquad b_y = -1.0 \ \mu m/cm$$

A systematic error of 60 μm was assigned to both the x and y coordinates of the beam. As a check of the beam position, we repeated the analysis for the jet data; the results are summarized in Figure 8 for three values of z. The boxes mark the limits of the beam coordinates obtained from the minimum bias data. The difference is probably due to the fact that the minimum bias analysis used an earlier version of the track reconstruction program. Whatever the reason, we felt that the difference was not large enough to warrant refitting all the tracks with run-by-run beam position constants. Our reasoning was that masses which are reconstructed from two oppositely charged tracks (e.g. the D^0) should not be terribly sensitive to small changes in the beam position because the increase in momentum of one track is balanced by a decrease in that of the other.

3.3 Event Selection

Starting with approximately $1.5 \cdot 10^5$ triggers, a first reduction of the data was achieved by requiring the leading jet, i.e.
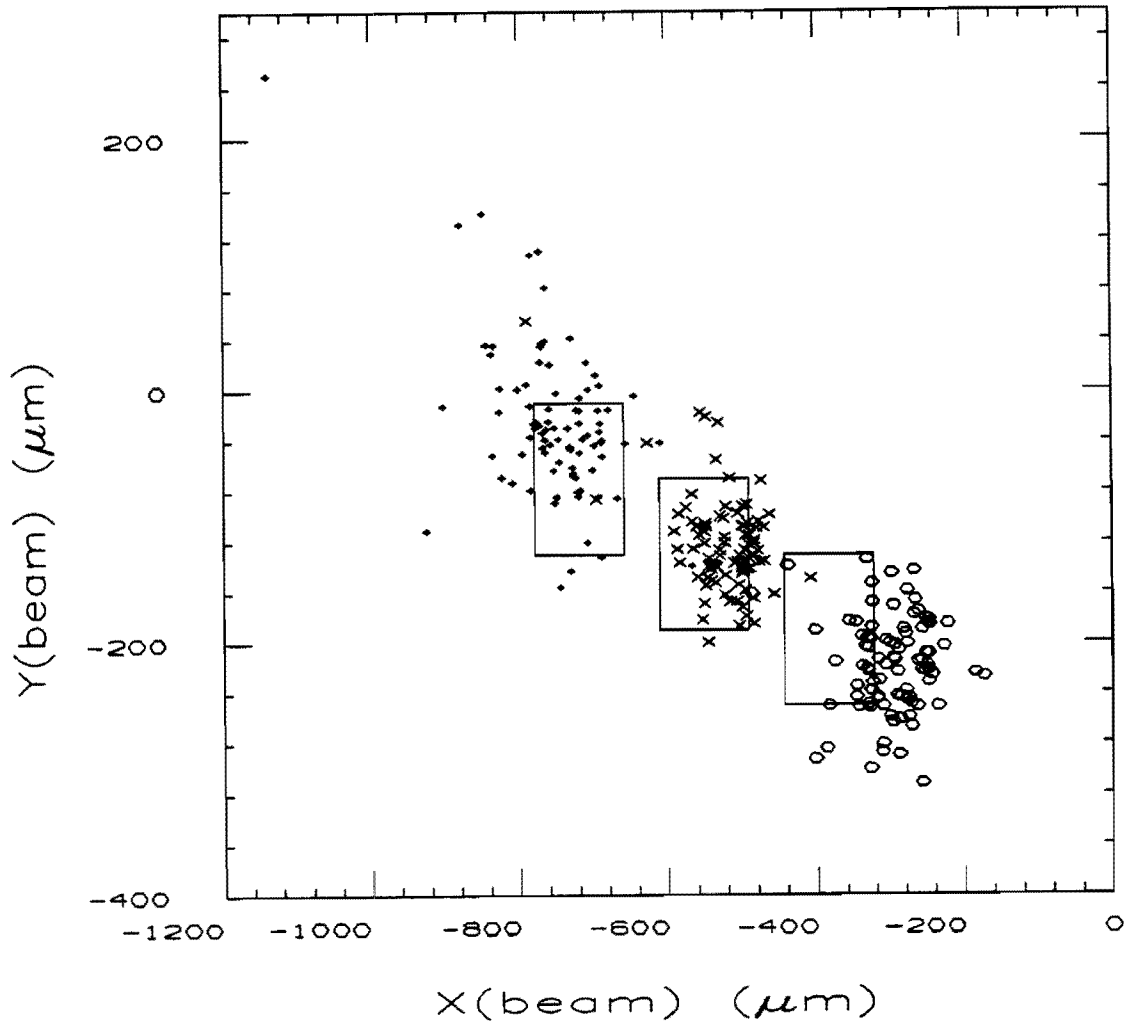
Figure 8. A scatterplot of the x and y positions of the beam for the runs selected for the D* analysis. The positions are shown for three values of z: -60cm (dots), 0 (crosses) and +60cm (circles). The boxes mark the limits of the beam position as determined from fits using the minimum bias data.

the one with the highest E_t, to have E_t greater than a threshold depending on the trigger hardware threshold as follows:

Trigger threshold (GeV)	Leading jet threshold (GeV)
20	20
30	25
40	40
45	40

Only jets with an EM fraction, i.e. (EM E_t)/(Total E_t), greater than 0.01 were considered in order to cut out cosmic ray showers in the hadron calorimeter which were in-time with the beam-crossing. This reduced the sample to approximately $6.5 \cdot 10^4$ events.

Only a subsample of these events were subjected to further selection cuts. Because the track reconstruction program requires a fair amount of CPU time (on the order of 40 sec. per event on the VAX 8600), it was impossible to track all of the selected events, given the heavy load on the Fermilab computing resources at the time. As a result only $4.3 \cdot 10^4$ of the approximately $6.5 \cdot 10^4$ events selected were actually tracked. Events were then required to have at least one well-measured track (to reject events in which the CTC was temporarily off) and a vertex within 60 cm of the center of the detector, reducing the number of events to $3.8 \cdot 10^4$. Figure 9a is a distribution of the number of tracks per event before the cut was applied on this quantity. Figure 9b shows the event vertex distribution along with a Gaussian fit.

Further cuts were applied to select the jets for this analysis. To ensure that the jets were well-contained within the central calorimeter, jets were required to have an energy centroid in the range $0.1 < |\eta| < 0.8$. Figure 10 shows the jet η distribution on which these cuts were applied. The rapid falloff in the distribution for $|\eta| \gtrsim 1.0$ is due to the fact that the hadronic part of the calorimeters in this region was not included in the trigger. There is also a dip at the center due to the crack in the detector where the two halves of the central detector meet. Energy lost in the
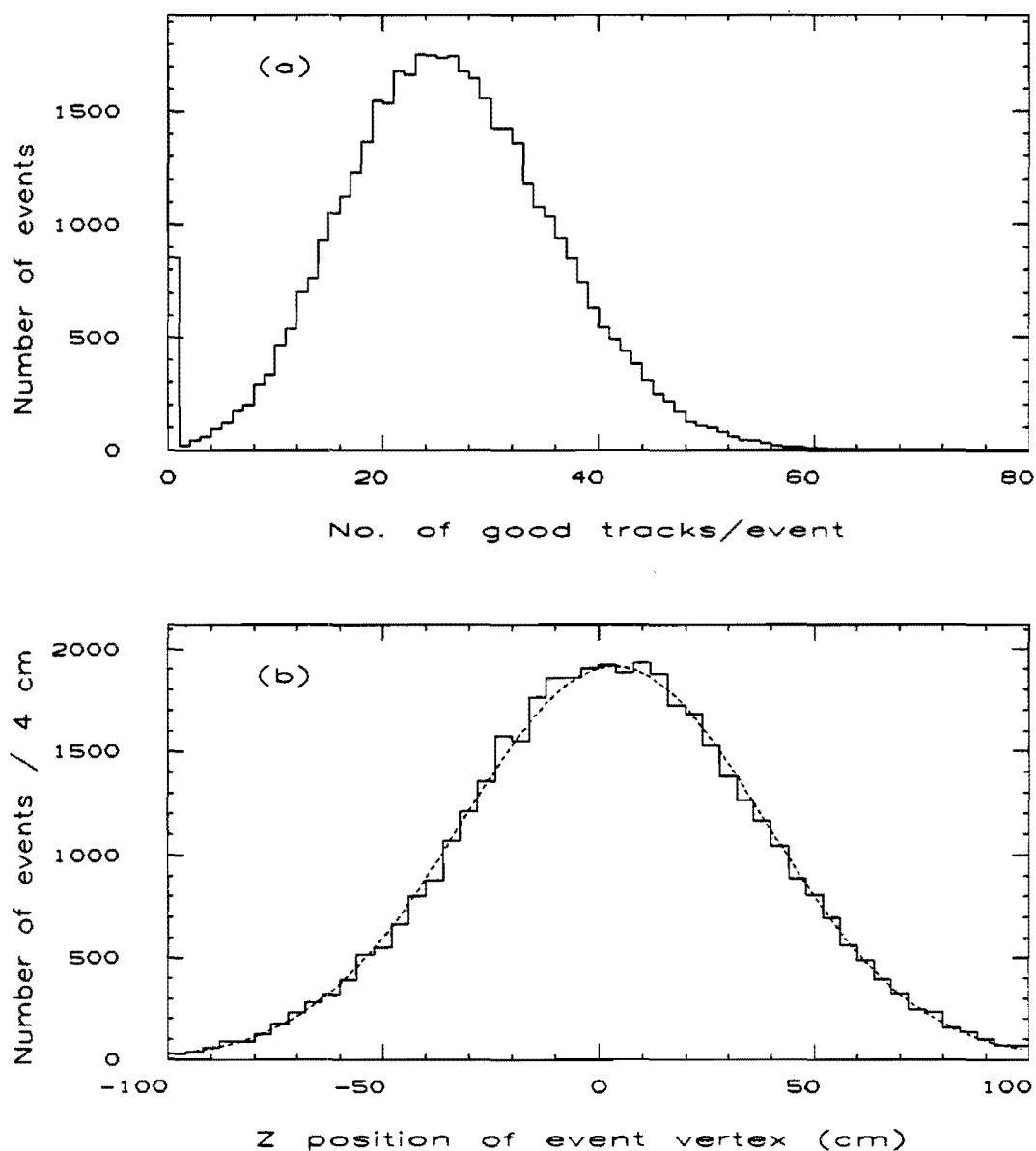
Figure 9. Distributions of the number of tracks per event and the z-position of the event vertex. a) The number of well-measured tracks per event in the tracked jet data. b) The distribution of the z-position of the event vertex together with a Gaussian fit.
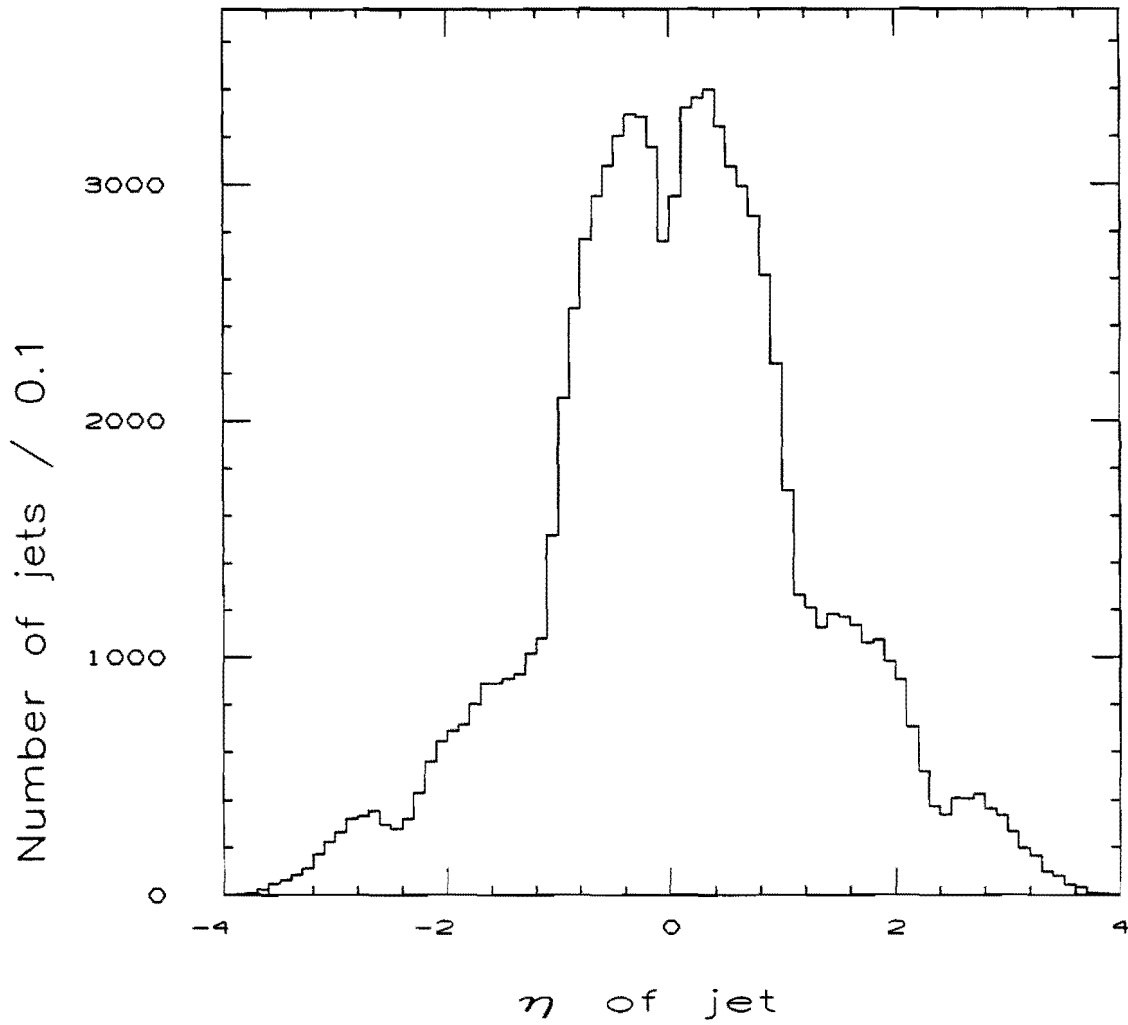
Figure 10. The η distribution of jets with E_t (uncorrected) greater than 10 GeV. The jets are from events passing the event selection criteria for this analysis.

uninstrumented crack caused fewer jets in this region to pass the trigger requirement.

The jet energies were then corrected for the following effects: 1) the nonlinear response of the calorimeter to low-energy charged particles, 2) energy deposited in uninstrumented regions, 3) energy lost outside the clustering cone, and 4) energy gained from the "underlying event", i.e. that energy which is not associated with the hard parton scattering. These corrections are described in more detail in Appendix C. For typical jets in this analysis, the correction increased the jet energy by 25%. The corrected E_t of the jets was then required to be greater than 30 GeV. Figures 11a-11d show the corrected jet E_t distributions for the four jet trigger thresholds before the 30 GeV cut was applied. The sharp edges in the plots reflect the cut on the leading jet E_t applied early in the event selection process. The E_t distribution for the jets used in the D^* search is shown in Figure 11e. Table 1 summarizes the cuts applied to select our sample of events and jets.

3.4 Jet Data Quality

We conclude this chapter with a small collection of plots to give a flavor of the quality of the jet data (Figure 12). The tracking data will be addressed in the next chapter. The azimuthal separation of the two leading jets in each event is peaked at 180°, indicating the dominance of two-jet events. The jet ϕ distribution shows the expected azimuthal symmetry, indicating the absence of any "hot" towers in the calorimeters. The "charged fraction", which we have defined as the scalar sum of the p_t of well-measured tracks within a cone of radius $\Delta R=1.0$ about the jet axis divided by the corrected jet E_t, shows a slight excess at 0, indicating that there is still some residual contamination from cosmic rays perhaps, but less than 0.2% in any case.

Table 1. A summary of the sample of events and jets used in this analysis, separated by trigger threshold.

	20 GeV	30 GeV	40 GeV	45 GeV	Total
Integrated luminosity (nb^{-1})					
For jet triggers	0.4	14.6	5.9	6.0	26.9
For tracked runs	0.1	9.1	5.9	6.0	21.1
Number of events: $(*10^3)$					
# of jet triggers	15.9	103.9	17.3	12.8	149.9
Estimated # of events selected to be tracked	5.4	50.6	4.3	4.6	64.9
# of events tracked	1.9	32.0	4.3	4.6	42.8
# of events after event selection cuts:					
a) ≥ 1 track in event	1.9	31.3	4.2	4.5	41.9
b) $|Z\ vertex| < 60$ cm	1.6	28.4	4.0	4.3	38.3
Number of jets: $(*10^3)$					
# of jets after event selection cuts (with E_t (uncorrected) > 10 GeV)	3.5	66.9	9.8	10.5	90.7
# of jets after jet selection cuts:					
a) $0.1 < |\eta| < 0.8$	1.7	33.1	4.4	4.8	44.0
b) E_t(corrected)>30 GeV	0.7	23.8	3.7	4.1	32.3
Mean jet E_t (GeV) after all cuts	39.0	42.7	58.8	59.7	46.6

Figure 11. The corrected E_t distribution of jets. (a) - (d) The corrected E_t distribution of jets after the η cut, separated by trigger threshold. (e) The corrected E_t distribution of the jets used in the D^* search.
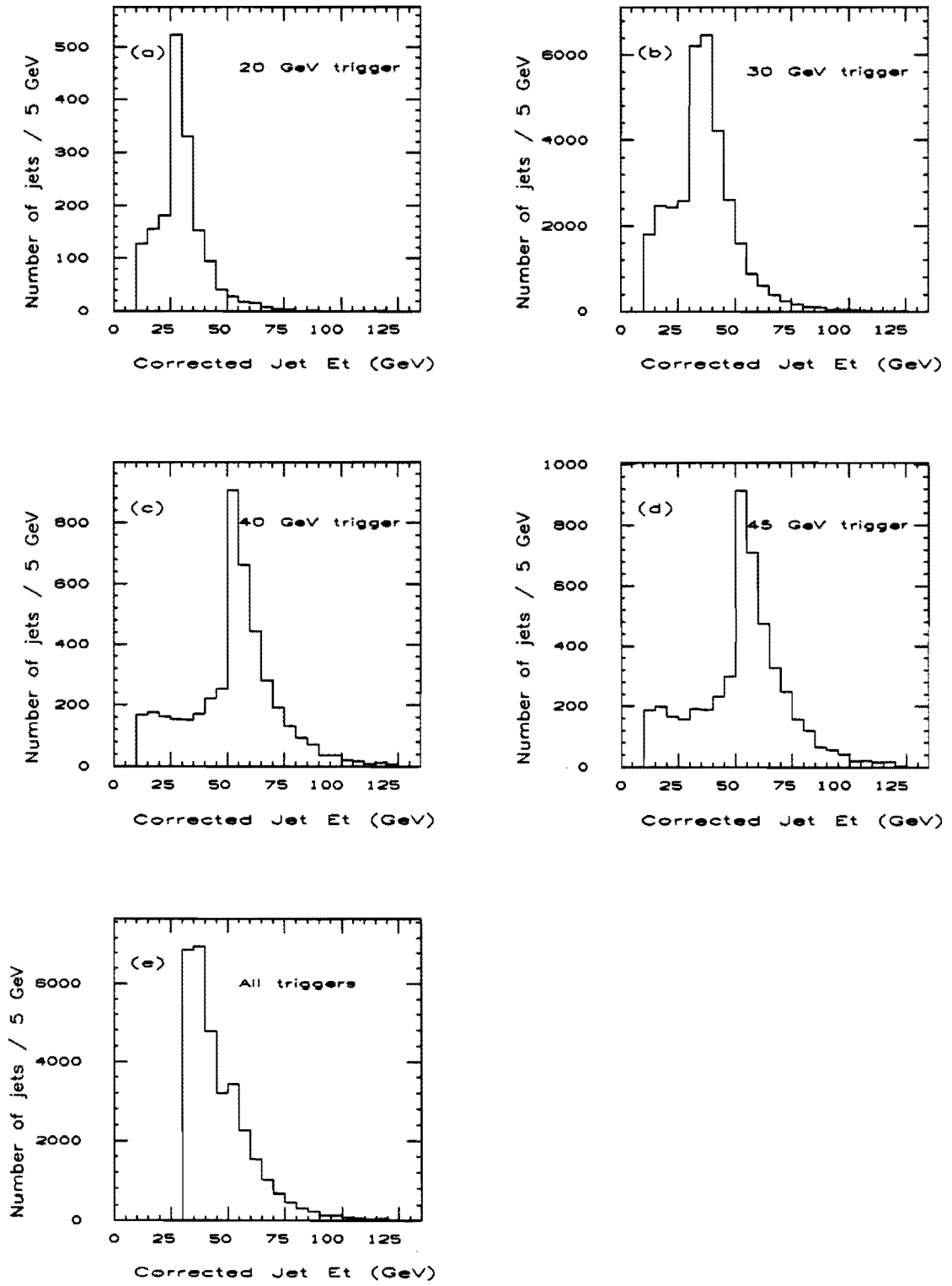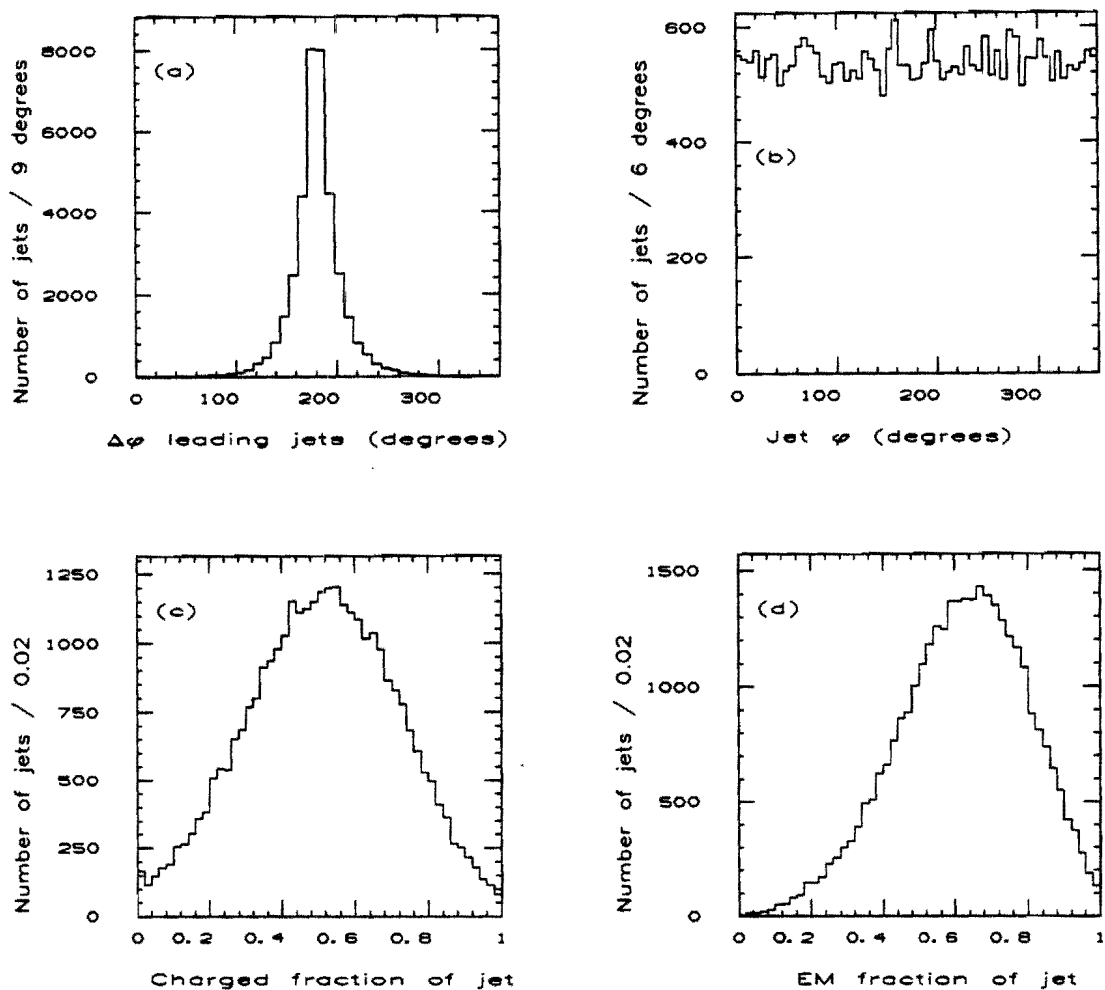
Figure 12. Distributions showing the quality of the jet data. a) The difference in azimuthal angle between the two highest E_t jets in each event shown after all the event selection cuts. b) The distribution of the azimuthal angle of all jets surviving the event and jet selection cuts. c) The "charged fraction" of the jets after all the event and jet selection cuts. d) The "EM fraction" of the jets after all the event and jet selection cuts. The EM fraction is defined as the ratio of the electromagnetic energy of the jet to the total jet energy.

CHAPTER 4

SIGNAL EXTRACTION

In this chapter the details of the extraction of the D^* signal are described. A discussion of the method of searching for the signal is followed by a description of the cuts applied to the data. The estimation of the signal and background are then described.

4.1 Method

The method used to search for D^*s is the well-known scheme[62] described in Chapter 1. To reiterate, one looks for the decay sequence

$$D^{*+} \rightarrow D^0 \pi^+$$
$$D^0 \rightarrow K^- \pi^+$$
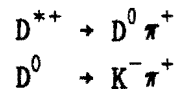
as well as the charge-conjugate mode by forming $K-\pi$ and $K-\pi-\pi$ mass combinations using tracks from the CTC. A D^* signal appears as a statistically significant enhancement in the number of mass combinations with a $K-\pi$ mass equal to the D^0 mass and a $K-\pi-\pi$ mass equal to the D^* mass.

The power of this method lies in the fact that the D^*-D^0 mass difference $(145.45 \pm 0.07 \text{ MeV/c}^2)$[10] is only slightly larger than the pion mass, resulting in a very small Q value for the D^* decay into $D^0 \pi$. In other words, in the D^* rest frame the D^0 and the π are almost at rest. The background, on the other hand, arises from random track combinations which have a low probability of being at rest in the center of momentum frame. This turns out to be the main handle on

background rejection.

Another handle is provided by the fact that we have two mass constraints, one on the K-π mass and the other on the K-π-π mass. In practice, one looks at the K-π-π, K-π mass difference rather than simply the K-π-π mass because some of the track reconstruction errors cancel in the difference, improving the mass resolution. The resolution on the mass difference is dominated by the momentum resolution on the pion from the D* decay to D$^0\pi$, which is relatively good. Due to the small Q value of the reaction, the momentum of the pion is very low (approximately 39 MeV/c in the D* rest frame and typically 400 MeV/c in the lab frame) so that it is measured with a precision limited by multiple scattering. (We will refer to this pion as the "slow pion".) This method also has the feature that the number of decay products is low, which helps to lower the number of random track combinations. Another important feature is that the sign of the two pions is always the same (given the low probability of D^0-$\bar{\text{D}}^0$ mixing).

The major difficulty of this method in jet events is the large number of random track combinations. The jets in our sample typically contain 10 tracks inside a cone of radius ΔR=1 (Figure 13). The typical number of right-sign 3-track combinations is about 300 per jet. At the same time, the branching ratio for this decay sequence is rather small. The latest numbers from the 1988 Particle Data Book are

$$\text{BR}(\text{D}^{*+} \to \text{D}^0\pi^+) = 49 \pm 7 \ \%$$

$$\text{BR}(\text{D}^0 \to \text{K}^-\pi^+) = 3.77 \ {}^{+ \ 0.37}_{- \ 0.32} \ \%$$

resulting in an overall branching ratio around 1.9%. One is therefore asking for an overall rejection on the order of

$$\frac{\text{\# of combinations per jet}}{\#(\text{D}^*)/\#(\text{jet}) \cdot 1.9\%} = \frac{16000}{\#(\text{D}^*)/\#(\text{jet})}$$
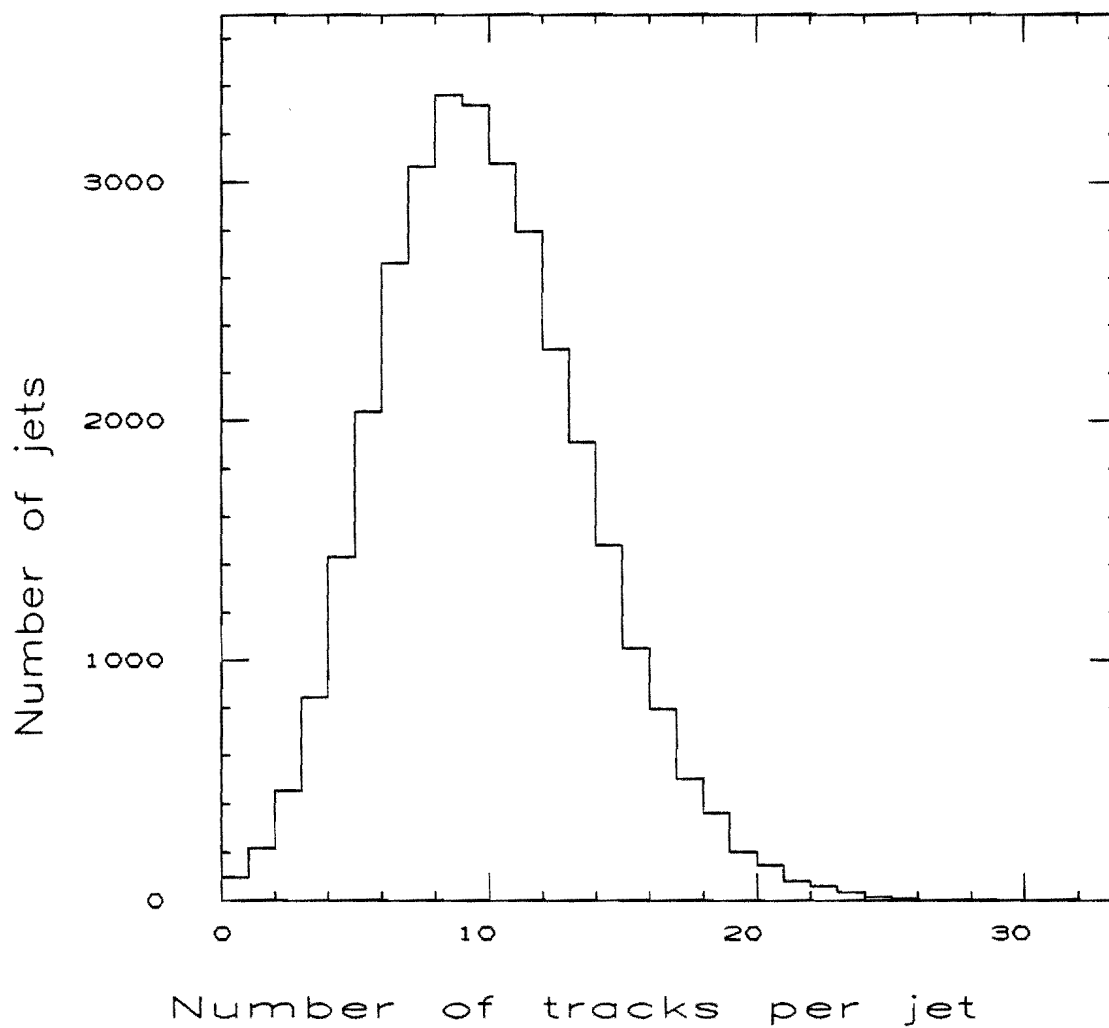
Figure 13. The number of tracks inside a cone of radius ΔR=1.0 with respect to the jet axis. This distribution is from the data.

Clearly particle identification (say at the level of rejecting pions in favor of kaons) would be a great help in reducing the combinatorics. One possibility along these lines is to look for

$$D^0 \rightarrow K_s + \text{charged tracks}$$
$$K_s \rightarrow \pi^+\pi^-$$

using the secondary vertex to identify the kaon. When one goes through the numbers, however, one finds that the branching ratios are too small to be of use in our data. Possible modes from the Particle Data Book are:

$$D^0 \rightarrow \bar{K}^0 \pi^+\pi^- \qquad BR = 5.6 \; {}^{+\, 0.7}_{-\, 0.6} \; \%$$

$$D^0 \rightarrow \bar{K}^0 K^+ K^- \qquad 1.16 \; {}^{+\, 0.25}_{-\, 0.22} \; \%$$

Assuming 50% of K^0s are K_s and using the branching ratio $K_s \rightarrow \pi^+\pi^- \sim$ 69% one obtains BR($D^0 \rightarrow K_s + \text{charged}$) $\sim$ (0.5)(0.69)(0.056+0.012) = 0.023 which is starting to get too small, given the size of our data sample. Furthermore, the efficiency for reconstructing the K_s has not yet been included. In addition, the advantage gained by the particle identification is partially offset by the fact that there are more charged tracks in these modes.

One other possible set of decay modes which can be considered is

$$D^0 \rightarrow K^-\rho^+ \rightarrow K^-\pi^+\pi^0 \text{ and}$$
$$D^0 \rightarrow K^{*-}\pi^+ \rightarrow K^-\pi^0\pi^+$$

where the π^0s are not identified. At e^+e^- colliders this gives rise to the so-called "satellite peak" at a mass of around 1.6 GeV/c^2.[63] Although the π^0s are not observed, the ρ direction can be estimated rather well since the charged pion tends to be emitted along (or opposite to) the ρ direction (due to the fact that the ρ is spin-1). What makes these modes worth some inspection is that the sum of the

branching ratios is around 13%; putting in a factor of 0.5 for the pions emitted backwards, this still amounts to 1.7 times the branching ratio to $K\pi$. The utility of this mode was investigated using a simple Monte Carlo which generated 5 GeV/c D^0s decaying to $K^-\rho^+ \rightarrow K^-\pi^+\pi^0$ and reconstructing the resulting invariant masses without putting in any detector resolution or efficiency. Unlike the e^+e^- case, our mass cuts have to be quite tight to beat down the combinatoric background; it therefore becomes difficult to take advantage of the "satellite peak" which, though definitely peaked, is still quite broad (Figure 14). For the cuts $1.61 < M_{K\pi} < 1.66$ GeV/c^2 and $144.5 < \Delta M < 146.5$ MeV/c^2, the relative contribution of this decay mode was found to be

$$\frac{\#(D\rightarrow K\rho) + \#(D\rightarrow K^*\pi)}{\#(D\rightarrow K\pi)} \sim 0.13$$

which is pretty useless. The upshot of all this is that our best bet is to stick with the $D^0 \rightarrow K\pi$ mode.

4.2 The Cuts

We began by applying a set of loose selection cuts to the CTC tracks in order to throw out those which were very poorly defined. The cuts were:

1) The track was required to be reconstructed in 3 dimensions.

2) The track was required to have:
    a) $|\eta| < 1.2$
    b) $p_t > 300$ MeV/c.

3) The impact parameter was required to be less than 0.5 cm. (Recall that the vertex-constrained fit was applied only to tracks with an impact parameter less than 0.5 cm.)

4) The number of hits used in the track fit was required to be greater than 50% of the number of hits the track would be expected to have, given its track parameters and the location of dead cells.[64]
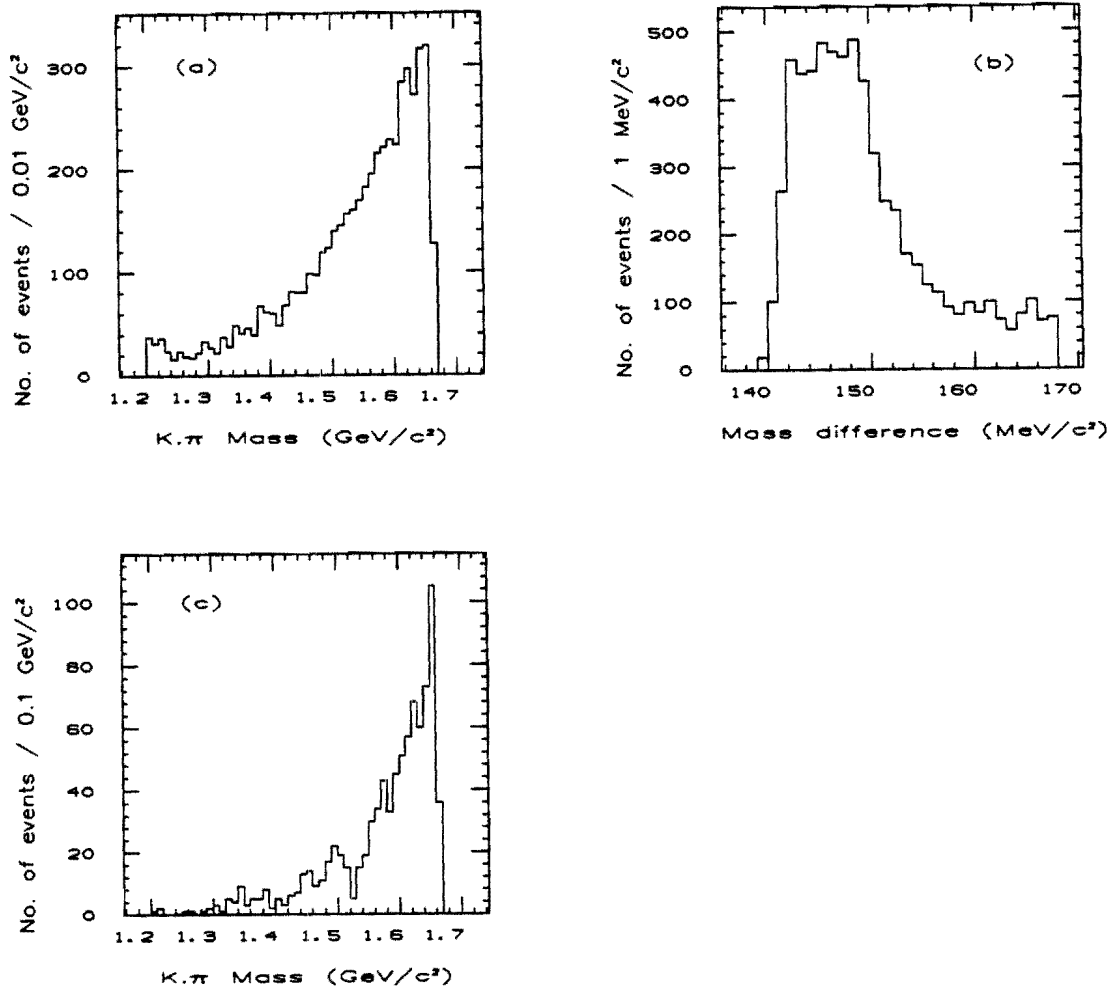
Figure 14. Mass distributions from a simple Monte Carlo for the decay sequence: $D^{*+} \rightarrow D^0 \pi^+ \rightarrow K^- \rho^+ \pi^+ \rightarrow K^- \pi^+ \pi^0 \pi^+$. (a) The distribution of the K, π^+ mass in $D^0 \rightarrow K^- \rho^+ \rightarrow K^- \pi^+ \pi^0$ decays. (b) The mass difference $\Delta M \equiv M_{K\pi\pi} - M_{K\pi}$ in the decay sequence $D^{*+} \rightarrow D^0 \pi^+ \rightarrow K^- \rho^+ \pi^+ \rightarrow K^- \pi^+ \pi^0 \pi^+$ where the π^0 is not observed. (c) The K, π mass from the decay sequence of (b) when one requires the mass difference $M_{K\pi\pi} - M_{K\pi}$ to be very close to the D^{*+} D^0 mass difference, namely between 144.5 and 146.5 MeV/c^2.

5) $\geq$ 2 "good" axial segments where a "good" segment is defined as one with 8 or more hits (out of a possible 12 in an axial superlayer).

6) $\geq$ 1 "good" stereo segments where "good" means 4 or more hits per segment (out of a possible 6 in a stereo superlayer).

Figure 15 shows the distributions of the quantities on which the cuts were placed. The cuts are placed in the order described above, and each distribution includes only those tracks which passed the cuts which preceded it. The effect of these cuts is summarized in the table below. (The "percentage" is defined as the fraction of tracks which have passed all the preceding cuts.)

	Percentage of tracks lost to each cut
3D track	0 by definition
$|\eta| < 1.2$	10.9
$p_t > 300$ MeV/c	3.4
|Impact parameter| < 0.5 cm	5.0
$>$ 50% of expected number of hits	5.8
$\geq$ 2 good axial segments	1.6
$\geq$ 1 good stereo segment	0.2

A total of 24.4% of the three-dimensional tracks were cut.

Looping over all tracks in the event which passed the selection cuts, K-π and K-π-π mass combinations which satisfied the pion charge requirements were then formed. Both kaon and pion assignments were tried for all tracks. To save CPU time, we rejected outright all combinations which failed either of the following cuts: $1.5 < M_{K\pi} < 2.4$ GeV/c^2 or $138 < \Delta M < 178$ MeV/c^2. To associate the K-π-π combination with a jet, the K-π-π system was required to be in the same hemisphere as a jet.

This was followed by a cut on the K-π mass modified to take into account our knowledge of the tracking resolution. Track parameter

Figure 15. Distributions for tracks from the data sample. (a) The η distribution for 3D tracks. (b) The p_t distribution of tracks after requiring $|\eta| < 1.2$. (c) The impact parameter distribution after requiring $p_t > 300$ MeV/c. (d) The ratio of the number of hits used in the track fit to the number of hits expected on the track, shown after requiring $|$impact parameter$| < 0.5$cm. (e) The number of good axial segments on the track after the ratio cut requiring the ratio > 0.5. Good segments were defined as those with 8 or more hits. (f) The number of good stereo segments on the track after requiring ≥ 2 good axial segments. Good stereo segments were defined as those with 4 or more hits.
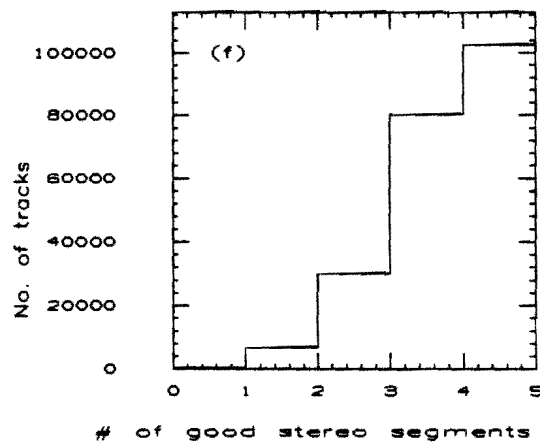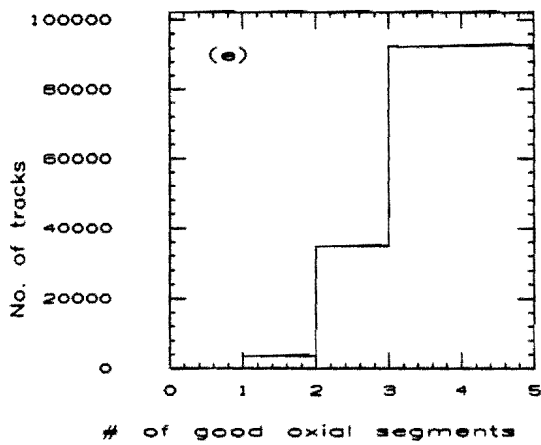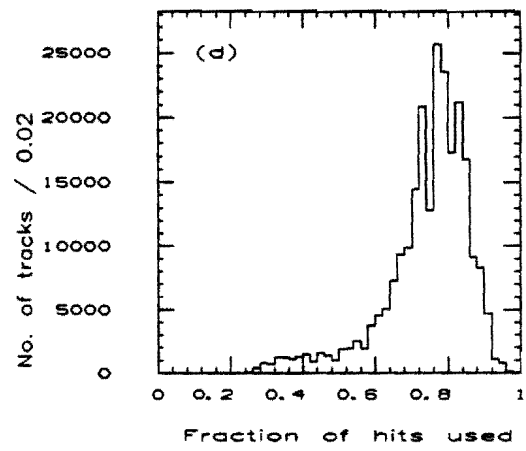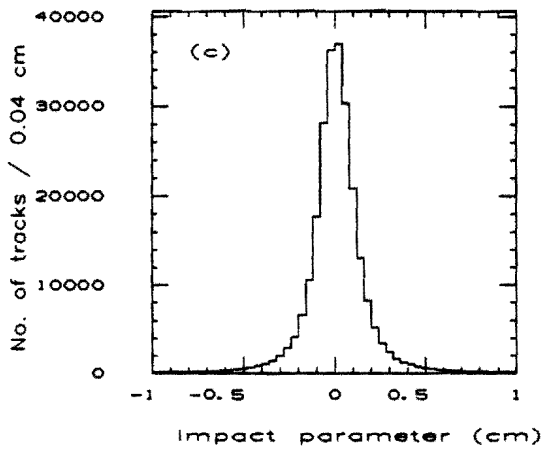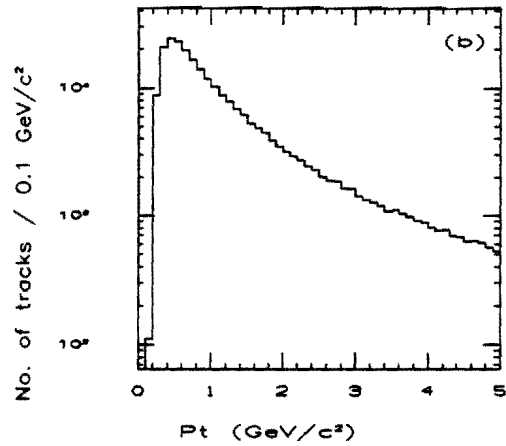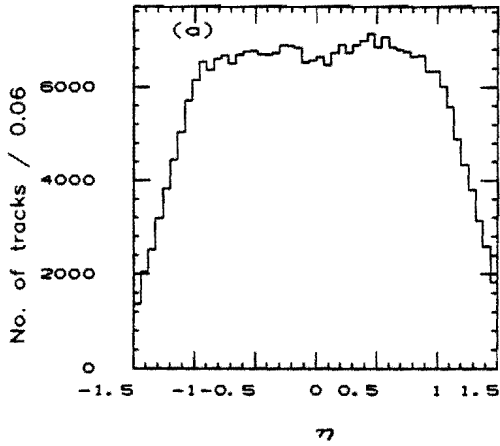
measurement uncertainties were estimated with a sample of jet data into which Monte Carlo D^* tracks were injected. (The details of the determination of the track parameter uncertainties are described in Chapter 6.) The uncertainty on the mass of each K-π pair was then estimated according to the error propagation formula:

$$\delta = \left\{ \sum_{K,\pi} \left[\left(\frac{\partial M}{\partial p_{ti}}\right)^2 (\Delta p_{ti})^2 + \left(\frac{\partial M}{\partial \phi_i}\right)^2 (\Delta \phi_i)^2 + \left(\frac{\partial M}{\partial (\cot \theta_i)}\right)^2 (\Delta \cot \theta_i)^2 \right] \right\}^{1/2}$$

where we have ignored the correlation terms between the track parameters. The values used for the track parameter uncertainties were:

$$\frac{\Delta p_t}{p_t} = \sqrt{(0.0012 p_t)^2 + (0.004)^2} \quad \text{with } p_t \text{ in units of GeV/c}$$

$$\Delta \phi = \sqrt{(0.3)^2 + (1.0/p_t)^2} \quad \text{mrad}$$

$$\Delta (\cot \theta) = 0.0022.$$

We then required $|M_{K\pi} - M_{D^0}| < 3\delta$. We felt that this was better than a straight mass cut because it cuts harder on well-measured track combinations and softer on poorly measured combinations. Figure 16a shows the distribution of $(M_{K\pi} - M_{D^0})/\delta$ for the Monte Carlo D^*s merged with the jet data. The distribution is well described by a Gaussian with a standard deviation (σ) of approximately 1. Since we are propagating 1σ uncertainties on the track parameters, this indicates that the correlation terms in the error propagation formula are small. Figure 16b shows the distribution of δ itself; the mean value of δ from the histogram is 19 MeV/c^2. Figure 17 shows the $M_{K\pi}$ distribution from the data, illustrating the shape of the δ cut. There is one entry
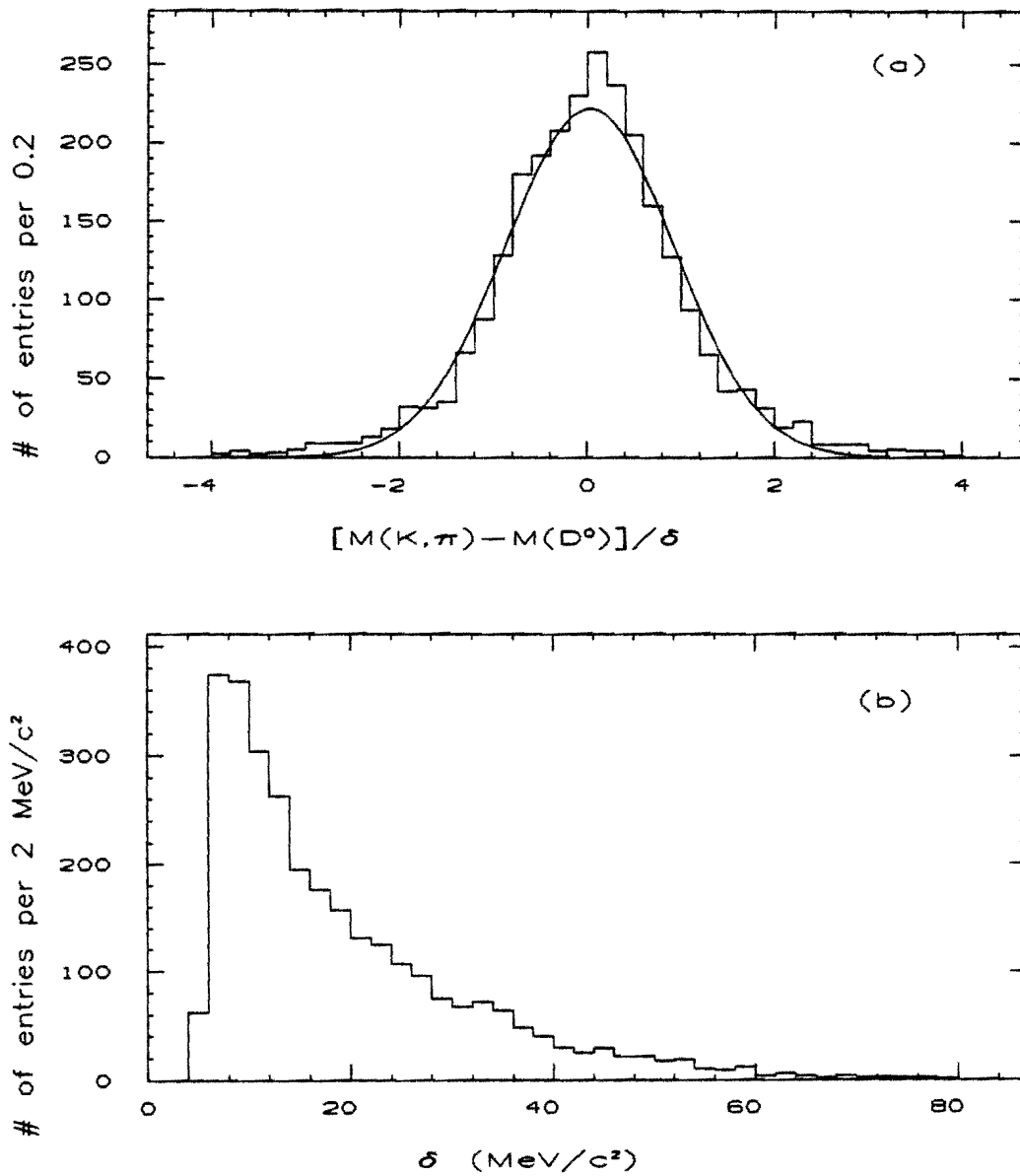
Figure 16. Distributions for the quantity δ. (a) The distribution of $|M_{K\pi} - M_{D^0}|/\delta$ for Monte Carlo D^*s which were mixed into real jet data. The curve is a Gaussian fit to the histogram; the σ of the Gaussian is 0.90. (b) The distribution of δ for the Monte Carlo D^*s which were mixed into the jet data.
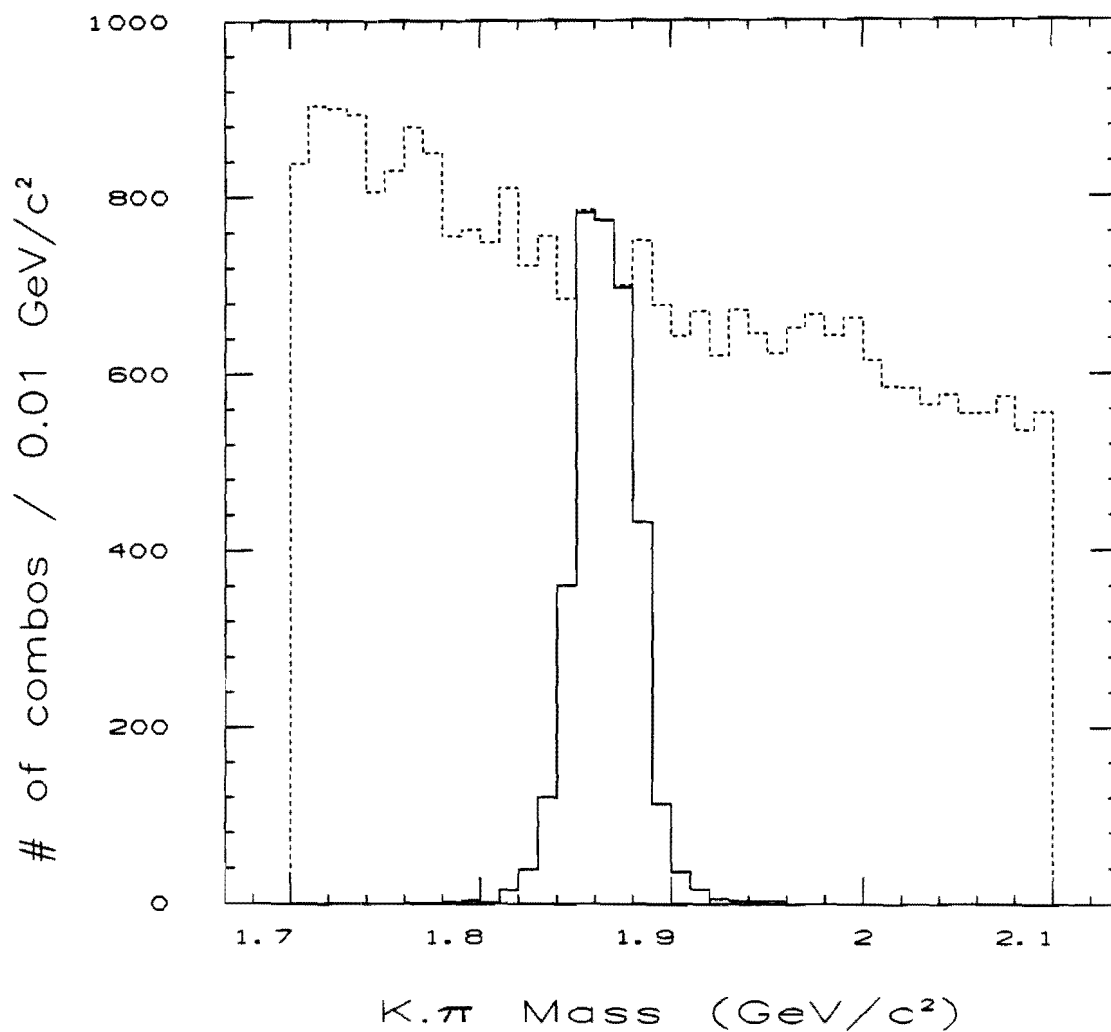
Figure 17. The shape in $M_{K\pi}$ of the δ cut. The dotted lines are a histogram of $M_{K\pi}$ from the data where there is one entry for every 3-track combination satisfying $138 < \Delta M < 178$ MeV/c^2. The solid histogram shows the distribution of $M_{K\pi}$ when one requires $|M_{K\pi}-M_{D^0}| < 3\delta$.

for every 3-track combination satisfying $138 < \Delta M < 178$ MeV/c^2. The δ cut is shaped so that one is able to retain a higher efficiency for the signal without letting in as much background as a straight cut would for the same efficiency. Note also that since the mass difference is relatively insensitive to errors in the reconstructed D^0 mass, the mass difference comes out more-or-less correct even for those D^{0}s which have reconstructed masses that differ considerably from the correct value but are picked up by the δ cut.

The next cut was on the so-called "helicity angle", θ_H, which is the polar angle of the kaon in the D^0 rest frame. (Here, the polar angle is defined with respect to the boost axis of the D^0.) Kaons from real D^0 decays will be distributed isotropically, i.e. flat in $\cos\theta_H$, since the D^0 is spin-0. Background combinations, however, peak at $\cos\theta_H = \pm 1$ (Figure 18). This is due to the fact that the typical opening angle between tracks in jets is small compared to the opening angle between the products of D^0 decays (at least for D^{0}s with $p \lesssim 10$ GeV/c). Figure 19 shows the relation between $\cos\theta_H$ and the opening angle between the K and the π in the lab frame for a 5 GeV/c D^0 decay. We see that most of the decays occur in a narrow band of opening angle between 40 and 50 degrees. On the other hand, random track pairs in jet events tend to come in one of two configurations. Either the tracks come from the same jet and are very close to one another in the lab frame, or they come from different jets and are nearly 180° apart because most of the events are dijet events. As we can see from the figure, in the first case the events pile up at $\cos\theta_H = -1$ and in the second case they pile up at $\cos\theta_H = 1$.

To determine where to place the cut we examined the $\cos\theta_H$ distribution (Figure 18) for the "sidebands", defined as $3\delta < |M_{K\pi} - M_{D0}| < 6\delta$; we also required $140.5 < \Delta M < 174.5$ MeV/c^2. The signal and background were defined as functions of X, the value of $|\cos\theta_H|$ where the cut is placed, as follows:
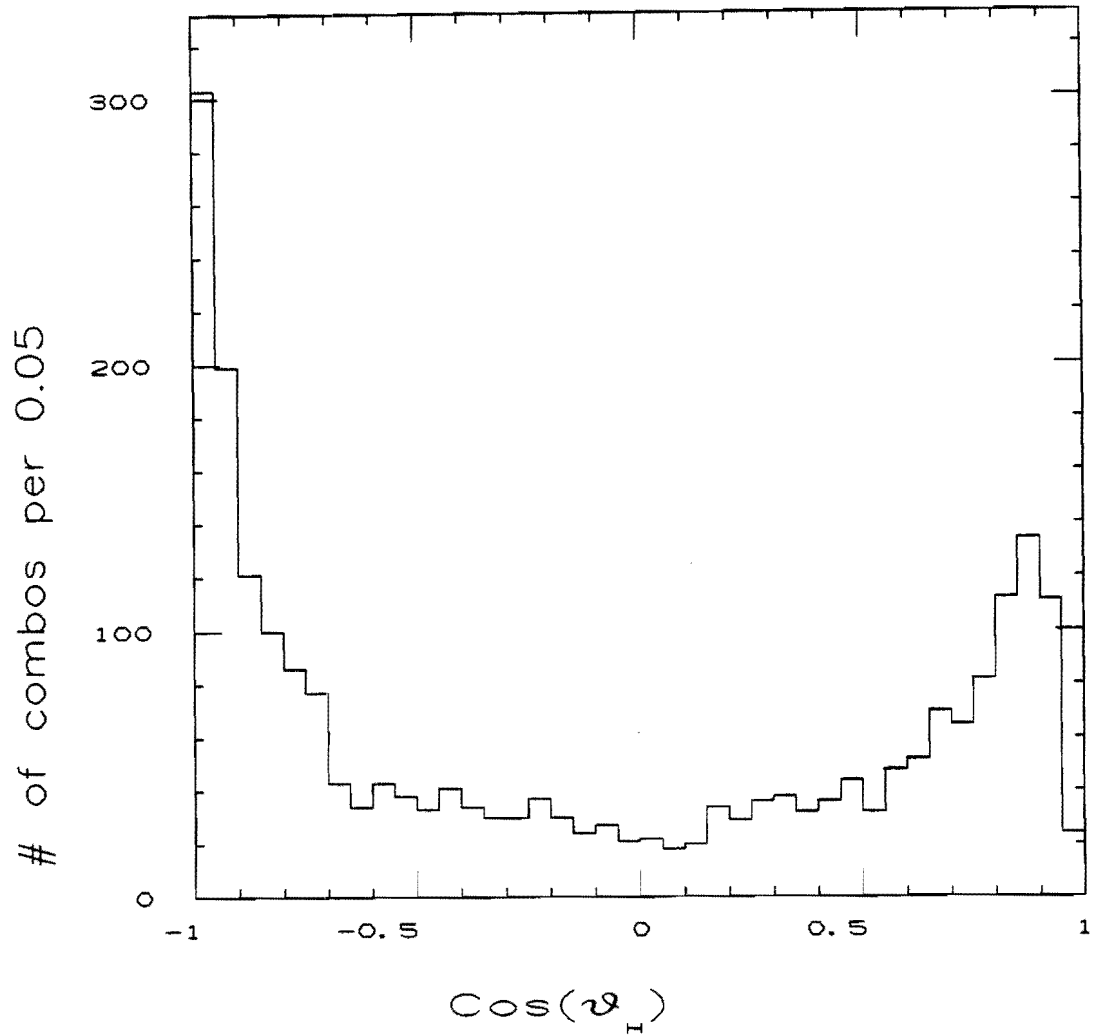
Figure 18. The distribution of the cosine of the helicity angle. The K-π combinations in this plot are from the "sidebands", i.e. $3\delta < |M_{K\pi}-M_{D^0}| < 6\delta$; in addition there was a requirement that $140.5 < \Delta M < 174.5$ MeV/c^2.
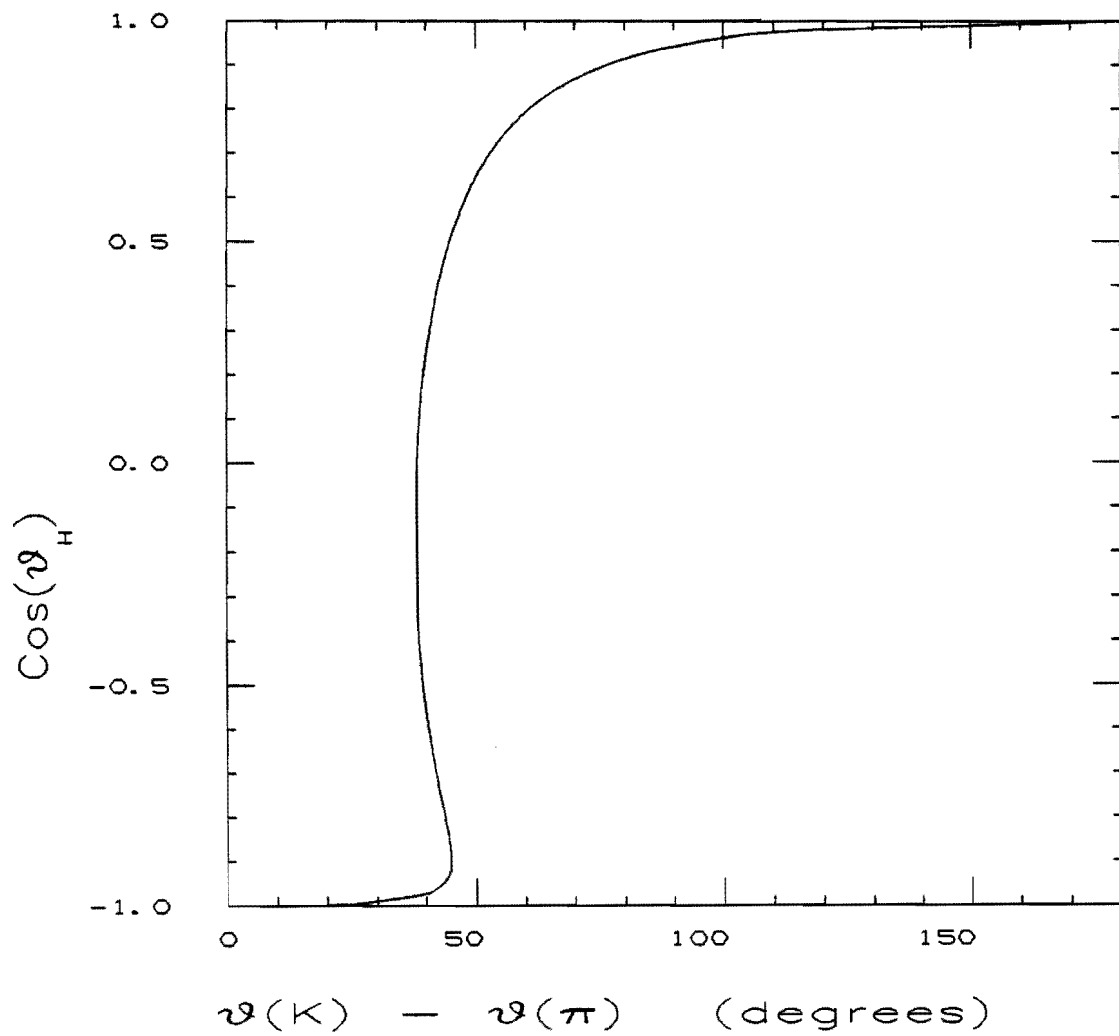
Figure 19. The helicity angle versus the opening angle between the K and the π in the lab frame for the decay of a 5 GeV/c D^0 in the Monte Carlo.

$$S = \int_{-X}^{X} S(\cos\theta_H) \; d(\cos\theta_H)$$

$$B = \int_{-X}^{X} B(\cos\theta_H) \; d(\cos\theta_H)$$

We tried to find the value of X which maximized the ratio

$$\frac{S(X)}{\sqrt{S(X)+B(X)}}$$

i.e. the statistical significance of our signal, assuming the signal to have a flat distribution in $\cos\theta_H$ normalized to 30 events and the background to be distributed as in Figure 18 normalized to 60 events (i.e. the approximate number of background events in the D^* region, 144.5 to 146.5 MeV/c^2, before the $\cos\theta_H$ cut). (We will see shortly that the normalization is not very important.) Figure 20 shows the expected statistical significance of the signal as a function of the location of the $\cos\theta_H$ cut. The significance is maximized by placing a cut somewhere between 0.8 and 0.9; this can be seen to hold approximately independently of the magnitude of the signal.

The statistical significance for $X > 0.8$ is inflated in Figure 20 because we have assumed that the $\cos\theta_H$ distribution is flat for the signal when in fact it goes to zero as $\cos\theta_H$ approaches one, just like the background (Figure 18). Thus, one does gain more in statistical significance by cutting on $\cos\theta_H$ than indicated in Figure 20. The reason for the asymmetry in Figure 18 is that when $\cos\theta_H \sim 1$, the pion from the D^0 decay is emitted backwards with respect to the boost direction and therefore has its momentum lowered in the lab frame to a value below the p_t cut at 300 MeV/c. Backwards-boosted kaons ($\cos\theta_H = -1$) are less affected due to their larger mass. The signal experiences the same asymmetry; this is illustrated in Figure 21 which shows the $\cos\theta_H$ distribution from the Monte Carlo where we have applied the same cuts as were applied to the data. Since the distribution is flat out
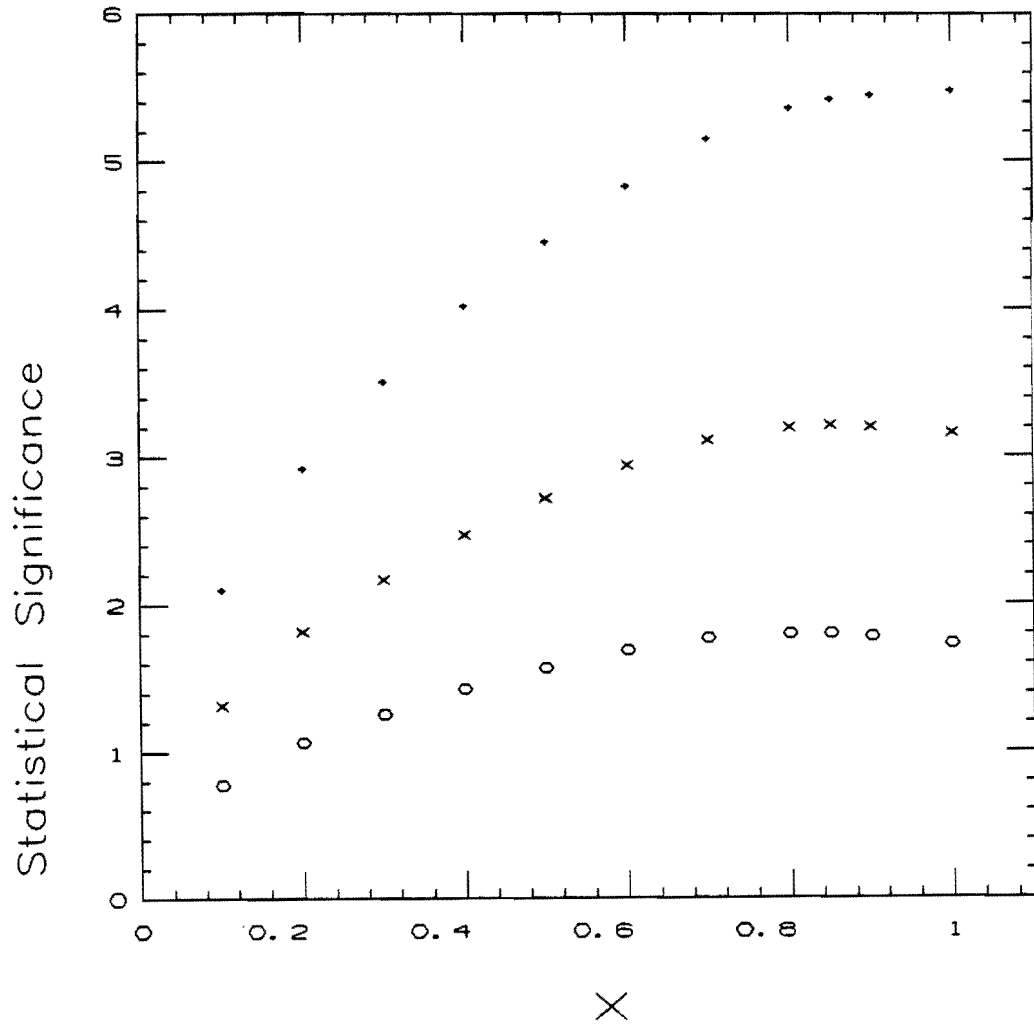
Figure 20. The expected statistical significance of the signal as a function of the location of the helicity angle cut. The x's are for a signal normalized to 30 events. The dots and open circles are for signals normalized to 60 and 15 events respectively.
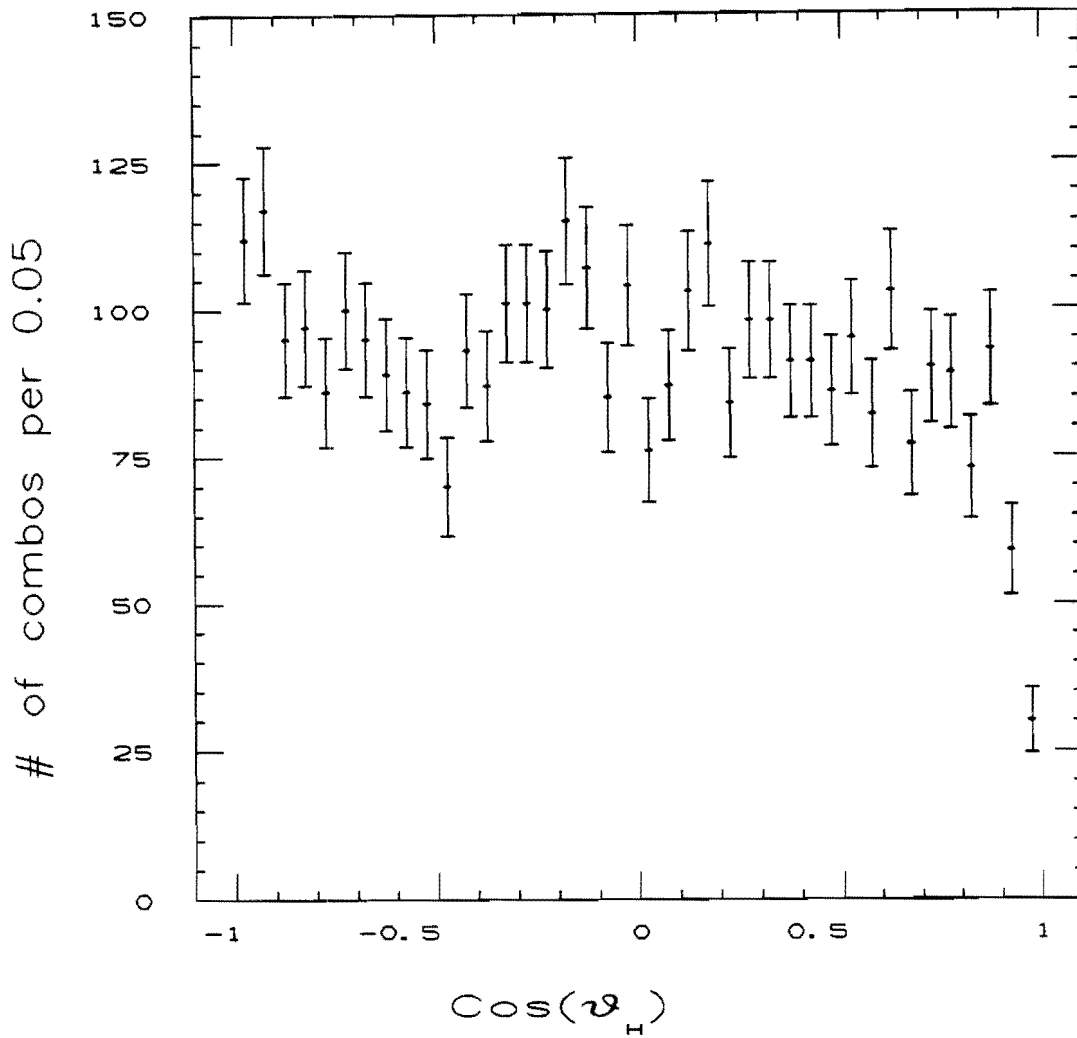
Figure 21. The distribution of the helicity angle for Monte
Carlo D*s which were merged with real jet data and subjected to the
same cuts as applied in the D* search.

to $\cos\theta_H = 0.8$ and since the statistical significance is maximized around that value, we have chosen to require $|\cos\theta_H| < 0.8$.

Finally, we required $z(K\pi\pi) > 0.1$ where z is defined as $p_\ell(K\pi\pi)/E_{jet}$. The quantity $p_\ell(K\pi\pi)$ is the longitudinal momentum of the K-π-π system projected onto the jet axis; E_{jet} is the jet energy. This cut was found to improve the signal-to-noise ratio; apparently the amount of signal rises less steeply than the background as one approaches $z=0$. The UA1 Collaboration also applied a cut at $z=0.1$ in their analysis.

The effect of all the cuts, together with the efficiency for D^*s (see Chapter 5) with $z>0.1$, is summarized in Table 2.

4.3 Signal/Background Estimation

The resulting ΔM distribution after all the cuts is shown in Figure 22 together with the distribution from a control sample of "wrong-sign" mass combinations, i.e. those where one tries to form a D^{*+} with the combination $K^+\pi^-\pi^+$ instead of $K^-\pi^+\pi^+$. The wrong-sign decay mode $D^{*+} \rightarrow K^+\pi^-\pi^+$ is forbidden to the extent that D^0-$\bar{D}^0$ mixing is rare.[65] There is a clear peak in the bin of width 2 MeV/c^2 centered at 145.3 MeV/c^2 which is absent in the wrong-sign distribution. The background was estimated as 25*2(sys), resulting in a signal of 25*2. We will describe how this was done shortly. The probability that a background of 25 events fluctuates up to $\geq$ 50 events is $7*10^{-6}$ which corresponds to exceeding 4.3σ on one side of a Gaussian.

Despite our high hopes for the δ cut, it appears that it does not significantly improve the signal-to-noise ratio. Figure 23 shows the results obtained with a straight mass cut requiring $1.84 < M_{K\pi} < 1.89$ GeV/c^2 instead of the cut on δ; here the background comes out to 22*2 events, corresponding to a signal of 23*2, or a 4.2σ effect.

Several other checks of the signal were performed. 1) The ΔM distribution for the sidebands, $3\delta < |M_{K\pi}-M_{D^0}| < 6\delta$, was examined (Figure 24a). There is no sign of any significant structure in the histogram. 2) The distributions for positive and negative D^*s were

Table 2. The effect of the cuts applied to extract the D^* signal. Also listed are the efficiencies of each of the cuts for D^*s which are measured with z>0.1.

	Number of track combinations	Efficiency for D^*s (z>0.1)
$p_t > 300$ MeV/c, $|\eta| < 1.2$	-----	0.85 ± 0.04
Track reconstruction and selection	-----	0.64 ± 0.10
$1.5 < M_{K\pi} < 2.4$ GeV/c^2, $\quad$ $138 < \Delta M < 178$ MeV/c^2	$4.54*10^4$	------
$|M_{K\pi}-M_{D^0}| < 3\delta$, $\quad$ $144.5 < \Delta M < 146.5$ MeV/c^2	90	0.78 ± 0.09
$|\cos\theta_H| < 0.8$	61	0.84 ± 0.02
$z > 0.1$	50	1.00 by definition
After all cuts	50	0.37 ± 0.09
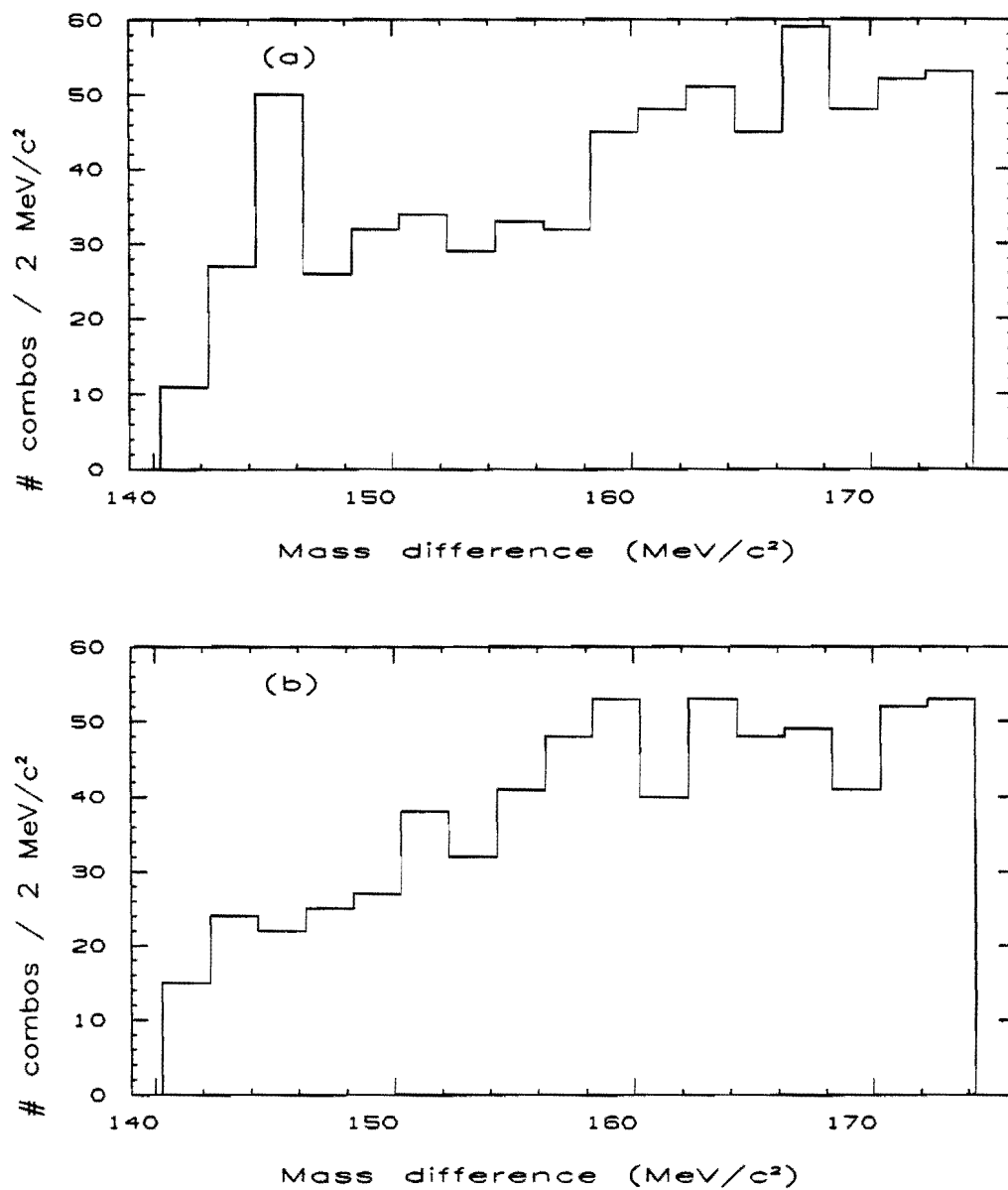
Figure 22. The mass difference distribution from the data after all the cuts. (a) "Right-sign" combinations. (b) "Wrong-sign" combinations, i.e. a D^{*+} formed with the combination $K^+\pi^-\pi^+$ instead of $K^-\pi^+\pi^+$.
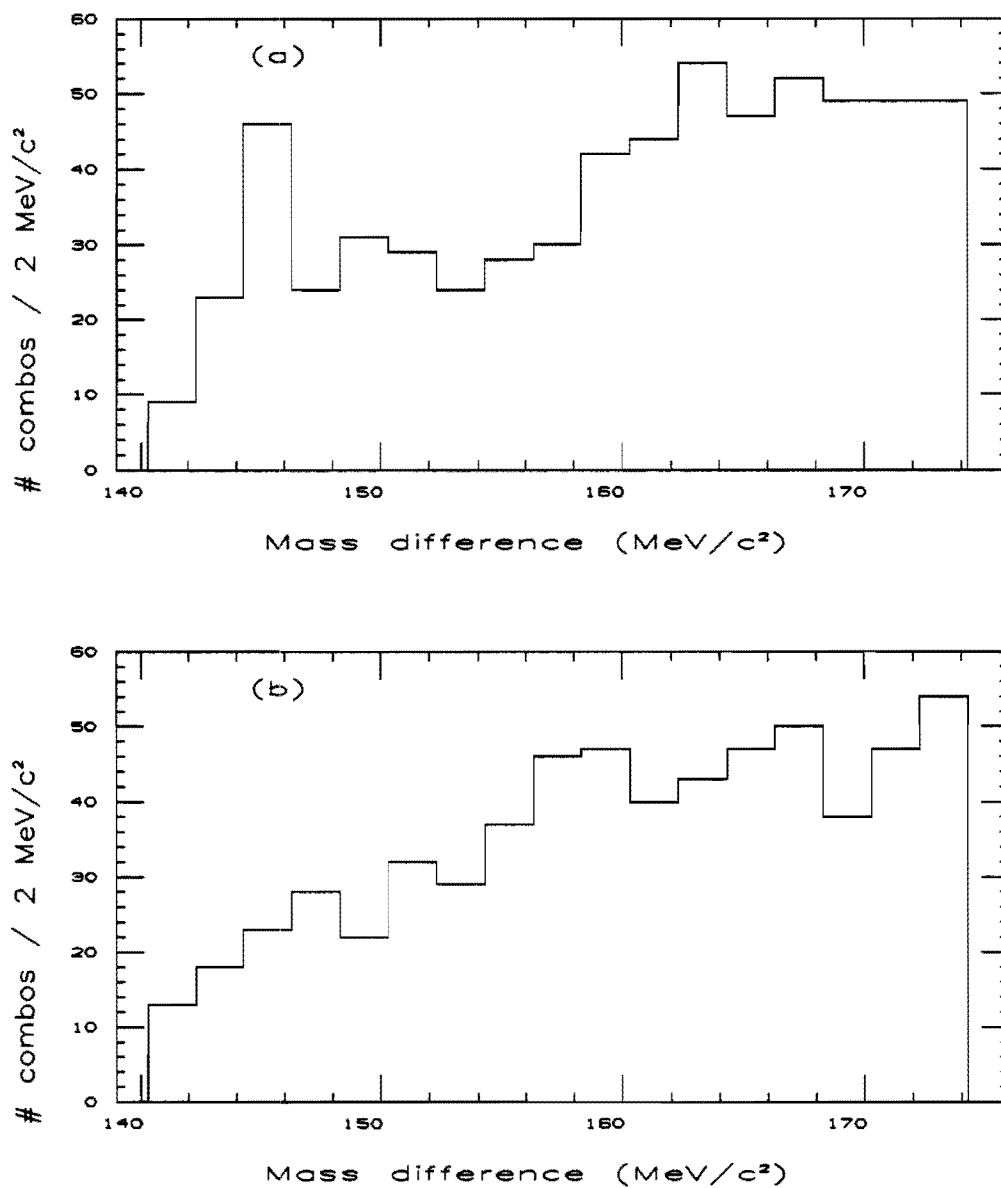
Figure 23. The mass difference distribution for a straight mass cut. The cut required $1.84 < M_{K\pi} < 1.89$ GeV/c^2 instead of $|M_{K\pi}-M_{D^0}| < 3\delta$. (a) "Right-sign" combinations. (b) "Wrong-sign" combinations.
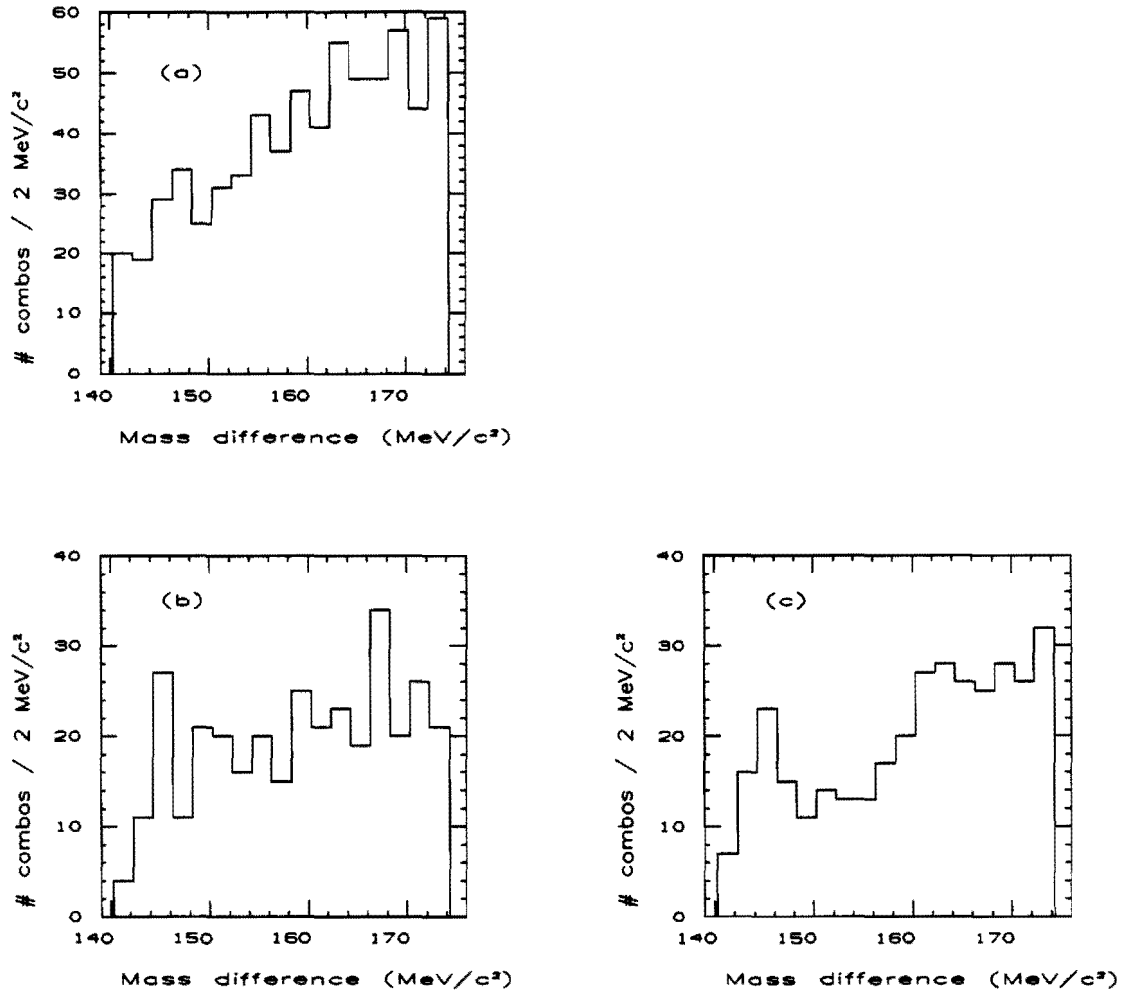
Figure 24. Further checks of the signal. (a) The mass difference distribution for the sidebands. The sidebands are defined by $3\delta < |M_{K\pi} - M_{D^0}| < 6\delta$. (b,c) The mass difference distribution separated into positive and negative D^*s.

compared (Figure 24b,c); they appear to be consistent. 3) The events in the signal bin were visually scanned to make sure that the run numbers were well distributed and to look for any pathologies. One of the events was found to have contributed twice to the signal bin by having the two pion candidates paired with different kaons. One of these entries was therefore removed. (We have taken this into account in the previous two paragraphs.)

The background was estimated by trying various fits to the ΔM distribution. The first was to fit the right-sign distribution as in Figure 22 to a background plus signal of the form

$$\frac{dN}{d(\Delta M)} = a(\Delta M - m_{\pi})^b + c \cdot \delta_{ij}$$

where δ_{ij} is 1 in the D^* signal bin and 0 otherwise. Simultaneously the wrong-sign distribution was fit to the same form without the signal term $c \cdot \delta_{ij}$. The wrong-sign distribution was used rather than the sidebands because the kinematics are guaranteed to be the same as in the signal band. This could be important near the endpoint where the background is varying the most rapidly. The normalization should be the same too. A background function parametrized as a horizontal parabola, i.e.

$$\frac{dN}{d(\Delta M)} = \frac{-b + \sqrt{b^2 + 4a(\Delta M - m_{\pi})}}{2a}$$

was also tried. In the second type of fit, the bin containing the peak and the one adjacent bin on either side of the peak were removed from the histogram. The remaining bins and the wrong-sign distribution were then simultaneously fit to just the background function. In the third type of fit, the bins were made narrower, and the ΔM distribution was fit to a Gaussian in the peak region plus a background function parametrized as above.

In all three fits, we examined the effects of changing the bin edges and the region over which the fits were performed as well as the effect of fitting with and without the wrong-sign distribution. The fits were performed with the MINUIT package[66] by minimizing the negative log-likelihood

$$-2 \ln \frac{L(\lambda(a,b,c))}{L(N)}$$

where $\lambda(a,b,c)$ is the expected number of entries per bin, computed by integrating the fitting function with the parameters a through c, and N is the number of entries per bin observed. L is the likelihood function defined as

$$L(\lambda) = \prod_{i=1}^{n} \frac{e^{-\lambda_i} \lambda_i^{N_i}}{N_i!}$$

where the product is taken over all the bins in the histogram.

Figure 25 shows three of the many fits tried, illustrating the range in the background. The fit in Figure 25a is to the form $a(\Delta M - m_\pi)^b$ + Gaussian. Figure 25b shows a fit to the horizontal parabola where the signal bin and two adjacent bins were removed from the histogram during the fit, and Figure 25c shows a fit to the form $a(\Delta M - m_\pi)^b + c\delta_{ij}$. Figure 25d shows the wrong-sign distribution which was fit simultaneously with the distribution of Figure 25c. The other two fits shown (Figures 25a,25b) were performed without fitting simultaneously to the wrong-sign distribution. For reference, the fit parameters are as follows:

Figure 25. Examples of fits to the mass difference distribution. (a) The mass difference distribution shown with a fit to a Gaussian in the peak region plus a background parametrized as $a(\Delta M - m_\pi)^b$. (b) A rebinned mass difference distribution shown with a fit to the background parametrized as a horizontal parabola. The bin with the peak and the bin immediately adjacent on either side of the peak were removed from the histogram for the fit. (c) The same mass difference distribution as in (b). Here, the histogram was fit to the form $a(\Delta M - m_\pi)^b + c \cdot \delta_{ij}$ where δ_{ij} is one in the bin containing the peak and zero otherwise. Simultaneously the wrong-sign distribution was fit without the signal term $c \cdot \delta_{ij}$. The dotted line shows the resulting background function. (d) The wrong-sign distribution corresponding to (c) with the same fitted function.

78
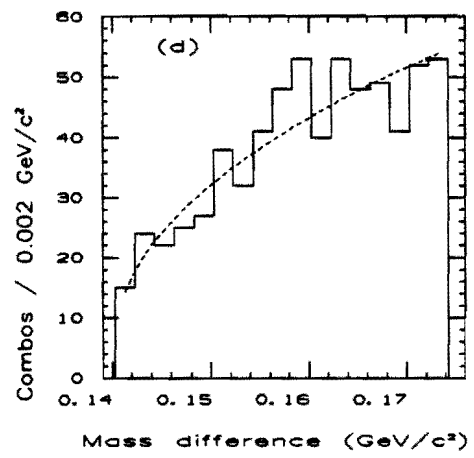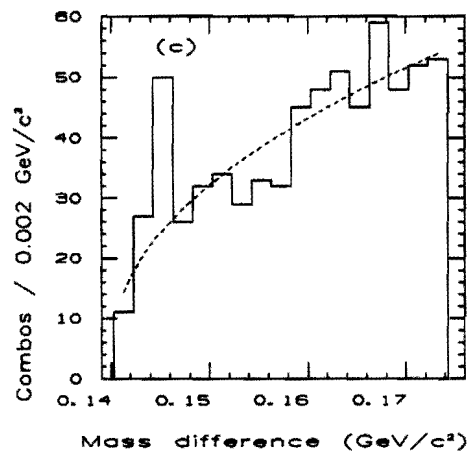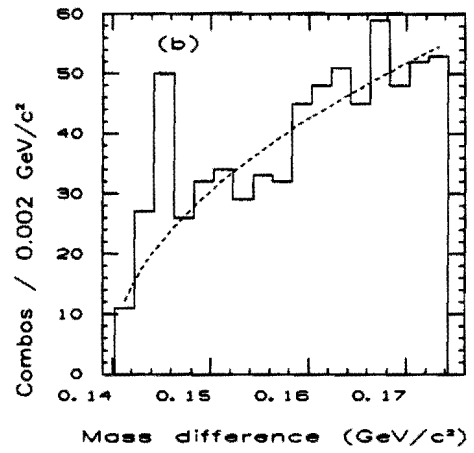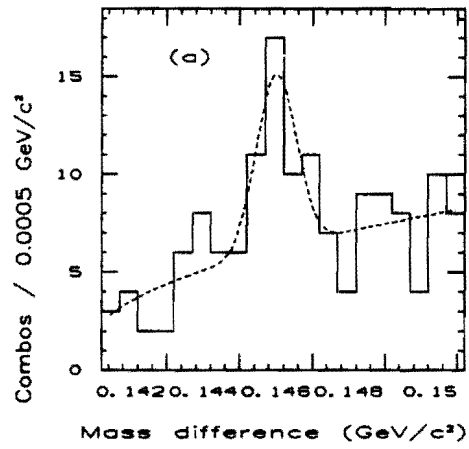
Figure 25a: $\frac{dN}{d(\Delta M)} = a \cdot (\Delta M - m_\pi)^b + A \cdot \exp\left[-\frac{1}{2}\left[\frac{(\Delta M - \overline{\Delta M})}{\sigma}\right]^2 \right]$

$a = (1.17 \, {}^{+ \, 1.63}_{- \, 0.63}) \cdot 10^5$

$b = 0.43 \, {}^{+ \, 0.17}_{- \, 0.15}$

Normalization $(A) = (1.86 \, {}^{+ \, 1.27}_{- \, 0.64}) \cdot 10^4 \quad (GeV/c^2)^{-1}$

Mean $(\overline{\Delta M}) = 0.1450 \pm 0.0002 \quad GeV/c^2$

$\sigma = 0.00052 \, {}^{+ \, 0.00030}_{- \, 0.00028} \quad GeV/c^2$

Figure 25b: $\frac{dN}{d(\Delta M)} = \frac{-b + \sqrt{b^2 + 4a(\Delta M - m_\pi)}}{2a}$

$a = (4.54 \pm 0.38) \cdot 10^{-11} \quad (GeV/c^2)^3$

$b = (-7.78 \cdot 10^{-12}) \pm (4.06 \cdot 10^{-7}) \quad (GeV/c^2)^3$

Figure 25c: $\frac{dN}{d(\Delta M)} = a(\Delta M - m_\pi)^b + c\delta_{ij}$

$a = (1.21 \, {}^{+ \, 0.24}_{- \, 0.20}) \cdot 10^5$

$b = 0.43 \pm 0.04$

$c = 25.4 \, {}^{+ \, 7.5}_{- \, 6.9}$

The errors shown are statistical and were obtained by doing a full MINUIT error analysis which gives the lower and upper bounds at which the negative log-likelihood (which is like a χ^2) varies by one unit. Defining our signal region by $144.5 < \Delta M < 146.5 \ MeV/c^2$, the background ranges from ~23 to ~26. Since there are 50 entries in this region, this corresponds to a signal in the range 24 to 27. We therefore decided to quote a signal of 25 events with a systematic uncertainty of ±2 events.

The statistical uncertainty, meanwhile, depends essentially on the total number of entries in the signal region. This can be seen by the following argument. The total number of entries represents the sum of a signal (S) and a background (B). An estimate of B (call it B′) is made by fitting the ΔM distribution, and S is then calculated by (S+B)-B′. Using the usual error propagation formula, the uncertainty on S is then given by $\sigma_S^2 = \sigma_{(S+B)}^2 - \sigma_B^2$. but B′ has a small statistical uncertainty since it is constrained by a fit to many points. We therefore find that σ_B, can be neglected in the expression for σ_S so that the statistical uncertainty in S is given by the uncertainty in the total number of events observed. This is borne out, for example, by the fit in Figure 25c where the uncertainty on the signal reported by MINUIT is close to $\pm\sqrt{50}$. Putting all the numbers together, then, we come up with 25 $^{+7.5}_{-6.9}$ ± 2 D^*s with $z{>}0.1$ from a sample of 32,340 jets with an E_t spectrum as shown in Figure 11e.

Multiple histogram entries per event are not a problem in this fitting procedure because most of the events which contribute to the final mass difference plot have only one entry per event (Figure 26). This is important because it ensures that all the entries in the histogram are statistically independent, a necessary condition for our fitting procedure to be valid. Had this not been the case, we could have forced one entry per event by picking, for example, the combination with mass difference closest to the correct value and then used the same criterion on the wrong-sign mass distribution to determine the bias which is introduced on the shape of the background.

4.4 Z Distribution

A variable which is commonly studied in jet fragmentation is the fraction of the momentum of the hard-scattered parton which is carried by the particles into which the parton materializes. Since the momentum of the scattered parton is not directly accessible experimentally, this fraction has been defined in several different ways. The UA1 Collaboration[67] used the definition $z \equiv \vec{p}_{hadron}$.
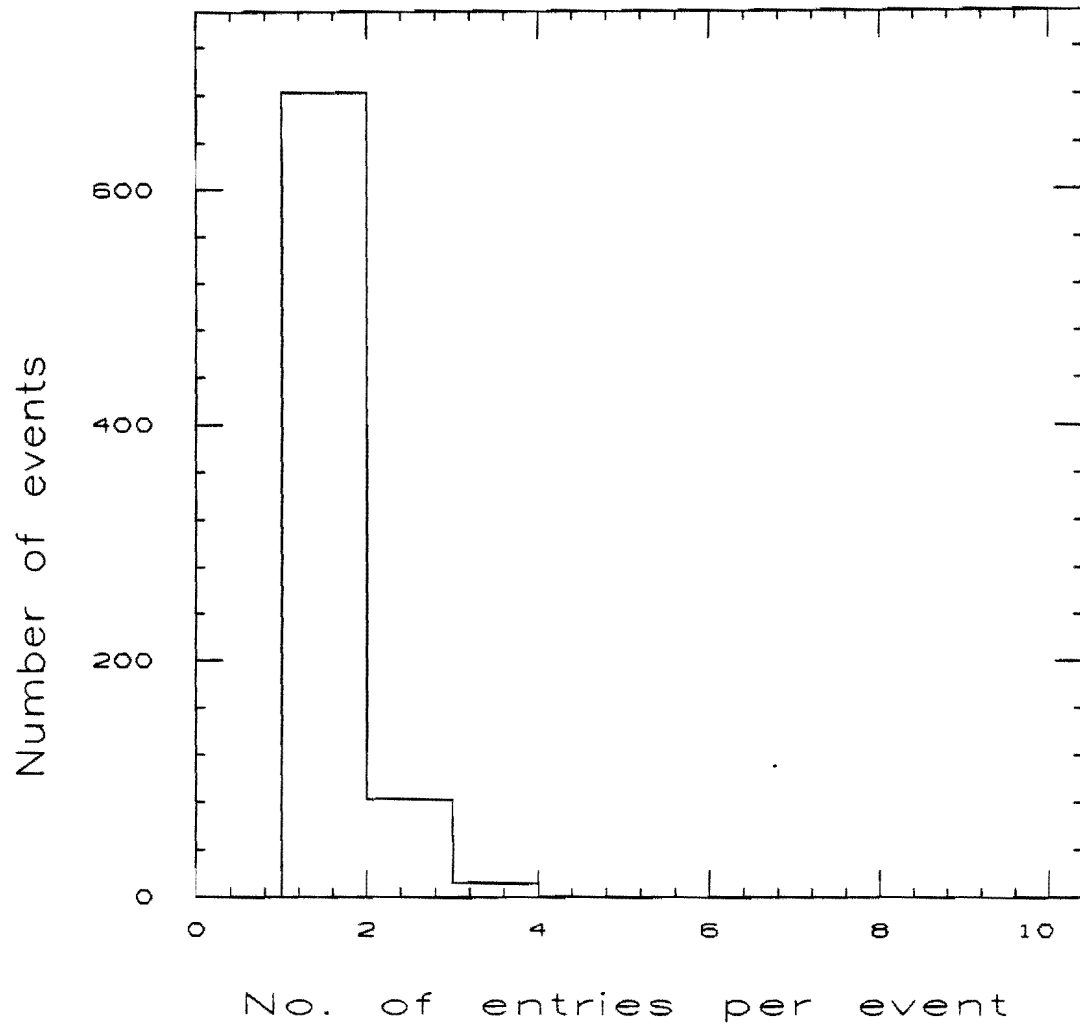
Figure 26. The number of entries per event which make it into the mass difference plot after all the cuts.

$\vec{p}_{jet}/|\vec{p}_{jet}|^2$ where $\vec{p}_{jet}$ is the vectorial sum of all the calorimetry cells belonging to the jet; each cell in the jet is assigned a vector whose direction is given by the location of the cell and whose magnitude is given by the energy in the cell. In this thesis, a similar definition of z is used but with $\vec{p}_{jet}$ defined as a vector whose direction is given by the jet energy centroid and whose modulus is given by the jet energy.

The z distribution was obtained by plotting the ΔM distribution for coarse slices in z and then fitting it to the form $a(\Delta M - m_\pi)^b + c\delta_{ij}$ where δ_{ij} is defined as before. We did not explore the systematic effects of the fitting procedure since the statistical uncertainties are overwhelming. Figure 27 shows the ΔM distributions for three z slices plotted together with curves for the background from the fits. The excess in each z bin from the fits was:

z	#(D*)
0.1-0.2	$15.3 ^{+6.2}_{-5.6}$
0.2-0.4	$8.0 ^{+4.1}_{-3.4}$
0.4-1.0	2.0 ± 2.0

The excess in the last z bin was simply estimated by eye.

The observed signal must now be corrected for a variety of instrumental effects before we can extract any physics. This is the subject of the next three chapters.
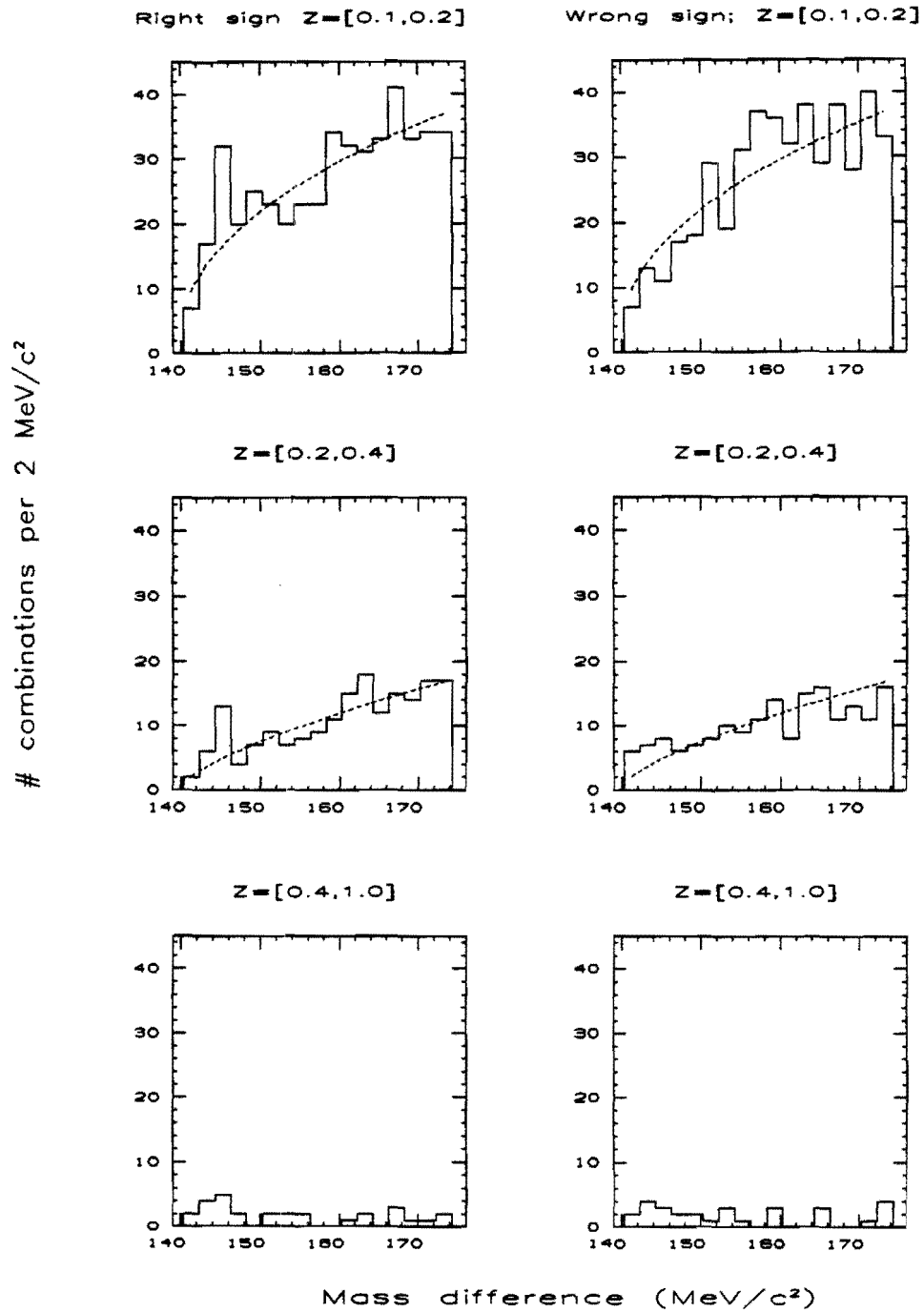
Figure 27. The mass difference distribution after all the cuts, broken down into z bins, for both right-sign and wrong-sign track combinations. Also shown are the results of the fits to the background.

CHAPTER 5

RECONSTRUCTION EFFICIENCY

We now begin a discussion of instrumental effects for which we must correct the observed D^* signal. The first of these is the efficiency for reconstructing D^*s in our jet data. This chapter describes how this efficiency was determined as a function of the fragmentation variable z, where z is defined as the fraction of the jet energy carried by the D^* parallel to the jet axis. We first describe the method and then examine the D^* efficiency and its dependence on the jet energy and track multiplicity. The sources of tracking inefficiency are described in more detail in Appendix B.

5.1 The Method

The efficiency was determined by taking Monte Carlo tracks from the decay $D^{*+} \rightarrow D^0 \pi^+ \rightarrow K^- \pi^+ \pi^+$, simulating the CTC hits that would be produced by these tracks, and then burying those hits among the hits produced in a real jet event. The track reconstruction program was then run on the event and we checked to see if the D^* daughters were successfully reconstructed.

By merging tracks in real data we are guaranteed to get at least some detector effects correctly, namely: 1) noise in the CTC, 2) the pulse widths of hits (except for the embedded Monte Carlo tracks), 3) the density of hits in the inner superlayers caused by spiraling tracks at very low p_t, and 4) the dead cells in the CTC.[68] We have also checked and, where necessary, tuned the ability of the Monte Carlo to reproduce the distributions of other variables which have a bearing on the efficiency. Figure 28 shows the distribution of the
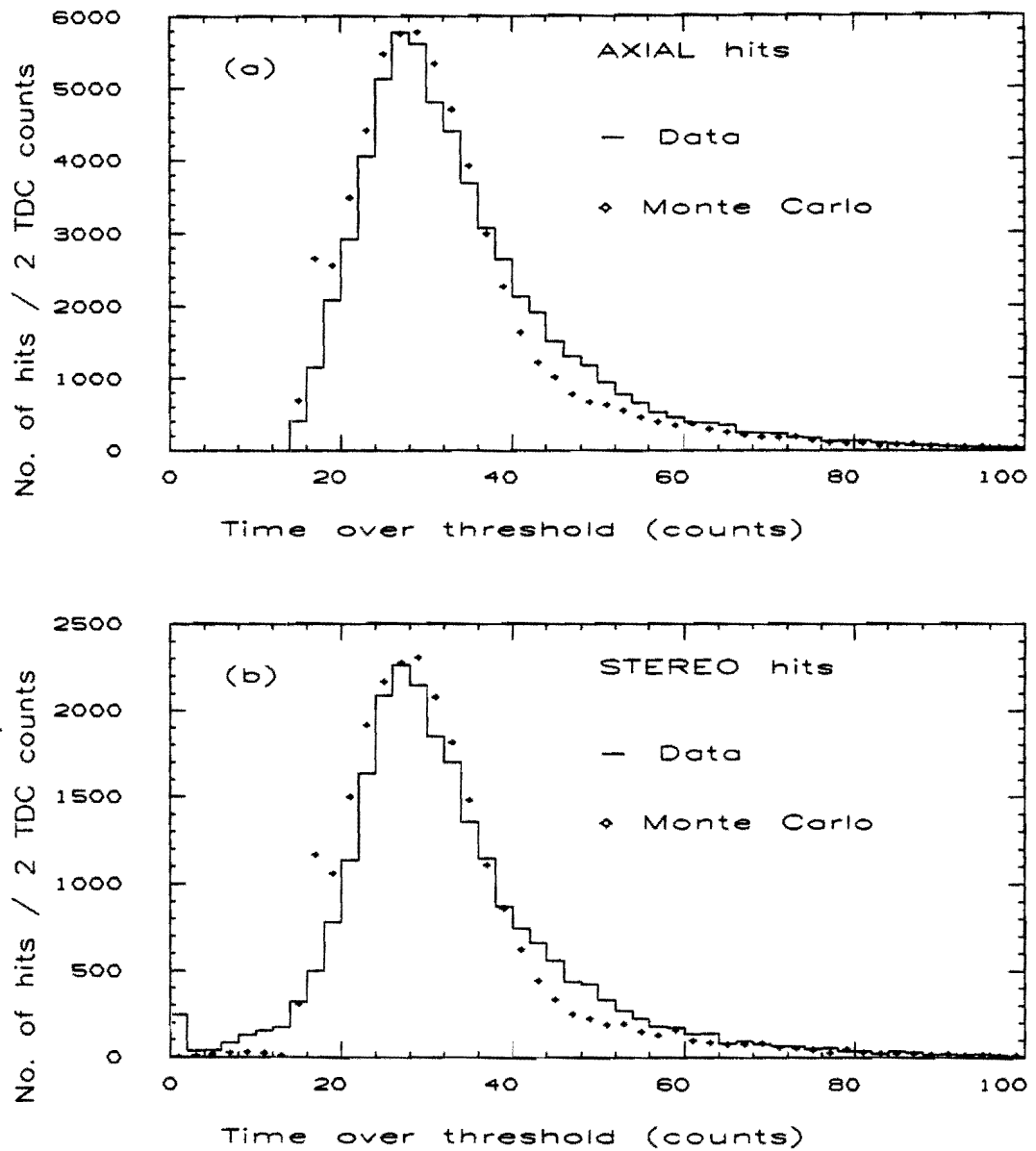
Figure 28. The distribution of the time-over-threshold of hits from Monte Carlo tracks compared to the data. The tracks were required to pass all the track selection criteria.

pulse widths, also known as the "time-over-threshold", i.e. the time that the pulse height is above a low threshold. The tails arise from a geometric effect of the slope of the track with respect to the sense wire plane. Figure 29 compares the number of hits per track. The shoulder at ~40 hits is due to the dead cells. Figure 30 compares the distribution of the layers on which hits are found. The deficiency in the innermost axial superlayer is due to the fact that it was operated at about 30% of the gain of the outer superlayers. The drop in the outermost axial superlayer is due to the dead quadrant.

Lastly, we have looked at the phi distribution of the tracks which were injected. Normally this is not an issue, but because of the dead cells we need to make sure that the right proportion of tracks passed through these regions. The input phi distribution ended up not being uniform (Figure 31) because the tracks were injected near the jet axes and the jet phi distribution was not uniform. The non-uniformity in the jet distribution is due to statistics; our study used only 530 independent jets with each jet being replayed 10 times (with a different D^* each time). Our results are still valid because the dead regions have been exposed to the same proportion of tracks as they would have been for a uniform distribution.[69] In Appendix B, we show that the single-track finding efficiency as a function of ϕ (which is independent of the input ϕ distribution) agrees in shape with the efficiency measured directly from the data.

5.2 Procedure

We began by selecting a jet with uncorrected calorimeter $E_t > 20$ GeV and $|\eta| < 1.0$. The jet energy was then corrected according to the prescription discussed in Chapter 3. Given a value of z generated according to a 1/z distribution (ranging from z of 0.1 to 1), we computed $\tilde{p}_L$, the longitudinal momentum of the D^* along the jet axis. (We will use the tilde to denote that the quantity is measured with respect to the jet axis.) We then generated $\tilde{p}_t$ according to a $\exp(-\alpha \tilde{p}_t)$ distribution with a mean of 0.7 GeV/c (where the mean was
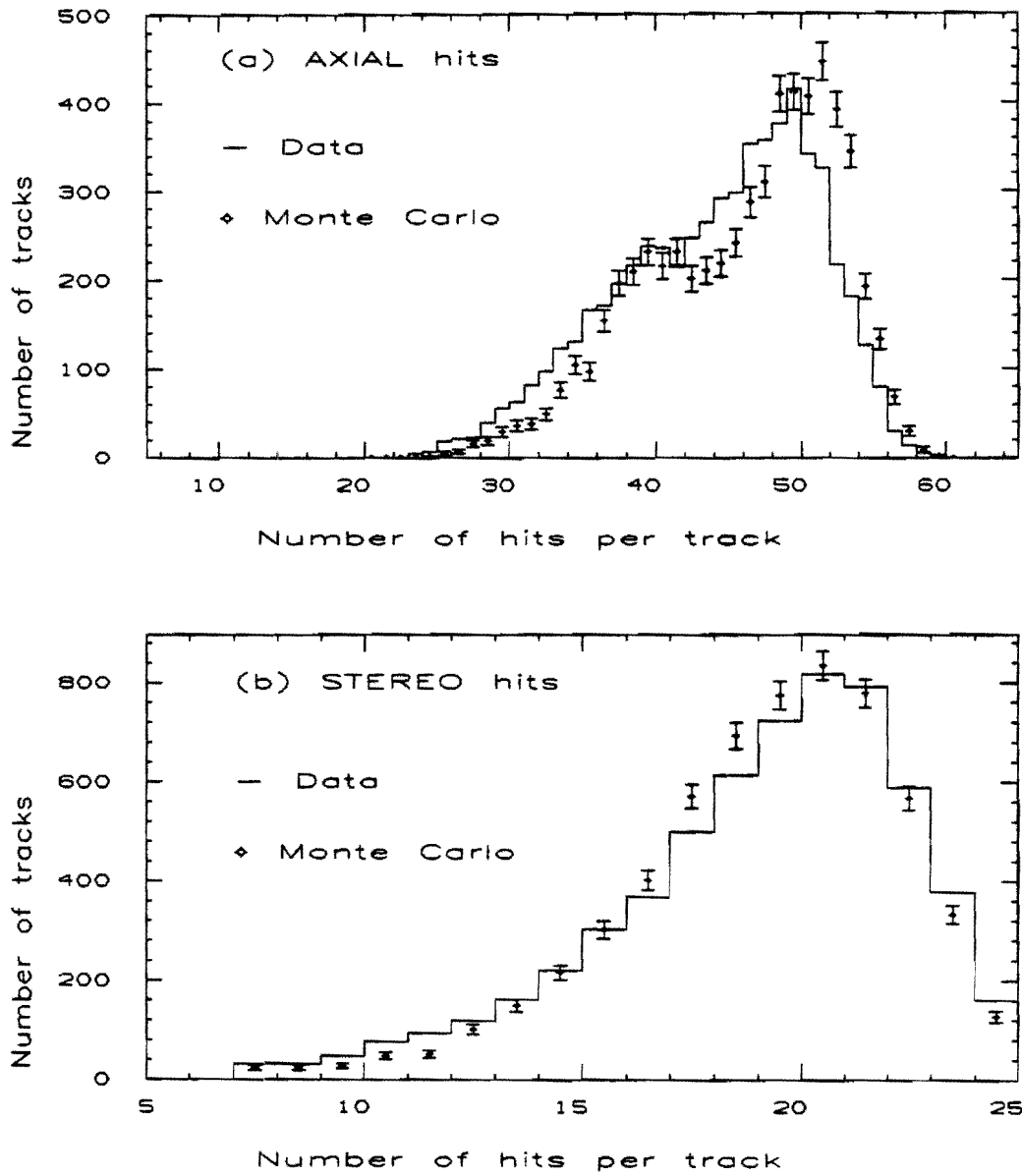
Figure 29. The number of hits per track, comparing Monte Carlo tracks to those from the data. The tracks were required to pass all the track selection criteria.
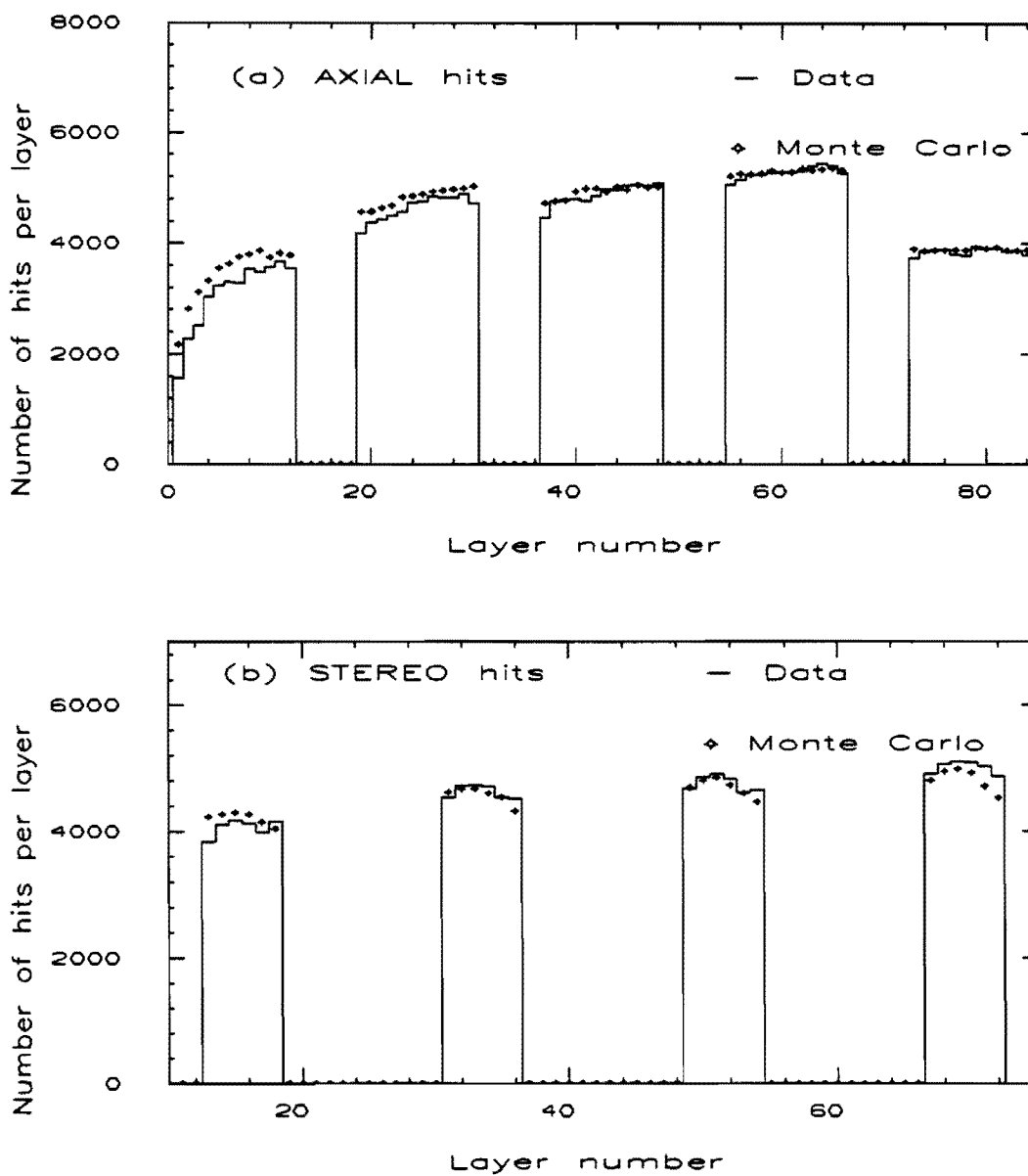
Figure 30. The layer number of the hits on tracks passing track selection, comparing Monte Carlo tracks to the data. The two distributions have been normalized to the same number of tracks.
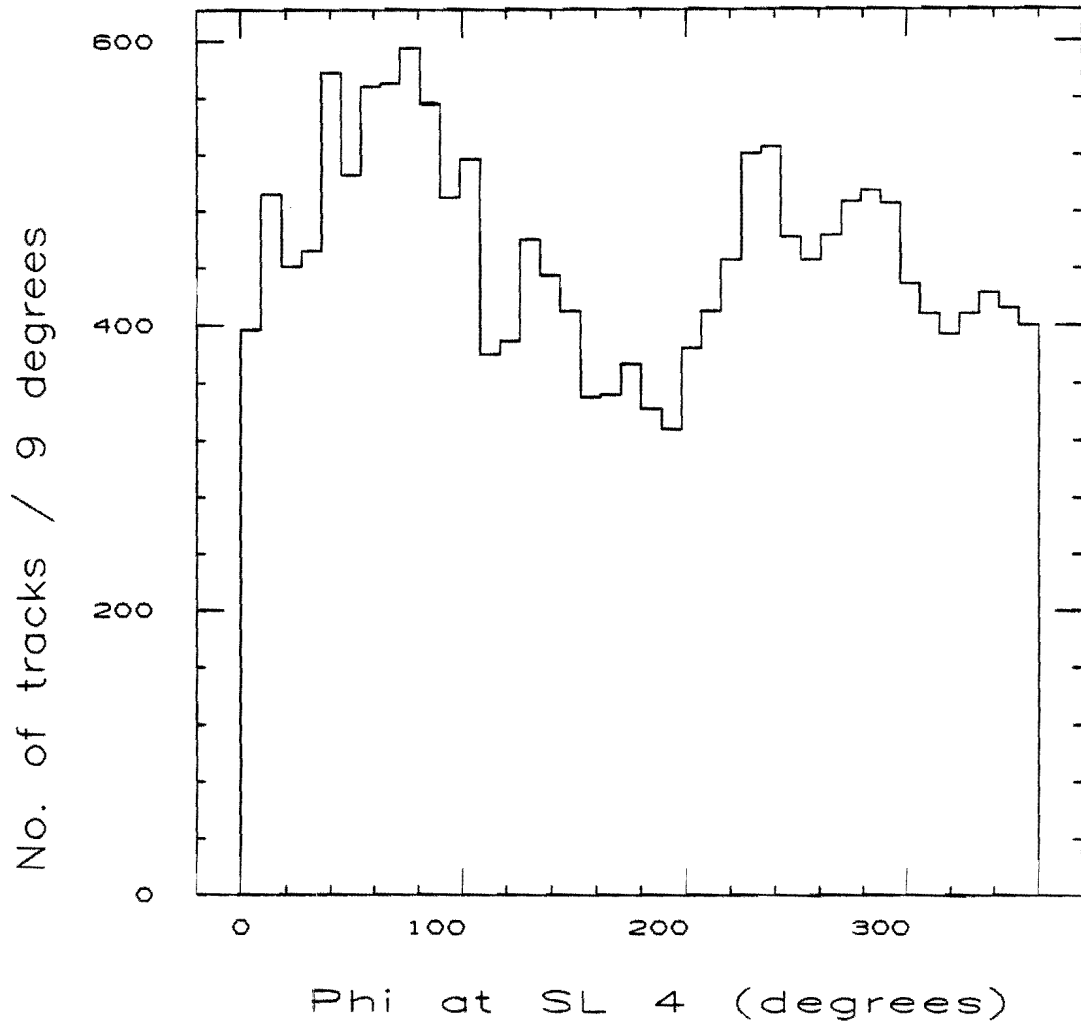
Figure 31. The input distribution of ϕ of the Monte Carlo tracks evaluated at the inner radius of superlayer 4.

motivated by UA1 measurements for single charged particle fragmentation).[70] ϕ was generated uniformly and the D^* was decayed according to phase space. The z-coordinate of the primary vertex for the D^* daughters was set to the vertex found by the VTPC for the event. For x and y, the beam position was used. To reduce wasted CPU time, the D^* daughters were required at this point to pass the kinematic cuts: $p_t > 300$ MeV/c and $|\eta| < 1.2$.

The full CTC simulation was then run on the D^* daughters with a few modifications. Random noise hits generated by the simulation throughout the chamber were turned off as these were provided by the real data. A global t_0 of 100 ns was added to all the drift times to match the convention in the real data. In addition to the Gaussian smearing of the drift distance by 200μm, the drift times were subjected to the inverse of the corrections applied to real data for effects due to high voltage variation, time slewing, and the aspect angle of the track. A t_0 correction per superlayer was also added. The simulated hit data were then merged with real CTC hits in the event, properly taking into account the overlap of the pulses, and the event was put through the track reconstruction program. Each event was replayed ten times with a different D^* injected each time. 5300 events were reconstructed.

The Monte Carlo track was declared to have been found if there was a reconstructed track whose hits matched at least 25% of the hits on the Monte Carlo track. (When we refer to the "Monte Carlo track" we are referring to one of the D^* tracks after passing it through the detector simulation but before running the track reconstruction program.) In cases where there was more than one such track, the one with the highest fraction was taken. Hits were considered to match when the rising- and falling-edge times each matched to one TDC count. Figure 32 shows the distribution of the ratio of the number of matched hits to the number of hits on the Monte Carlo track. There is one entry for every reconstructed track. The huge spike at 0 shows that most tracks in the event do not share any hits with the merged Monte Carlo track, making it relatively straightforward to distinguish
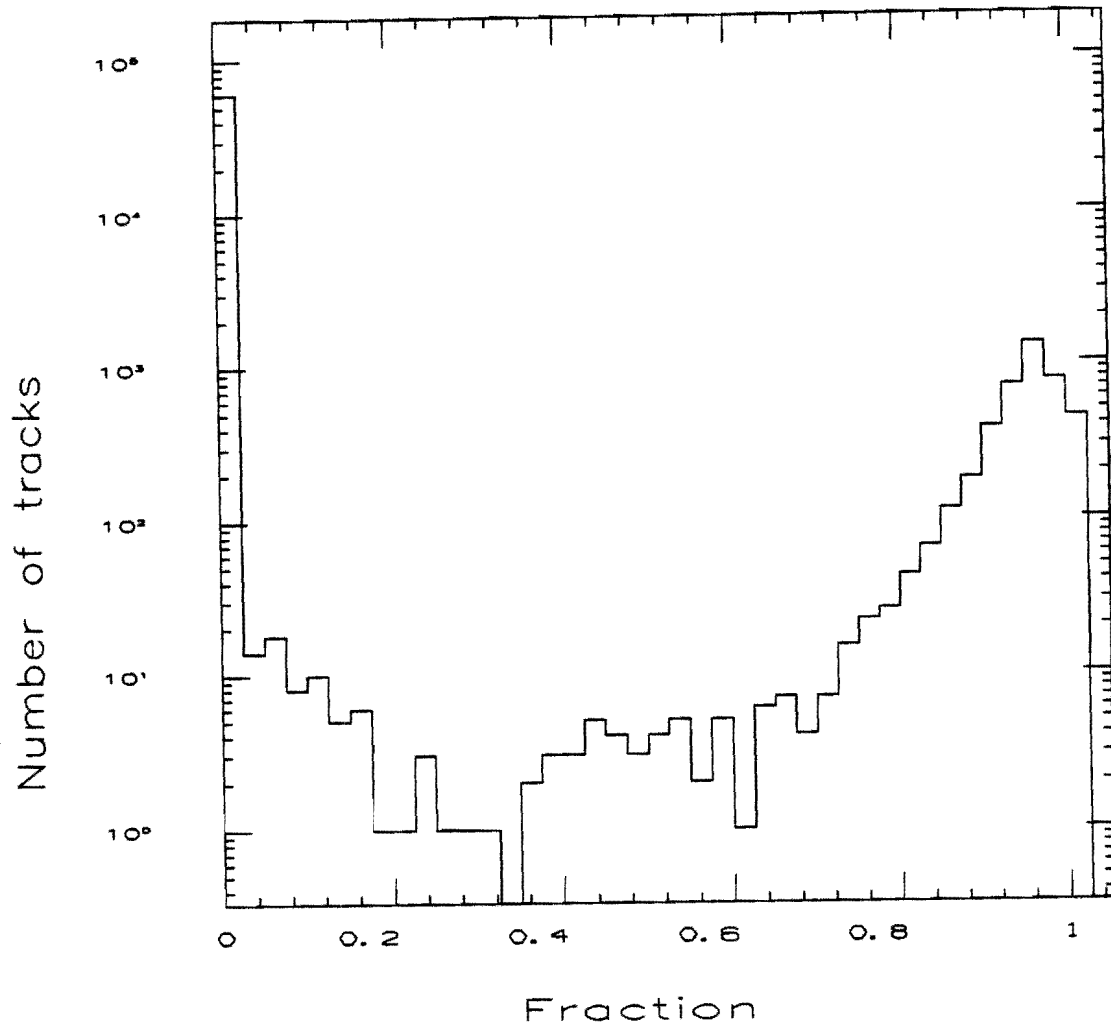
Figure 32. The number of hits on a reconstructed track which match those of the Monte Carlo track, divided by the number of hits on the Monte Carlo track. There is one entry for every reconstructed track in the event.

between tracks from the real data and the tracks we embedded. By cutting at 25% we remove essentially all tracks unrelated to the merged track. At the same time the quality of the reconstructed track which we decide to associate with the Monte Carlo track is minimally biased. The end results are the same even if one pushes the cut up to 80%. However, when the fraction is this high one automatically selects tracks which are well reconstructed (i.e. the subsequent track quality cuts have no effect).

The reconstructed track with the best match was then subjected to the same track quality cuts which were applied in the D^* search, namely:

1) The track was required to be reconstructed in the r, ϕ and z dimensions.
2) The number of hits used in the track was required to be greater than 50% of the number expected.
3) The number of good axial segments was required to be ≥ 2, where a "good" segment has ≥ 8 hits per segment
4) The number of good stereo segments was required to be ≥ 1, where "good" means ≥ 4 hits per segment.

Jets were required to have a corrected $E_t > 30$ GeV and $0.1 < |\eta| < 0.8$, again just like the jets selected for the D^* search. The D^* was declared to have been found if

1) All the daughters were found, i.e.

a) each daughter had a corresponding reconstructed track matching at least 25% of its hits and

b) each daughter passed the track selection cuts (including a cut on the impact parameter requiring $|D| < 5mm$).

2) The reconstructed D^*s satisfied the cuts used in the data analysis, namely

a) $z(D^*) > 0.1$ where z is the fraction of the jet momentum carried by the D^* along the jet axis.

b) $|\cos\theta_H| < 0.8$ where θ_H is the angle in the D^0 rest frame between the kaon and the boost axis of the D^0.

c) $|M_{K\pi} - M_{D^0}| < 3\delta$ where δ is a measure of the uncertainty on the mass of the K-π track pair as a function of the track parameters.

d) 144.5 MeV/c^2 < ΔM < 146.5 MeV/c^2 where ΔM is the mass difference between the K-π-π and K-π combinations.

The D* efficiency was defined as the ratio of the number of D*s surviving all the cuts to the number of input Monte Carlo D*s.

5.3 D* Efficiency

Figure 33 shows the D* efficiency as a function of z, broken down into jet E$_t$ bins, after the kinematic cuts p$_t$ > 300 MeV/c and $|\eta|$<1.2; also shown is the efficiency after we have folded in the E$_t$ spectrum (Figure 11e from Chapter 3) of the jets used in the D* search. The drop in the efficiency at low values of z is due to the slow pion which fails the p$_t$ cut.

Figure 34 shows the efficiency of the track selection cuts alone. The falling efficiency at low values of z is due to the falling efficiency for low p$_t$ tracks (primarily the slow pion again) and the difficulty in reconstructing particles which have decayed before traversing the entire radius of the CTC (primarily the kaon). As the jet E$_t$ is raised, the efficiency at low z increases because, for a fixed value of z, the p$_t$ of the D* is increased. Integrated over the observed jet E$_t$ spectrum, the efficiency of the track selection cuts reaches a plateau of approximately 85%. The single-track efficiency in jets is approximately 95% (see Appendix B) once we get away from p$_t$ and η thresholds. The plateau in Figure 34 at 85% is consistent with finding three tracks each with an efficiency of 95%.

Figure 35 shows the effect of the cosθ_H cut. Since the D^0 is spin-0, the distribution of cosθ_H is flat except near cosθ_H=1 where the pion from the D^0 is boosted backwards in the lab frame and fails

Figure 33. The efficiency of the kinematic cuts for D^*s as a function of the fragmentation variable z, broken down into jet E_t bins. Also shown is the efficiency after folding in the E_t spectrum (shown in Figure 11e of Chapter 3) of the jets used in the D^* search.

Jet Et=[30,40]GeV
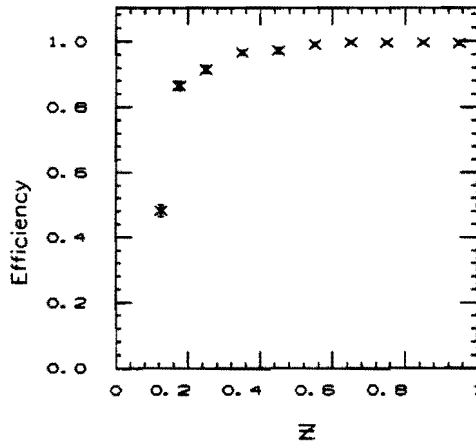
Jet Et=[40,50]GeV
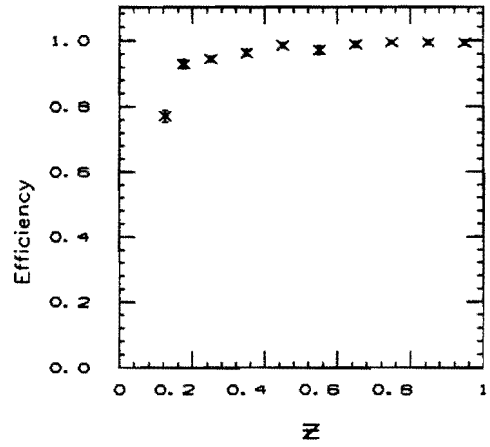
Jet Et=[50,60]GeV
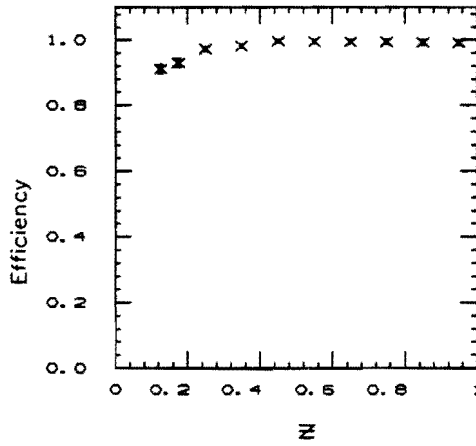
Jet Et=[60,70]GeV
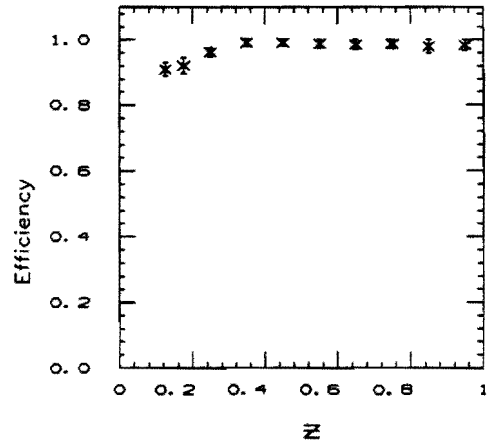
Jet Et > 70 GeV
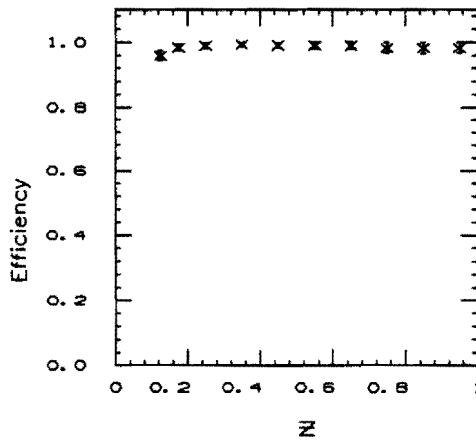
All Jets
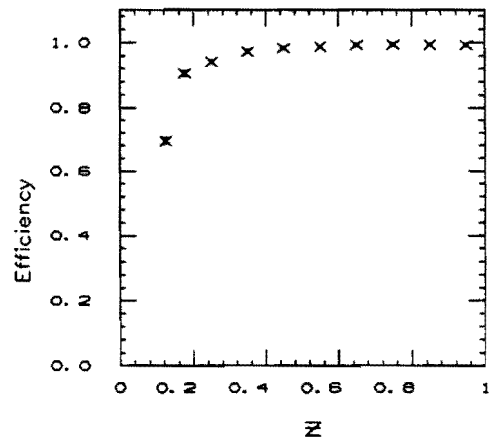
Figure 34. The efficiency of the track selection cuts for D^*s as a function of z, broken down into jet E_t bins. Also shown is the efficiency after folding in the E_t spectrum of the jets used in the D^* search.

Jet Et=[30,40]GeV

Jet Et=[40,50]GeV

Jet Et=[50,60]GeV

Jet Et=[60,70]GeV

Jet Et > 70 GeV

All Jets
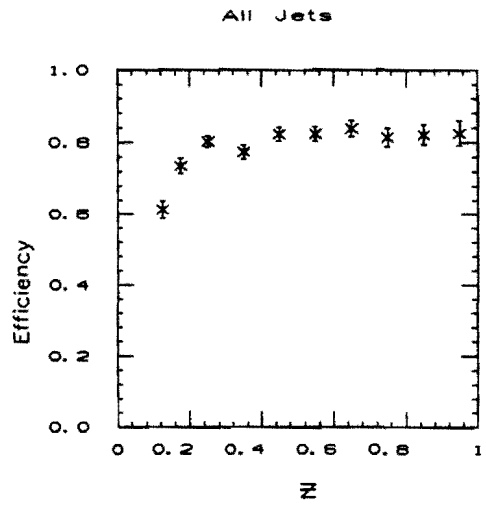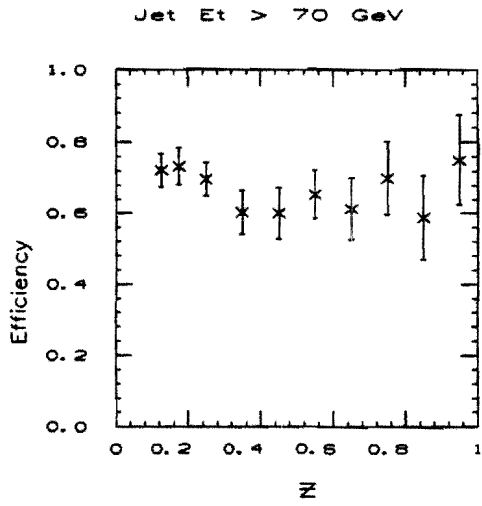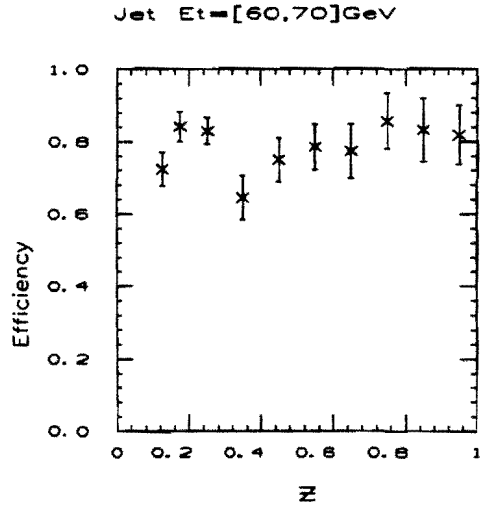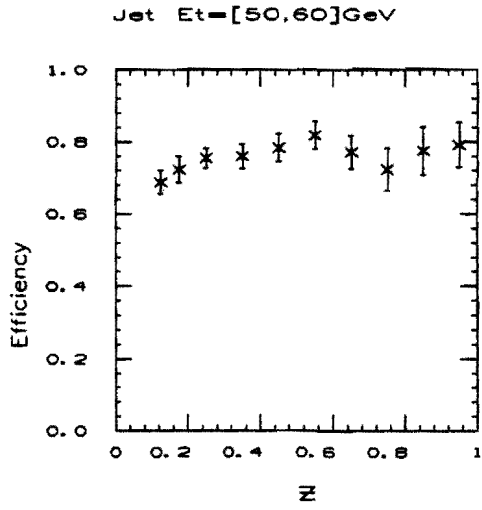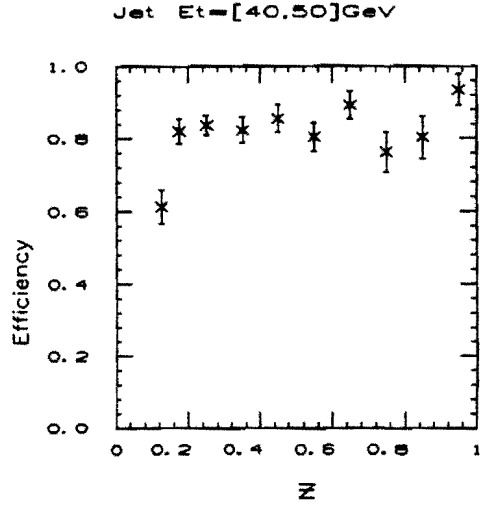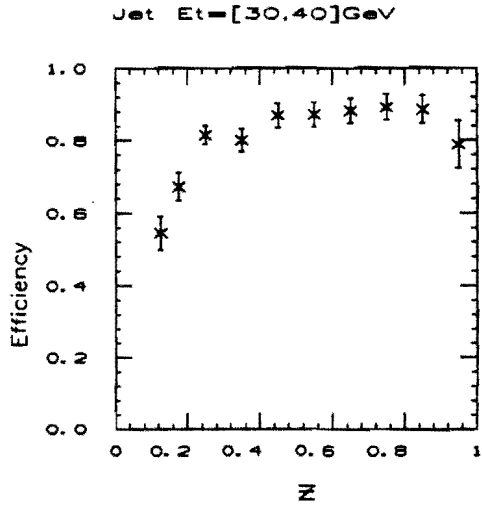
Figure 35. The same as Figure 34 except for the $\cos\theta_H$ cut.

99

Jet Et=[30,40]GeV

Jet Et=[40,50]GeV

Jet Et=[50,60]GeV

Jet Et=[60,70]GeV

Jet Et > 70 GeV

All Jets
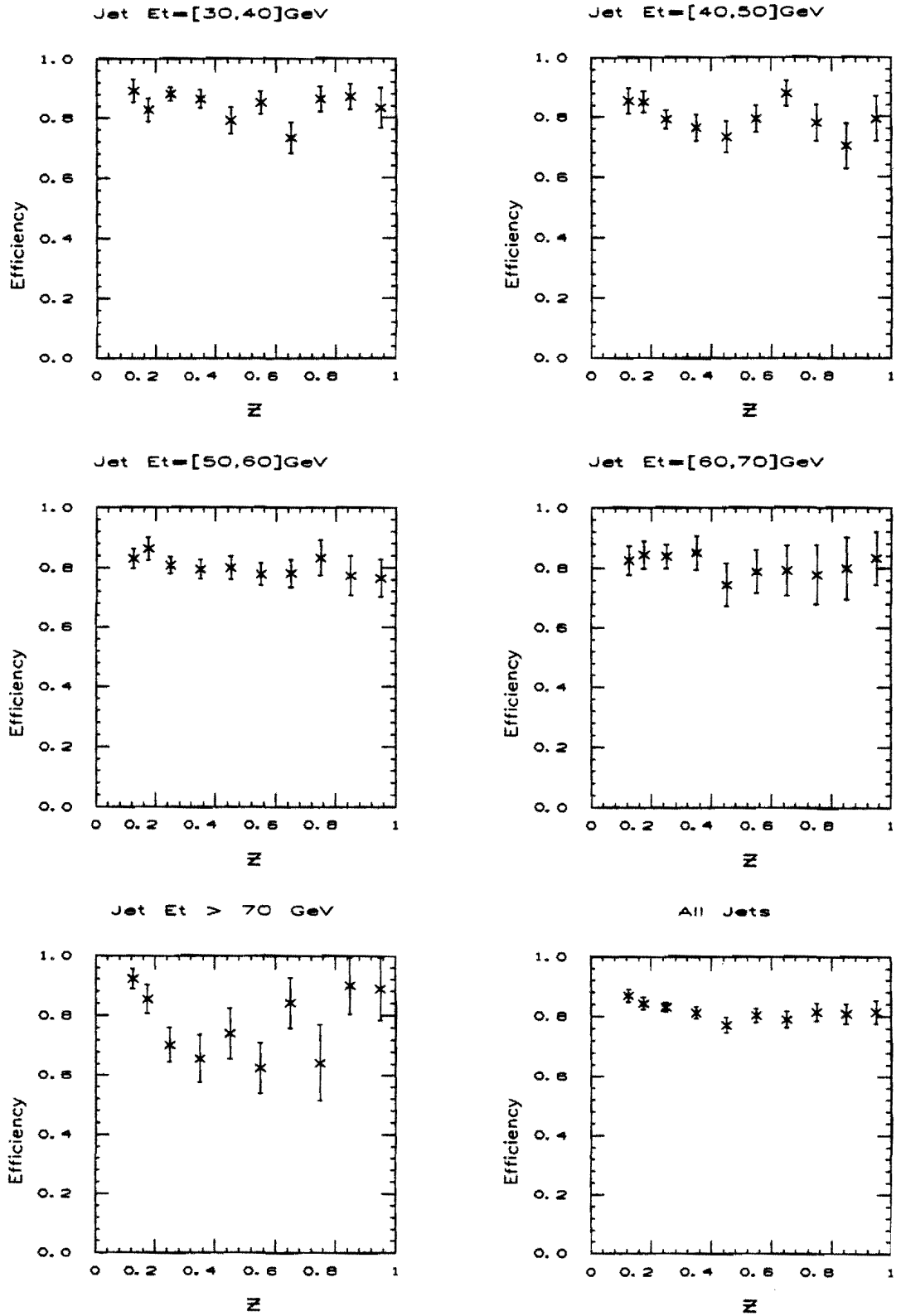
to survive the p_t cut. We therefore expect the efficiency of the cut requiring $|\cos\theta_H|<0.8$ to be slightly greater than 80%.

Figure 36 shows the effect of the mass cuts. At higher values of z the cuts become less efficient because the mass resolution is getting worse, due to the increased p_t of the D^*. This inefficiency is dominated by the fixed cut on ΔM because we have constructed the $M_{K\pi}$ cut in such a way that its window is scaled to take the broadening mass resolution into account.

Finally, in figures 37 and 38 (Table 3) we show the D^* efficiency including the effect of all the above cuts.

5.3.1 The Average Efficiency for z>0.1

To obtain the average efficiency for z > 0.1, the efficiency as a function of z was folded in with a probability distribution for z. The z distribution was obtained by taking the values from Chapter 4 for the excess above background in the D^* bin for slices of z and fitting the excess as a function of z to the form $dN/dz \sim 1/z \cdot e^{-\beta z}$ (Figure 39). The average efficiency was then computed as the product $\epsilon(z_i) \cdot dN/dz_i$ summed over z bins from 0.1 to 1. For each bin, $\epsilon(z_i)$ is the efficiency from Figure 38 and dN/dz_i is the integral of the fitted function over that bin. The value of β from the fit was $\beta=5.0\pm3.1$ with a χ^2 of 0.007 for two degrees of freedom. The extremely low value of the χ^2 simply reflects the fact that the uncertainties on the fitted points are enormous. Figure 40a is a scatterplot of the mean efficiency versus the value of β; Figure 40b is the projection of Figure 40a onto the efficiency axis. We see that the efficiency ranges from 0.415 to 0.455. This efficiency is dominated by the low-p_t reconstruction efficiency which is just turning on for most of the D^*s in our analysis (see Appendix B).

Figures 40c and 40d show the efficiency as a function of β for a sample of jets with track multiplicity $\geq$ 20. The track multiplicity is defined as the number of tracks (after selection) inside a cone of radius $\Delta R=1$ with respect to the jet axis. In this sample, the average

Figure 36. The same as Figure 34 except for the mass cuts.

Jet Et=[30,40]GeV

Jet Et=[40,50]GeV

Jet Et=[50,60]GeV

Jet Et=[60,70]GeV

Jet Et > 70 GeV

All Jets
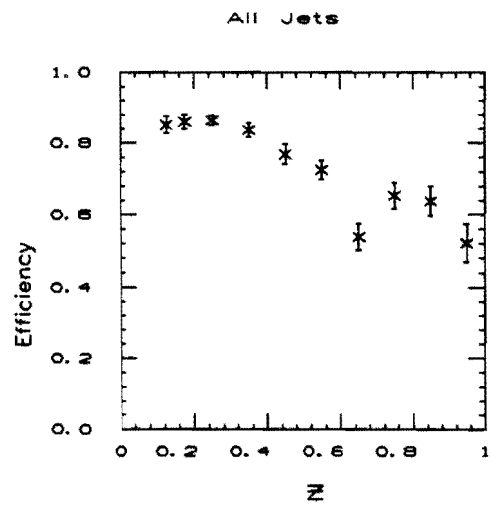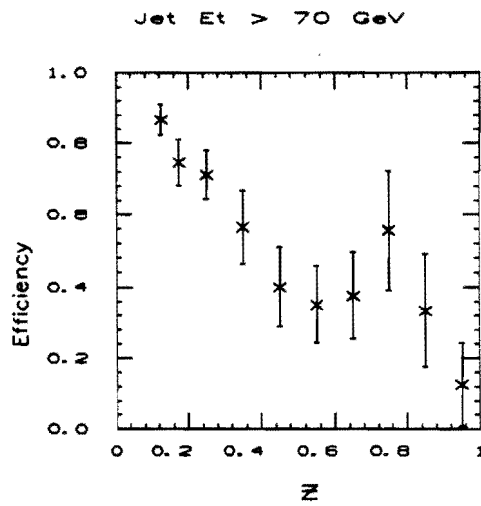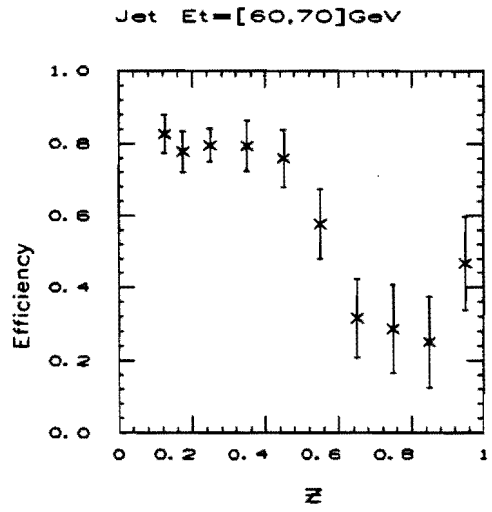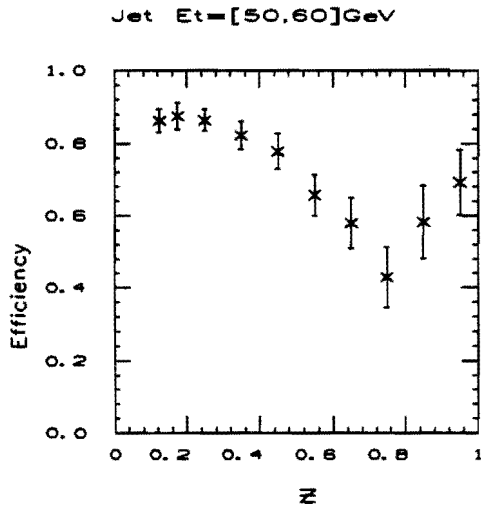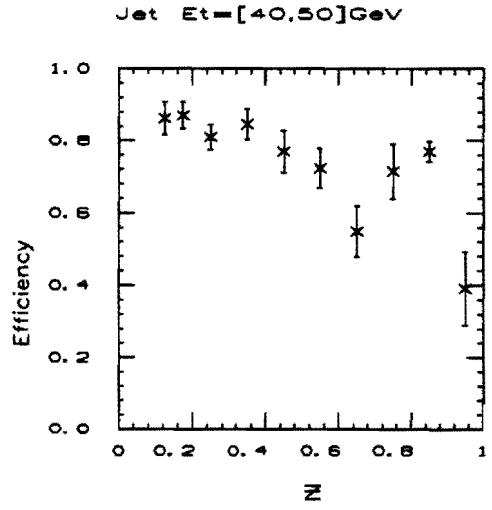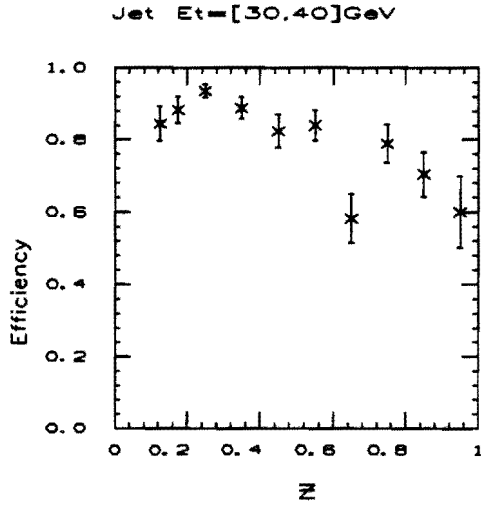
Figure 37. The efficiency for finding D*s in jets after all
the cuts.

Jet Et=[30,40]GeV

Jet Et=[40,50]GeV

Jet Et=[50,60]GeV

Jet Et=[60,70]GeV

Jet Et > 70 GeV
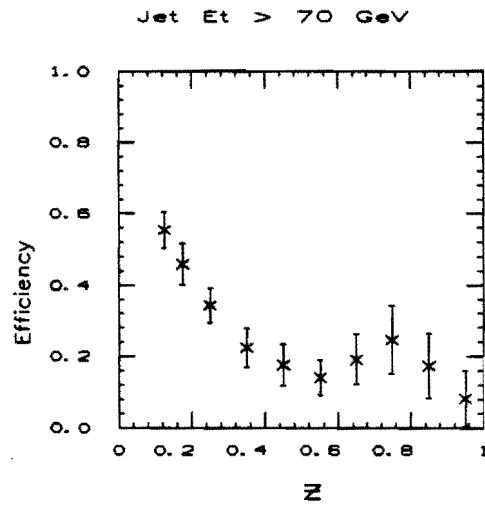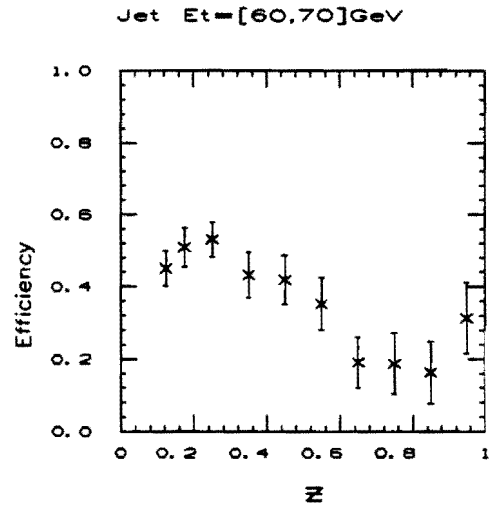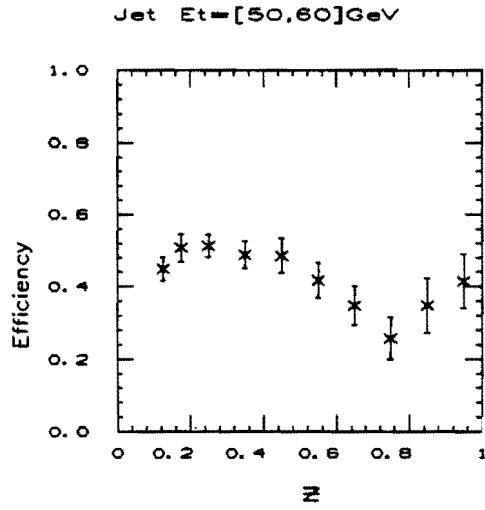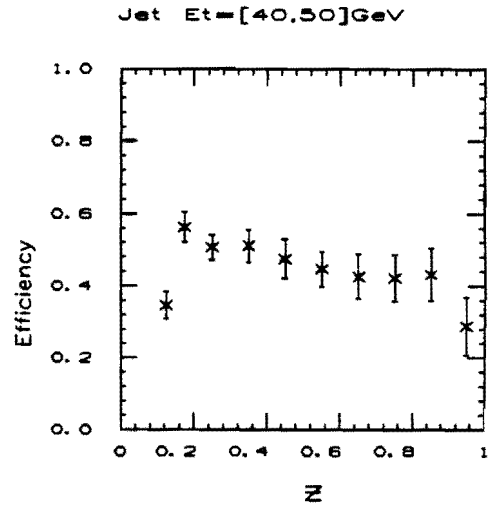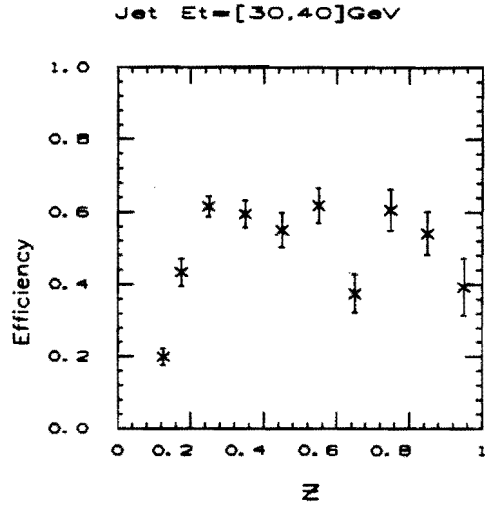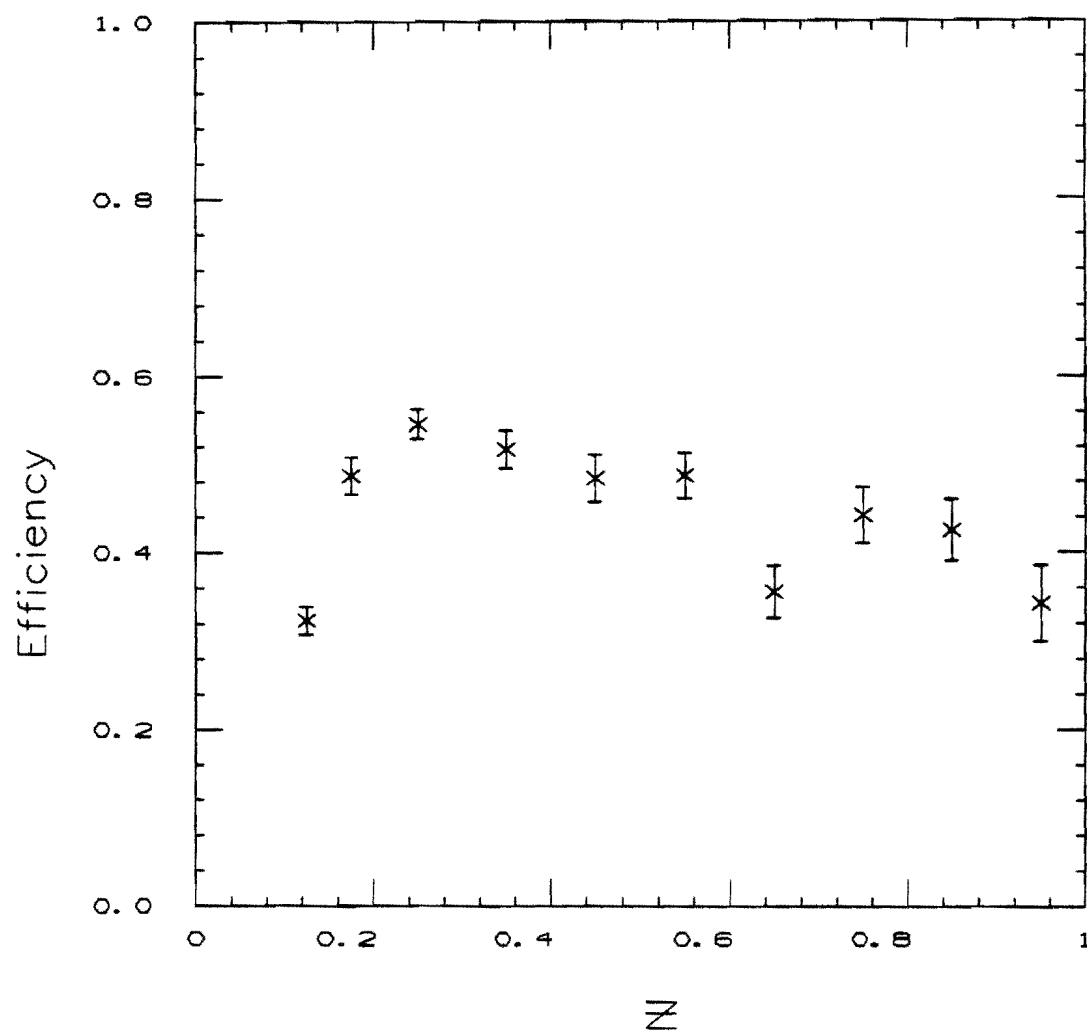
Figure 38. The overall efficiency for finding D^*s in jets, folding in the jet E_t spectrum.

Table 3. The D* efficiency in jets as a function of the fragmentation variable z, the track multiplicity in the jet, and the mass difference resolution for $z<0.5$. Refer to the text for the exact conditions.

$\langle z \rangle$	Average track multiplicity	High track multiplicity	Avg. mult., $\sigma(\Delta M)=0.75$ MeV	High mult., $\sigma(\Delta M)=0.75$ MeV
0.125	0.324 ± 0.016	0.235 ± 0.022	0.276 ± 0.015	0.201 ± 0.020
0.175	0.487 ± 0.021	0.387 ± 0.039	0.410 ± 0.021	0.327 ± 0.037
0.25	0.546 ± 0.017	0.477 ± 0.032	0.464 ± 0.017	0.406 ± 0.031
0.35	0.517 ± 0.022	0.508 ± 0.040	0.452 ± 0.022	0.441 ± 0.039
0.45	0.484 ± 0.027	0.440 ± 0.047	0.444 ± 0.027	0.403 ± 0.045
0.55	0.487 ± 0.026	0.410 ± 0.052	0.487 ± 0.026	0.410 ± 0.052
0.65	0.356 ± 0.029	0.395 ± 0.058	0.356 ± 0.029	0.395 ± 0.058
0.75	0.442 ± 0.032	0.299 ± 0.060	0.442 ± 0.032	0.299 ± 0.060
0.85	0.425 ± 0.035	0.346 ± 0.073	0.425 ± 0.035	0.346 ± 0.072
0.95	0.343 ± 0.043	0.449 ± 0.095	0.343 ± 0.043	0.448 ± 0.095
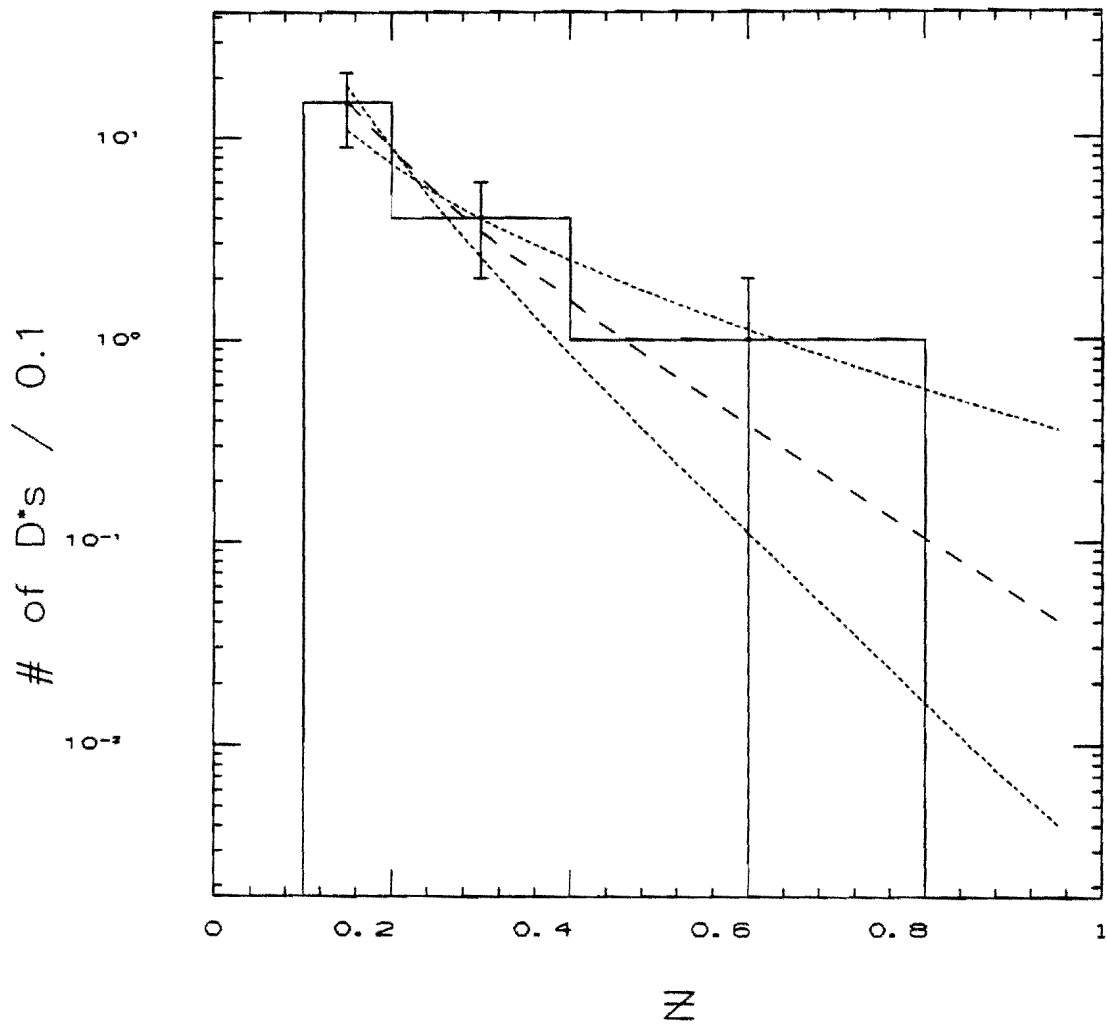
Figure 39. The raw dN/dz spectrum for D^*s. The solid line is a fit to the form $dN/dz \sim 1/z * e^{-\beta z}$ and the dotted lines show the effect of changing β by 1σ.

Normal Multiplicity

High Multiplicity
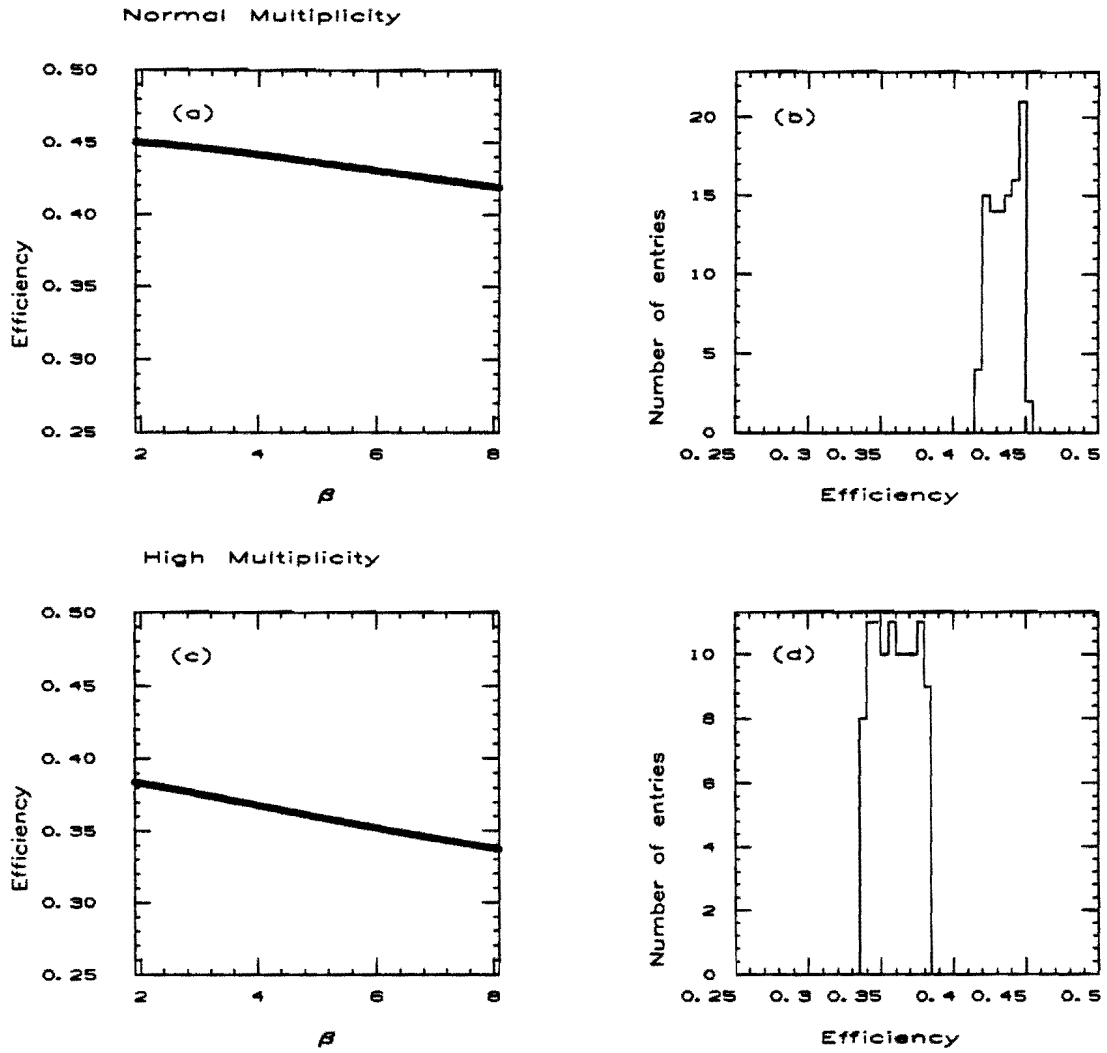
Figure 40. The sensitivity of the efficiency to the slope parameter β in the parametrization of the raw D^* dN/dz spectrum. (a) The mean D^* efficiency for $z > 0.1$ as a function of β. (b) The projection of (a) onto the efficiency axis. (c) The same as (a) for the high multiplicity jet sample. (d) The projection of (c) onto the efficiency axis.

efficiency ranges from 0.335 to 0.385. The main loss in efficiency occurs in the low-z region (Figure 41) where, unfortunately, most of the signal is found.

Our reason for examining the efficiency in high-track-multiplicity jets was that there was some evidence that the multiplicity of tracks in jets containing D^*s was higher than the multiplicity in average jets. Figure 42 shows the track multiplicity of jets which had a track combination with a mass difference ΔM in the D^* signal region, $144.5 < \Delta M < 146.5$ MeV/c^2; also shown is the track multiplicity in jets which had a wrong-sign combination in the D^* signal bin. Subtracting the wrong-sign distribution from the right-sign distribution, the mean track multiplicity for the remaining jets comes out to 12.5, slightly higher than the 10 tracks typically associated with average jets (see Figure 13, Chapter 4). As an upper limit to the track multiplicity associated with D^* production, we selected a sample of jets with track multiplicities $\geq$ 20.

In hindsight, this seems to be a far too conservative upper limit. The main effect on our final answer will be to inflate the systematic uncertainty. If we use just the average-multiplicity jets, the efficiency is 0.435 ± 0.020; if we include the high-multiplicity data, the efficiency becomes 0.395 ± 0.060 where the systematic uncertainty has been expanded to cover the full range of efficiencies from both data samples. The average efficiency therefore changes only by about 9% of itself.

We have also examined the sensitivity of the efficiency to the uncertainty in the mass resolution. We will discuss the resolution in more detail in Chapter 6, but briefly the problem is as follows. The Monte Carlo predicts a ΔM resolution of 0.40 MeV/c^2 for low values of z, while a fit to the D^* data indicates a resolution of 0.55 MeV/c^2 with a large uncertainty, $^{+0.24}_{-0.17}$ MeV/c^2. While the resolution from the data is consistent with that from the Monte Carlo, it is also consistent with being worse than the Monte Carlo would predict. We therefore took as an upper limit a resolution of 0.75 MeV/c^2 from the data and a lower limit from the Monte Carlo of 0.4 MeV/c^2. The effect
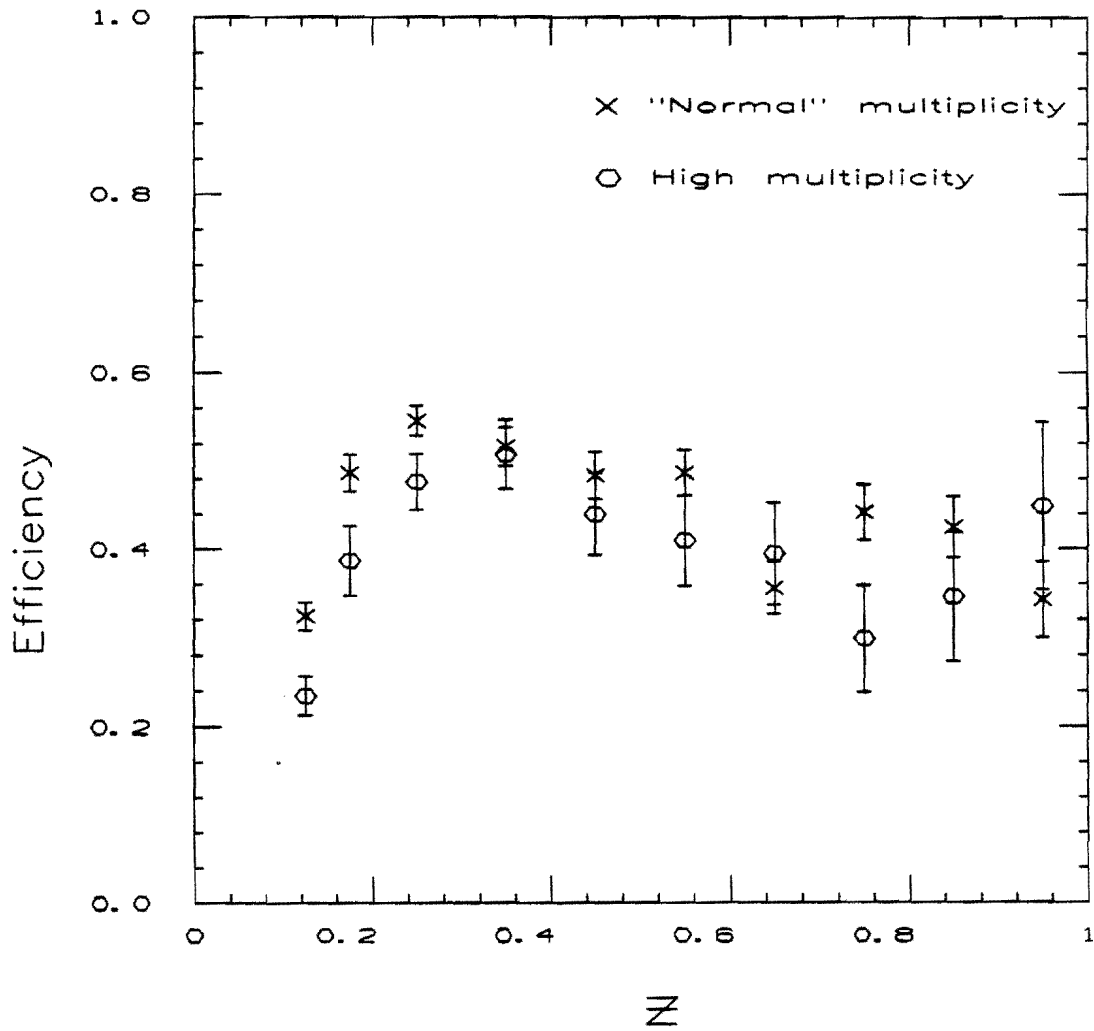
Figure 41. The overall efficiency for D^*s in high multiplicity events. For comparison, the efficiency in average multiplicity events is also shown.
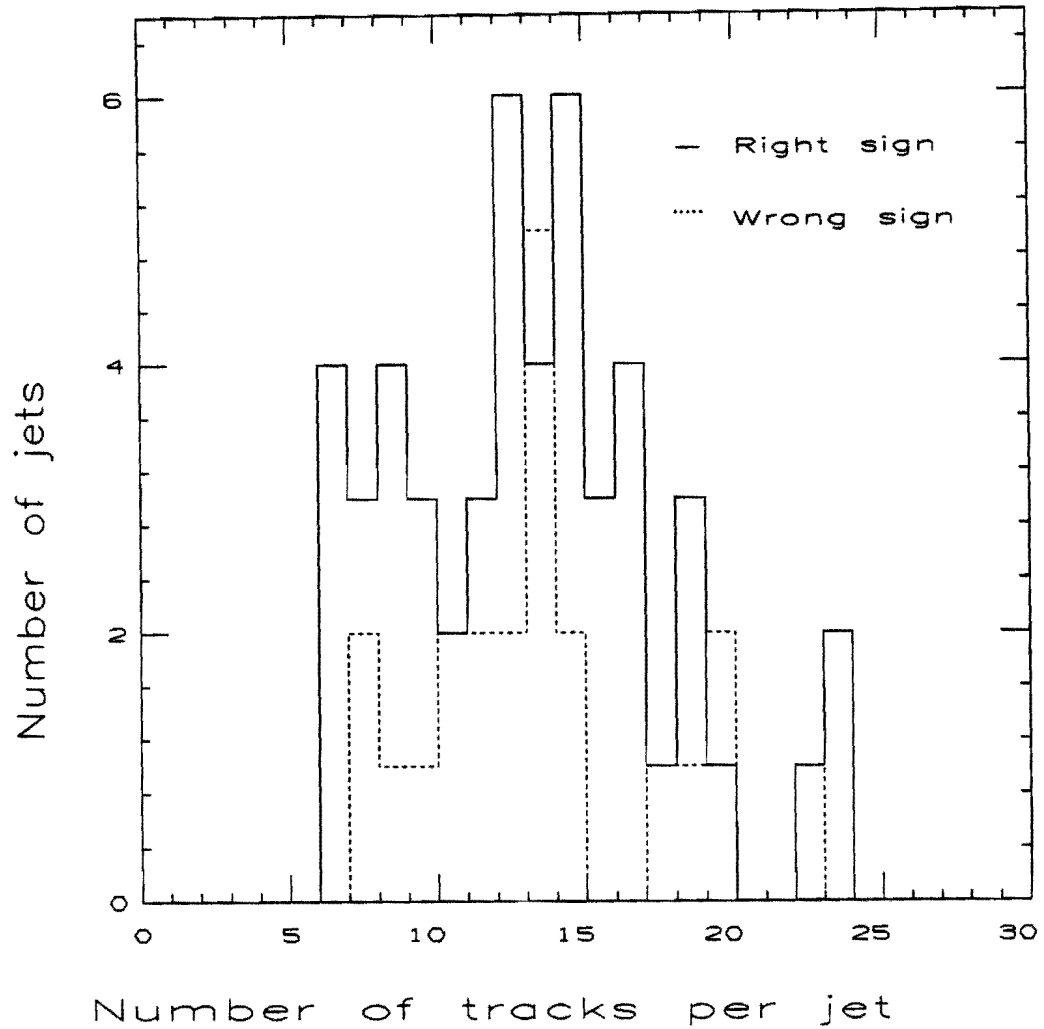
Figure 42. A comparison of the track multiplicity in jets associated with D^* production with that in typical jets. Solid histogram - The track multiplicity for those jets which had a track combination with a mass difference ΔM in the D^* signal region: $144.5 <$ $\Delta M < 146.5$ MeV/c^2. Dotted histogram - The track multiplicity for those jets with a wrong-sign mass combination in the D^* signal region.

on the efficiency of changing the resolution from 0.40 MeV/c^2 to 0.75 MeV/c^2 is shown in Figure 43. Again, the mean efficiency is not very sensitive, changing from 0.395 to 0.37. However, to cover the full range of values for the efficiency, we have had to increase the systematic uncertainty from 0.06 to 0.09.

Using the same procedure, we have also obtained the average efficiency for $z > 0.1$ separately for each of the cuts applied in the D* search. The results are summarized in Table 4.

Figure 43. The effect on the efficiency of changing the ΔM resolution in the region of z where the Monte Carlo resolution is suspect. The ΔM resolution was changed from 0.40 MeV/c^2 to 0.75 MeV/c^2 in the following regions:

Jet E_t	Z region
30-40 GeV	$z < 0.5$
40-50 GeV	$z < 0.4$
50-60 GeV	$z < 0.3$
60-70 GeV	$z < 0.2$
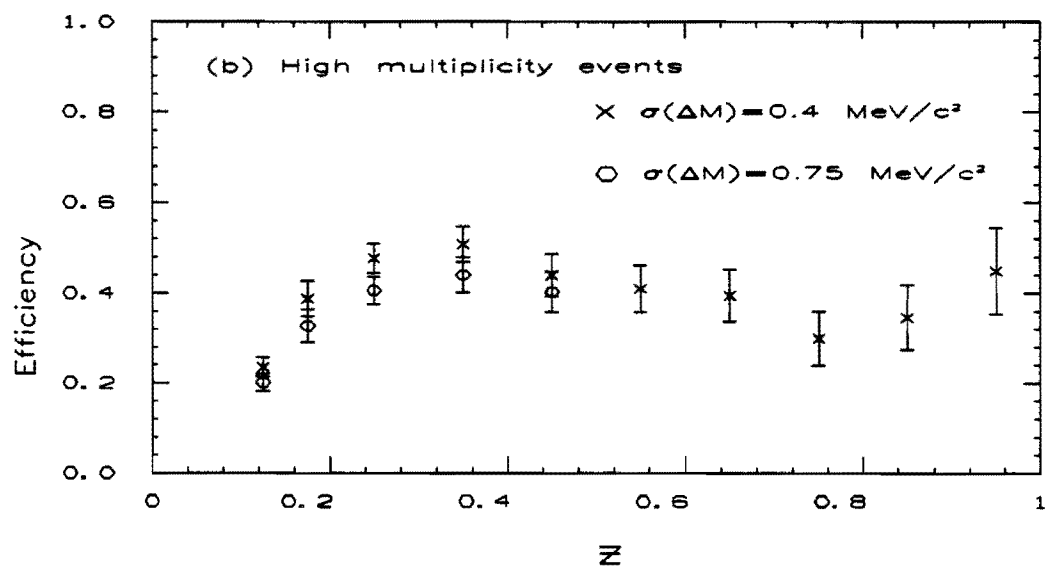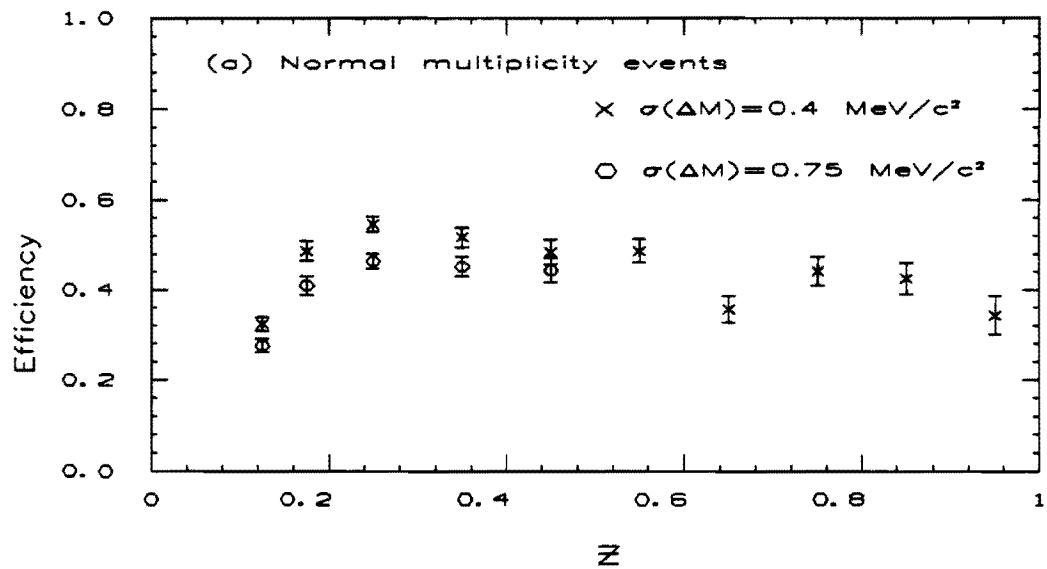
Table 4. The average efficiency for D^*s with $z>0.1$ for each of the cuts applied in the D^* search.

Cut	Average trk. multiplicity	High trk. multiplicity	Avg. mult. $\sigma(\Delta M)=$ 0.75 MeV	High mult. $\sigma(\Delta M)=$ 0.75 MeV	Overall
1	0.81 → 0.89				0.85 ± 0.04
2	0.69 → 0.74	0.54 → 0.63			0.64 ± 0.10
3	0.83 → 0.85	0.84 → 0.86			0.84 ± 0.02
4	0.82 → 0.86	0.79 → 0.83	0.71 → 0.73	0.69 → 0.71	0.78 ± 0.09

The cuts are as follows:

Cut	Content
1	$p_t > 300$ MeV/c, $|\eta| < 1.2$
2	Track reconstruction and selection
3	$|\cos\theta_H| < 0.8$
4	$|M_{K\pi}-M_{D^0}| < 3\delta$, $144.5 < \Delta M < 146.5$ MeV/c^2

Each column in the table shows the range in the efficiency for a particular condition of track multiplicity in the jet and the mass difference resolution for $z<0.5$; the range is due to the uncertainty in the shape of the z distribution for D^*s. The rightmost column shows the overall efficiency for the cut, taken so as to cover the entire range of efficiencies in the four columns to the left.

CHAPTER 6

TRACKING RESOLUTION ISSUES

In this chapter we discuss the tracking resolution and its effects on our analysis. First we describe how the resolution was estimated for the track parameters p_t, ϕ and $\cot\theta$. The results of a simple Monte Carlo are then presented to give the reader some feeling for how the resolution for the various track parameters contributes to the mass resolution for D^*s and D^0s. Finally, we address the issue which has the most immediate bearing on our result, namely the efficiency of the mass cuts which were applied to extract the D^* signal and the sensitivity of the efficiency to the mass resolution.

6.1 Method for Estimating the Resolution

The track parameter resolution was estimated with Monte Carlo D^* tracks merged into real jet data, using the data described in Appendix B for the study of the single-track-finding efficiency. A comparison of the track parameters of the reconstructed Monte Carlo track with the known parameters with which the tracks were generated was used to estimate the resolution. One of the main contributions to the resolution is expected to be errors in associating the proper hits with the proper tracks; this effect should be simulated rather well by this method since the Monte Carlo tracks are buried in real jet data. The other major contribution to the resolution is our knowledge of the relationship between the drift-time and the drift-distance; it is not clear that this is equally well simulated.

To gain some confidence on this second point, we examined the tracking residuals for the Monte Carlo tracks and compared them to

those for ordinary tracks from the data. Recall that a "residual" is the distance between a hit that is associated with a track, and the fitted location of the track itself. The same procedure was followed as in Chapter 5 to establish which of the reconstructed tracks corresponds to the Monte Carlo track. The tracks were then subjected to the same selection criteria before they were considered in this study. Figures 44 and 45 show the results in bins of track p_t. A visual inspection of the figures suggests that above a p_t of 700 MeV/c, the agreement between the Monte Carlo and the data is good; below 700 MeV/c, the agreement is still fairly good until we drop below 500 MeV/c where the distributions from the data are somewhat broader than those from the Monte Carlo. This is thought to be due to the fact that tracks at these momenta have a substantial component of motion along the (azimuthal) drift direction, causing the leading edge drift electrons to come from a different point in the drift cell compared to tracks at normal incidence. This is illustrated in Figure 46. A correction for this effect is applied in the track reconstruction, and is included in the residual distributions for the data shown in Figures 44 and 45. We will see later on in this chapter that the overall efficiency for D^*s is not terribly sensitive to the disagreement between the data and the Monte Carlo.

6.2 Track Parameter Resolution

The p_t resolution was obtained by plotting the p_t difference between the reconstructed track and the original track, $\Delta p_t / p_t^2 \equiv (p_{ti} - p_{tr})/p_{tr}^2$, for slices of p_{ti}, where we have denoted the p_t of the implanted and reconstructed tracks by p_{ti} and p_{tr}, respectively. The difference was then fit to a Gaussian in each p_t slice. Figure 47 is a plot of the σ of the Gaussian versus the mean p_t in each bin for vertex constrained tracks. The horizontal error bar indicates the r.m.s. of the p_t in each bin. Also shown is a fit to the form

Figure 44. A comparison, in bins of track p_t, of the axial residuals for tracks in jet events with the residuals for Monte Carlo tracks. The solid histogram is from the data, the points with error bars from the Monte Carlo. The residuals from the data have been normalized to the same number of entries as the Monte Carlo.
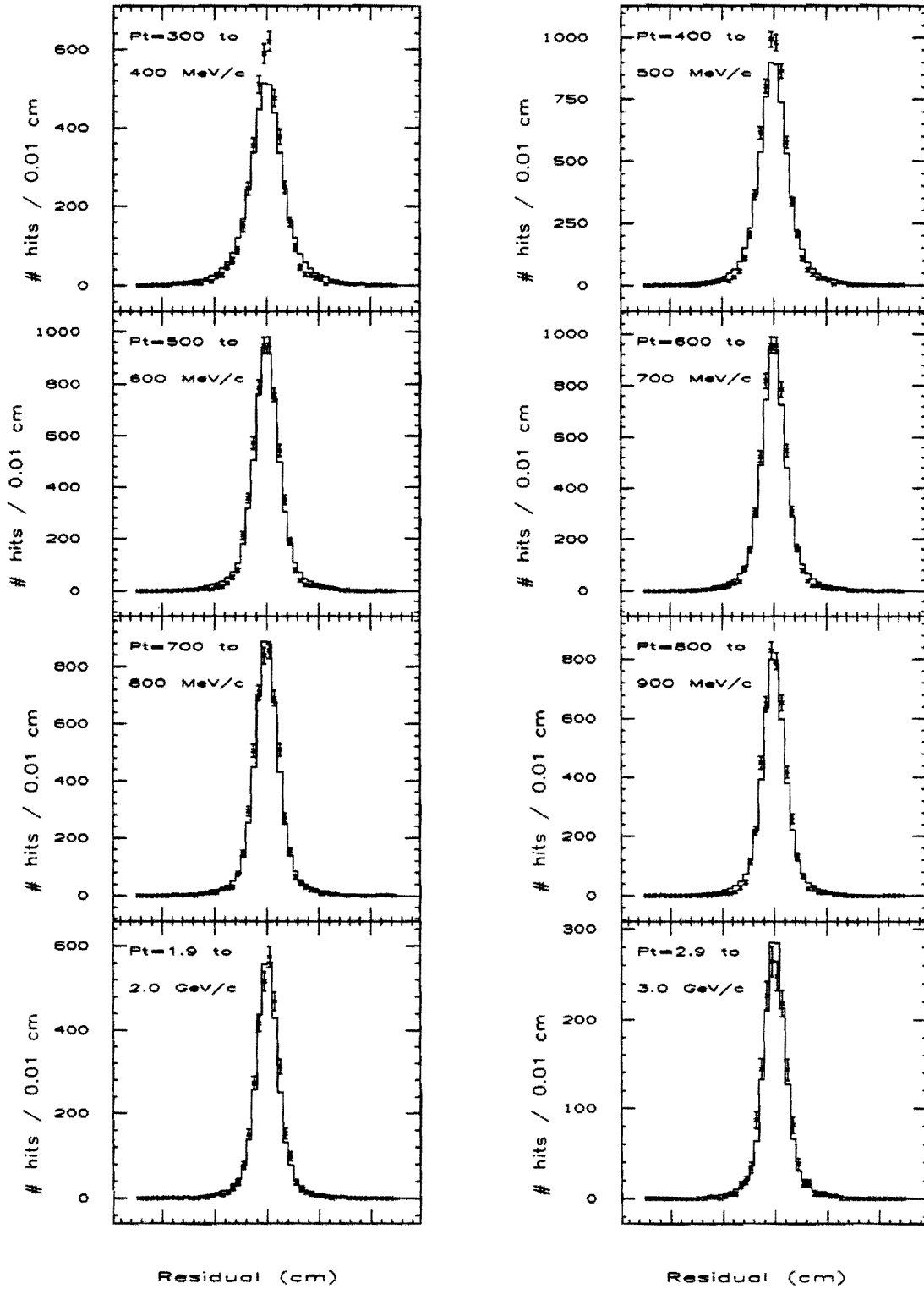
Residual (cm)

Figure 45. The same as Figure 44 except for the stereo residuals.

121

Residual (cm)   Residual (cm)
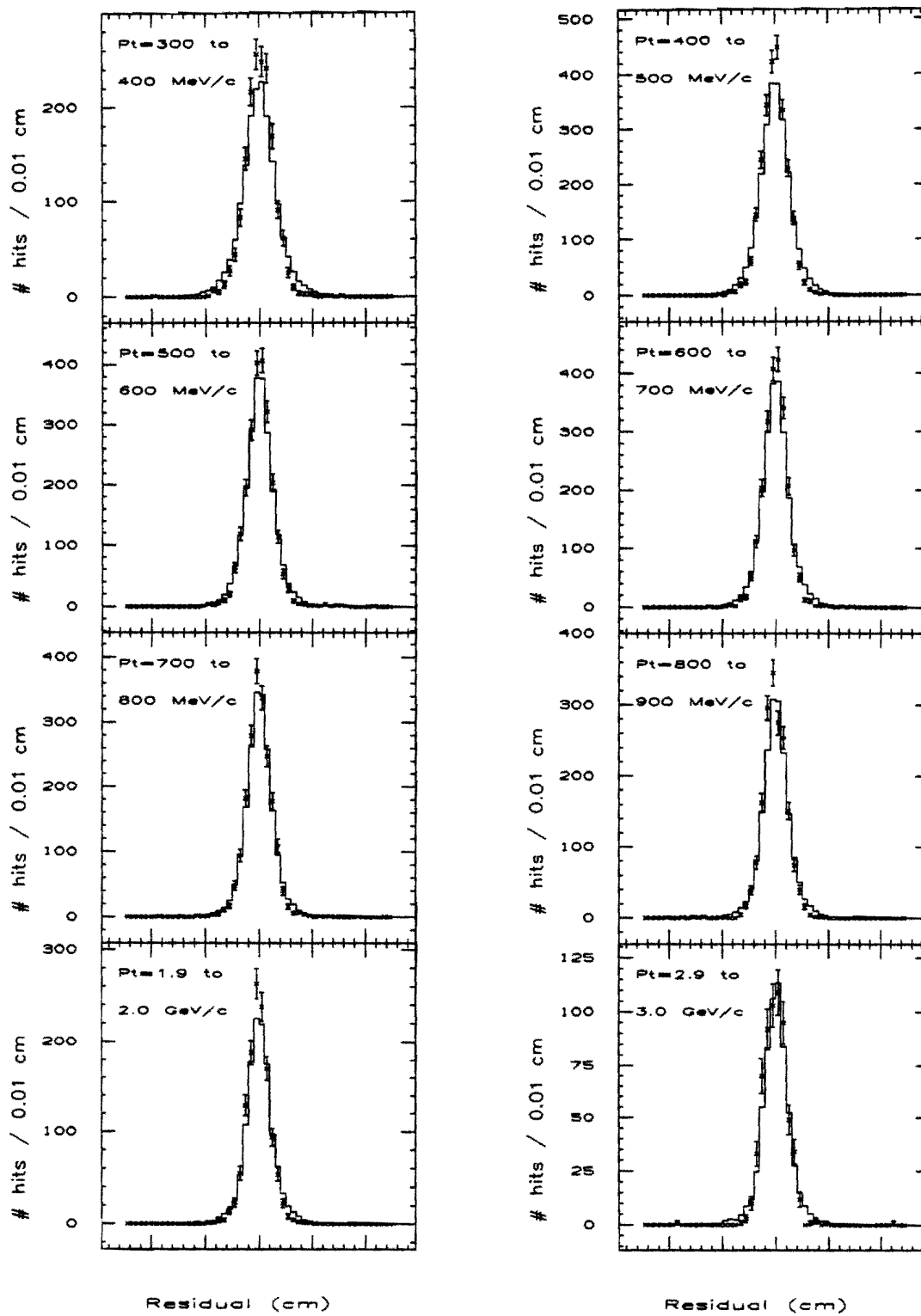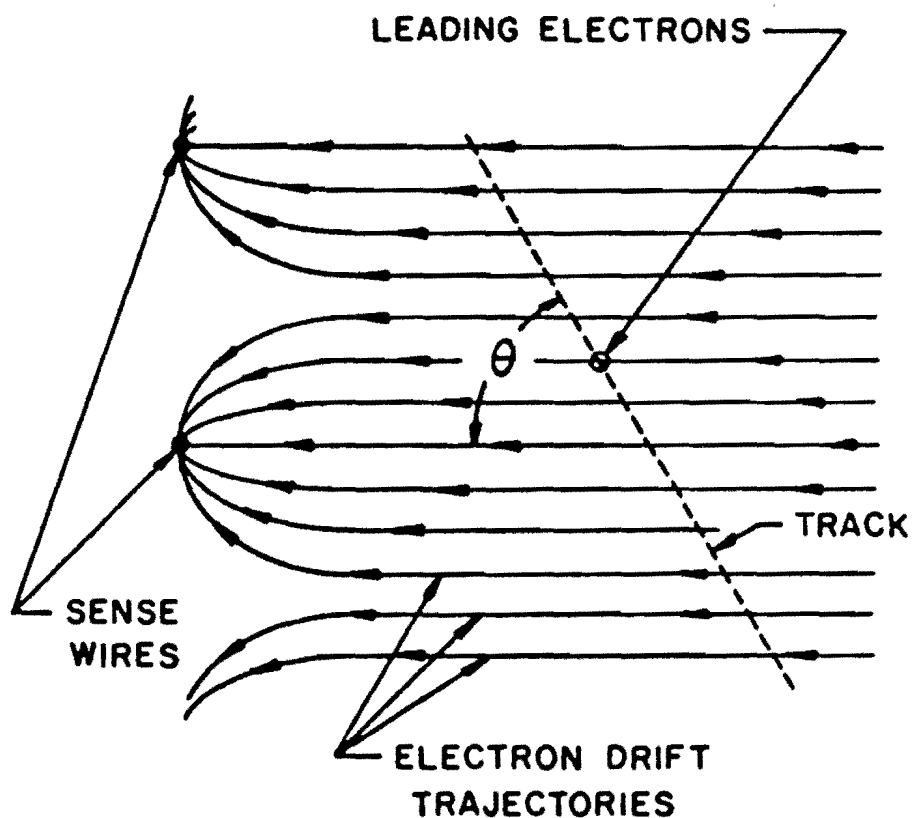
Figure 46. An illustration of how the originating point of the leading-edge drift electrons differs from the center of the cell as the angle of the track with respect to the sense wire plane changes.
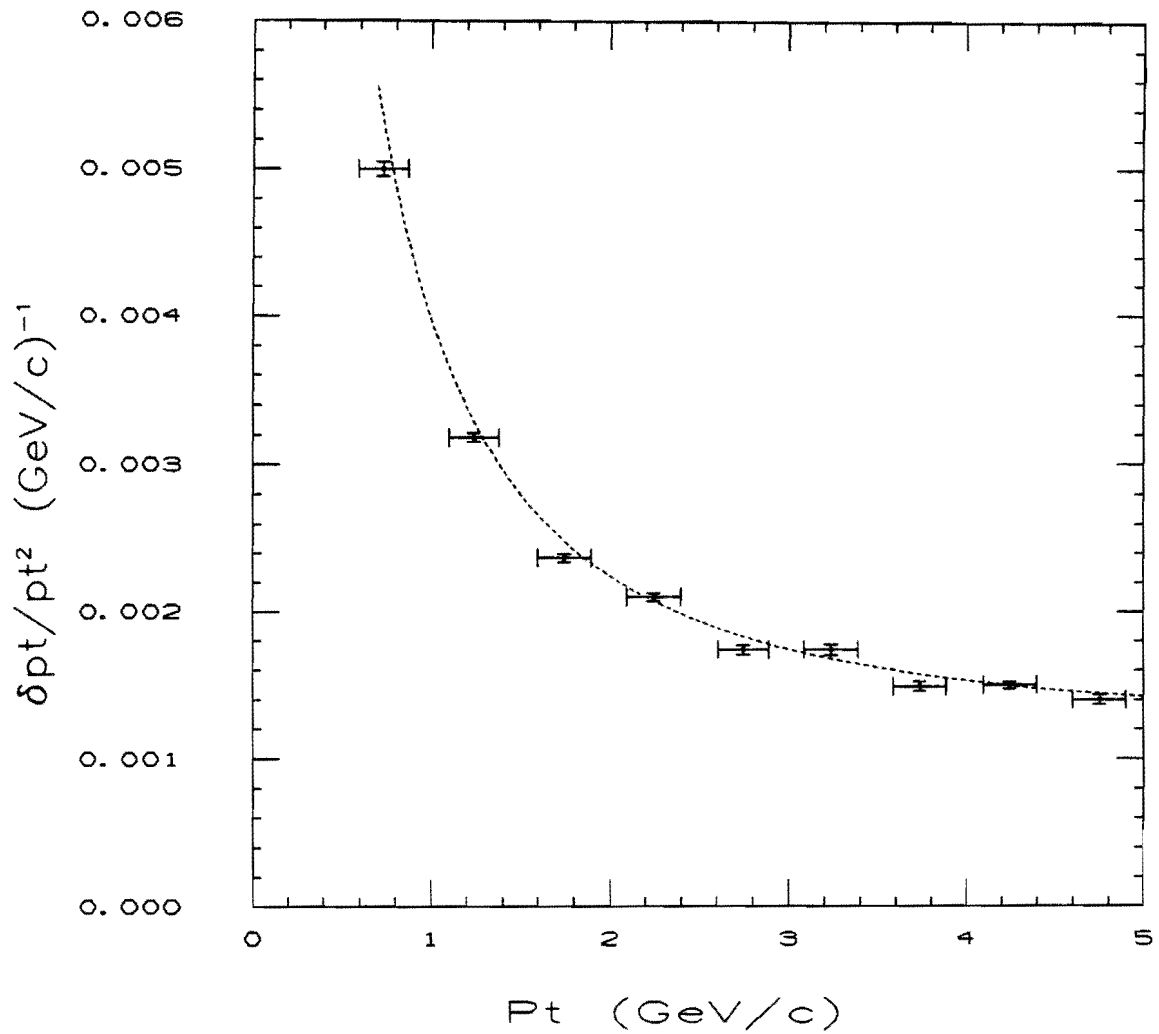
Figure 47. The difference between the reconstructed track p_t and the true p_t for Monte Carlo tracks merged into jets as a function of the mean p_t in each bin. The horizontal error bar indicates the r.m.s of the p_t in each bin. The dashed line is a fit to the form $\Delta p_t/p_t^2 = [a^2 + (b/p_t)^2]^{0.5}$.

$$\frac{\Delta p_t}{p_t^2} = \sqrt{a^2 + (b/p_t)^2} \quad (\text{GeV/c})^{-1}$$

where the term $(b/p_t)^2$ parameterizes the effect of multiple scattering. Since we did not have a fitting routine which took errors on both axes into account, we translated the horizontal error into a vertical error using the above functional form and the usual error propagation formulae. This error was then added in quadrature to the error on σ which came from the Gaussian fit for each point. The same procedure was followed for ϕ. Figure 48 shows the σ of the $\Delta\phi$ distribution in each p_t bin; this was then fit to the same functional form as for the p_t resolution. The $\cot\theta$ difference is shown in Figure 49 along with a Gaussian fit. The results of the fits were:

$$\frac{\Delta p_t}{p_t^2} = \sqrt{(0.0012)^2 + (0.0038/p_t)^2} \quad (\text{GeV/c})^{-1}$$

$$\Delta\phi = \sqrt{(0.32)^2 + (1.0/p_t)^2} \quad (\text{mrad})$$

where p_t is in GeV/c

$$\Delta(\cot\theta) = 0.0022$$

These values are for vertex-constrained tracks above 700 MeV/c. For reference, the same procedure for non-vertex-constrained tracks yields:

$$\frac{\Delta p_t}{p_t^2} = \sqrt{(0.0023)^2 + (0.0041/p_t)^2} \quad (\text{GeV/c})^{-1}$$

$$\Delta\phi = \sqrt{(0.83)^2 + (1.9/p_t)^2} \quad (\text{mrad})$$

where p_t is in GeV/c

$$\Delta(\cot\theta) = 0.0075$$
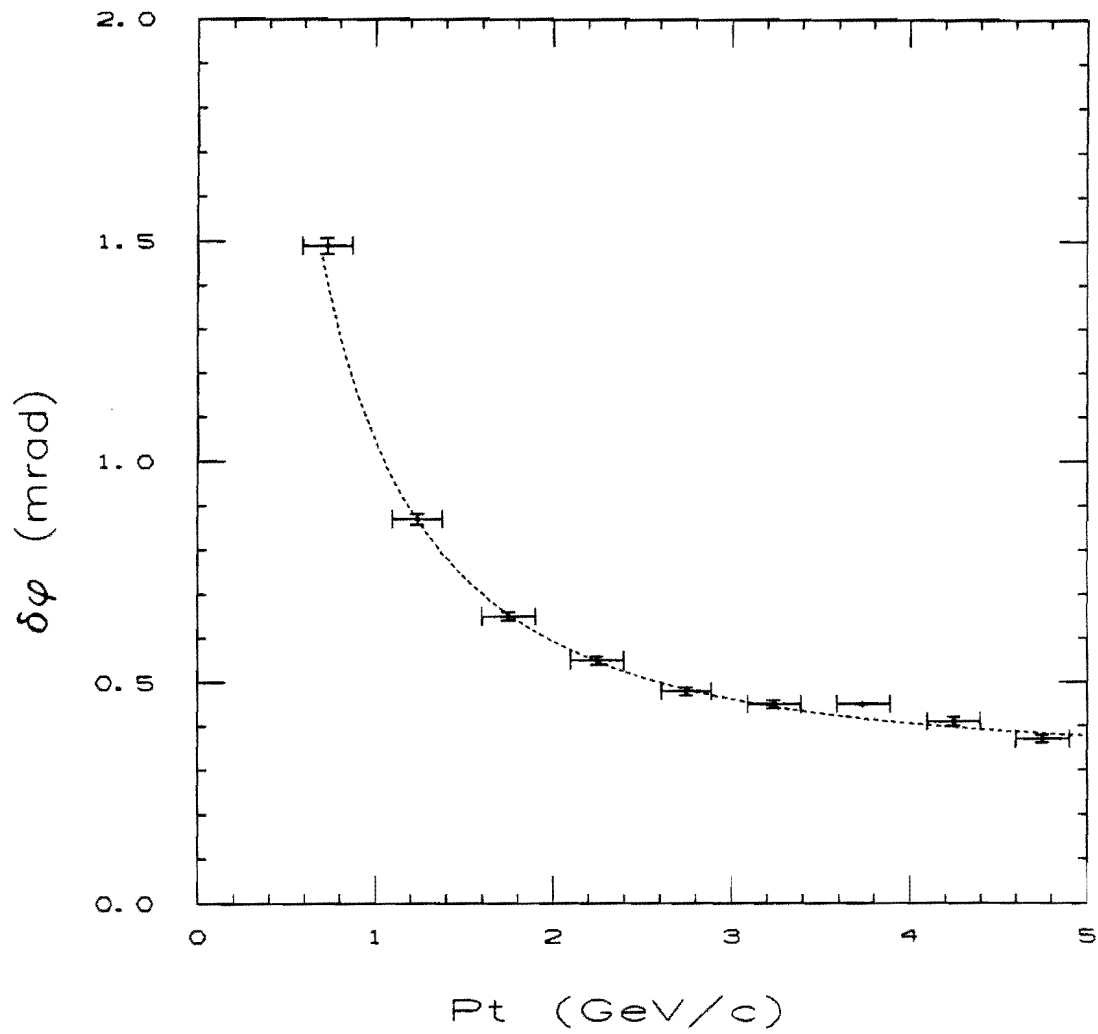
Figure 48. The same as Figure 47 except for $\Delta\phi$.
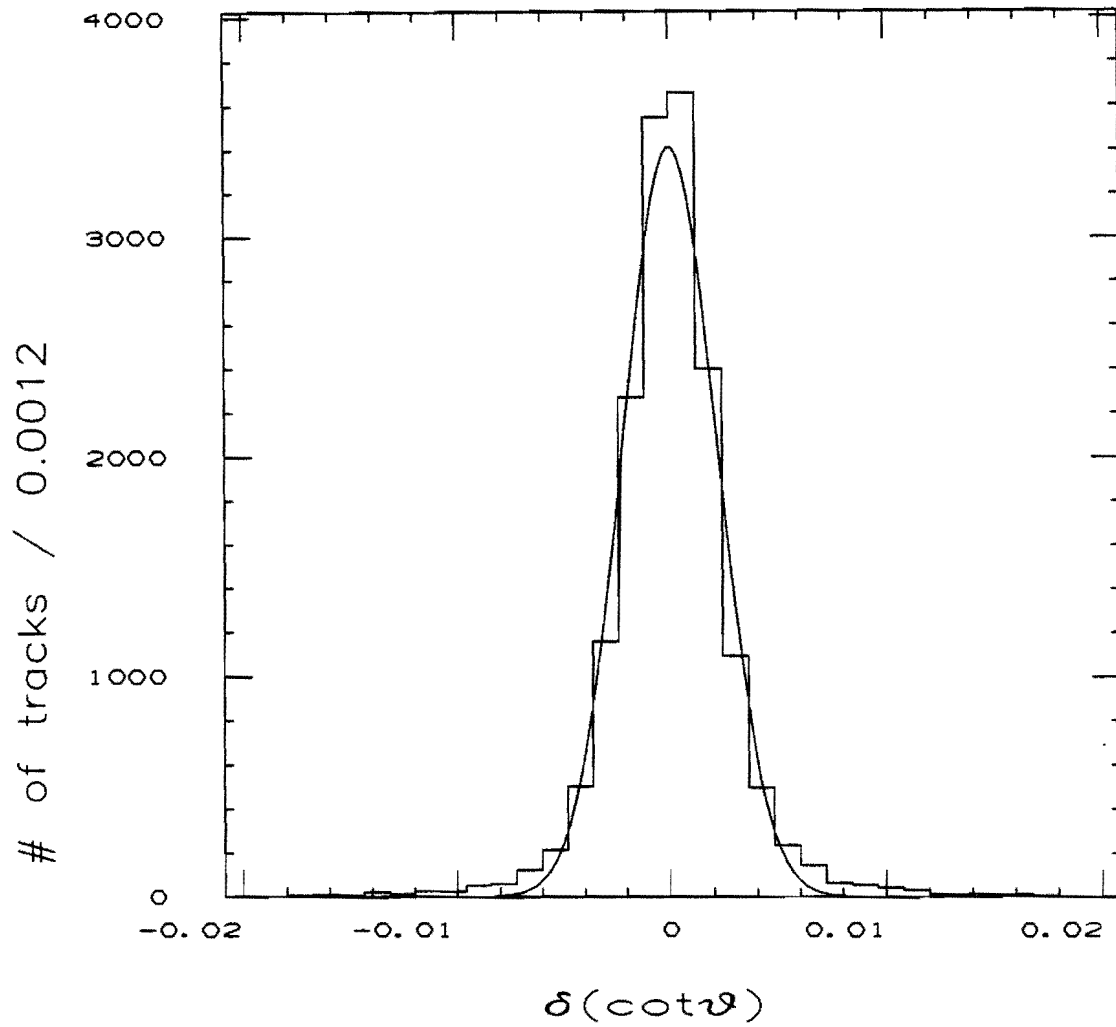
Figure 49. The difference between the reconstructed $\cot\theta$ and the true $\cot\theta$ along with a Gaussian fit.

The $\cot\theta$ resolution is larger than what one expects from a naive calculation for a vertex-constrained straight-line fit in the r-z plane with a z resolution of 4mm ($\sim 200\mu/\sin 3°$, where 3° is the angle of the stereo wires with respect to the axial wires). For a straight-line fit with fixed intercept, the error on the slope (i.e. $\Delta(\cot\theta)$) is given by

$$\Delta(\cot\theta) = \frac{\sigma_z}{\sqrt{\sum r_i^2}}$$

where r_i are the radial positions of the stereo sense wires. If we take a track with 20 stereo hits (e.g. hits in all layers except the four innermost layers), we obtain $\Delta(\cot\theta) = 10^{-3}$. One possible reason for the larger value for the $\cot\theta$ resolution from the Monte Carlo is the effect of pattern recognition errors, associating the track with the wrong hits in the stereo view.

We also note that the multiple scattering error on the p_t and ϕ measurements begins to overtake the intrinsic resolution of the chamber when the p_t of the track drops below about 3 GeV/c in the vertex-constrained case. The slow pion in the decay $D^* \rightarrow D^0 \pi$ is almost always in this multiple scattering region due to the soft fragmentation of gluons into D^*s and the small Q value in the decay.

6.3 Where Does the Mass Resolution Come From?

To get some feeling for how these track parameter uncertainties contribute to the mass resolution, a simple Monte Carlo was written to generate D^* decays and smear the track parameters according to the above parametrizations for vertex-constrained tracks. Correlations between the track parameters were ignored. Figure 50 shows the mass resolution from this "toy" Monte Carlo as a function of the p_t of the D^*. As expected, the multiple scattering contribution to
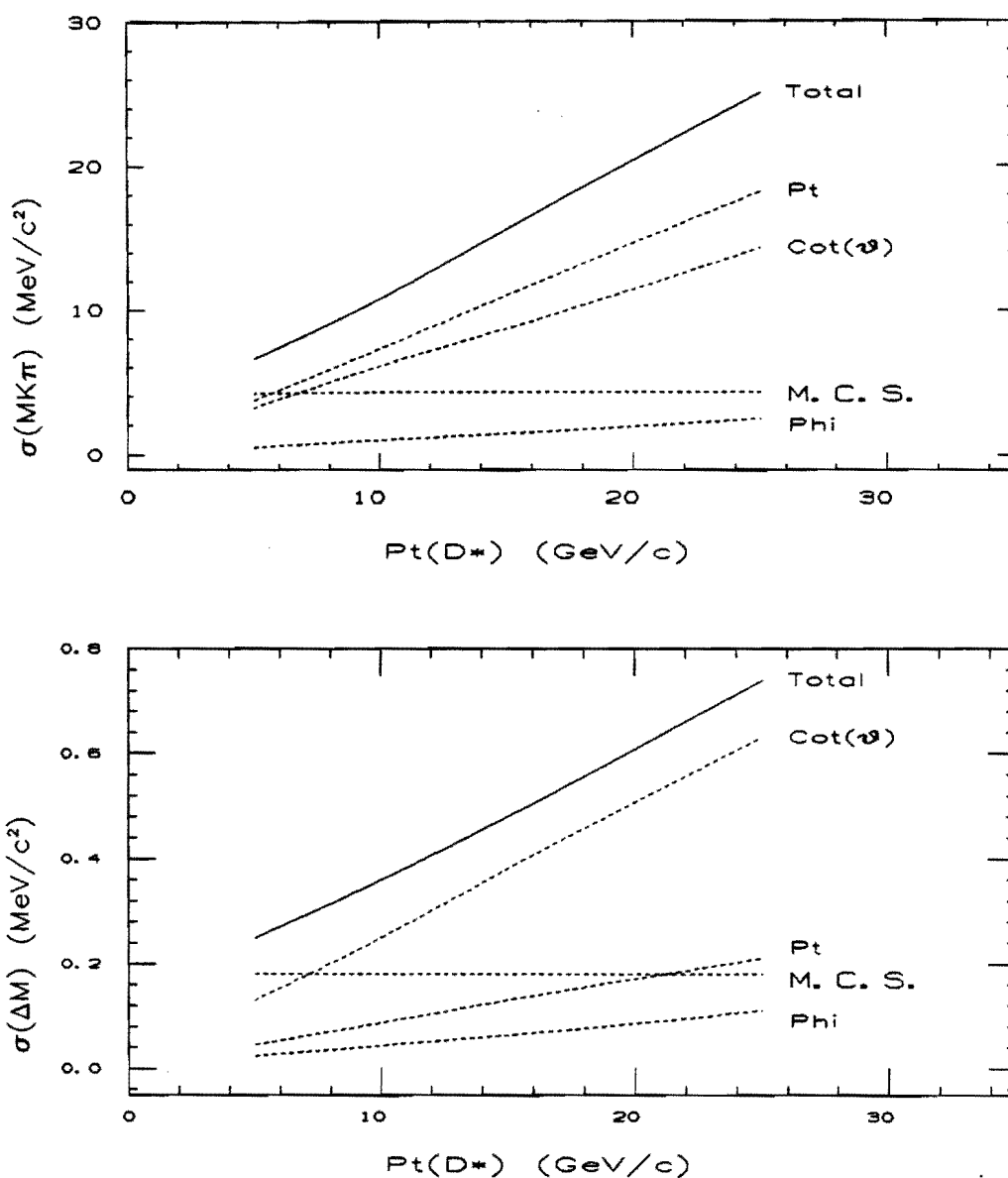
Figure 50. The resolution for the D^0 mass and the D^*-D^0 mass difference obtained from a "toy" Monte Carlo as a function of the p_t of the D^*. The contributions of the various track parameter measurement errors are shown separately. "M.C.S" refers to the contribution of multiple Coulomb scattering.

the resolution is significant for low p_t D^*s, especially for the mass difference. It might be interesting in the future to try to reduce this component by taking multiple scattering into account in the track fit.[71] We also note that the p_t contribution plays a far smaller role for the mass difference resolution (unlike the case for the K-π mass); as we mentioned in Chapter 4, this is because the mass difference resolution is dominated by the resolution on the slow pion.

6.4 The Efficiency of the Mass Cuts

Let us first recall the mass cuts which were used in Chapter 4 to extract the D^* signal. To be counted as a D^* candidate, a track combination was required to satisfy the cuts:

$$|M_{K\pi} - M_{D0}| < 3\delta$$

$$144.5 < \Delta M < 146.5 \ \text{MeV/c}^2$$

As described in Chapter 4, δ is a measure of the uncertainty in the mass of the K-π combination, computed from the above-determined track parameter uncertainties according to the error-propagation formula

$$\delta = \left\{ \sum_{K,\pi} \left[\left(\frac{\partial M}{\partial p_{ti}}\right)^2 (\Delta p_{ti})^2 + \left(\frac{\partial M}{\partial \phi_i}\right)^2 (\Delta \phi_i)^2 + \left(\frac{\partial M}{\partial (\cot\theta_i)}\right)^2 (\Delta \cot\theta_i)^2 \right] \right\}^{1/2}.$$

Typically one determines the efficiency of such cuts directly from the data by fitting the signal to a suitable form (typically a Gaussian) and then estimating how much of the signal falls outside the cuts. Unfortunately in this analysis the signal is too low to permit this kind of fitting for all z bins. We have therefore had to resort to using the Monte Carlo.

For the D^0 efficiency, the effect of the δ cut can be well estimated by the Monte Carlo because the decay kinematics forces the

D^0 daughters to take up most of the momentum of the D^* and hence to almost always have p_t greater than 700 MeV/c (where the agreement of the residual distributions with the data is good). The effect of the kinematics can be seen in Figure 51 which is a scatterplot of the p_t of the K and the π (from the D^0) from the Monte Carlo after all the cuts except the mass cuts. The plot has been restricted to those daughters from D^*s with $0.1 < z < 0.2$ from jets with E_t between 30 and 40 GeV. Both the K and the π are above 700 MeV/c in 96% of the events. Furthermore, the proportion of such events is even higher for higher values of z and jet E_t.

Unfortunately, these arguments are not always valid for the ΔM resolution since the p_t of the slow pion is very often below 700 MeV/c. Figure 52 shows scatterplots of the slow pion p_t versus the z of the D^* for bins of jet E_t. If we accept that the Monte Carlo is good above 700 MeV/c, then from these plots we would conclude that we can trust the ΔM resolution from the Monte Carlo in the following regions:

Jet E_t	Good z region	Avg. ΔM resolution
30–40 GeV	z > 0.5	0.71 ± 0.03 MeV/c^2
40–50 GeV	z > 0.4	0.74 ± 0.03
50–60 GeV	z > 0.3	0.76 ± 0.03
60–70 GeV	z > 0.2	0.77 ± 0.03

i.e. for D^*s with $p_t \gtrsim 13$ GeV/c. (The errors are the statistical errors issued by the fitting routine.) Outside these regions we must try to estimate the error introduced by using the Monte Carlo.

Fortunately, the (little) D^* data that we have comes from these regions of z where the agreement between the residuals is poor. We can therefore try to get an estimate of the ΔM resolution directly. Figure 53 shows the ΔM distribution from the data in 0.5 MeV/c^2 bins along with a fit to a Gaussian plus a smooth background of the form $a(\Delta M - m_\pi)^b$. The fit yielded $\sigma = 0.55 \, {}^{+\,0.24}_{-\,0.17}$ MeV/c^2, which is consistent with the resolution from the Monte Carlo, 0.40 MeV/c^2, but is also
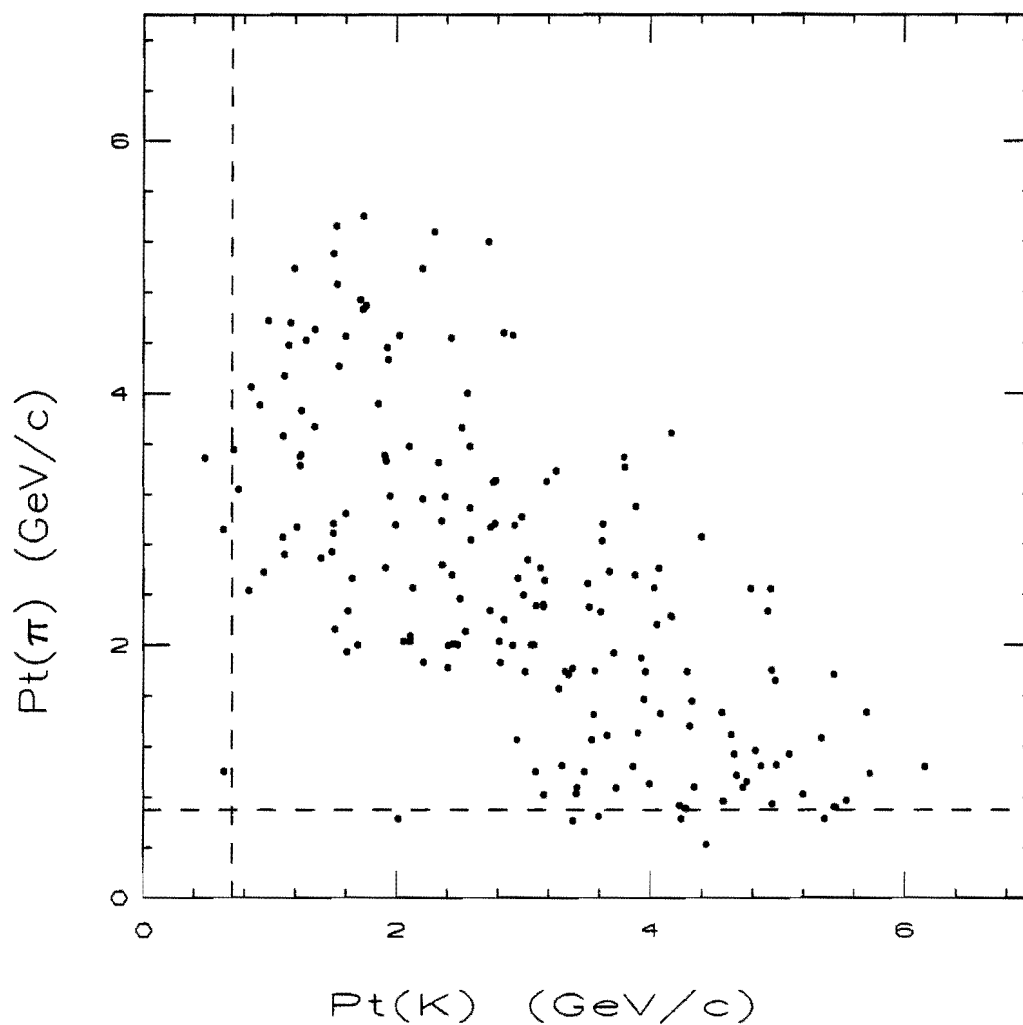
Figure 51. The p_t of the D^0 daughters from the Monte Carlo after all the cuts except the mass cuts. The D^0s shown come from D^*s with $0.1 < z < 0.2$ from jets with E_t between 30 and 40 GeV. The dotted lines indicate the boundary where the daughters have a p_t of 700 MeV/c.

Jet Et: [30,40]GeV

Jet Et: [40,50]GeV

Jet Et: [50,60]GeV

Jet Et: [60,70]GeV
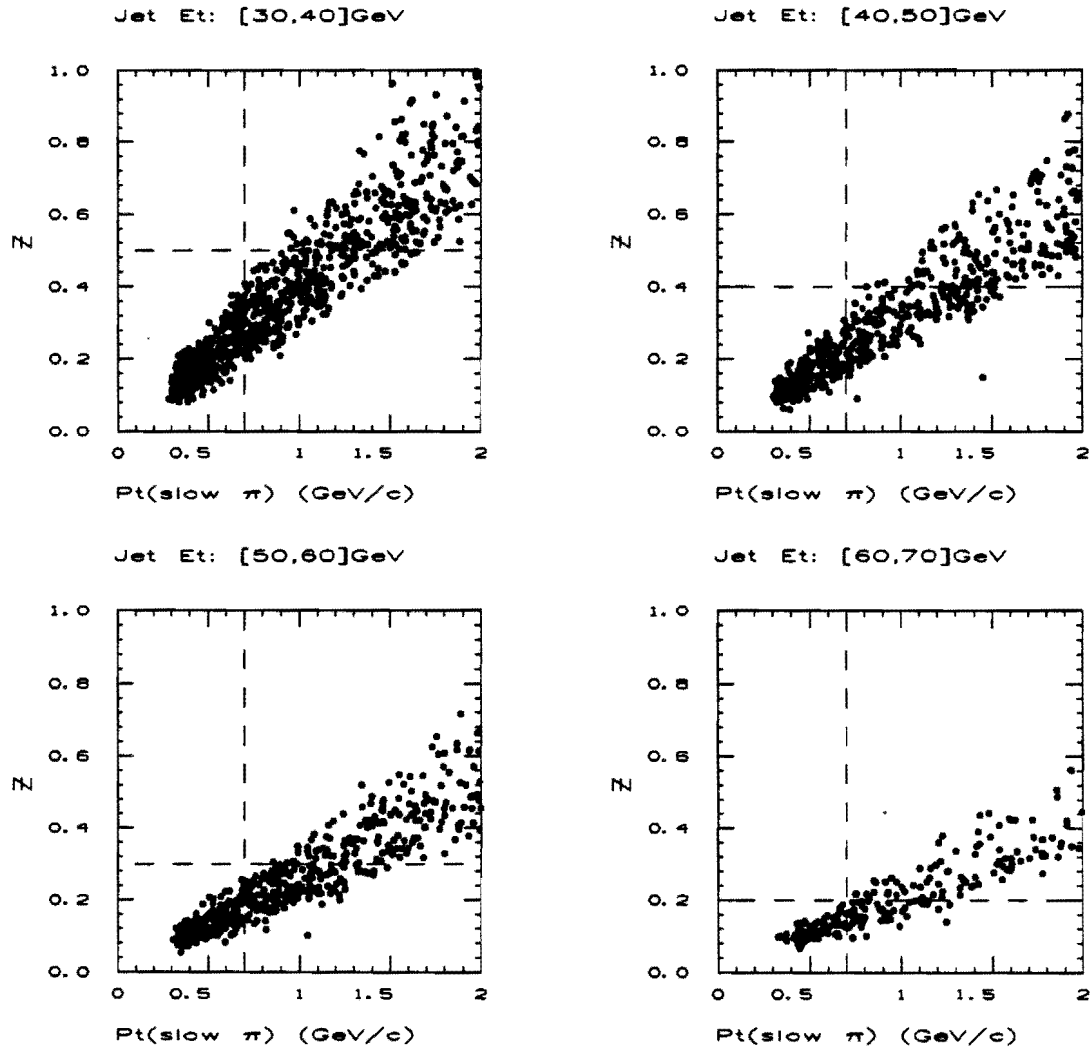
Figure 52. The p_t of the slow pion versus the z of the D^* for bins of jet E_t. The vertical dotted line is at a p_t of 700 MeV/c. The horizontal dotted line indicates the z value above which all slow pions have p_t greater than 700 MeV/c.
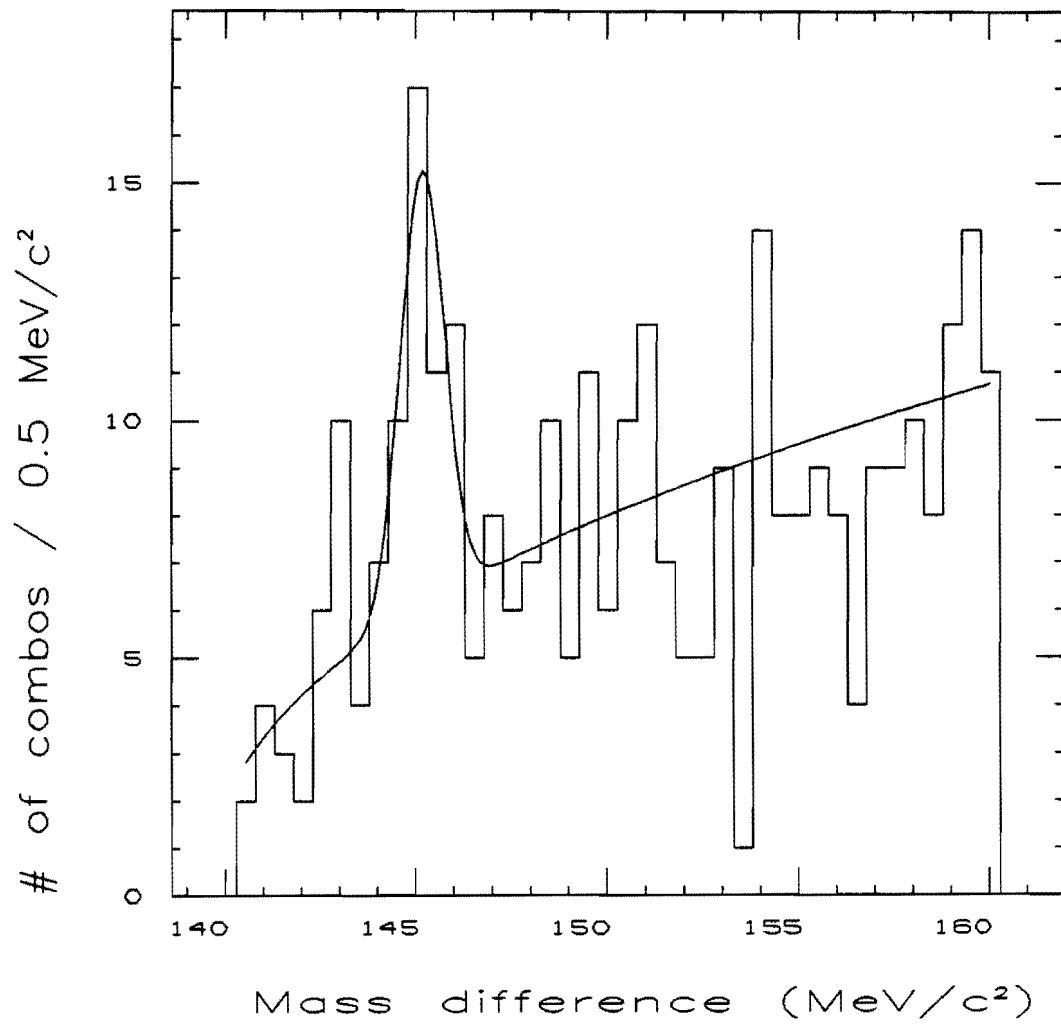
Figure 53. The ΔM distribution from the data in 0.5 MeV/c^2 bins. The fit is to the form Gaussian + $a(\Delta M - m_\pi)^b$.

consistent at 1σ with being as high as 0.8 MeV/c^2. (The mean of the Gaussian was 145.2 ± 0.2 MeV/c^2.) Figure 54 shows the efficiency of our cut on ΔM (144.5 < ΔM < 146.5 MeV/c^2) as a function of the ΔM resolution. Figure 55 shows the overall efficiency for D*s with z>0.1 as a function of the ΔM resolution. We find that for the ΔM resolution of 0.4 MeV/c^2 predicted by the Monte Carlo, the efficiency is 0.40 ± 0.06. If, on the other hand, we use the ΔM resolution of 0.75 MeV/c^2 indicated by the ~1σ upper limit on the resolution from a fit to the data, then the efficiency comes out to 0.34 ± 0.06. To cover this range of efficiencies, therefore, we will quote an efficiency of 0.37 ± 0.09. We note that our final value for the efficiency differs from the value one obtains using the Monte Carlo resolution by only 8% of itself and thus does not cause a terribly big change in the central value of our result for the number of D*s per jet. However, we have had to pay by increasing our systematic uncertainty on the efficiency from 0.06 to 0.09.

6.5 Summary

We summarize here the chain of reasoning which was used in this chapter to determine the tracking resolution in jets and the efficiency of the mass cuts applied in the process of extracting the D* signal. Monte Carlo D*s injected into real jet data were used to measure the mass resolution for the reconstructed D^0 and the D*-D^0 mass difference. We were forced to do this rather than measure the resolution directly from the data by fitting the mass peak to a resolution function because the D* signal was not large enough to determine the resolution for all values of the fragmentation variable z. By comparing the tracking residuals in the data to those in the Monte Carlo, we argued that the Monte Carlo described the data rather well for tracks with p_t greater than 700 MeV/c. This gave us confidence in the resolution from the Monte Carlo for the D^0 daughters since the kinematics forces almost all of the daughters to be above
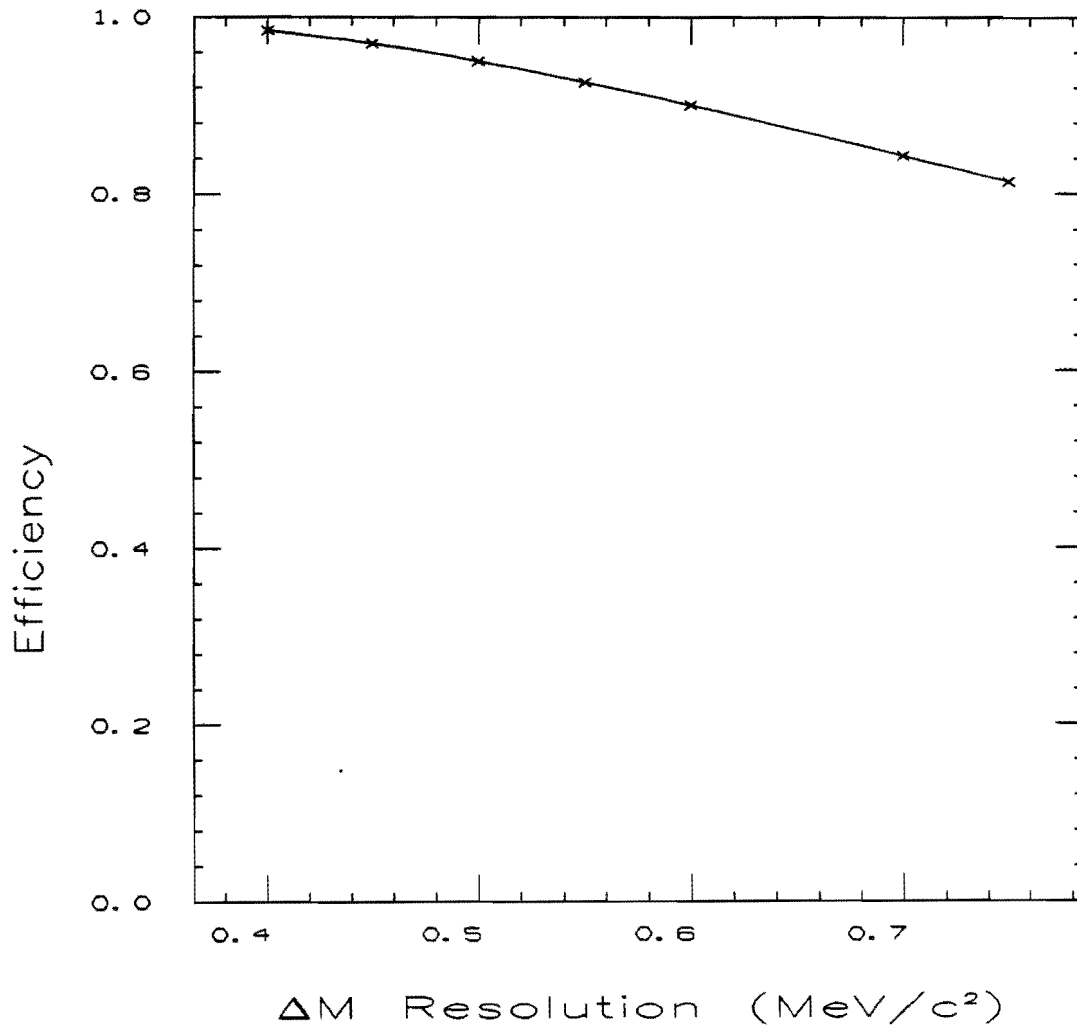
Figure 54. The efficiency of the ΔM cut as a function of the ΔM resolution. This efficiency is restricted to the following regions, where the agreement between the residuals in the data and the Monte Carlo are relatively poor:

Jet E_t	Z region
30–40 GeV	$z \leq 0.5$
40–50 GeV	$z \leq 0.4$
50–60 GeV	$z \leq 0.3$
60–70 GeV	$z \leq 0.2$
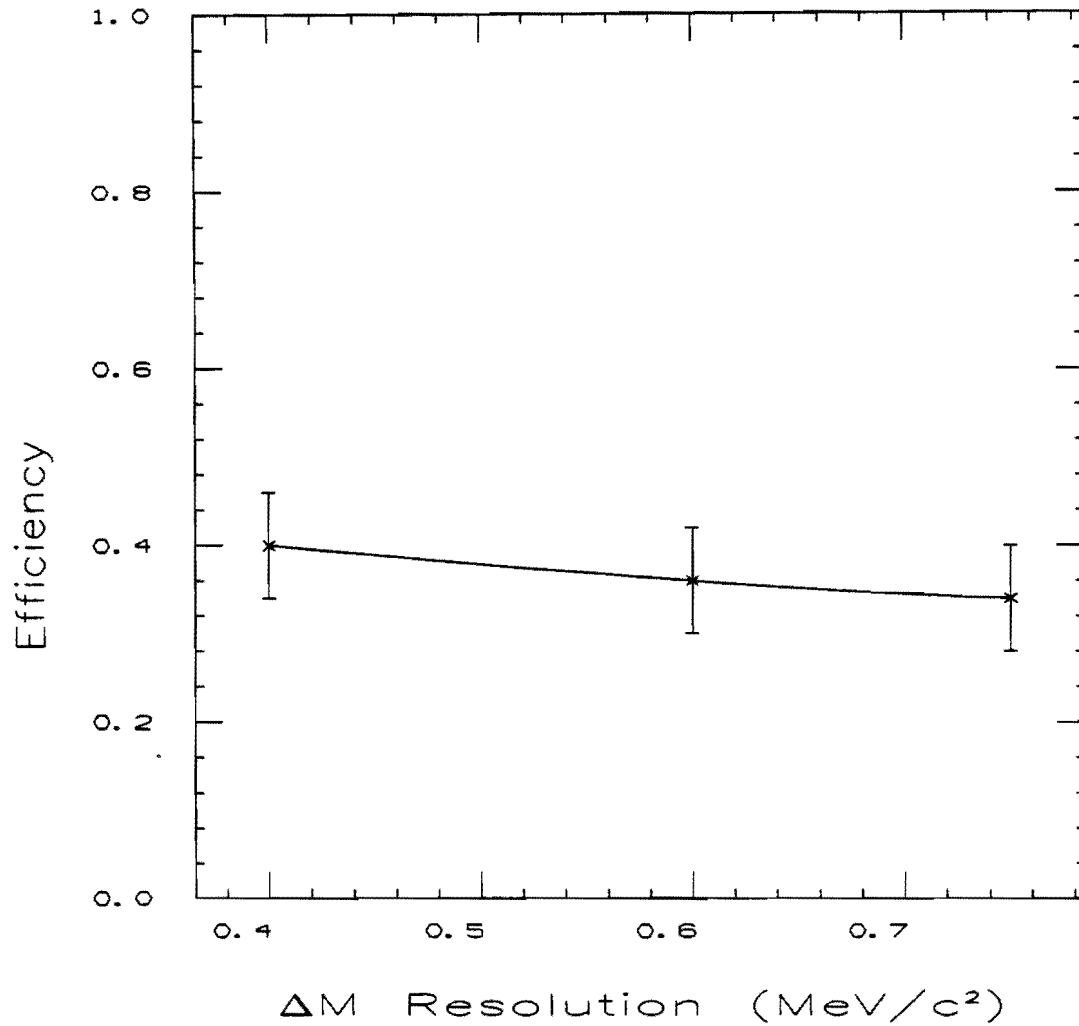
Figure 55. The overall efficiency for finding D^*s in jets with $z > 0.1$ as a function of the ΔM resolution in the region of poor agreement between the data and the Monte Carlo. The error bars indicate the uncertainty due to insufficient knowledge of the z distribution of D^*s and the charged track multiplicity in D^* events.

700 MeV/c. For the mass difference resolution, we had reason to be nervous about the Monte Carlo estimate since the slow pion often fell into the region of poor agreement between the residuals in the data and the Monte Carlo. Since most of our signal was in this region of poor agreement, we attempted a direct measurement of the ΔM resolution from the data. The resulting resolution was $\sigma(\Delta M) = 0.55 \, {}^{+\,0.24}_{-\,0.17}$ MeV/c^2. Using a range in the resolution consistent with both the Monte Carlo value and the 1σ upper bound from the data, the corresponding efficiency for D*s was found to be 0.37 ± 0.09. The effect of the disagreement between the data and Monte Carlo for the ΔM resolution was mostly to increase the systematic uncertainty in the overall efficiency from 0.06 to 0.09. The central value of the efficiency changed only by 8% of itself.

CHAPTER 7

JET ENERGY ISSUES

This chapter discusses the effects on our analysis of the uncertainty in the jet energy scale and of the jet energy resolution. The chapter begins with an overview of how the jet energy measurement dominates the measurement uncertainty in the fragmentation variable z. This is followed by a brief description of a Monte Carlo we used to estimate the effects of the jet energy uncertainty. The result of the Monte Carlo is the correction which has to be applied to the observed D^* signal to get the true number of events produced above the z cut of 0.1. Details of the determination of the jet energy scale and the energy resolution can be found in Appendices C and D respectively. The details of the Monte Carlo are described in Appendix E.

7.1 Overview of the Problem

The goal of this thesis is to measure the integral of the z distribution for D^*s in jets above a threshold at $z=0.1$. The object of this chapter is to understand how the uncertainty in z affects the value we obtain for the integral. As the z distribution for D^*s is consistent with being concentrated near the threshold (see Chapter 5), a small shift in the threshold can have a significant effect on the integral.

Since we have defined z as $z \equiv p_\ell(D^*)/E_{jet}$, where p_ℓ is the longitudinal component of the D^* momentum along the jet axis, both track momentum and jet energy measurement uncertainties contribute, in principle, to the z uncertainty. The uncertainty on the jet energy

scale is roughly 10% (see Appendix C). The track momentum scale, meanwhile is known to much better accuracy as evidenced by the fact that the mean of the D^* peak comes out to 145.2±0.2 MeV/c^2 (see Chapter 6) to be compared with the world average value for the D^*-D^0 mass difference of 145.45±0.07 MeV/c^2. As for random errors, the jet energy resolution is determined to be (see Appendix D)

$$\delta E_t(\text{GeV}) = 1.86 \cdot \sqrt{E_t(\text{GeV})} - 6.73$$

for jets with E_t greater than 25 GeV. The p_ℓ resolution, meanwhile, is dominated by the p_t resolution for D^*s which is approximately

$$\frac{\delta p_t}{p_t} = \frac{1}{\sqrt{2}} \sqrt{\left(\frac{0.0012\ p_t}{2}\right)^2 + (0.0038)^2} \ .$$

Note that this is better than the single track resolution (Chapter 6) because the D^* momentum is approximately equally shared by the K and the π making up the D^0 (especially since we have required $|\cos\theta_H| <$ 0.8 which cuts out very asymmetric decays of the D^0). Taking $E_t = 50$ GeV and $z = 0.1$ (i.e. $p_t = 5$ GeV/c) as a typical case, we therefore have

$$\frac{\delta E_t}{E_t} = \frac{1.86\ \sqrt{50} - 6.73}{50} = 0.13$$

$$\frac{\delta p_t}{p_t} = \frac{1}{\sqrt{2}} \sqrt{\left(\frac{0.0012 \cdot 5}{2}\right)^2 + (0.0038)^2} = 0.003$$

so that we can safely neglect tracking effects.

7.2 Correcting the Observed D^* Signal

A simple Monte Carlo was used to estimate the correction factor to convert the observed number of D^* events to the true number

of D^* events which were produced with $z>0.1$. Jets were generated uniformly in pseudorapidity between $|\eta|$ of 0.1 and 0.8 according to an E_t distribution of the form $dN/dE_t \sim E_t^{-n}$ where n ranged from 5 to 6. D^*s were then generated according to a z distribution of the form $dN/dz \sim 1/z \cdot e^{-\beta z}$ where β was taken to be 8.4 as a worst case. The observed jet E_t was obtained from the generated E_t by: 1) performing the inverse of the jet energy scale correction, 2) applying a factor to account for the uncertainty in this correction, 3) smearing the resulting jet E_t according to a Gaussian resolution function characterized by the standard deviation δE_t, and 4) applying the jet energy scale correction back again. The observed value of z was then calculated according to

$$ z_{obs} = \frac{z_{true} \cdot E_{true}}{E_{obs}} $$

We then plotted z_{obs} and z_{true} for those jets which were observed to have $E_t>30$ GeV. The ratio of the number of events with $z_{true}>0.1$ to the number of events with $z_{obs}>0.1$ was taken to be the multiplicative correction factor. We will refer to this ratio as R. The main ingredients of the Monte Carlo are described in Appendix E.

7.3 Results of the Monte Carlo

We begin by considering the effect of the uncertainty in the jet energy scale separately from the effect of the jet energy resolution. This will help us later in the section to understand their combined effects. We first consider the case where the jet energy resolution is perfect but where the jet energy scale is uncertain (by approximately 10% - see Appendix C). The result is that the observed value of z is shifted from the true value by about 10%. If the observed energy is higher than the true energy, the observed value of z is lower than its corresponding true value. The shift is in the opposite direction if the observed energy is lower than the true

energy. Since we are integrating the observed z distribution above $z=0.1$, the effect of the shift in the z scale is to integrate more or less (depending on the direction of the shift) of the spectrum than we really should. The uncertainty in the integral can get as high as 17% depending on the steepness of the z distribution (Figure 56); for a slope parameter β equal to 8.4 this is, in fact, the dominant effect.

Next we consider the case where the energy scale is known perfectly but where the jet energy resolution is now finite. The observed z distribution is now a convolution of the true distribution with some kind of z resolution function. Although the jet energy resolution is approximately Gaussian, the z resolution function is asymmetric because we have required the jets to be above a cut in E_t. Jets which are produced with E_t below the cut but which are measured to be above the cut are included in our sample while jets produced above the cut and measured below are not. In the first instance, the measured value of z is lower than the true value whereas in the second instance the measured value is higher. The jet E_t cut skews the z resolution function by preferentially selecting events in which the measured value of z is lower than the true value. The asymmetry is non-zero because the jet E_t spectrum is falling very fast above the cut. Figure 57 is the result from our Monte Carlo, showing the essential effects of the jet E_t resolution: 1) a fewer number of events observed above $z=0.1$ than were produced (in this case, about 10%), and 2) an observed spectrum that is steeper (although only slightly) than the true spectrum. The true z distribution shown in the figure was generated with a slope parameter β equal to 8.4. The observed distribution is described by $\beta = 8.7$.

We have examined the dependence of R on the slope of the jet E_t spectrum, the D^* z distribution, and the resolution (Figure 58). In all instances, the effect is in the same direction (unlike the effect of the energy scale). The true number of events above $z=0.1$ is always underestimated. The size of the effect grows as the resolution becomes poorer, and the slopes of the jet E_t distribution and the D^* z
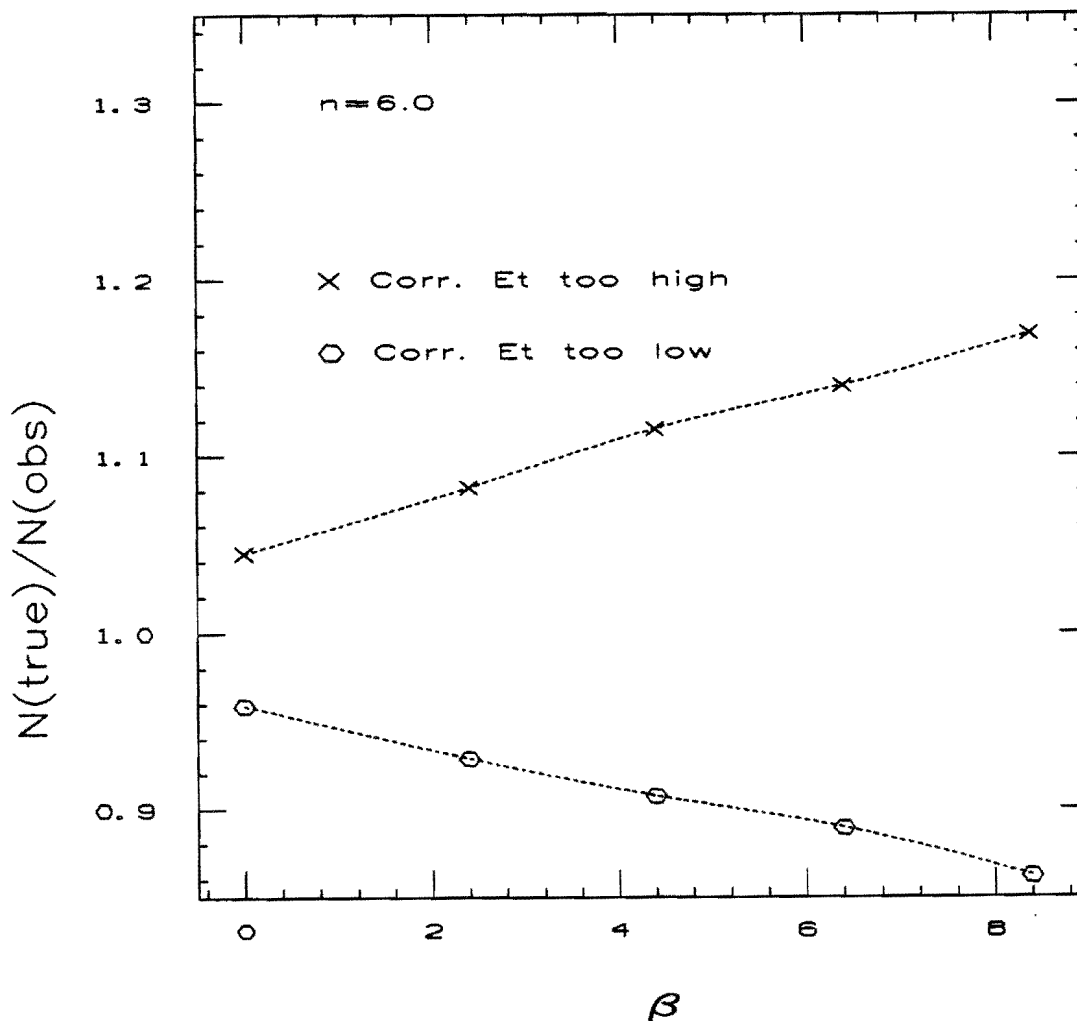
Figure 56. Results from the Monte Carlo showing the effect on R of an energy scale uncertainty. (R is the ratio of the true number of D^*s above z=0.1 to the observed number.) The jet E_t resolution is assumed here to be perfect. R is shown as a function of β, the slope parameter in the z distribution of D^*s. A higher value of β indicates a steeper slope. The crosses show the case where the energy scale correction was bigger than it should have been. The circles show the case where the correction was smaller.
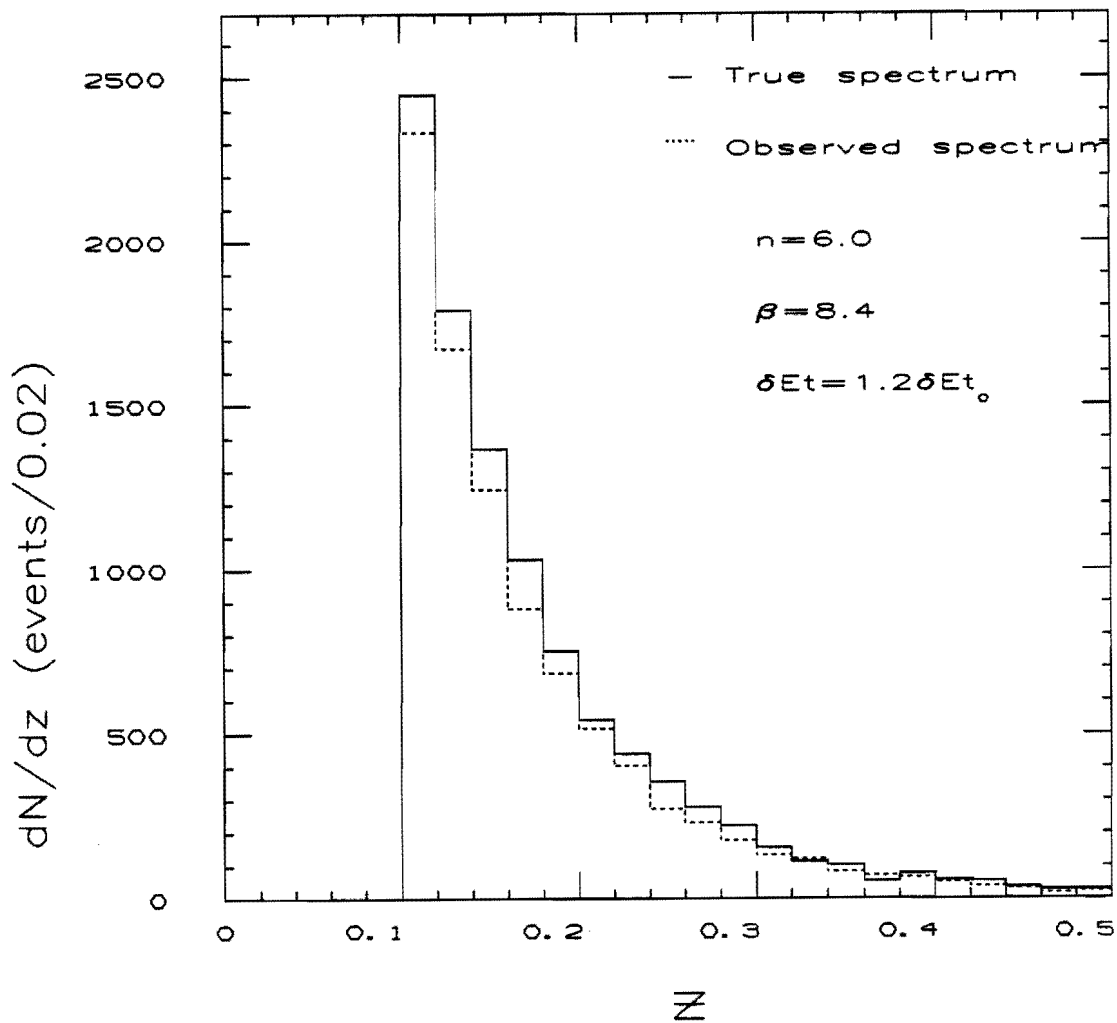
Figure 57. The z distribution for D*s from the Monte Carlo, showing the effect of the jet E_t resolution. The solid histogram shows the true z distribution, and the dotted histogram shows the z distribution after the jet energies have been smeared. The jet energy scale is assumed here to be known perfectly. The width of the resolution function has been taken to be 1.2 times the width measured from the jet data.

Figure 58. Results from the Monte Carlo showing the effect of the jet E_t resolution on R. The jet energy scale is assumed to be known perfectly.

(a) R as a function of the exponent n in the parametrization of the jet E_t distribution. The slope parameter β for the z distribution has been set to 8.4. Three different levels of the jet E_t resolution are considered. The diagonal crosses show the case where the width of the resolution function is taken to be 1.2 times the nominal width measured from the jet data. The vertical crosses show the case where the width is equal to the nominal width. The open circles show the case where the width is 0.8 times the nominal width.

(b) R as a function of the slope parameter β for the z distribution. The exponent for the jet E_t distribution has been set to 6. As in (a), three different levels of the jet E_t resolution are illustrated.
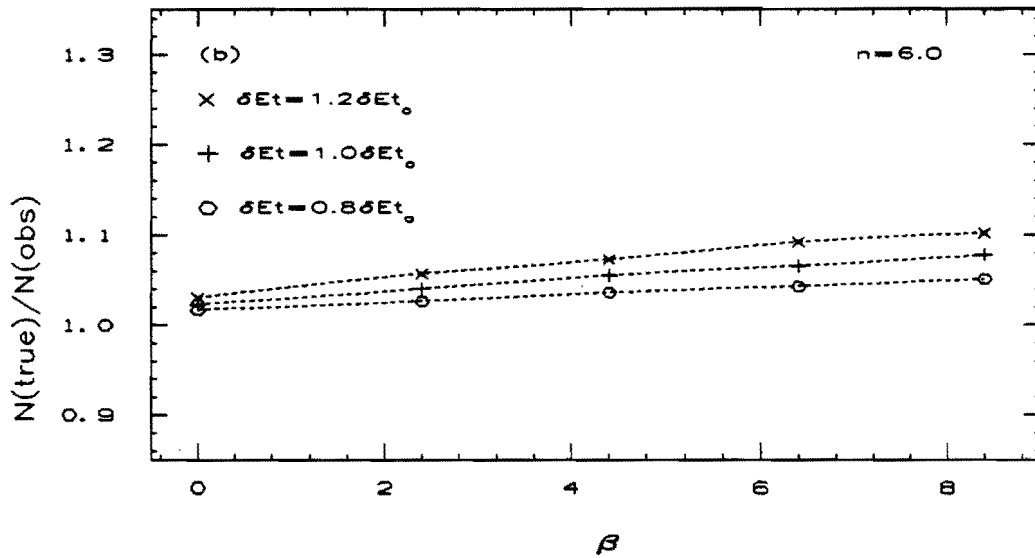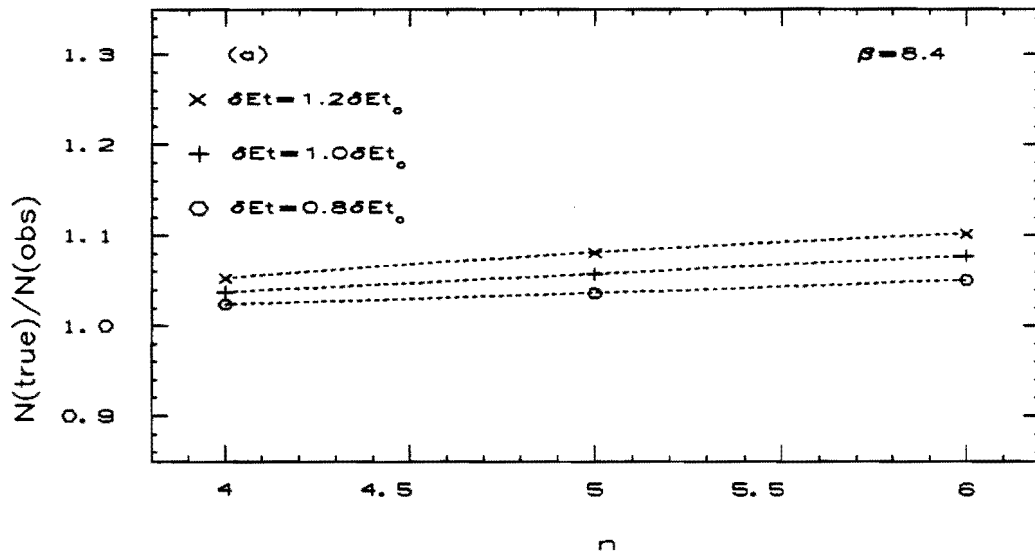
distribution grow steeper. The maximum size of the effect is about 10%; this is about 60% of the effect of the energy scale.

We are now ready to consider the combined effects of the uncertainty in the jet energy scale and of the jet energy resolution. When the energy scale uncertainty is such that the observed energy is higher than the true value, the energy scale and the resolution conspire to work in the same direction, causing the observed value of z to be less than the true value and thus causing the number of events observed above z=0.1 to be less than the true number. The largest correction in this direction is therefore obtained when the resolution is poorest and the distributions of the jet E_t and the z of the D^* are at their steepest. On the other hand, when the observed jet energy is lower than the true value, the migration of events from low z to high z due to the energy scale uncertainty is countered by a flow in the opposite direction due to the resolution. In this case, the largest correction is obtained when the resolution is better and the E_t spectrum less steep. This is illustrated in Figure 59. The multiplicative correction ranges from 0.90 (for β=8.4, n=5.0, and δE_t=0.8δE_{t0}, where δE_{t0} is the nominal width of the resolution function as cited in Section 7.1) to 1.31 (for β=8.4, n=6.0 and δE_{t0}=1.2δE_{t0}). We have therefore decided to use a correction of 1.1, assigning a systematic uncertainty of 0.2 to the correction. This uncertainty is dominated by the uncertainty in the jet energy scale, and by our need to assume a very steep z distribution for D^*s as a worst case.

Figure 59. Results from the Monte Carlo showing the combined effect of the uncertainty in the jet energy scale and the jet E_t resolution on R. (a) and (b) illustrate the case where the corrected jet energy scale is larger than the correct value. (c) and (d) illustrate the opposite case.

(a) R as a function of n. β has been set to 8.4. The crosses show the case where the width of the resolution function is taken to be 1.2 times the nominal width, and the circles show the case where the width is 0.8 times nominal.

(b) R as a function of β. n has been set to 6.0. The crosses and circles are as in (a).

(c,d) Analogous to (a) and (b) but for the case where the corrected jet energy scale is smaller than the correct value.
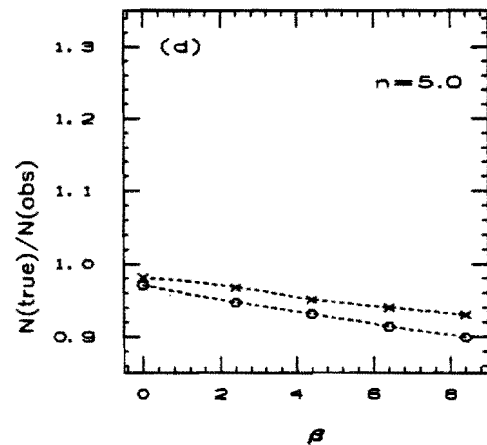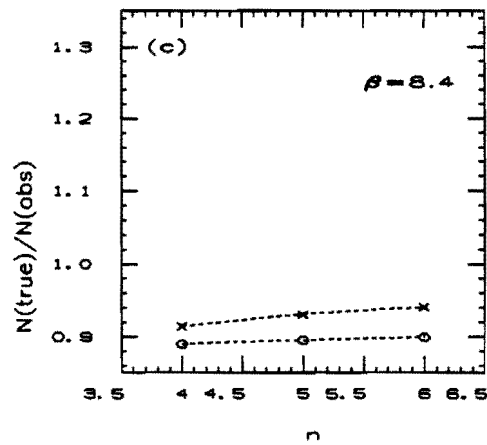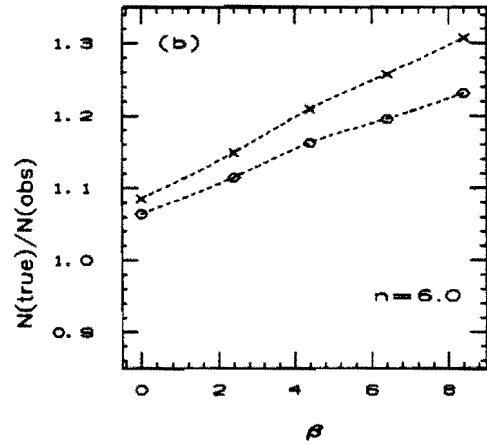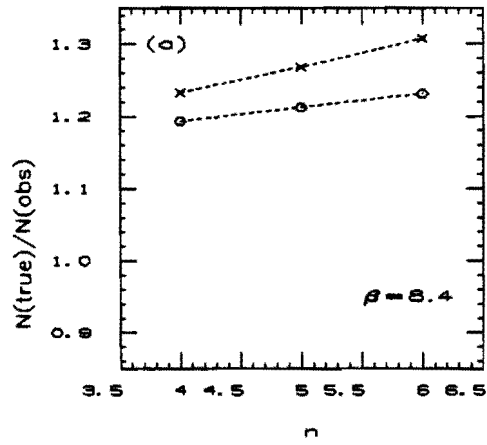
CHAPTER 8

DISCUSSION OF RESULTS

Now that we have established a D^* signal and understood the corrrections for the effects of D^* detection efficiency, tracking resolution and the uncertainty in the jet energy, we are in a position to extract some results on the physics of D^* production in jets. We will discuss the D^* multiplicity and the z distribution, comparing our measurements with previous work by UA1 and with predictions of QCD. We will then discuss the prospects for an improved measurement using the data from the 1988-1989 CDF run.

8.1 The Number of D^*s per Jet

The observation of $25 \, {}^{+ \, 7.5}_{- \, 6.9}$ (stat) $\pm$ 2 (sys) $D^* \rightarrow D^0 \pi \rightarrow K\pi\pi$ decays was converted to the number of charged D^*s per jet with $z(D^*) >$ 0.1 as follows:

$$\frac{N(D^*)}{N(jet)} = \frac{1}{N(jet)} \cdot \frac{N_{obs}(D^* \rightarrow K\pi\pi)}{\epsilon \cdot BR(D^* \rightarrow K\pi\pi)} \cdot R$$

where $N(jet)$ = the number of jets in our sample
$$= 32,340$$

$N_{obs}(D^* \rightarrow K\pi\pi)$ = the number of observed $D^* \rightarrow K\pi\pi$ decays
$$= 25.0 \, {}^{+ \, 7.5}_{- \, 6.9} \text{ (stat) } \pm 2 \text{ (sys)}$$

ϵ = the efficiency for reconstructing the decay sequence $D^{*+} \rightarrow$
$D^0 \pi^+ \rightarrow K^- \pi^+ \pi^+$ for D^*s with $z > 0.1$

= 0.37 ± 0.09 (sys)

$BR(D^* \rightarrow K\pi\pi)$ = the branching ratio for the decay sequence D^{*+}
$\rightarrow D^0 \pi^+ \rightarrow K^- \pi^+ \pi^+$

= 0.0239 ± 0.0028 ± 0.0028

and $\quad R = \dfrac{N_{gen}(z>0.1)}{N_{obs}(z>0.1)}$

= the correction factor from Chapter 7 for the effects of
the jet energy scale uncertainty and the jet energy
resolution

= 1.1 ± 0.2 (sys).

The branching ratios used were from measurements by the Mark III
Collaboration:

$$BR(D^{*+} \rightarrow D^0 \pi^+) = 0.57 \pm 0.04 \pm 0.04 \ [72]$$

$$BR(D^0 \rightarrow K^- \pi^+) = 0.042 \pm 0.004 \pm 0.004 \ [73]$$

We obtain the result

$$\frac{N(D^{**})}{N(jet)} = 0.096 \pm 0.031 \text{ (stat)} \pm 0.032 \text{ (sys)}$$

for jets with an average E_t of 47 GeV. This is consistent with
previous UA1 results:

$$\frac{N(D^{**})}{N(jet)} = 0.65 \pm 0.19 \pm 0.33$$

and $\quad \dfrac{N(D^{**})}{N(jet)} = 0.08 \pm 0.02 \pm 0.04$

for jets with an average E_t of 28 and 32 GeV respectively.[74]

We now try to compare these results to the predictions of QCD. In Chapter 1, the QCD prediction of Mueller and Nason for the number of charm quarks per gluon jet was given as

$$\frac{N(quark)}{N(jet)} = \frac{2}{3\pi} \int_{4M^2}^{Q^2} \frac{dK^2}{K^2} \, \alpha_s(K^2) \left[1 + \frac{2M^2}{K^2} \right]$$

$$\cdot \left[\frac{1}{4} - \frac{M^2}{K^2} \right]^{1/2} n_g(Q^2, K^2) \qquad [8.1]$$

where $n_g(Q^2, K^2)$ is the so-called "gluon multiplicity" factor. To compare this with our results we must take into account the fact that we observed D^* mesons with a fractional momentum z greater than 0.1, whereas equation 8.1 applies to charm quarks without any z cutoff. Unfortunately, the introduction of a z cutoff introduces difficulties in the calculation of higher-order contributions which, in the inclusive case, are summed up neatly into the "gluon multiplicity"; there is some worry that the z cutoff prevents all the higher-order terms from summing nicely.[75] The lowest-order contribution, however, can be readily calculated.[76] Retaining terms up to order M^2/Q^2, the QCD prediction for the number of charm quarks per gluon jet with $z > z_0$ reads:

$$\frac{N(c)}{N(jet)} = \frac{1}{2\pi} \int_{(1-\beta)/2}^{(1+\beta)/2} dz \, \theta(z-z_0) \int_{4M^2}^{Q^2} \frac{dK^2}{K^2} \, \alpha_s(K^2) \, \cdot$$

$$\left[[z^2 + (1-z)^2] + \frac{2M^2}{K^2} \right] \theta(K^2(1-z)z - M^2)$$

$$\equiv \int_{(1-\beta)/2}^{(1+\beta)/2} dz \, \theta(z-z_0) \, \rho_c(z) \qquad [8.2]$$

where

$$\beta = \sqrt{1 - \frac{4M_c^2}{Q^2}}$$

θ is the Heaviside step function

and Q^2 is to be taken as the square of the jet E_t.

Equation 8.2 defines $\rho_c(z)$ which is the number density of charm quarks in an interval of z per gluon jet. (We will refer to $\rho_c(z)$ later.) It can be verified that the lowest-order inclusive result is restored by setting z_0 to 0.

To get the correct z dependence for D^* mesons we must now fold in the fragmentation function for D^*s from charm quarks, i.e. the probability that a D^* takes up a fraction z of the charm quark momentum. It is common to parametrize the fragmentation function for heavy quarks according to the "Peterson form"[77]

$$f(z) = \frac{A}{z \left[1 - \frac{1}{z} - \frac{\epsilon}{1-z} \right]^2} \qquad 0 < z < 1$$

where the parameter ϵ is a function of the quark mass. Several experiments at e^+e^- colliders have measured the fragmentation of charm quarks into D^*s; the fitted values for ϵ from some of these measurements are listed below:[78]

Experiment	$\sqrt{s}$ (GeV)	ϵ
CLEO	10.5	0.10 ± 0.02
HRS	29.0	0.36 ± 0.12
DELCO	29.0	$0.36 \, {}^{+\,0.14}_{-\,0.10}$
TASSO	34.4	0.18 ± 0.07

Figure 60 shows the Peterson function for two values of ϵ, 0.15 and 0.3. We will see shortly that the choice of ϵ has a negligible effect, compared to the magnitude of other uncertainties, on the comparison of the data to QCD.

The normalization constant, A, is determined by the probability that a charm quark materializes as a D^{**} meson. Naively, one expects charm quarks to greatly favor turning into D or D^* mesons rather than charmed baryons or charmed-strange mesons due to the relative ease with which u and d quarks can be pulled out of the vacuum compared to diquarks or s quarks. We will therefore neglect the production of anything but D's and D^*s. Furthermore, based on the number of available spin states, one expects D^* (spin-1) production to be favored over D (spin-0) production by a factor of 3 to 1. Assuming an equal probability for charged and neutral mesons via isospin invariance, one therefore arrives at the following probabilities:

$$P(c \rightarrow D^{*+} \text{ or } D^{*-}) = 37.5\%$$
$$P(c \rightarrow D^{*0} \text{ or } \bar{D}^{*0}) = 37.5\%$$
$$P(c \rightarrow D^{+} \text{ or } D^{-}) = 12.5\%$$
$$P(c \rightarrow D^{0} \text{ or } \bar{D}^{0}) = 12.5\%$$

Experimental values are consistent with this picture.[79]

Choosing A such that $\int_0^1 f(z)dz = 0.375$, the number of charged D^* mesons per jet was calculated according to
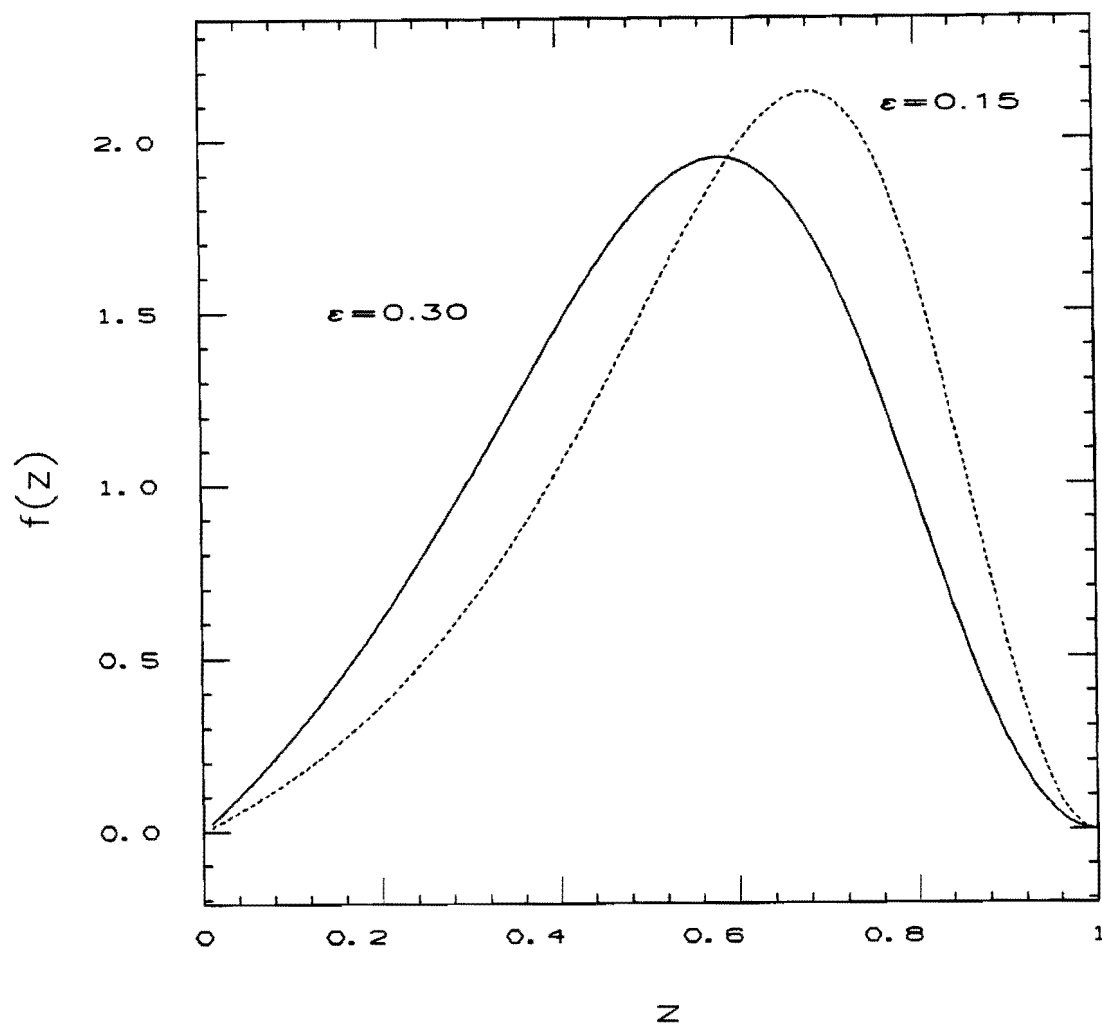
Figure 60. The Peterson function, commonly used to describe heavy quark fragmentation, shown for two values of the parameter ϵ. The solid line is for $\epsilon=0.3$ and the dotted line for $\epsilon=0.15$. These two values are inspired by fits from e^+e^- experiments measuring the fragmentation of charm quarks into D^*s.

$$\frac{N(D^*)}{N(jet)} \;=\; \int_{0.1}^{1} \rho_{D*}(z_{D*}) \; dz_{D*}$$

$$=\; \int_{0.1}^{1} \int_{(1-\beta)/2}^{(1+\beta)/2} dz_c \; \rho_c(z_c) \; f\!\left[\frac{z_{D*}}{z_c}\right] d\!\left(\frac{z_{D*}}{z_c}\right)$$

$$=\; \int_{0.1}^{1} dz_{D*} \int_{(1-\beta)/2}^{(1+\beta)/2} \frac{dz_c}{z_c} \; \rho_c(z_c) \; f\!\left[\frac{z_{D*}}{z_c}\right]$$

where, $\rho_c(z)$ is the number density of charm quarks in an interval of z per gluon jet (equation 8.2). The distribution $\rho_{D*}(z)$ is the analog of $\rho_c(z)$ for D^* mesons. The QCD coupling constant was evaluated according to

$$\alpha_s(Q^2) \;=\; \frac{12\pi}{(33 - 2N_f)\,\ln(Q^2/\Lambda^2)}$$

The number of flavors, N_f, was set according to the Q^2 scale

$$N_f = 4 \qquad M_c^2 < Q^2 < M_b^2$$
$$N_f = 5 \qquad Q^2 > M_b^2$$

where M_c, the charm quark mass, was allowed to vary from 1.2 GeV/c^2 to 1.8 GeV/c^2, and M_b, the bottom quark mass, was taken to be 5 GeV/c^2. Since α_s has to be continuous as the flavor threshold is crossed, Λ was adjusted according to the number of flavors via

$$\Lambda^{(5)} \;=\; \Lambda^{(4)} \left[\frac{\Lambda^{(4)}}{M_b}\right]^{2/23}.$$

$\Lambda^{(4)}$ was taken to be $200\,{}^{+150}_{-80}$ MeV.[10]

The resulting lowest-order prediction for the number of charged D^*s with z > 0.1 per gluon jet is shown in Figure 61 (solid

Figure 61. A comparison of the data and the predictions of QCD for the number of charged D^*s with $z > 0.1$ per gluon jet as a function of the momentum-transfer scale, Q^2. The data points are from this experiment and a previous measurement by the UA1 Collaboration (Reference 26). Q^2 has been taken to be the square of the mean jet E_t in the respective data samples. The error bars reflect the sum in quadrature of the statistical and systematic uncertainties. The solid lines show the lowest-order QCD prediction, using two extreme values for the charm quark mass and the QCD parameter Λ. The dotted lines show the corresponding predictions when no lower cutoff is applied to z. The dashed curve is the QCD prediction including higher-order terms but without a lower cutoff on z. The parameters for this last curve were $M_c = 1.2$ GeV/c^2 and $\Lambda = 350$ MeV, chosen to give the largest value for the number of D^*s per jet.
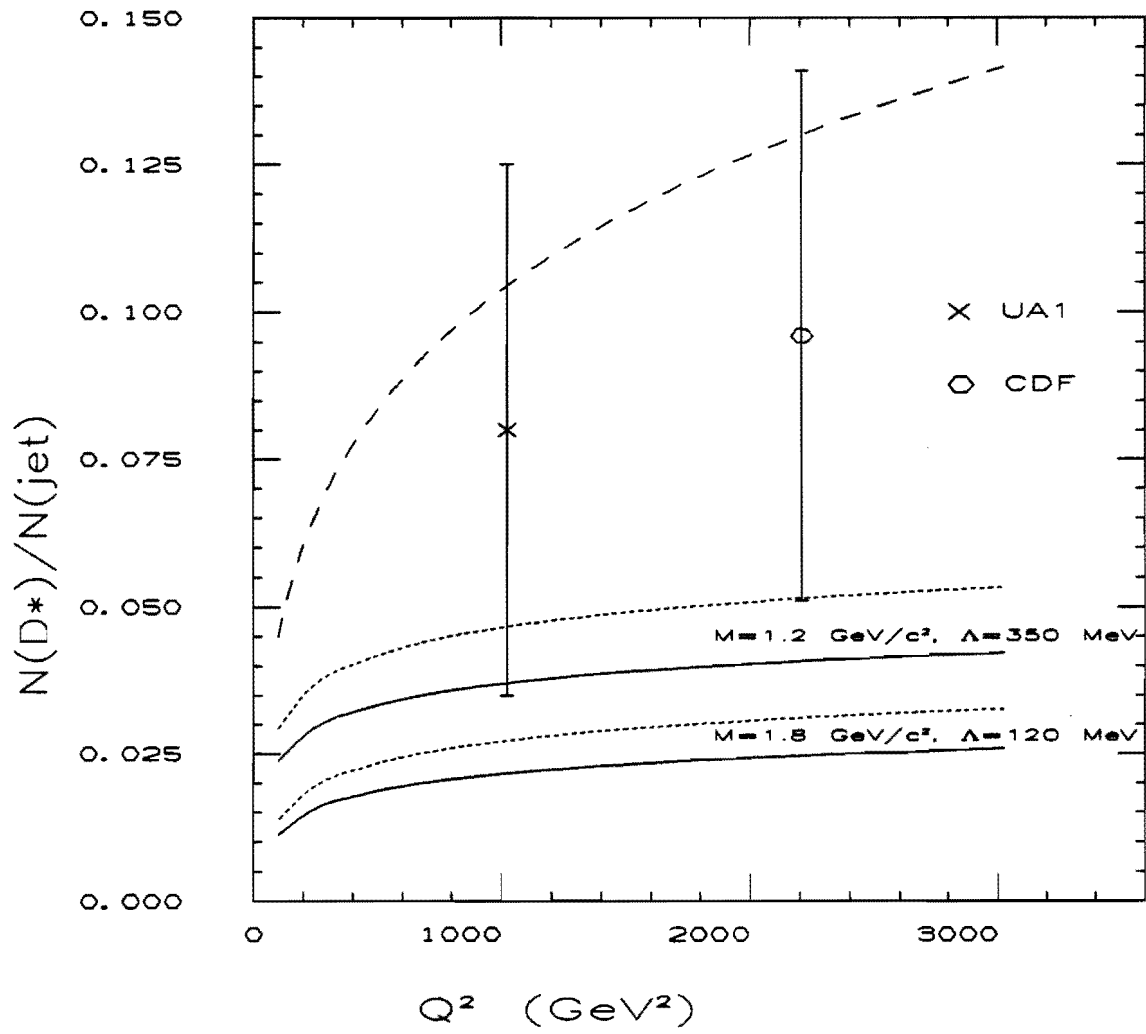
curve) for two extreme choices of both the charm quark mass and $\Lambda^{(4)}$. For reference, the dotted lines show the lowest-order result for D^*s with no z cutoff. We see that by requiring z to be greater than 0.1, we reduce the predicted number of D^*s by 20%. Also shown are data points from this experiment and from $UA1$[26] where Q^2 has been taken to be the square of the mean jet E_t in the respective data samples.

The experimental points are about 1σ above the lowest-order prediction. However, higher-order corrections should move the theoretical curves up. As an upper limit to the theoretical prediction for the number of D^*s with $z > 0.1$ per gluon jet, we show in Figure 61 (dashed curve) the prediction of Mueller and Nason for inclusive charm production (see Equation 8.1) rescaled by 0.375 to account for the probability that a charm quark materializes as a charged D^* meson. The charm quark mass and Λ have been chosen to give the largest value for the number of D^*s per jet. This curve includes the higher-order contributions but no z cutoff; for this reason, we have called it an upper limit to the theoretical prediction. We have seen above that in the lowest-order case, the z cutoff reduces the result by about 20%. When higher-order terms are included, we might expect the reduction to be somewhat larger since the gluon that finally splits into the $c\bar{c}$ pair would be carrying a smaller fraction of the jet energy than in the lowest-order case. We conclude that QCD predictions are entirely consistent with the data.

We should mention that in this comparison we have ignored the fact that some fraction of the jets in our data sample are from light quarks rather than gluons. This serves to decrease somewhat the theoretical prediction for the D^* multiplicity. To understand the size of this effect, the $ISAJET$[80] Monte Carlo was used to estimate the fraction of jets which are produced with rapidity $|y| < 0.8$ and which are initiated by gluons in the final state at $\sqrt{s} = 1.8$ TeV. The result is shown in Figure 62 as a function of jet E_t for a typical choice of structure functions.[81] For the jet energies relevant to this measurement, the fraction is around 80%. The multiplicity of charm quarks in light-quark initiated jets is expected to be 4/9 that in
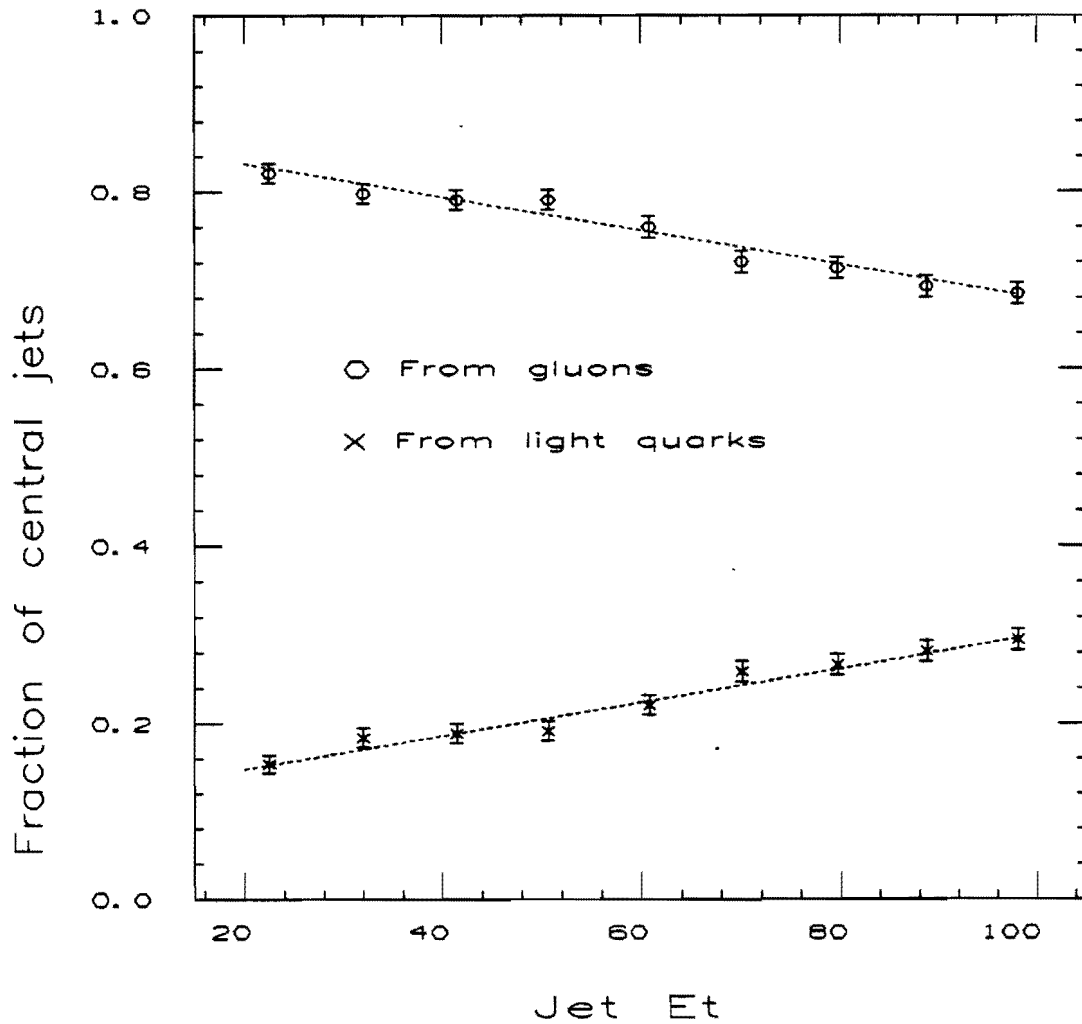
Figure 62. The fraction of jets which are produced with rapidity $|y| < 0.8$ at $\sqrt{s} = 1.8$ TeV and which are initiated by gluons in the final state. The values shown were estimated with version 5.2 of the ISAJET Monte Carlo. The dotted lines are linear fits to the points. For the fraction of gluon jets, we find $f(E_t) = 0.87 - 0.0019 \cdot E_t$, where E_t is in units of GeV. For light quarks, we obtain $f(E_t) = 0.11 + 0.0019 \cdot E_t$.

gluon initiated jets (at least in the inclusive case).[15] Taking the inclusive process as a guide, therefore, the predicted number of D^*s in our jet sample would be something like 80% + 4/9*(20%) or 89% of the result for gluon jets alone. We have not included this factor in Figure 61.

8.2 $\underline{Z}$ Distribution

The lowest-order QCD calculation for the z distribution is shown in Figure 63. The z distribution for charm quarks is symmetric about $z=1/2$ as expected from the symmetry of the Altarelli-Parisi function for gluon splitting into quarks:

$$P_{q \leftarrow g}(z) = \frac{1}{2}\left[z^2 + (1-z)^2\right]$$

A significant softening of the spectrum is introduced by the convolution with the charm fragmentation function; 20% of the area underneath the D^* spectrum is concentrated below $z=0.1$. It is also clear from this figure that the choice of ϵ in the Peterson function is irrelevant at our level of sensitivity.

The observed z distribution, corrected for the detection efficiency of the D^*, is compared to a previous measurement by UA1[22] and to the lowest-order QCD calculation in Figure 64. The efficiency corrections are summarized in Table 5. No further corrections have been made to the data for distortions to the shape of the spectrum due to tracking and jet energy resolution. As we saw in Chapter 7, these distortions are negligible compared to the statistical uncertainty in the z distribution. The theoretical curve and the UA1 data points have been normalized to the same area as our data. The two measurements are consistent in shape, while the theoretical curve seems to be less steeply falling than the data. Corrections to the data for distortions due to the jet E_t resolution would make the data less steep but not enough to account for the difference. The choices for the charm quark
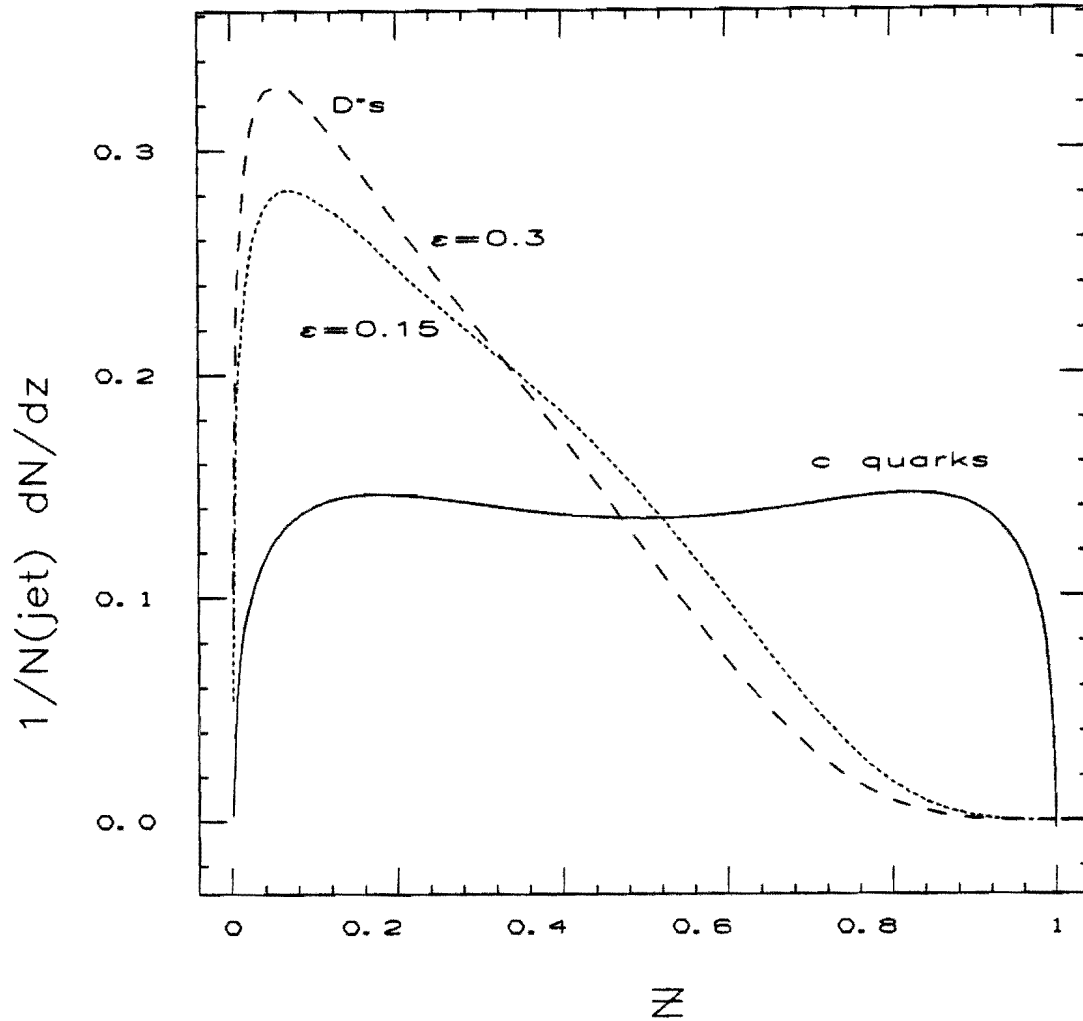
Figure 63. The lowest-order QCD calculation for the z distribution of charm quarks produced in gluon jets (solid curve). Also shown is the expected z distribution for D^*s assuming a charm fragmentation function given by the Peterson form. Two curves are shown for the D^* distribution, corresponding to two values for the parameter ϵ. The dotted curve is for $\epsilon = 0.15$ and the dashed curve is for $\epsilon = 0.30$. The D^* distributions have been normalized to the same area as the charm quark distribution (i.e. the probability that a charm quark materializes as a D^* has been set to 1).
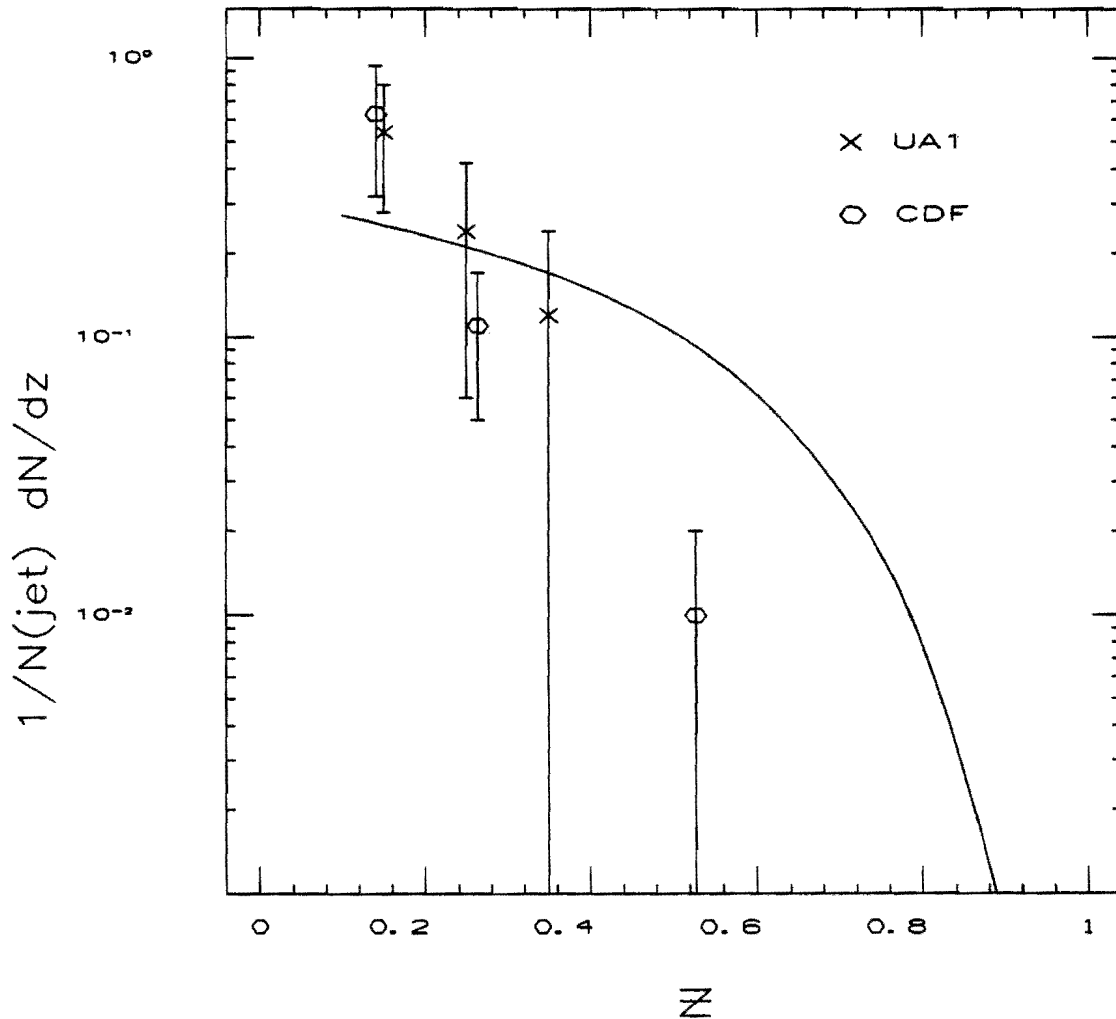
Figure 64. The observed z distribution for D^*s, corrected for detection efficiency. The open circles show CDF data; the crosses show data from Reference 22. The solid curve is the lowest-order QCD calculation for D^*s as in Figure 63, using $\epsilon=0.3$ for the charm quark fragmentation. Both the curve and the UA1 data have been normalized to our data.

Table 5. The observed z distribution for D^*s in jets from CDF and UA1 data, corrected for detection efficiency. The UA1 data are from R. Frey, Ph.D. Thesis, UC Riverside (1984), but have been normalized to the same number of events (after efficiency corrections) as the CDF data.

CDF

z bin	0.1-0.2	0.2-0.4	0.4-1.0
$\langle z \rangle$	0.14	0.26	0.53
$N_{obs}(D^*)$	15 ± 6	8 ± 4	2 ± 2
Efficiency	0.31±0.07	0.47±0.06	0.43±0.05
Efficiency corrected $N(D^*)$	48.4±22.2	17.0±8.8	4.7±4.7
$N(D^*)/N(jet)$ (B.R. corrected)	0.063±0.031	0.022±0.012	0.006±0.006
$1/N(jet) \cdot dN(D^*)/dz$	0.63±0.31	0.11±0.06	0.01±0.01

UA1

z bin	0.1-0.2	0.2-0.3	0.3-0.4
$\langle z \rangle$	0.15	0.25	0.30
$N(D^*)$ (Efficiency corrected)	4.5±2.0	2.0±1.4	1.0±1.0
$N(D^*)$ normalized to CDF data	42.0±18.7	18.7±13.2	9.3±9.3
$N(D^*)/N(jet)$ (B.R. corrected)	0.054±0.026	0.024±0.018	0.012±0.012
$1/N(jet) \cdot dN(D^*)/dz$	0.54±0.26	0.24±0.18	0.12±0.12

mass and the QCD parameter Λ cannot account for the difference either as we have found that the theoretical distribution is insensitive to these parameters. Again, however, we must keep in mind that the charm quark is still relatively light so that the contribution of higher-order terms is most likely quite significant. These higher-order diagrams would tend to soften the theoretical z distribution due to the larger number of parton branchings before the charm quark is produced. A possible test would be to compare the data to the prediction of the HERWIG Monte Carlo[82] which sums these higher-order contributions. It might be interesting to try this when more data is available; we have not pursued this here.

8.3 Possibilities with the 1988-1989 Run

The CDF Collaboration recently obtained a total integrated luminosity of approximately 4.65 pb^{-1} in the 1988-1989 run which ended in June of this year. This is a factor of 220 improvement in the overall exposure compared to the data on which this thesis is based. Unfortunately, the number of jet events written to tape did not increase in the same proportion because the low E_t jet triggers were prescaled by factors of 30 and 300 for jets in the range $20 < E_t < 40$ GeV and $40 < E_t < 60$ GeV, respectively. (By "prescaled", we mean that only one event was accepted for every 30 or 300 events passing the trigger). Nevertheless, after applying the same event vertex cuts as in this analysis, it is estimated that there are on the order of 135,000 central jets above 30 GeV in the new data, a factor of 4 improvement over the sample used here.

Projecting our results obtained with the old data, we would expect to see a signal of 100 events on a background of similar size, thereby reducing the statistical uncertainty on the number of D^*s by a factor of 2. More work will therefore be needed on systematic effects. We should keep in mind, however, that a large portion of the systematic uncertainty in this measurement arose from our inability to measure certain distributions for D^*s due to the poor statistics. With

a larger sample of D^*s we should be able to improve our knowledge of the z distribution, for example; it is likely that we will find the z distribution less steep that we have had to assume, thus decreasing our sensitivity to the uncertainty in the jet energy scale. The larger data sample should also allow us to get a better measurement of the mass resolution directly from the data, thereby reducing the uncertainty associated with the efficiency of our mass cuts. The charged track multiplicity in D^* events would also be better determined, reducing the uncertainty associated with the dependence of the efficiency on the track multiplicity. (Even with the old data, we have probably been too pessimistic in our estimate of this uncertainty, as we remarked in Chapter 5.) We believe, therefore, that our handles on the systematic effects should be able to keep pace with the increase in statistics.

Someday in the future, CDF will probably dedicate some running time to record a very large sample of central jets ($\sim 10^6$ jets) with an E_t threshold of about 20 GeV in order to try to reconstruct the W/Z bosons from their jet decay modes. This has been done by the UA2 Collaboration[83] which succeeded in observing an excess of jet pairs with masses in the vicinity of the W and Z masses with a statistical significance of about 3σ above QCD background.[84] Such a jet sample would be nice for a measurement of D^* production as well. One complication is that during data-taking, the tracking data would have to be read out in addition to the calorimeter data. Depending on the luminosity, this could substantially increase the dead-time since the cross section is quite large for these low energy jets. On the other hand, we expect that the tracking data will also be useful for the W/Z analysis to improve the jet mass resolution by correcting for the non-linear response of the calorimeter.

8.4 Conclusion

We have described a measurement of the production rate of charged D^* mesons in jets from $\bar{p}p$ collisions at $\sqrt{s} = 1.8$ TeV, using

the CDF detector. In a sample of 32,340 jets obtained from an integrated luminosity of 21.1 nb^{-1}, we observed 25.0 $\pm$ 7.5(stat) $\pm$ 2(sys) $D^{*+} \to D^0\pi^+ \to K^-\pi^+\pi^+$ events above background. To obtain the number of D^*s per jet, the observed number of events was corrected for the effects of detection efficiency, tracking resolution, and uncertainties in the jet energy. Our result is

$$\frac{N(D^{*+} + D^{*-})}{N(\text{jet})} = 0.096 \pm 0.031 \text{ (stat)} \pm 0.032 \text{ (sys)}$$

for D^*s produced with fractional momentum $z > 0.1$. This is consistent with previous measurements by the UA1 Collaboration. Estimates from perturbative QCD are also consistent with this result. The z distribution is soft with approximately 70% of the observed D^*s produced with z between 0.1 and 0.2.

APPENDIX A

THE 1987 CDF COLLABORATION

F.Abe,[16] D.Amidei,[3] G.Apollinari,[11] G.Ascoli,[7] M.Atac,[4] P.Auchincloss,[14] A.R.Baden,[6] A.Barbaro-Galtieri,[9] V.E.Barnes,[12] F.Bedeschi,[11] S.Behrends,[12] S.Belforte,[11] G.Bellettini,[11] J.Bellinger,[17] J.Bensinger,[2] A.Beretvas,[14] P.Berge,[4] S.Bertolucci,[5] S.Bhadra,[7] M.Binkley,[4] R.Blair,[1] C.Blocker,[2] J.Bofill,[4] A.W.Booth,[4] G.Brandenburg,[6] D.Brown,[6] A.Byon,[12] K.L.Byrum,[17] M.Campbell,[3] R.Carey,[6] W.Carithers,[9] D.Carlsmith,[17] J.T.Carroll,[4] R.Cashmore,[4] F.Cervelli,[11] K.Chadwick,[4,12] T.Chapin,[13] G.Chiarelli,[11] W.Chinowsky,[9] S.Cihangir,[15] D.Cline,[17] D.Connor,[10] M.Contreras,[2] J.Cooper,[4] M.Cordelli,[5] M.Curatolo,[5] C.Day,[4] R.DelFabbro,[11] M.Dell'Orso,[11] L.DeMortier,[2] T.Devlin,[14] D.DiBitonto,[15] R.Diebold,[1] F.Dittus,[4] A.DiVirgilio,[11] J.E.Elias,[4] R.Ely,[9] S.Errede,[7] B.Esposito,[5] B.Flaugher,[14] E.Focardi,[11] G.W.Foster,[4] M.Franklin,[6,7] J.Freeman,[4] H.Frisch,[3] Y.Fukui,[8] A.F.Garfinkel,[12] P.Giannetti,[11] N.Giokaris,[13] P.Giromini,[5] L.Gladney,[10] M.Gold,[9] K.Goulianos,[13] C.Grosso-Pilcher,[3] C.Haber,[9] S.R.Hahn,[10] R.Handler,[17] R.M.Harris,[9] J.Hauser,[3] T.Hessing,[15] R.Hollebeek,[10] P.Hu,[14] B.Hubbard,[9] P.Hurst,[7] J.Huth,[4] H.Jensen,[4] R.P.Johnson,[4] U.Joshi,[14] R.W.Kadel,[4] T.Kamon,[15] S.Kanda,[16] D.A.Kardelis,[7] I.Karliner,[7] E.Kearns,[6] R.Kephart,[4] P.Kesten,[2] H.Keutelian,[7] S.Kim,[16] L.Kirsch,[2] K.Kondo,[16] U.Kruse,[7] S.E.Kuhlmann,[12] A.T.Laasanen,[12] W.Li,[1] T.Liss,[3] N.Lockyer,[10] F.Marchetto,[15] R.Markeloff,[17] L.A.Markosky,[17] P.McIntyre,[15] A.Menzione,[11] T.Meyer,[15] S.Mikamo,[8] M.Miller,[10] T.Mimashi,[16] S.Miscetti,[5] M.Mishina,[8] S.Miyashita,[16] N.Mondal,[17] S.Mori,[16] Y.Morita,[16] A.Mukherjee,[4] C.Newman-Holmes,[4] L.Nodulman,[1] R.Paoletti,[11] A.Para,[4] J.Patrick,[4] T.J.Phillips,[6] H.Piekarz,[2] R.Plunkett,[13] L.Pondrom,[17] J.Proudfoot,[1] G.Punzi,[11] D.Quarrie,[4] K.Ragan,[10] G.Redlinger,[3] J.Rhoades,[17] F.Rimondi,[4] L.Ristori,[11] T.Rohaly,[10] A.Roodman,[3] A.Sansoni,[5] R.Sard,[7] V.Scarpine,[7] P.Schlabach,[7] E.E.Schmidt,[4] P.Schoessow,[1] M.H.Schub,[12] R.Schwitters,[6] A.Scribano,[11] S.Segler,[4] M.Sekiguchi,[16] P.Sestini,[11] M.Shapiro,[6] M.Sheaff,[17] M.Shibata,[16] M.Shochet,[3] J.Siegrist,[9] P.Sinervo,[10] J.Skarha,[17] D.A.Smith,[7] F.D.Snider,[3] R.St.Denis,[6] A.Stefanini,[11] Y.Takaiwa,[16] K.Takikawa,[16] S.Tarem,[2] D.Theriot,[4] A.Tollestrup,[4] G.Tonelli,[11] Y.Tsay,[3] F.Ukegawa,[16] D.Underwood,[1] R.Vidal,[4] R.G.Wagner,[1] R.L.Wagner,[4] J.Walsh,[10] T.Watts,[14] R.Webb,[15] T.Westhusing,[7] S.White,[13] A.Wicklund,[1] H.H.Williams,[10] T.Yamanouchi,[4] A.Yamashita,[16] K.Yasuoka,[16] G.P.Yeh,[4] J.Yoh,[4] and F.Zetti[11]

[1] Argonne National Laboratory, Argonne, Illinois 60439
[2] Brandeis University, Waltham, Massachusetts 02254
[3] University of Chicago, Chicago, Illinois 60637
[4] Fermi National Accelerator Laboratory, Batavia, Illinois 60510
[5] Laboratori Nazionali di Frascati of the Istituto Nazionale di Fisica Nucleare, Italy
[6] Harvard University, Cambridge, Massachusetts 02138
[7] University of Illinois, Urbana, Illinois 61801
[8] National Laboratory for High Energy Physics (KEK), Tsukuba, Ibaraki 305, Japan
[9] Lawrence Berkeley Laboratory, Berkeley, California 94720
[10] University of Pennsylvania, Philadelphia, Pennsylvania 19104
[11] Istituto Nazionale di Fisica Nucleare, University and Scuola Normale Superiore, Pisa, Italy
[12] Purdue University, West Lafayette, Indiana 47907
[13] Rockefeller University, New York, New York 10021
[14] Rutgers University, Piscataway, New Jersey 08854
[15] Texas A&M University, College Station, Texas 77843
[16] University of Tsukuba, Tsukuba, Ibaraki 305, Japan
[17] University of Wisconsin, Madison, Wisconsin 53706

APPENDIX B

SOURCES OF TRACKING INEFFICIENCY

To understand some of the sources of the tracking inefficiency for D^*s, we have looked at the single-track efficiency as a function of p_t, η, and the level of activity (ρ, to be defined) in the chamber in the vicinity of the track. Because of the dead cells we have also looked at the ϕ dependence of the efficiency. We expect that the single-track efficiency can be factorized, i.e. $\epsilon(p_t, \eta, \rho, \phi) \sim \epsilon(p_t) \cdot \epsilon(\eta) \cdot \epsilon(\rho) \cdot \epsilon(\phi)$.

B.1 Data Sample

The data sample for our study of the single-track efficiency is slightly different from the data sample of Chapter 5. First of all, we have not simulated the effects of decays, hadronic interactions, or delta-ray production so as not to confuse the efficiency of the tracking code with inefficiencies introduced by these effects. In particular, decays are significant for low-p_t K^*s.

Secondly, some of the quantities in the Monte Carlo had not been tuned to reproduce the distributions in the data. Figure 65 compares the distributions of the time-over-threshold. The disagreement at low times, i.e. below 40 counts, affects the efficiency only for tracks which are "close" to one another. (At 2ns/count and a nominal drift velocity of 51μ/ns, this amounts to an r-ϕ separation of 4mm.) Since the phase space for this is rather small (as we will see later) we expect that the salient features of the single-track efficiency can still be observed. Figure 66 compares the number of hits per track. The axial hit distribution has an excess of
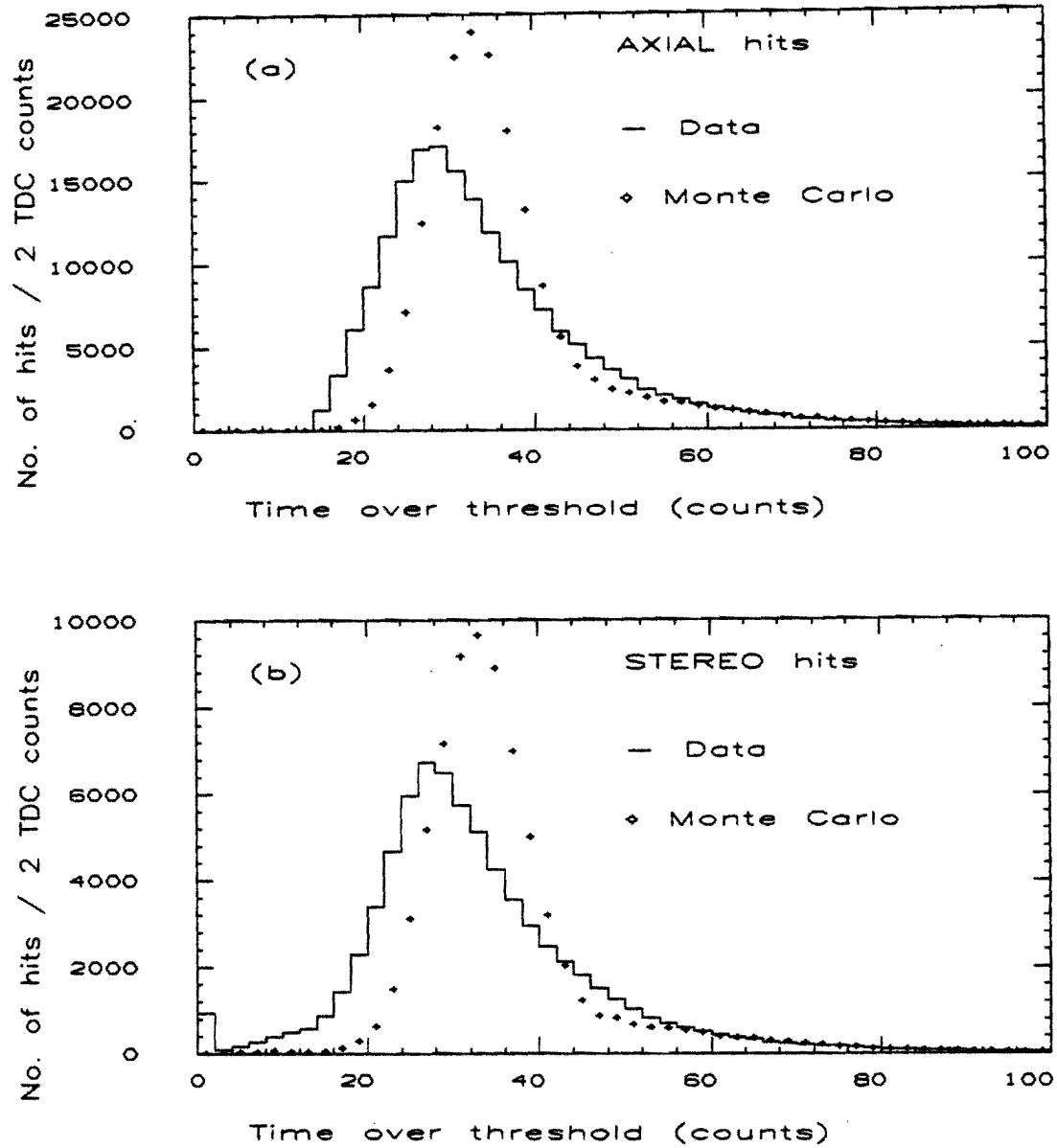
Figure 65. The distribution of the time-over-threshold of hits from Monte Carlo tracks (before tuning) compared to the data. The tracks were required to pass all the track selection criteria.
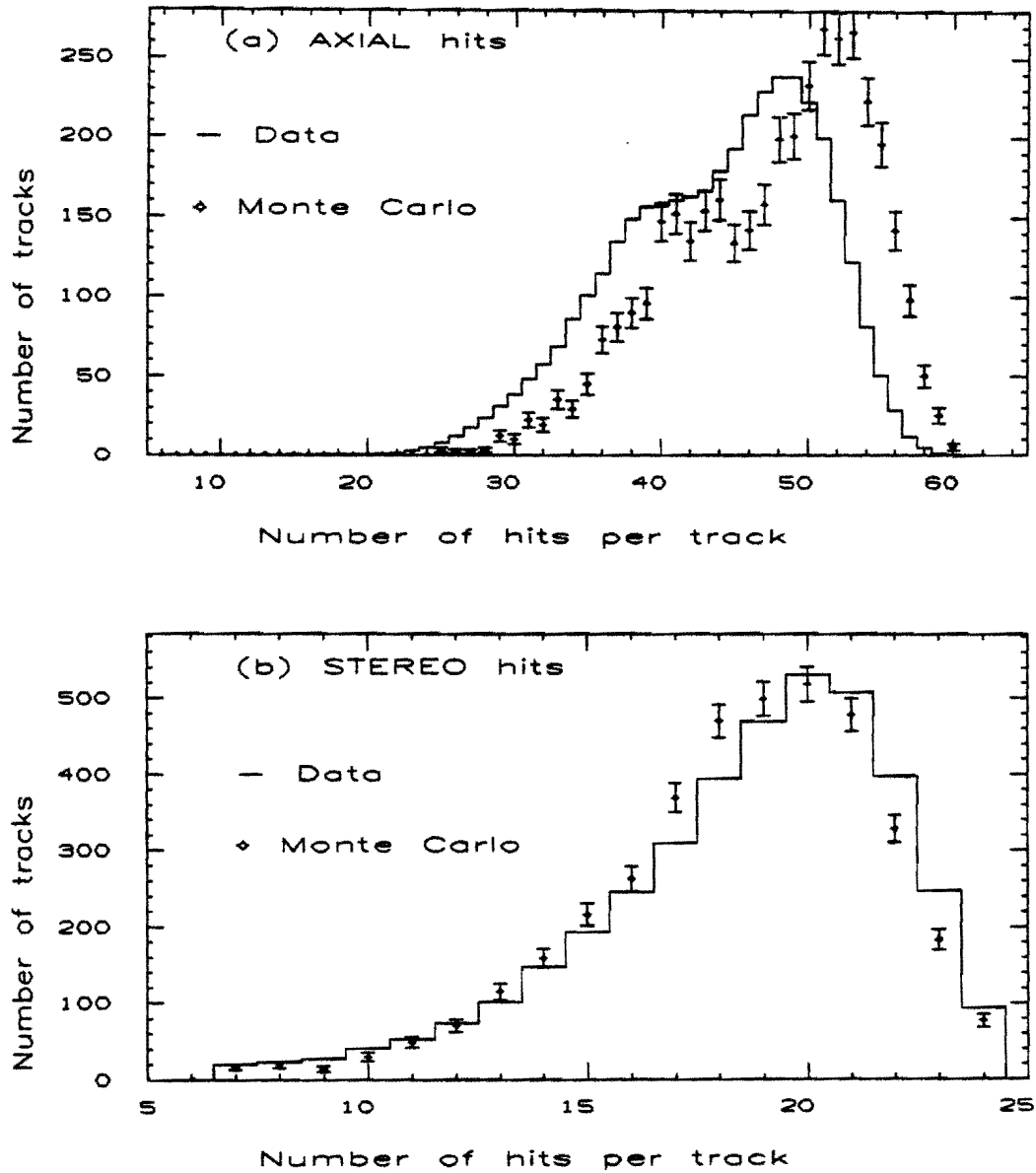
Figure 66. The number of hits per track, comparing Monte Carlo tracks (before tuning) to those from the data. The tracks were required to pass all the track selection criteria.

about three hits per track for Monte Carlo tracks. The excess hits come from the innermost superlayer (Figure 67), where the wire efficiency was not tuned for the lower gain at which this superlayer was operated. Again, we do not expect the main features of the efficiency to be affected.

D^* tracks were embedded in jets according to the same procedure as described in Chapter 5. 6000 events were reconstructed. Reconstructed tracks which best matched the embedded Monte Carlo tracks were subjected to the same track quality cuts as in Chapter 5. The single-track efficiency was defined as the ratio of the number of tracks surviving all the cuts to the number of input Monte Carlo tracks.

B.2 Results

The efficiency as a function of p_t for $|\eta| < 1$ is shown in Figure 68 and tabulated in Table 6; the uncertainties shown are statistical. Within the error bars, no asymmetry is seen between positive and negative tracks even at low p_t. Above 500 MeV/c the efficiency is flat at around 95%; by comparison, the corresponding efficiency in minimum bias events was found[85] to be 99% (Figure 69). One might wonder why the efficiency doesn't reach a plateau in jet events until p_t exceeds about 500 MeV/c when it only takes 300 MeV/c for a track to pass through all layers of the chamber. For the D^* analysis it is important to try to understand this in order to maximize the number of reconstructed D^*s; this number depends on the reconstruction efficiency for the "slow pion" which is concentrated in this p_t region. Figure 70 shows the evolution of the efficiency for several p_t bins as the cuts are applied. Below 500 MeV/c or so, the biggest drop in the efficiency occurs after the first cut requiring a reconstructed track which matches the Monte Carlo track; these tracks are simply not found in any form or fashion.

Part of the reason for this appears to be a cut placed in the early stages of the pattern recognition on the angle made by the seed
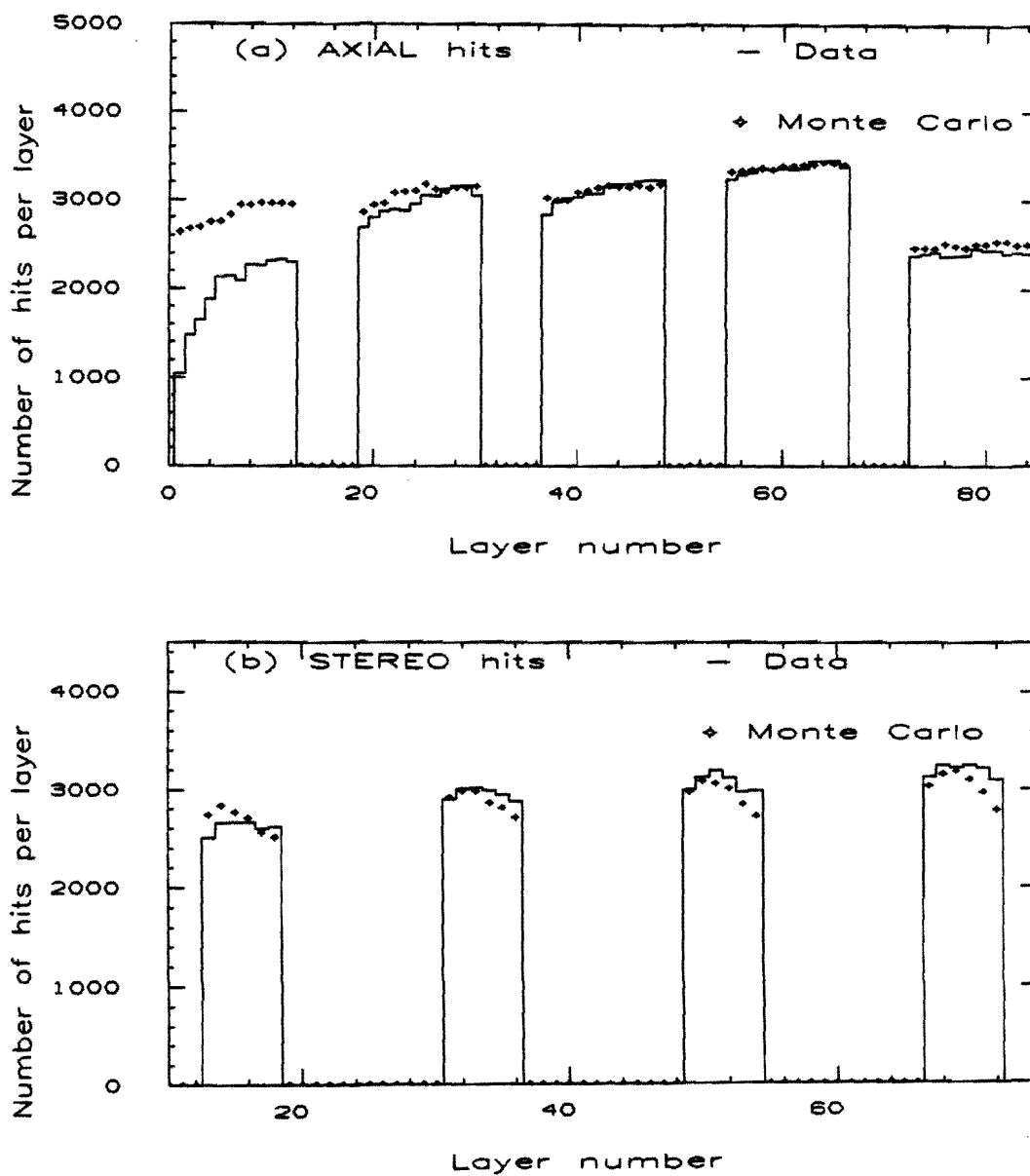
Figure 67. The layer number of the hits on tracks passing track selection, comparing Monte Carlo tracks (before tuning) to the data. The two distributions have been normalized to the same number of tracks.
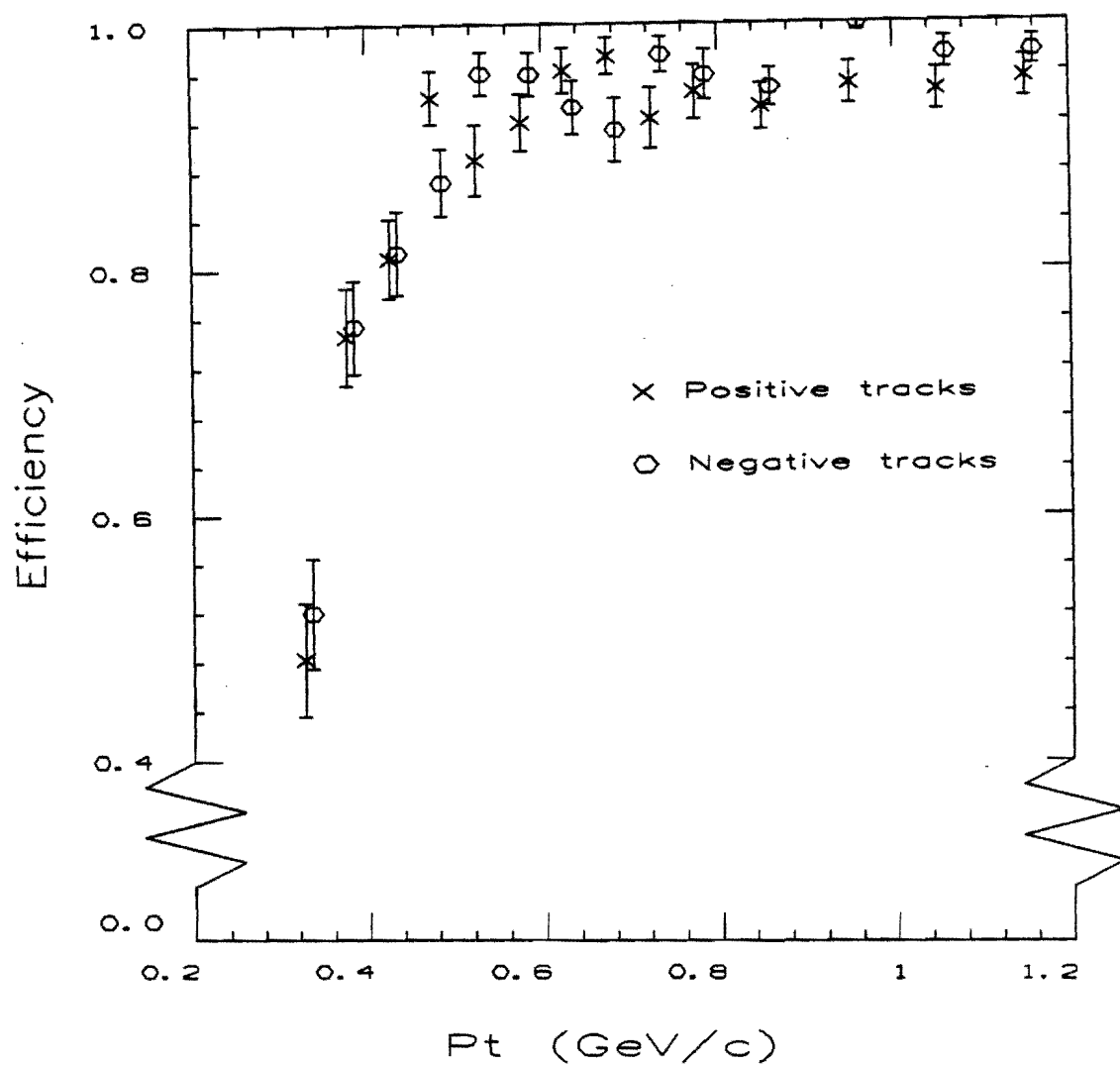
Figure 68. The single-track finding efficiency as a function of track p_t for tracks with $|\eta|<1$. The points for the negative tracks have been horizontally shifted for easier viewing.

Table 6. The single-track finding efficiency in typical jet events as a function of the track p_t.

$\langle p_t \rangle$ (MeV/c)	Positive tracks	Negative tracks	Overall
325	0.48 ± 0.05	0.52 ± 0.05	0.50 ± 0.03
375	0.75 ± 0.04	0.75 ± 0.04	0.75 ± 0.03
425	0.81 ± 0.03	0.81 ± 0.03	0.81 ± 0.02
475	0.94 ± 0.02	0.87 ± 0.03	0.90 ± 0.02
525	0.89 ± 0.03	0.96 ± 0.02	0.93 ± 0.02
575	0.92 ± 0.02	0.96 ± 0.02	0.94 ± 0.02
625	0.96 ± 0.02	0.93 ± 0.02	0.95 ± 0.02
675	0.97 ± 0.02	0.91 ± 0.03	0.94 ± 0.02
725	0.92 ± 0.02	0.97 ± 0.01	0.95 ± 0.01
775	0.94 ± 0.02	0.96 ± 0.02	0.95 ± 0.02
850	0.93 ± 0.02	0.95 ± 0.02	0.94 ± 0.01
950	0.95 ± 0.02	0.99 ± 0.01	0.98 ± 0.01
1050	0.95 ± 0.02	0.97 ± 0.01	0.96 ± 0.01
1150	0.95 ± 0.02	0.98 ± 0.01	0.97 ± 0.01
1250	0.98 ± 0.01	0.92 ± 0.02	0.95 ± 0.01
1350	0.97 ± 0.01	0.97 ± 0.01	0.97 ± 0.01
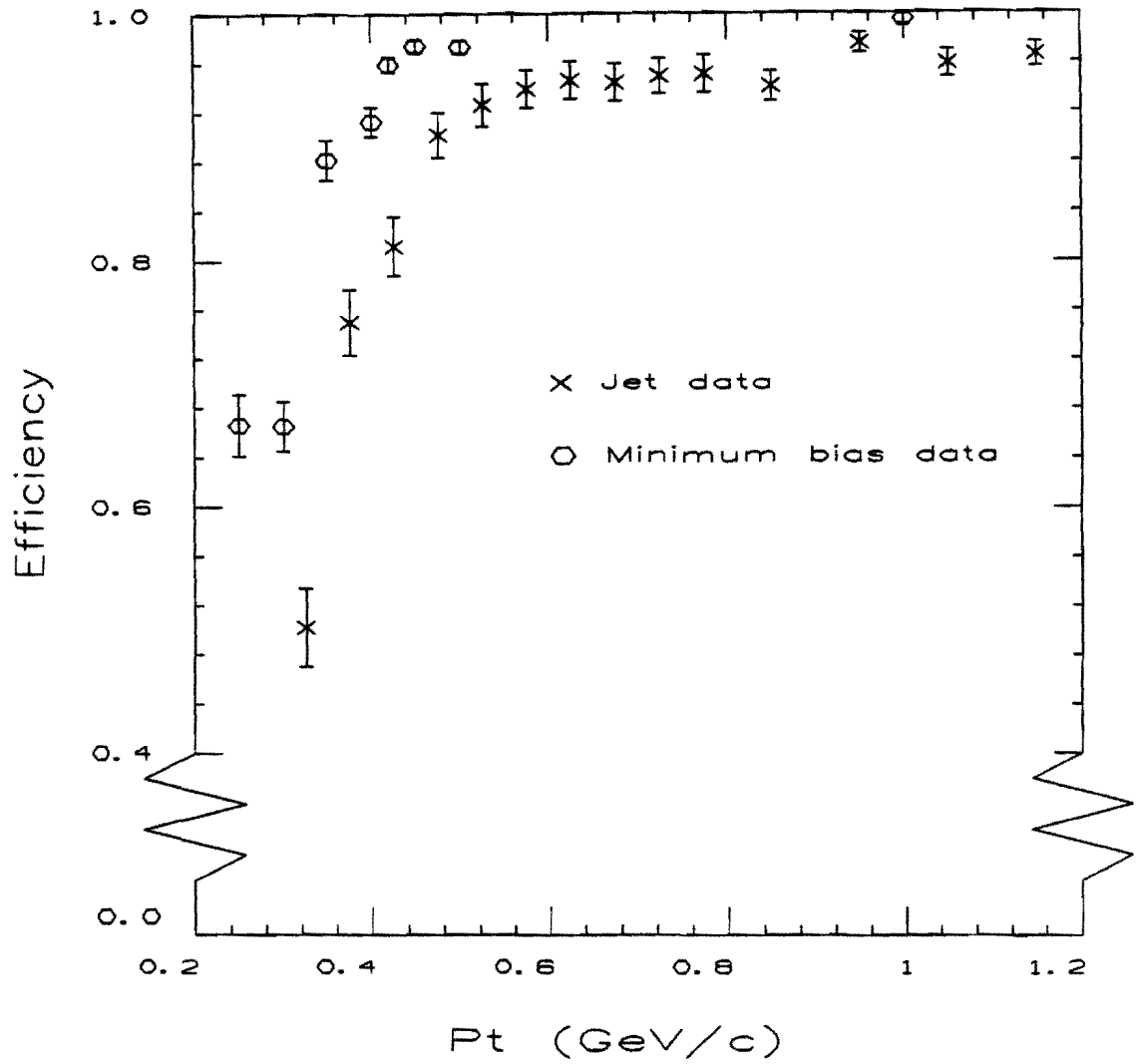
Figure 69. The single-track finding efficiency as a function of track p_t for tracks with $|\eta|<1$ in jet events compared with minimum bias events.

Figure 70. The efficiency as a function of the number of cuts applied, shown for various track p_t bins. The cuts are:

1) >25% of the Monte Carlo hits matched on the reconstructed track
2) The track is reconstructed in three dimensions.
3) The number of hits used in the track > 50% of the number expected
4) $\geq$ 2 good axial segments
5) $\geq$ 1 good stereo segment

segment with respect to the sense wire plane. Recall that the pattern recognition starts in the outermost axial superlayer looking for a set of hits consistent with a line segment (here called the seed segment) crossing the sense wire plane. Once such a segment is found, the search for other hits from this potential track is conducted both inward and, if possible, outward in a circular road passing through the segment and the z axis. The search for seed segments not already associated with tracks continues inward through all the axial superlayers. Figure 71 shows the angle between the tangent to a track and the radial direction evaluated at various superlayer radii for different values of track p_t. The pattern recognition requires this angle to be less than approximately 31° in order to have at least five hits contributing to the segment from the same drift cell. This means that for tracks below 450 MeV/c a seed segment must be found in one of the three innermost axial superlayers, a task made difficult by the comparatively large number of hits in these layers, especially in jet events (Figures 72,73). This probably also partially explains why the efficiency turns on faster in minimum bias events. To take an extreme case, the search for a 300 MeV/c track must begin in superlayer 2 (where superlayer 0 is the innermost layer). Between 350 and 450 MeV/c, the search starts in superlayer 4, while for tracks between 450 and 550 MeV/c, the search begins in superlayer 6. We can see a hint of this quantization in Figure 70.

The efficiency at low-p_t falls even faster in the sample of jets with high track multiplicity (Figure 74). This is probably a worse case of the effect described above; the innermost axial superlayers become even busier in these high-multiplicity events (Figure 75).

Figure 76 (Table 7) shows the efficiency as a function of η; it is flat out to a value of 1.0. Beyond that the efficiency begins to suffer from the loss of high quality stereo information from the outermost stereo superlayer. Figure 77 shows that the tracks in the last two bins past $|\eta|$ of 1 are in fact often actually found, but only in the r-ϕ projection.
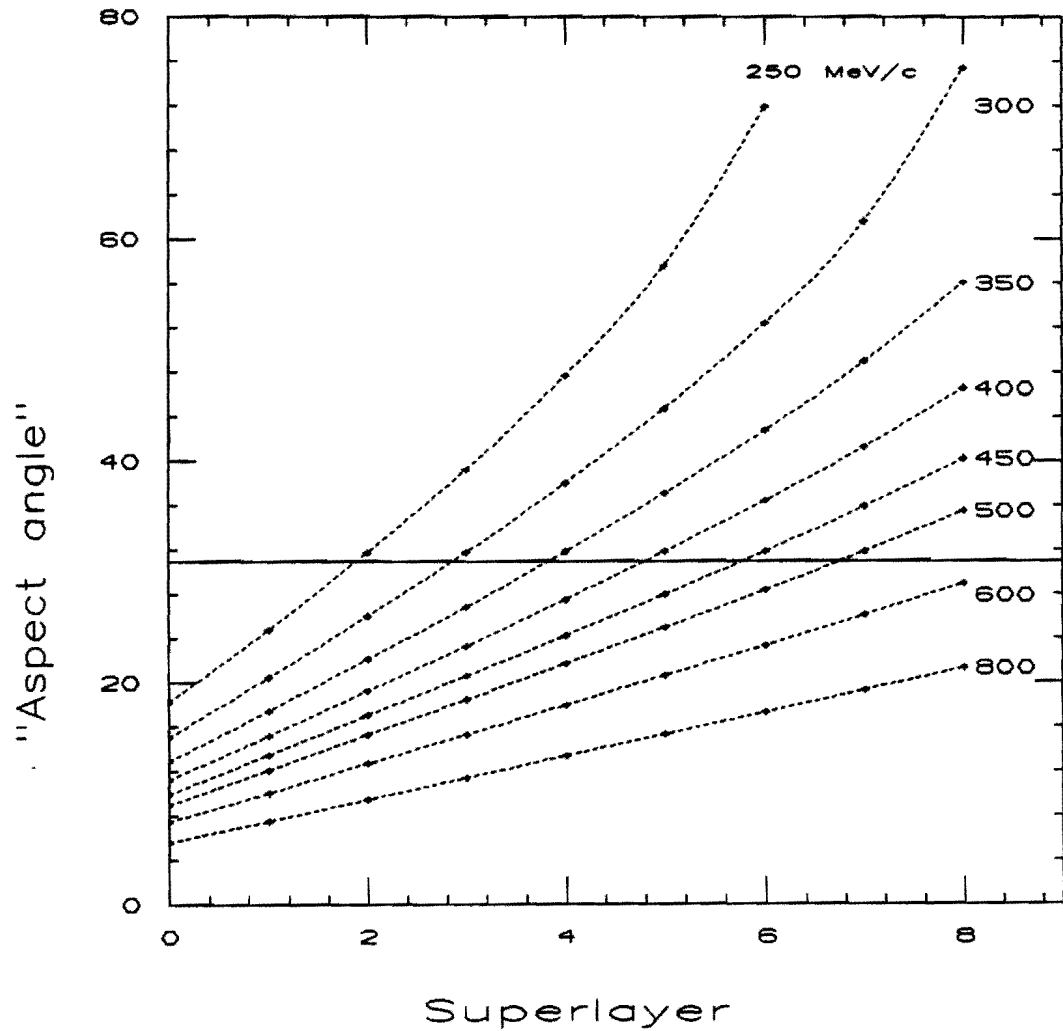
Figure 71. The "aspect angle" evaluated at the center of each superlayer, shown for various values of track p_t. The "aspect angle" shown here is defined as that between the tangent to a track and the radial direction.
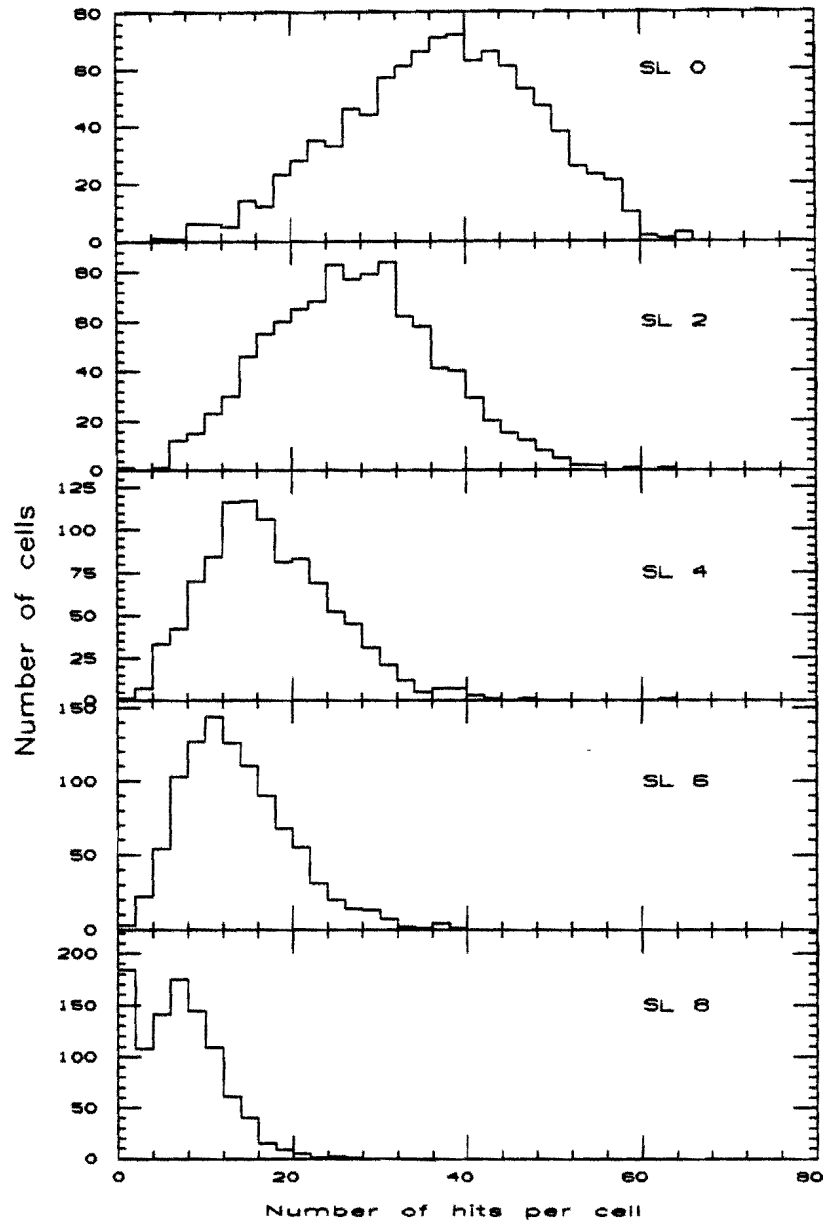
Figure 72. The number of hits per cell for the five axial superlayers for jets from a run taken with the 45 GeV trigger. Only those cells within 0.7 radians in ϕ with respect to the jet axis are considered. Excessively narrow hits ($\leq$ 4ns) and excessively wide hits ($\geq$ 1020ns) have been excluded. The jets were required to have E_t(corrected)>30 GeV and $0.1<|\eta|<0.8$.
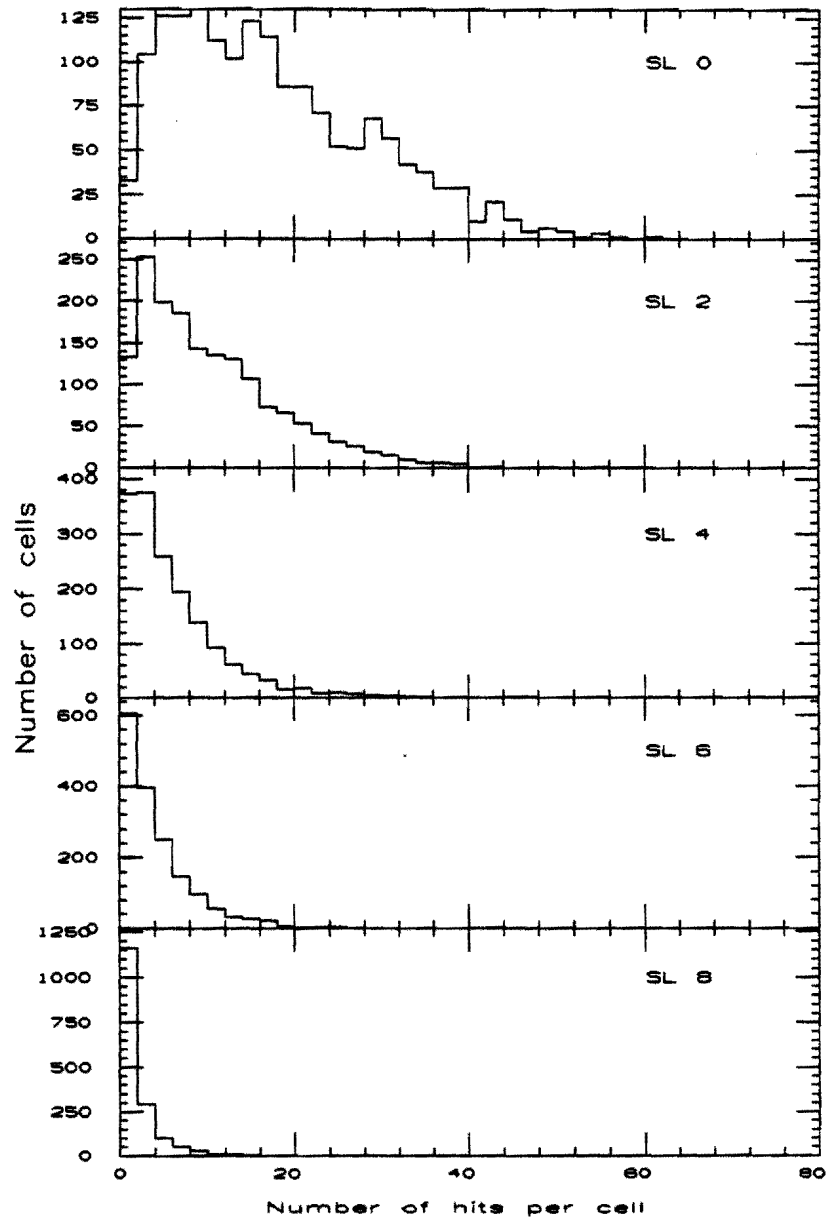
Figure 73. The number of hits per cell in minimum bias events. Only those cells within 0.7 radians of the highest p_t track are considered. As before, excessively narrow hits ($\leq$ 4ns) and excessively wide hits ($\geq$ 1020ns) have been excluded.
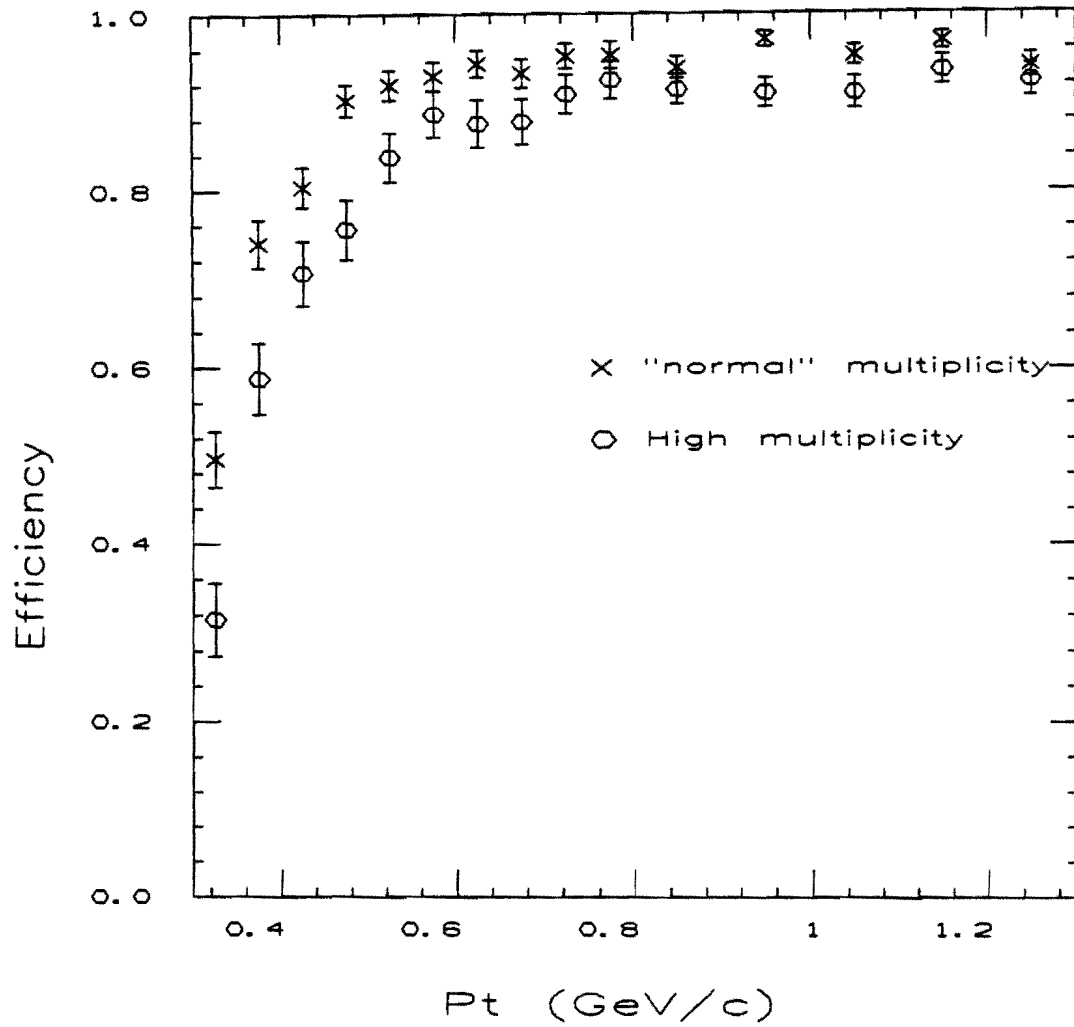
Figure 74. The single-track finding efficiency as a function of track p_t for the high multiplicity jet sample, shown together with the efficiency for more typical jets.
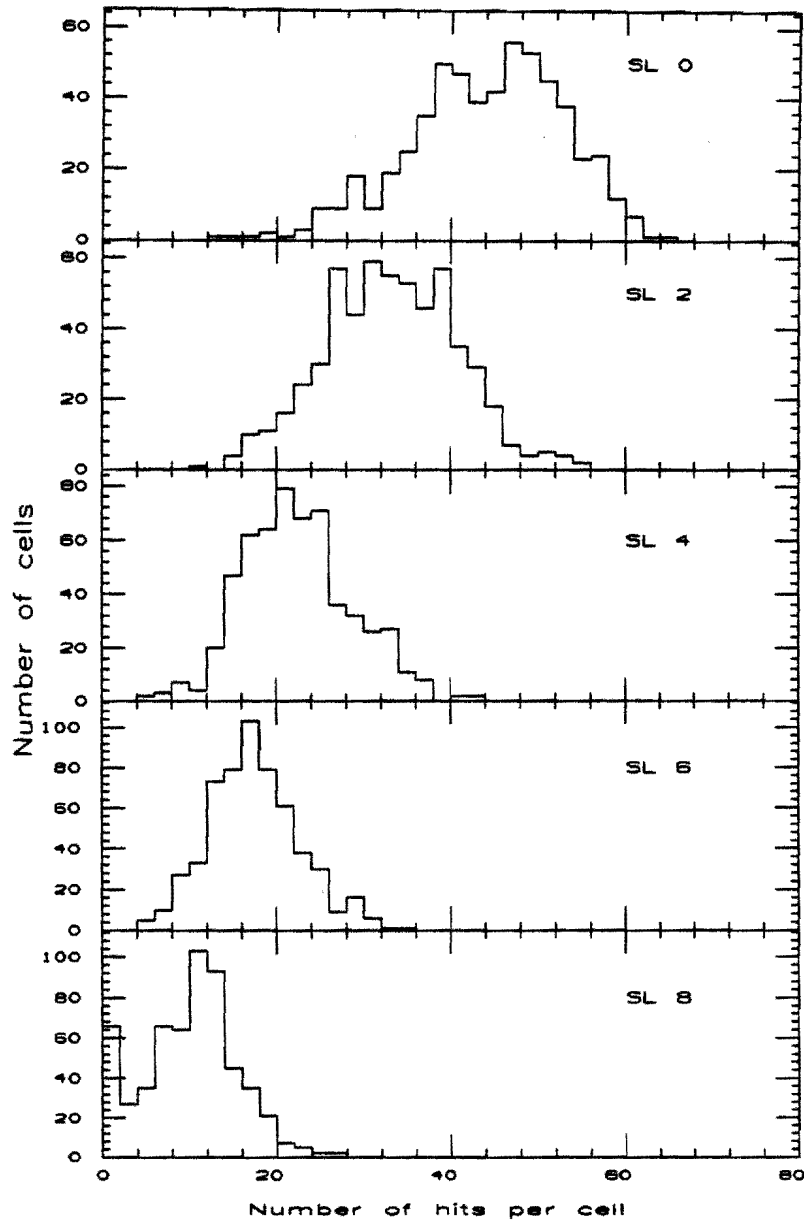
Figure 75. The number of hits per cell for the high multiplicity jet data, to be compared with figures 72 and 73.
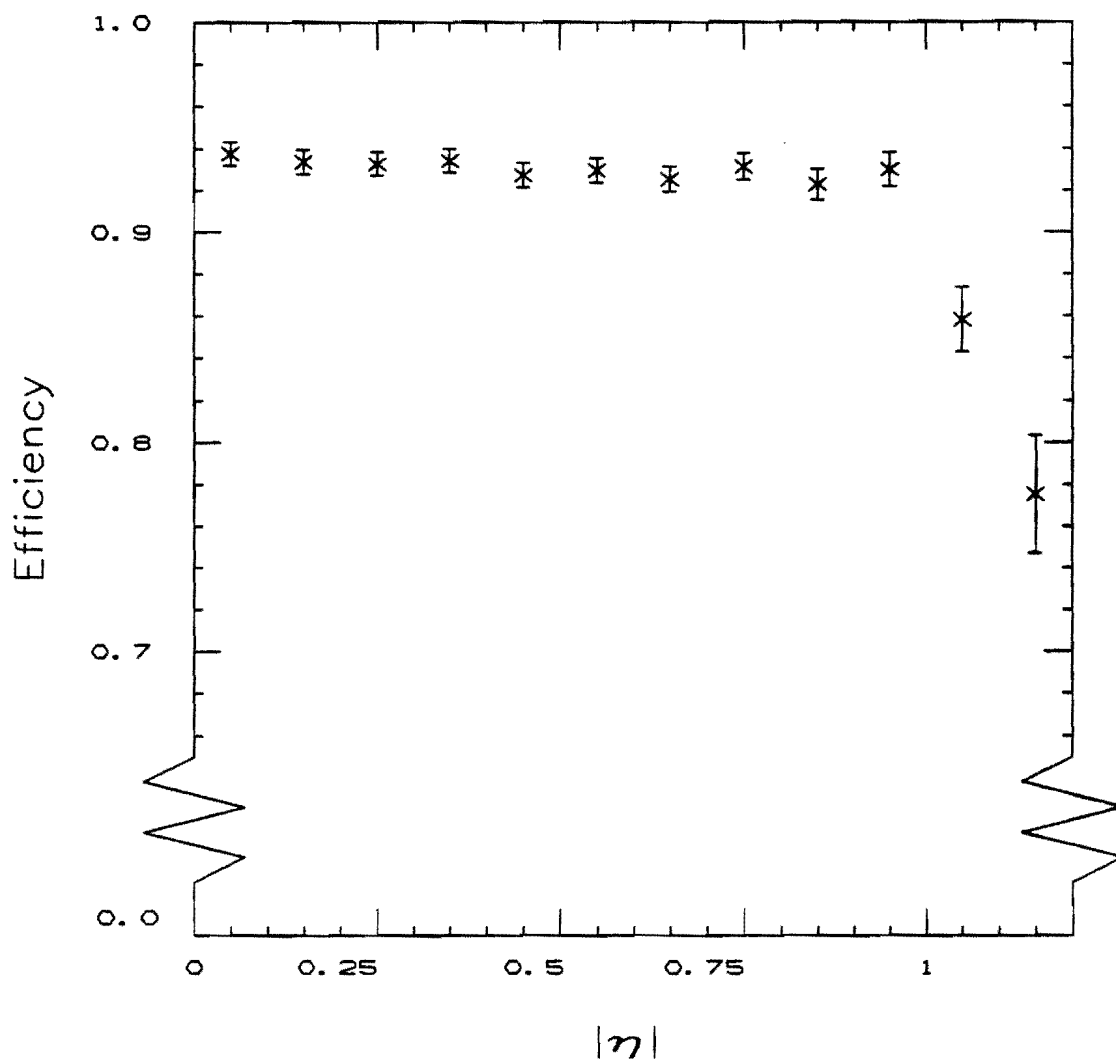
Figure 76. The single-track efficiency as a function of $|\eta|$.

Table 7. The single-track finding efficiency in jets as a function of $|\eta|$ of the track.

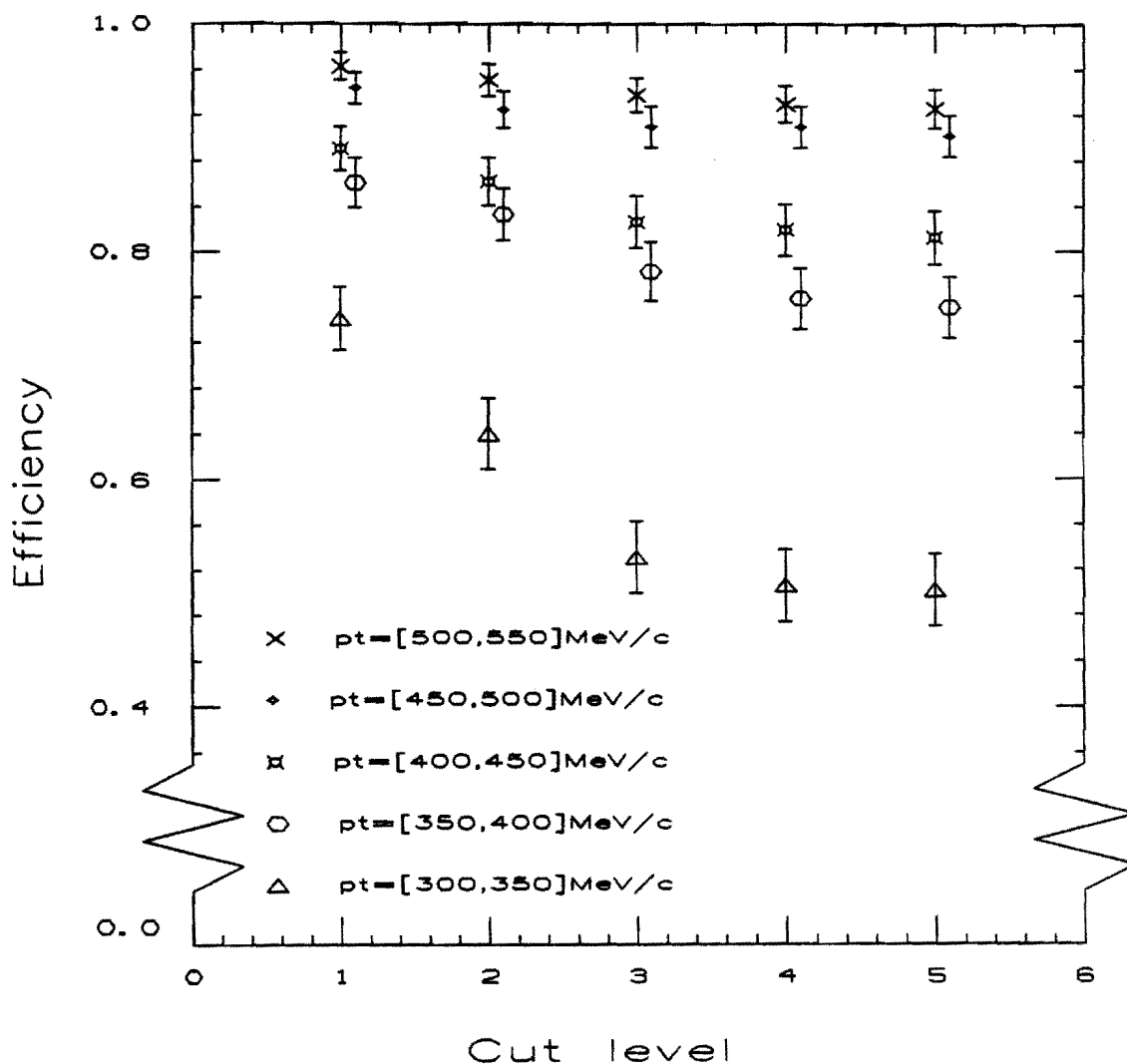| $< |\eta| >$	Efficiency
0.05	0.938 ± 0.006
0.15	0.934 ± 0.006
0.25	0.933 ± 0.006
0.35	0.934 ± 0.006
0.45	0.927 ± 0.006
0.55	0.929 ± 0.006
0.65	0.925 ± 0.006
0.75	0.931 ± 0.006
0.85	0.923 ± 0.007
0.95	0.930 ± 0.008
1.05	0.858 ± 0.015
1.15	0.775 ± 0.028
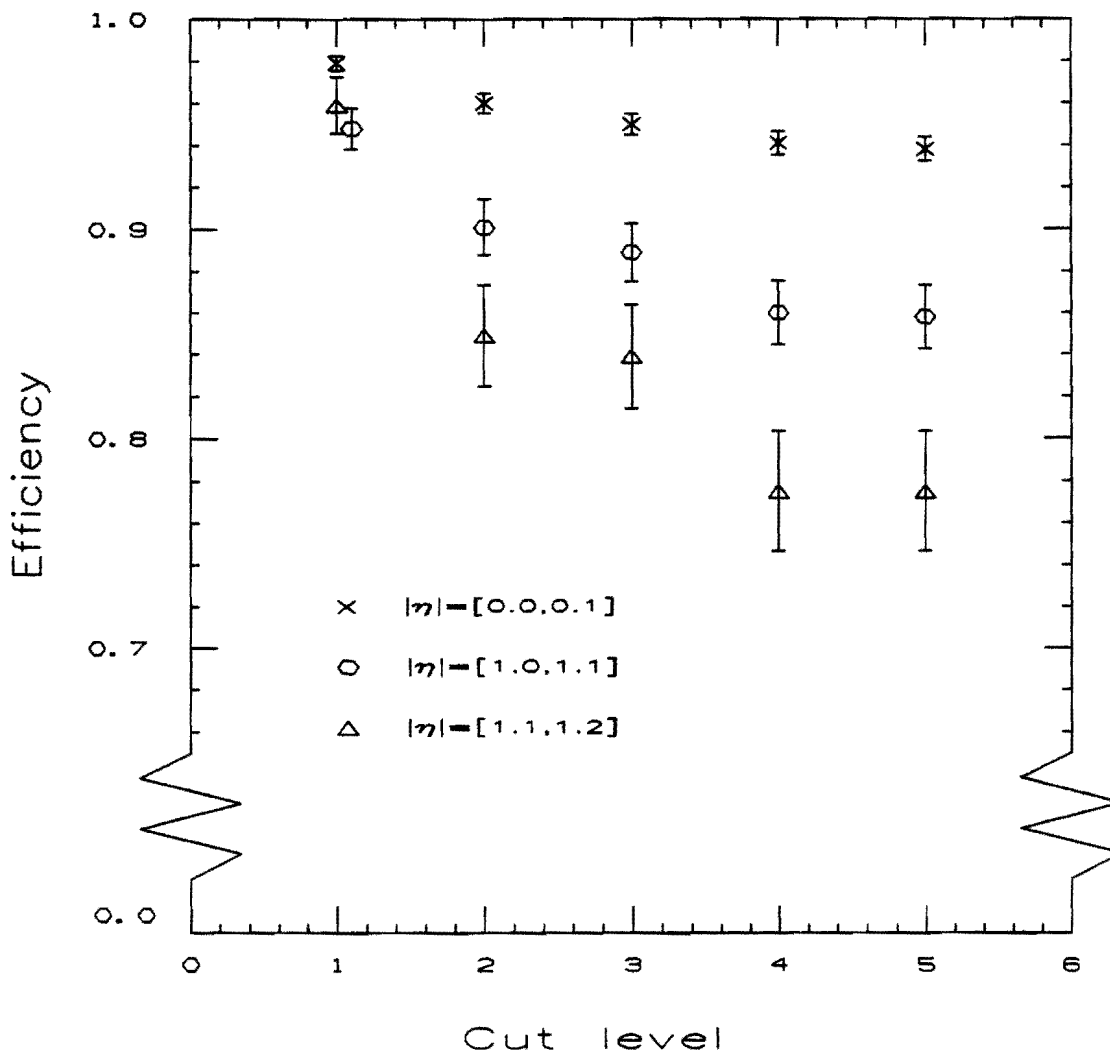
Figure 77. The efficiency as a function of the number of cuts applied, shown for various $|\eta|$ bins. The cuts are:

1) >25% of the Monte Carlo hits matched on the reconstructed track
2) The track is reconstructed in 3 dimensions.
3) The number of hits used in the track > 50% of the number expected
4) $\geq$ 2 good axial segments
5) $\geq$ 1 good stereo segment

We now turn to the dependence of the efficiency on the level of activity in the chamber. One quantity we have examined is the average separation in the r-ϕ plane between a track and its nearest neighbor; the r-ϕ separation was computed at the radial positions of all the sense wires and then an average was taken. Figure 78 (Table 8) shows the efficiency as a function of the r-ϕ separation between the Monte Carlo track and the closest reconstructed track (excluding of course the reconstructed track that corresponds to the Monte Carlo track!) for tracks above 500 MeV/c.[86] Again it appears that most tracks at low r-ϕ separation are actually found but only in the r-ϕ plane (Figure 79). This inefficiency at low values of r-ϕ separation does not play a major role in the overall efficiency, however, because the phase space for having tracks so close to one another is relatively small (Figure 80).

We have also looked at the dependence of the efficiency on the hit density around the track. This was done by counting the number of hits in a helical road whose r-ϕ width was set to 10 cm. (To set the scale, the width of a CTC cell is something like 7 cm.) The hit density was defined as the number of hits in this road divided by the length of the track; this includes the hits due to the track itself (typically 70 hits on a track of length 140 cm, or a density of 0.5). This quantity is anti-correlated with the r-ϕ separation (Figure 81). Figure 82 (Table 9) shows the efficiency for tracks above 500 MeV/c. As with the r-ϕ separation discussed above, the hit density does not substantially contribute to the overall inefficiency because the probability of having a track in a region of very high hit density is relatively small (Figure 83).

The efficiency as a function of ϕ (evaluated at the inner radius of superlayer 4) is shown in Figure 84. It compares reasonably well with the raw ϕ distribution of tracks from the jet data which have passed the track selection cuts. The jet data were normalized so that they overlapped with the Monte Carlo in the region around $\phi=300°$.
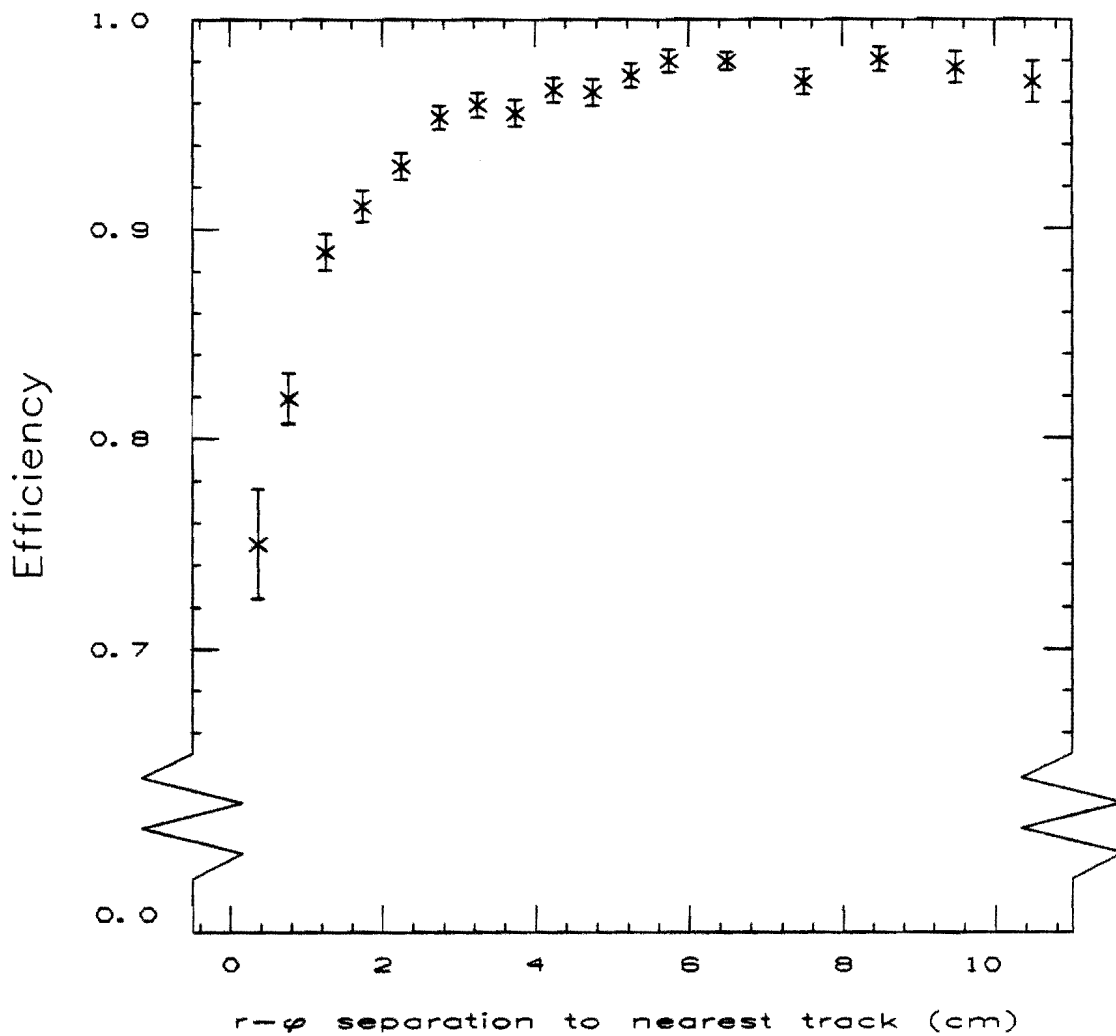
Figure 78. The single-track efficiency as a function of the r-
ϕ separation between a track and its nearest neighbor. The tracks in
this plot were required to have $p_t > 500$ MeV/c.

Table 8. The single-track finding efficiency in jets as a function of the r-ϕ separation to the nearest track.

$\langle r$-ϕ separation$\rangle$ (cm)	Efficiency
0.37	0.750 ± 0.026
0.77	0.819 ± 0.012
1.25	0.889 ± 0.009
1.75	0.911 ± 0.007
2.25	0.930 ± 0.006
2.75	0.953 ± 0.006
3.25	0.959 ± 0.006
3.75	0.955 ± 0.006
4.25	0.966 ± 0.006
4.75	0.965 ± 0.006
5.25	0.973 ± 0.006
5.74	0.980 ± 0.006
6.50	0.980 ± 0.004
7.50	0.970 ± 0.006
8.50	0.981 ± 0.006
9.50	0.977 ± 0.008
10.50	0.970 ± 0.010
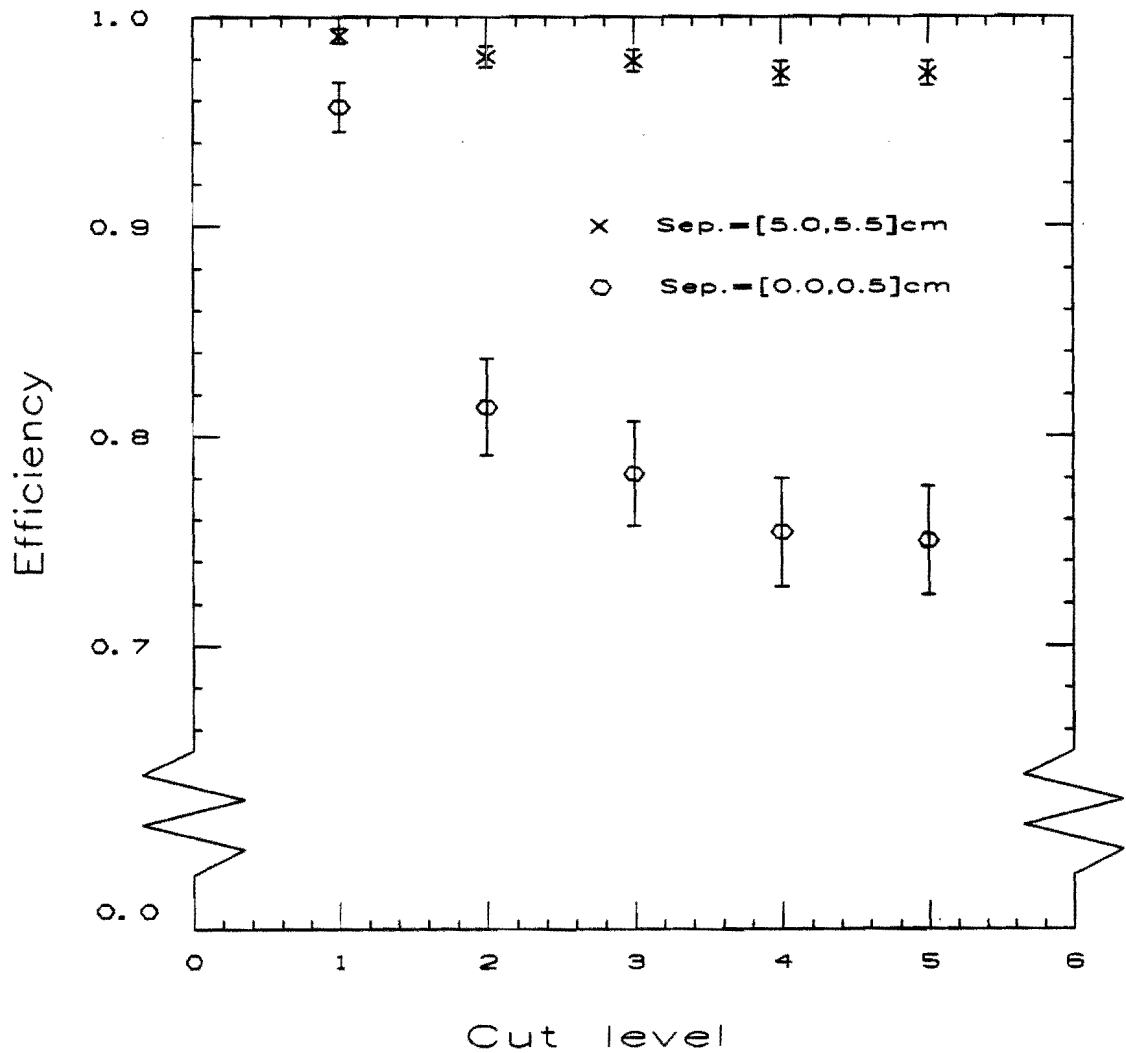
Figure 79. The efficiency as a function of the number of cuts applied, shown for various bins of r-ϕ separation. The cuts are:

1) >25% of the Monte Carlo hits matched on the reconstructed track
2) The track is reconstructed in 3 dimensions.
3) The number of hits used in the track > 50% of the number expected
4) $\geq$ 2 good axial segments
5) $\geq$ 1 good stereo segment

190
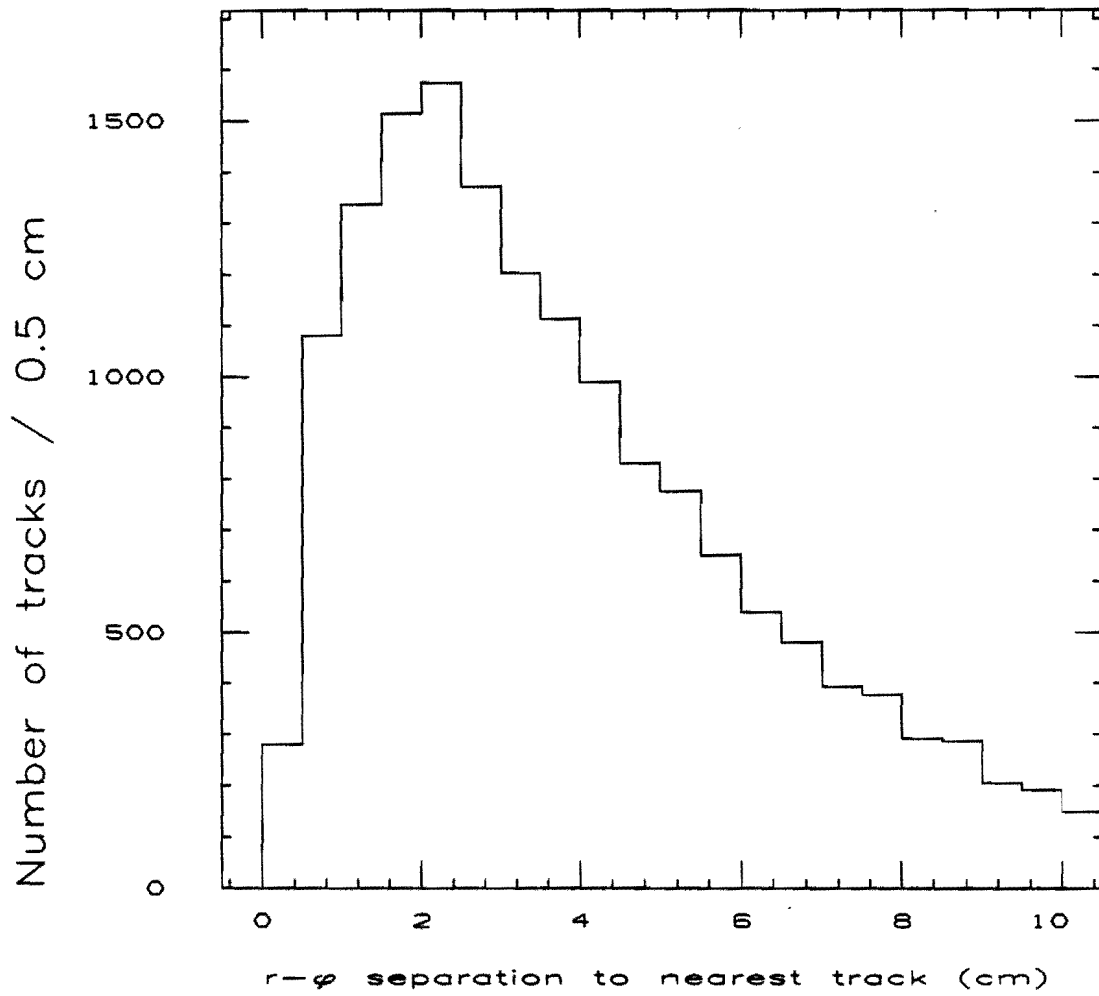
Figure 80. The distribution of the r-ϕ separation for the Monte Carlo tracks above 500 MeV/c.
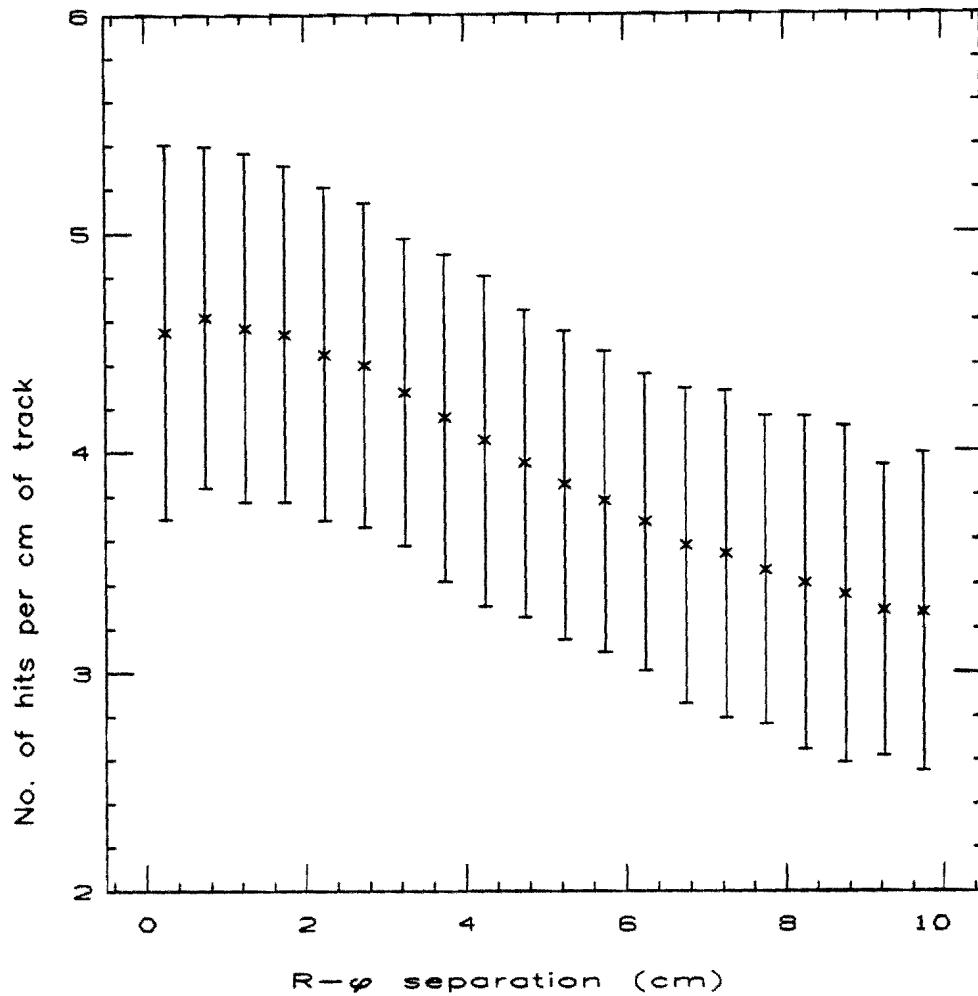
Figure 81. The hit density around the track versus the r-ϕ separation to the nearest track. The plot shows the mean and rms hit density for each bin of r-ϕ separation. The hit density is defined as the number of hits in a helical road with an r-ϕ width of 10cm centered about the track divided by the length of the track. This includes the hits due to the track itself (typically 0.5 hits per cm).
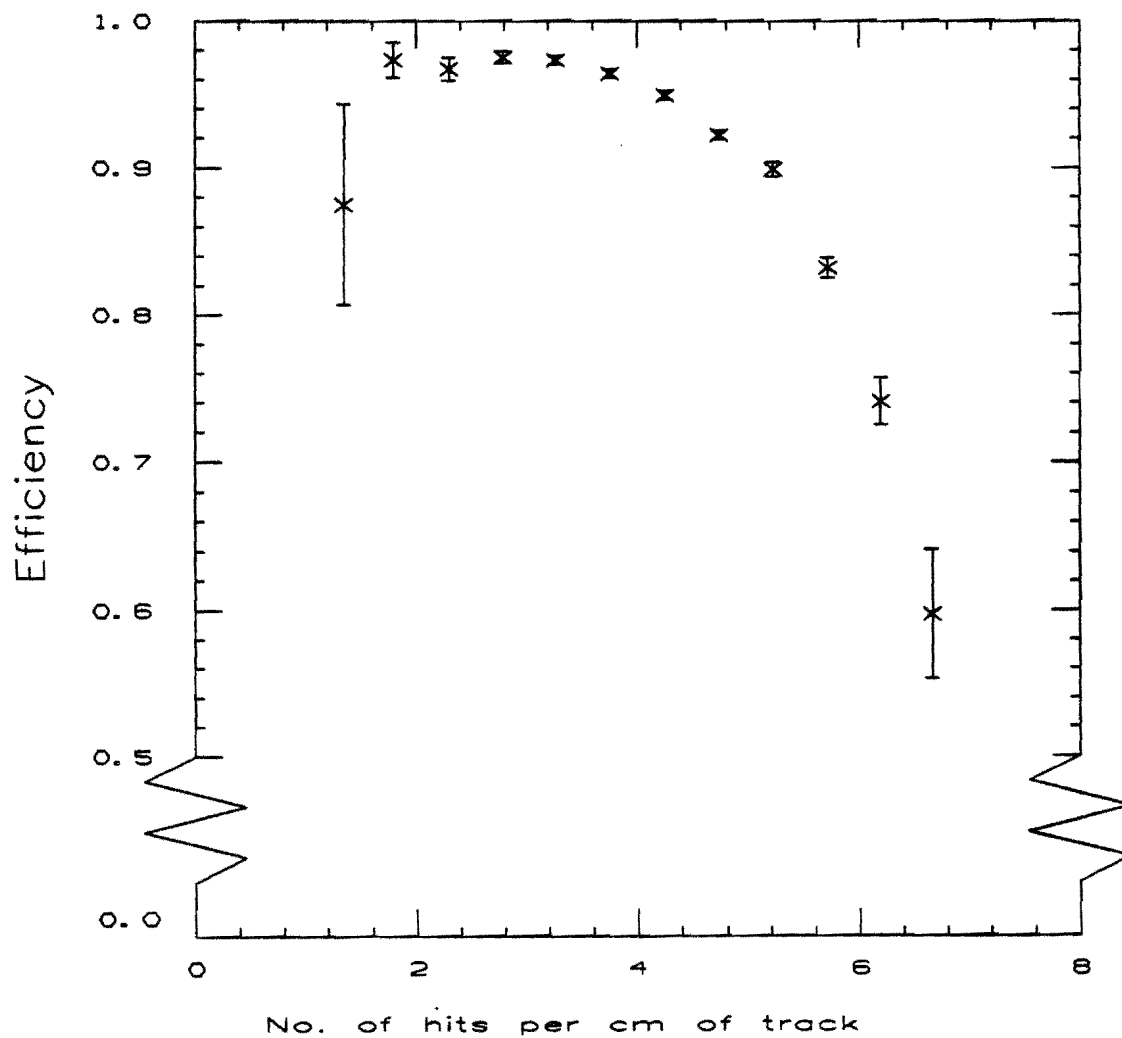
Figure 82. The single-track efficiency as a function of the hit density around the track. The tracks in this plot were required to have $p_t > 500$ MeV/c.

Table 9. The single-track finding efficiency in jets as a function of the hit density around the track. The hit density is defined as the number of hits in a helical road of $r-\phi$ width equal to 10 cm divided by the length of the track.

Hit density (hits/cm)	Efficiency
1.35	0.875 ± 0.068
1.79	0.973 ± 0.012
2.30	0.967 ± 0.008
2.79	0.975 ± 0.004
3.27	0.973 ± 0.003
3.76	0.964 ± 0.003
4.26	0.949 ± 0.003
4.74	0.922 ± 0.003
5.23	0.899 ± 0.005
5.72	0.832 ± 0.007
6.20	0.741 ± 0.016
6.67	0.597 ± 0.044
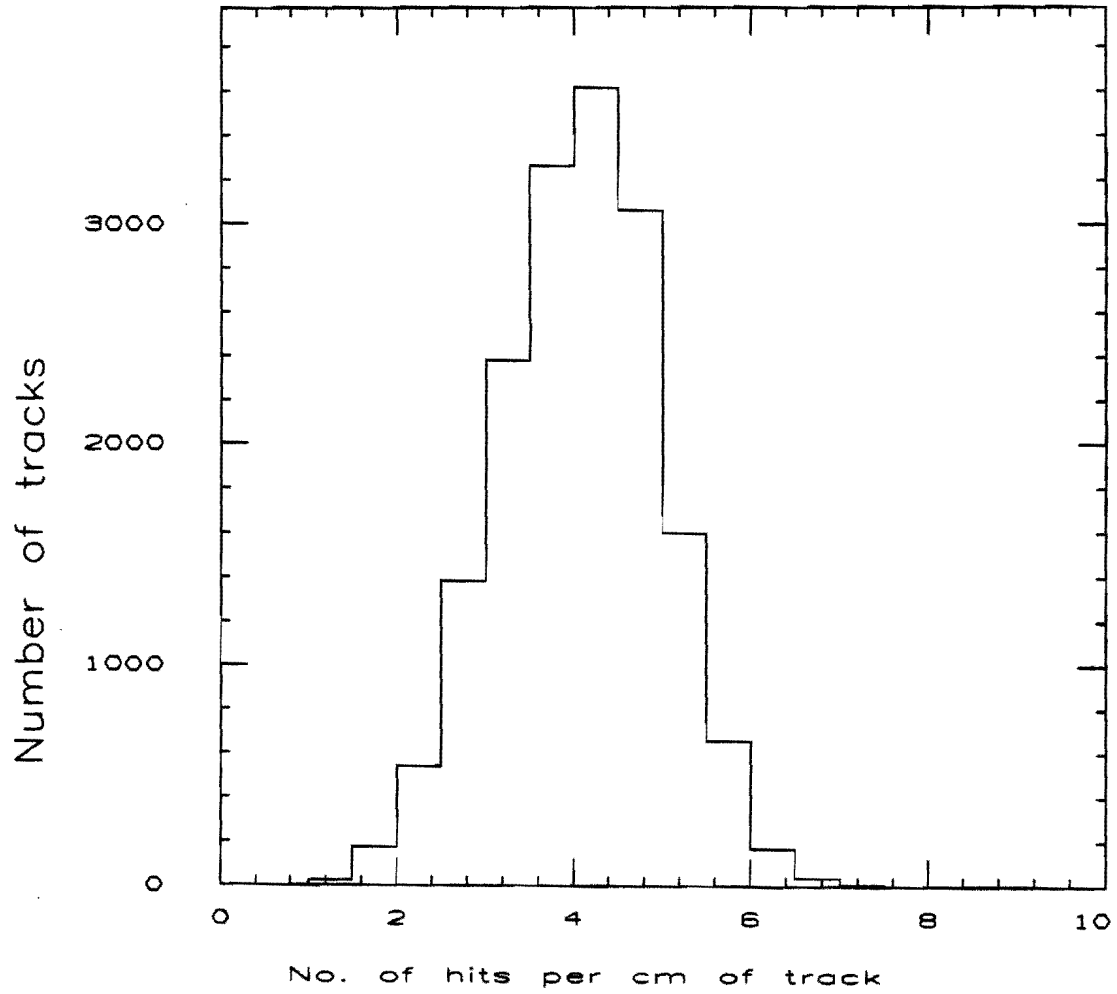
Figure 83. The distribution of the hit density around the Monte Carlo tracks.
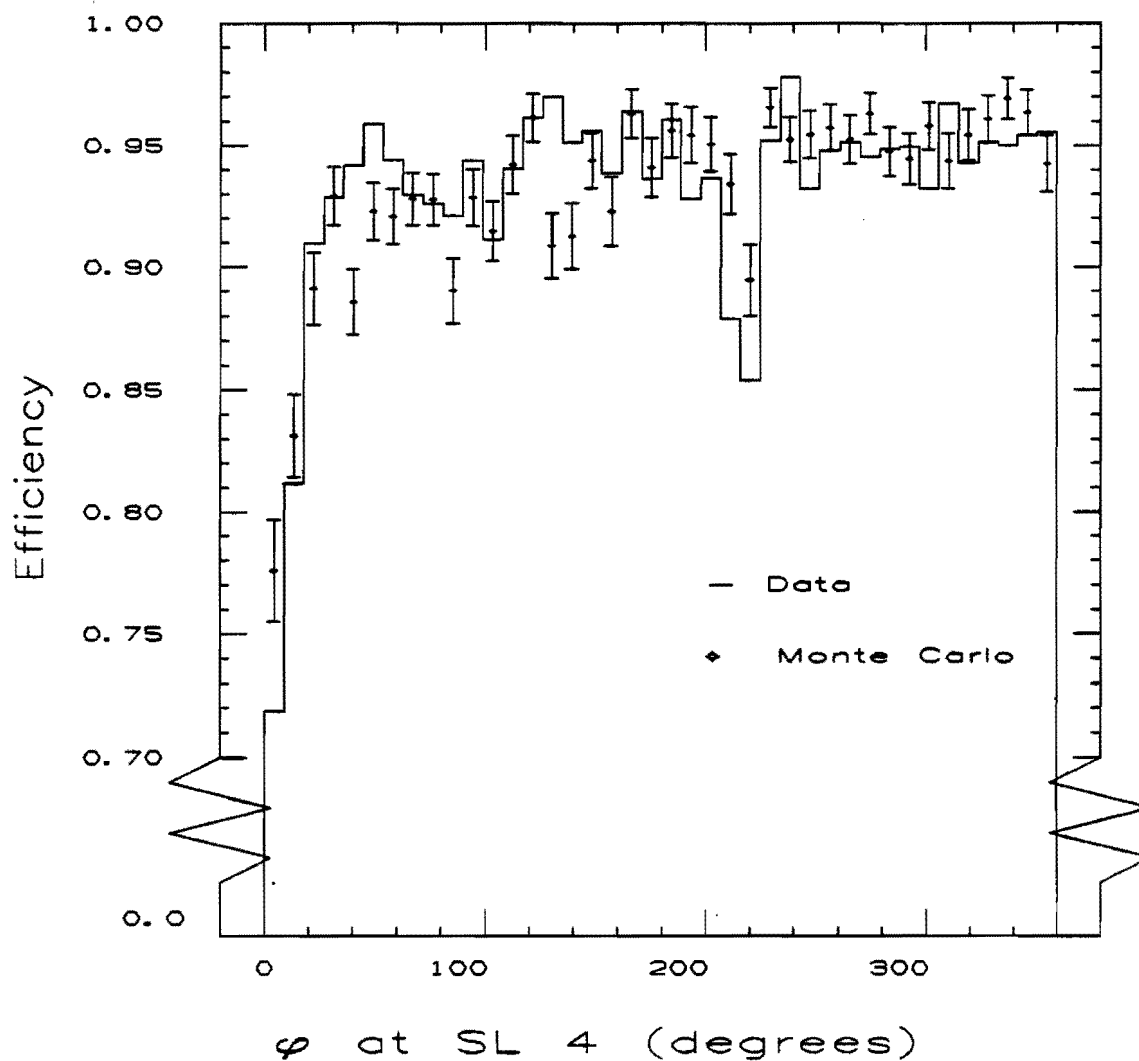
Figure 84. The efficiency as a function of ϕ of the Monte Carlo track evaluated at the inner radius of superlayer 4. This is compared to the ϕ distribution for tracks from the jet data. The two distributions were normalized so that they overlap in the region around $\phi=300°$.

B.3 Summary

The tracking efficiency in jets is generally very high (~95%), although there are certain regions of phase space where it is somewhat lower. For p_t below about 500 MeV/c, the tracking is made difficult because the search for potential track elements starts closer to the beam where the activity in the chamber is quite high. The other major source of inefficiency is the difficulty of performing the stereo portion of the reconstruction in extreme conditions. These extreme conditions include: 1) not having as many stereo hits due to geometric effects, e.g. for tracks with $|\eta| > 1.0$, and 2) having a very high density of hits in the vicinity of the track, making the pattern recognition in the stereo view difficult.

APPENDIX C

DETERMINATION OF THE JET ENERGY SCALE

A first estimate of the jet energy scale is obtained from the calibration of the calorimeters in the test beam. Corrections then have to be made for 1) the nonlinear response of the calorimeters to low-energy particles, 2) energy lost in uninstrumented regions of the calorimeters, 3) energy added to the jet from the so-called "underlying event", i.e. those particles not directly associated with the hard parton scattering, and 4) energy lost outside the clustering cone. This is a large body of work which was performed by other members of the CDF Collaboration and documented elsewhere.[87] Our discussion here will therefore be relatively brief.

C.1 Test Beam Calibration

The calibration of calorimeters to measure jet energies is a complicated process because there is no such thing as a source of well-measured jets.[88] At CDF, the EM calorimeters were calibrated[89] with a beam of electrons ranging in momentum from 10 to 100 GeV/c and the hadron calorimeters[90] with a beam of charged pions in the momentum range 10 to 150 GeV/c. In the range for which the calibrations were performed, the response of both calorimeters was found to be linear with the beam energy, an important feature since one measures the jet energy by summing the energies of single particles inside the jet. After removal from the test beam, the calibration was maintained over time with radioactive sources.[91]

C.2 Low Energy Response

Unfortunately, the bulk of the calibration data for the central calorimeters was performed with beams of momenta 50 GeV/c and higher; no data were taken below 10 GeV/c whereas a significant fraction of the particles in the kinds of jets used in this analysis (i.e. with energy around 50 GeV) have momenta below 10 GeV/c. To remedy this situation, isolated tracks with well-measured momenta in the minimum-bias data were used to pin down the response of the calorimeters to these low momentum particles.[92]

The CDF calorimeter is "non-compensating" in the jargon of high energy physics, meaning that the response to charged hadrons is different from that to electrons or photons. This means, for example, that if we are given a charged pion of a given energy, the calorimeter will report a different energy when the pion starts showering in the EM compartment compared to when it showers entirely in the hadronic compartment. The fraction of energy deposited in the EM compartment depends on the incident momentum of the particle (approximately as $\ln p$).[93] At low momenta, therefore, the calorimeter response to charged hadrons becomes non-linear; at high momenta, the fraction deposited in the EM compartment is approximately constant (since $\ln p \sim$ constant for large p) so that linearity is restored. Figure 85 shows the calorimeter response to charged pions from the test beam and to isolated charged particles in the minimum-bias data. The error bars include both statistical and systematic uncertainties where the latter dominate below about 4 GeV/c and come from the uncertainties involved in subtracting the energy deposited in the calorimeter by (trackless) neutral particles. The response can be as low as 65% of the true energy. Note also that although the calorimeter energy scale was set in the test beam at 50 GeV, the ratio of the measured energy to the particle momentum is not one at that energy. This is because the calibration in the test beam was carried out by requiring the pion to be minimum-ionizing in the EM compartment whereas no such requirement was made for the data points in this plot.
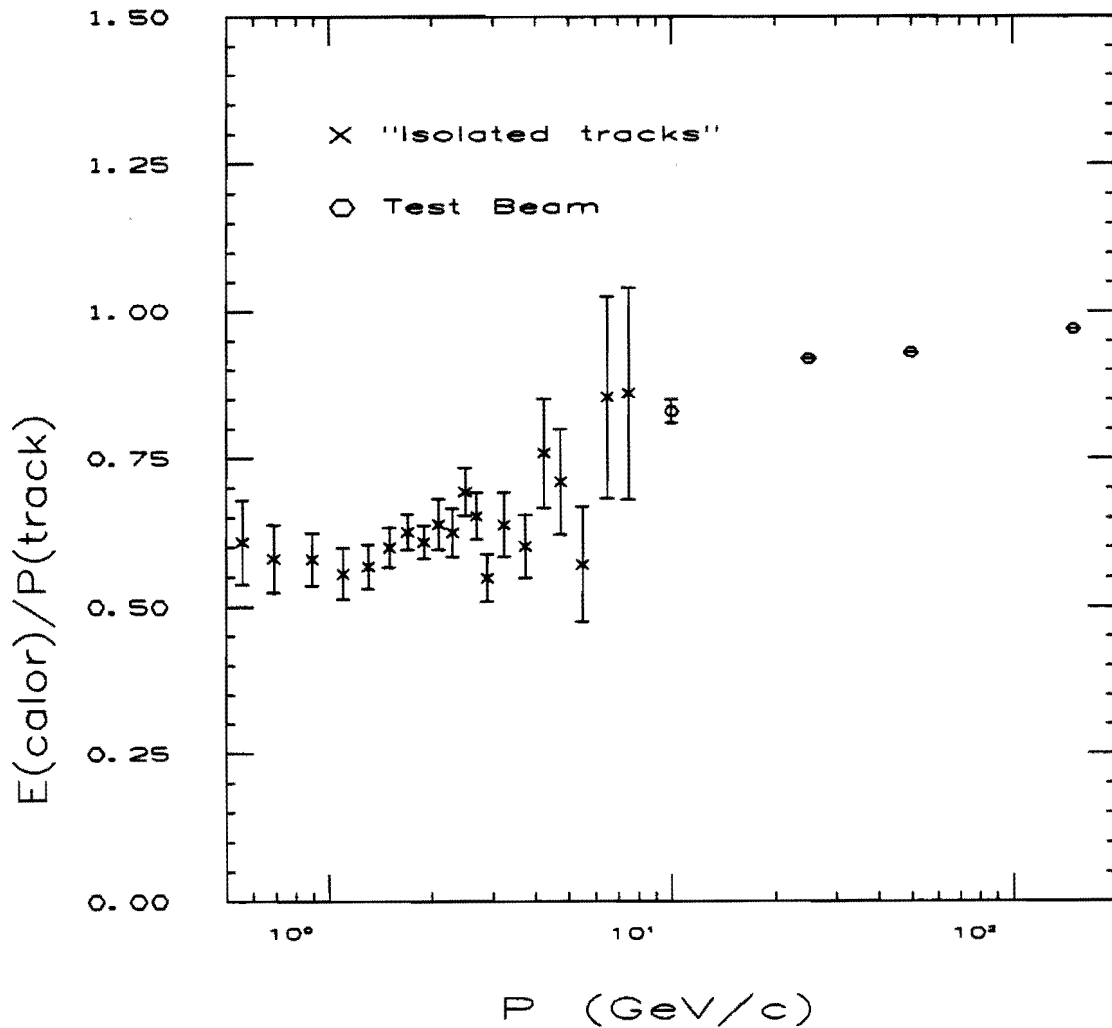
Figure 85. The response of the central calorimeters to charged particles, shown as the ratio of the measured calorimeter energy to the momentum of the particle. The crosses show the response measured using isolated tracks in the minimum-bias data while the open circles show the response measured in the test beam to charged pions. The error bars include both statistical and systematic uncertainties. The figure is from S. Behrends et al., CDF Note 583.

The nonlinearity of the response means that, for a fixed incident jet energy, the measured jet energy will be shifted from the correct value by an amount which depends on the momentum spectrum of particles inside the jet. An <u>average</u> jet energy correction was obtained using the ISAJET Monte Carlo[80] and a full detector simulation. The calorimeter simulation was tuned[94] to reproduce the response to low-energy charged particles and the response across the face of the calorimeter module, including the uninstrumented "cracks" at the ϕ boundaries between modules. (The face response was measured in the test beam.) The jet fragmentation in the Monte Carlo was performed according to the Feynman-Field model[95] and was tuned by comparing the following quantities to the data:

1) The fraction of the jet energy carried by charged particles
2) The invariant mass of the charged particles in the jet
3) The average track momentum transverse to the <u>jet</u> axis
4) The momentum spectrum of tracks transverse to the <u>beam</u> axis
5) The average charged track multiplicity in a cone of radius $\Delta R = 0.7$ about the jet axis
6) A charged fragmentation function where z_{ch} is defined as the longitudinal momentum of a track projected onto the jet axis divided by the sum of the momenta of all tracks inside the jet

Note that, apart from the charged-to-total-energy ratio, all comparisons to the data were performed only with quantities which are measured in the CTC, i.e. the tuning is independent of the calorimeter response to jets (which is what is going to be measured). The result of the Monte Carlo studies was that the measured jet energy is approximately 75% of the true energy for typical jets with energies of 50 GeV. Of the 25% of the energy which is lost, approximately 15% is lost to the low-energy response and the remaining 10% to cracks, curling tracks which fail to reach the calorimeter, and energy lost in the solenoid.

C.3 Energy Gained from the "Underlying Event"

The amount of energy included inside the jet cone from the underlying event was estimated from the jet data by assuming the underlying energy to be uniformly distributed in η-ϕ space.[96] Two-jet events were selected by demanding the absence of a third jet with E_t>15 GeV and requiring the azimuthal angle between the two jets to be 180°±10°. These cuts were chosen to reject obvious multi-jet events without seriously biasing the measurement against high fluctuations in the underlying event. Two sets of events were then selected based on the event topology; the first required both jets to be in the central detector, while the second required one jet in the central detector and the other to have $|\eta|$>2. The energy density 90° in azimuth from the "thrust axis" was then measured. (Roughly speaking, the thrust axis is the same as the jet axis for clean two-jet events.) Within statistical uncertainties, the results from the two samples agreed, indicating that the contribution from the jets themselves to the energy density 90° from the thrust axis was small. For a clustering cone size of ΔR=1.0, it was estimated that the underlying event contributes 3.1±1.1 GeV to the jet energy, independent of the jet energy. This is a small effect compared to the effect of low energy response and energy lost in cracks.

C.4 Energy Lost Due to the Clustering Algorithm

The effect of the clustering cone size and single tower threshold on the jet energy was estimated from the jet data by varying these parameters and comparing the resulting jet energies after subtracting the contribution from the underlying event.[97] For a clustering cone of radius ΔR=1.0, it was found that essentially no energy was lost outside the cone and that the single tower threshold of 200 MeV caused 470 MeV of the jet energy (independent of jet energy) to be lost, a small effect.

C.5 Correction to Central Jet Energies

For a clustering cone size of $\Delta R = 1.0$, a fit to the total central jet energy correction yielded:[98]

For measured jet energies (E_{meas}) below 70 GeV:

$$E_{corrected} = (-0.174*10^{-2})(E_{meas})^2 + 1.37E_{meas} - 2.36 \text{ GeV}$$

For E_{meas} above 70 GeV:

$$E_{corrected} = 1.115E_{meas} + 6.68 \text{ GeV}.$$

In our studies described in Chapter 7, we have chosen to simplify the arithmetic by casting these corrections in the form $E_{corrected} = 1.25E_{meas}$. This turns out to be quite a good approximation for the bulk of the jets used in this analysis, namely those with energies ranging from 25 to 50 GeV uncorrected, as shown below:

E(measured) (GeV)	E(Quadratic correction)	1.25·E(measured)
20	24.3	25.0
30	37.2	37.5
35	43.5	43.8
50	61.8	62.5

The differences are negligible compared to the systematic uncertainties in the jet energy correction which we describe next.

Figure 86 shows the uncertainties in the correction. The largest contribution comes from the low energy response where there is an uncertainty in the subtraction of the energy deposited by unseen neutral particles (mostly π^0s) accompanying the "isolated" charged track. The uncertainty in the response was estimated at one limit by eliminating the π^0 subtraction altogether and at the other limit by doubling the subtraction. The uncertainty in the fragmentation was estimated by trying different parameters for the light quark splitting function in the Feynman–Field model. An upper limit on the correction was obtained from the default splitting function in ISAJET which was
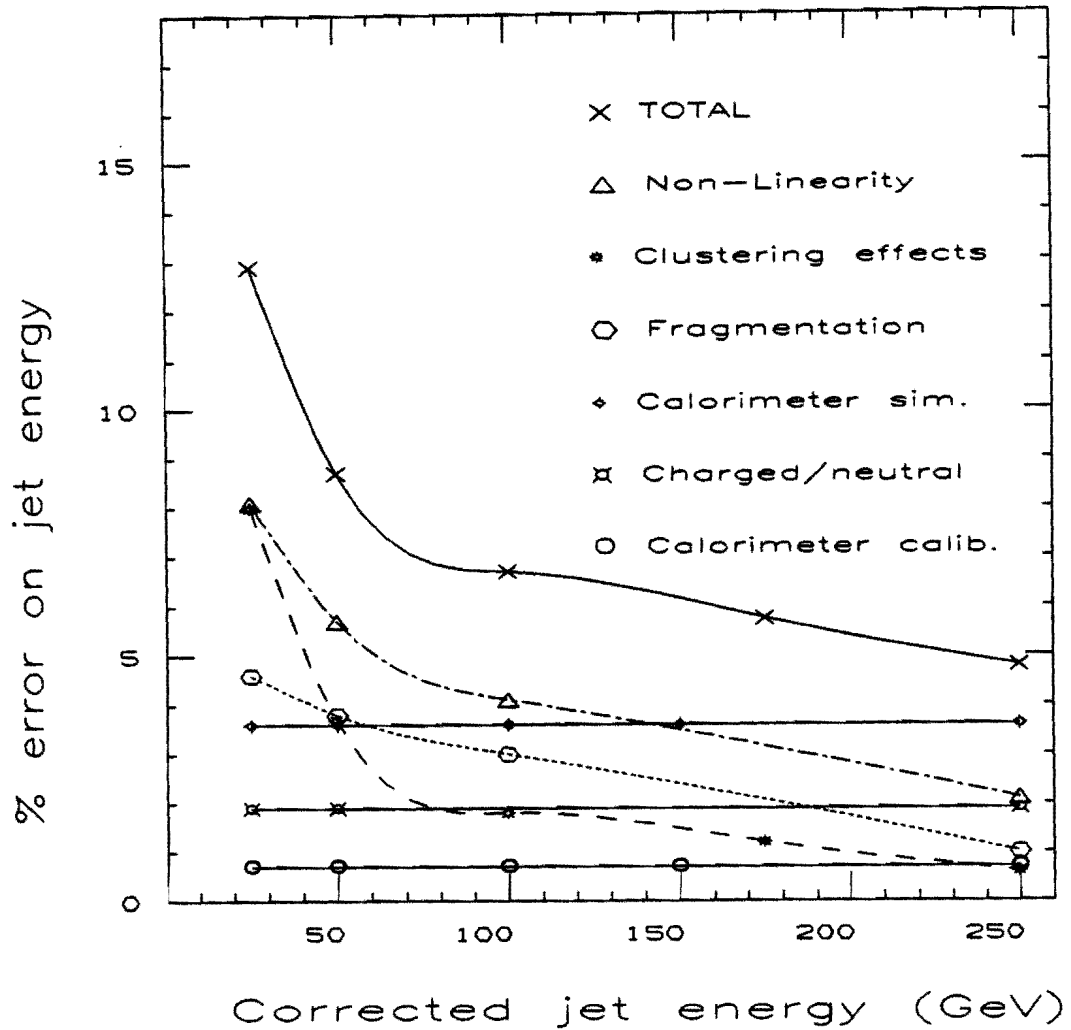
Figure 86. The systematic uncertainty in the jet energy correction, broken down by source. The curve labeled "Total" is the sum in quadrature of the individual contributions. Cubic spline fits were used to interpolate between the data points. "Charged/neutral" refers to the ratio of charged to neutral particles in the jet fragmentation. The figure is from S. Kuhlmann et al., CDF Note 686.

based on fits to data from the AFS Collaboration and preliminary data from UA1, and which gives a fragmentation function which is softer than that measured at CDF. The lower limit was obtained with the parameters deduced by the TASSO Collaboration[99] which correspond to a harder fragmentation function. For the details of the other contributions to the systematic error, the reader is invited to consult Reference 98.

APPENDIX D

DETERMINATION OF THE JET ENERGY RESOLUTION

The jet energy resolution was determined by a method introduced by the UA2 Collaboration.[100] The method employs the fact that in a naive picture of dijet production, where the final state jets are viewed as the end product of the scattering of two partons with no initial transverse momenta, the transverse momenta of the two jets should balance from momentum conservation. Deviations from this balance then reflect the energy resolution for jets. (We will treat momentum and energy equivalently since the mass of the jet, typically 5 GeV/c^2, is negligible.) Unfortunately, even with a perfect detector, the balance would not be perfect because of radiation from the initial- and/or final-state partons. The problem is therefore to extract that part of the dijet p_t imbalance due to detector resolution from the observed imbalance which also includes a piece from initial- and final-state radiation. We will refer collectively to the p_t caused by initial- and final-state radiation as "intrinsic p_t".

To disentangle these two effects, the observed p_t of the two-jet system is decomposed into two components: K_ξ and K_η, where K_η is the component of the p_t along the azimuthal angular bisector of the two-jet system, and where K_ξ is the component along an axis which is orthogonal to the η-axis (Figure 87). Using the fact that the azimuthal angle $\Delta\phi$ between the two jets is close to 180°, it can be shown that

$$K_\xi \sim p_{t1} - p_{t2}$$

$$\text{and} \quad K_\eta \sim (p_{t1} + p_{t2}) \left[\frac{\pi - \Delta\phi}{2} \right]$$

$\eta-\text{axis}$

Pt of 2-jet system

Jet 1

$\xi-\text{axis}$

Jet 2
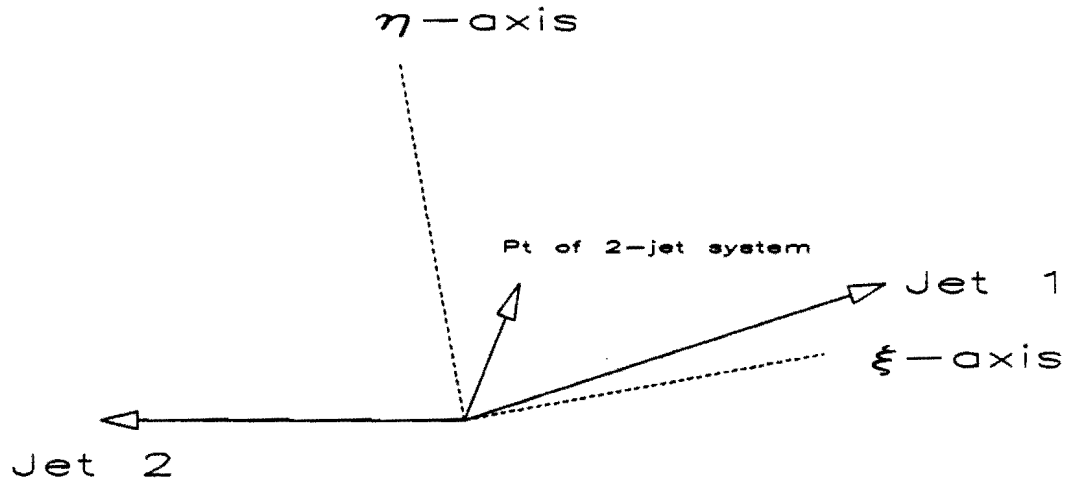
Figure 87. A schematic diagram illustrating the definitions of the ξ and η axes used in the measurement of the jet E_t resolution. The η-axis bisects the azimuthal angle between the two leading jets. The ξ-axis is defined to be orthogonal to the η-axis.

where p_{t1} and p_{t2} are the transverse momenta of the two jets. The key to this method lies in the fact that K_ξ is sensitive to both detector resolution and to the intrinsic p_t of the two-jet system while K_η is sensitive primarily to the intrinsic p_t only.[101] The K_η distribution can therefore be used to measure the contribution of the intrinsic p_t to K_ξ. Under the assumption that the intrinsic p_t is independent of ϕ,[102] the value of K_η should be equal on average to the amount of intrinsic p_t along the ξ-axis. It therefore becomes possible to subtract statistically the contribution of the intrinsic p_t to the width of the K_ξ distribution, i.e.

$$\sigma' = \sqrt{\sigma_{K\xi}^2(\text{measured}) - \sigma_{K\eta}^2(\text{measured})}$$

where σ' is used to denote the width of the K_ξ distribution due to detector resolution effects alone. Now, since

$$\sigma' \sim \sqrt{2}\ \delta p_t$$

we have

$$\delta p_t \sim \sqrt{\frac{\sigma_{K\xi}^2 - \sigma_{K\eta}^2}{2}}$$

Clean two-jet events, where the two leading jets were in the central detector, were selected to measure the resolution. To measure K_ξ, the two leading jets were required to have an opening angle in azimuth in the range $160° < \Delta\phi < 200°$ in order to keep valid the small-angle approximation which was used to derive the expression for K_ξ. For K_η, no cut was applied. Figure 88 shows σ', $\sigma_{K\xi}$ and $\sigma_{K\eta}$ for a cone size of $\Delta R=1.0$ as a function of $\sqrt{E_t}$, where E_t is calculated as the mean uncorrected E_t of the two leading jets. A linear fit to the form $\delta E_t = \alpha + \beta\sqrt{E_t}$ gives

208
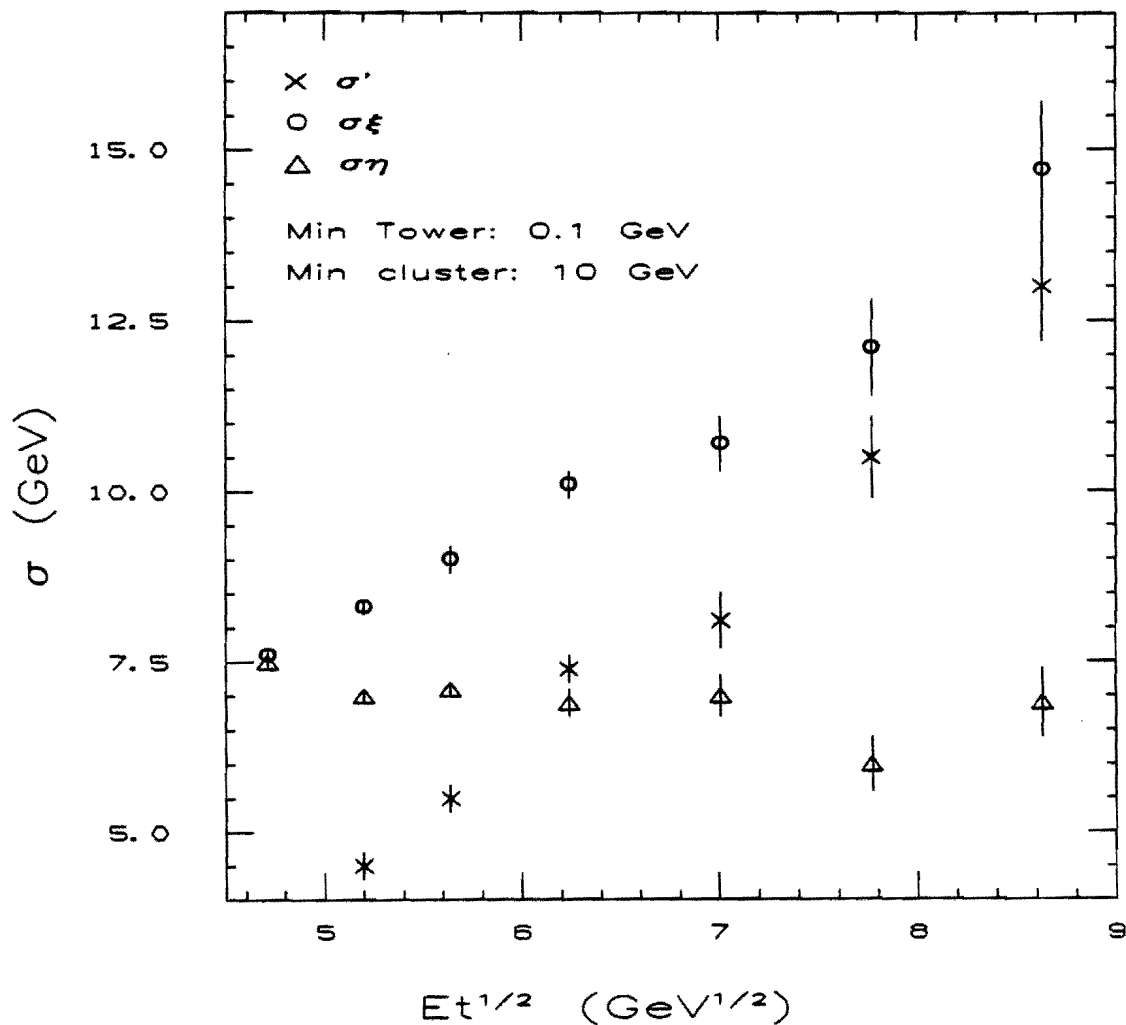
Figure 88. The jet E_t resolution as a function of $\sqrt{E_t}$. The open circles show the resolution for the ζ-component of the dijet E_t imbalance. The triangles show the resolution for the η-component. The crosses show the difference in quadrature between σ_ζ and σ_η which differs from the jet E_t resolution by a multiplicative factor of $\sqrt{2}$. The figures are from R.D. St. Denis, Ph.D. Thesis, Harvard University (1988).

$$\alpha = -5.38 \pm 0.62 \text{ GeV}$$
$$\beta = 1.66 \pm 0.10 \text{ GeV}^{1/2}$$
$$\chi^2 = 7.2 \text{ for 4 degrees of freedom.}$$

In terms of the corrected jet energies, the resolution is derived as follows. Defining the corrected transverse energy of the jet $(E_t{'})$ according to

$$E_t{'} = a \cdot E_t \qquad (\text{where } a=1.25)$$

we have

$$
\begin{aligned}
\delta E_t{'} &= a \cdot \delta E_t \\
&= a \cdot (\alpha + \beta \sqrt{E_t}) \\
&= a\alpha + a\beta \sqrt{\frac{E_t{'}}{a}} \\
&= a\alpha + \beta \sqrt{a E_t{'}} \\
&= 1.86 \sqrt{E_t{'}} - 6.73
\end{aligned}
$$

which is the expression we used in section 7.1.

To explore the sensitivity of the subtraction technique to initial- and final-state radiation, the analysis was performed on several sets of events selected by changing the cut on the maximum E_t of the third jet (Figure 89). The cone size was $\Delta R=0.6$ for this study. It is reassuring to see that $\sigma_{K\eta}$ is essentially independent of $\sqrt{E_t}$, thus suggesting that K_η is not affected by the jet resolution. In addition, the level of $\sigma_{K\eta}$ shows the expected behavior of increasing as the restrictions on third jet activity are relaxed. Figure 89c shows that $\sigma{'}$ is very close to being independent of the level of third jet activity in the event; we interpret this as an indication that the uncertainty in the resolution, due to assumptions about initial- and final-state radiation, is small.
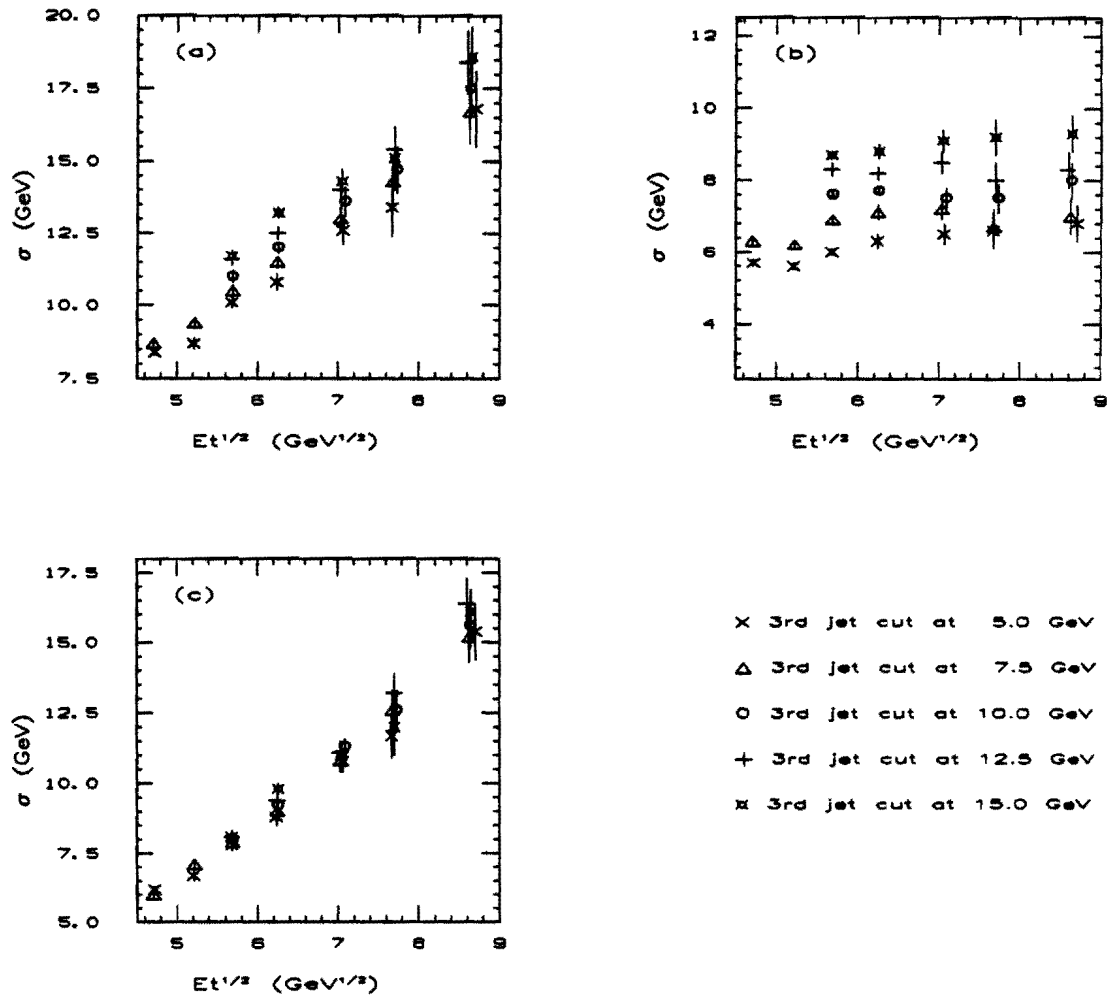
Figure 89. An examination of the sensitivity of the resolution measurement to third-jet activity in the event. a) σ_ξ, b) σ_η, c) σ' for different cuts on the maximum E_t of the third jet in the event. From R.D. St. Denis, Ph.D. Thesis, Harvard University (1988).

APPENDIX E

MONTE CARLO TO STUDY JET ENERGY ISSUES

To understand the effects of jet energy uncertainties on the measurement of D^* production, we have used a Monte Carlo as described in Chapter 7. In this appendix we describe the main ingredients of this Monte Carlo in more detail. These ingredients are: 1) the jet E_t distribution, 2) the z distribution for D^*s, 3) the correction to the jet energy scale, 4) the uncertainty in this energy scale correction, and 5) the jet E_t resolution.

E.1 Jet E_t Distribution

The parameters of the generated jet E_t spectrum were determined by fitting to the inclusive jet cross section measured by CDF[103] where the fit was applied for jets between 30 and 100 GeV. Both statistical and (highly correlated) E_t-dependent systematic errors were included in the error matrix for the fit as follows:

$$\sigma_i^2 = \sigma_i^2(\text{sys}) + \sigma_i^2(\text{stat})$$
$$\text{and} \qquad \sigma_{ij} = \sigma_i(\text{sys}) \cdot \sigma_j(\text{sys}).$$

We will explain this prescription shortly. The result of a fit to the form $dN/dE_t \propto E_t^{-n}$ was an exponent n equal to $5.30*0.12$. The jets were then generated with E_t greater than 17.5 GeV; this threshold is low enough not to bias the observed E_t spectrum (i.e. the E_t after putting in energy scale and resolution effects) above 30 GeV.

We now present an argument[104] for the form of the error matrix. Writing the deviation of variable i from its "true" value as

δ_i, σ_{ij} is given by $\langle\delta_i\delta_j\rangle$ where the brackets indicate that the quantity is averaged over the distributions of variables i and j. The deviation δ_i is partly statistical and partly systematic. Writing δ_i as the sum $\delta_i(stat)+\delta_i(sys)$, one then expands $\langle\delta_i\delta_j\rangle$ as a sum of four terms, three of which average to zero for i≠j (the "stat-stat", "sys-stat", and "stat-sys" terms), while two go to zero for i=j ("sys-stat" and "stat-sys"). One then obtains the above expressions.

E.2 Z Distribution for D*s

For the z distribution of D*s we used $\beta=8.4$ from a fit to the single charged particle fragmentation function[105] as an upper limit to how fast the D* z distribution could fall. This is an upper limit because D*s are closer to the original parton in the fragmentation chain so that we expect them to have a less steeply falling z distribution compared to single charged tracks. We are interested only in the steepest slope because the corrections will turn out to be largest when the slope is steepest.

We have also attempted to obtain some bounds on the slope of the z distribution using the D* signal itself. Unfortunately, due to the poor statistics, it turns out to be impossible to set any useful bounds on β in this way. For example, a fit to the efficiency-corrected z distribution observed from the data gives $\beta = 6.4\pm4.0$ so that at 1σ the z distribution for D*s ends up being steeper than the z distribution for single charged particles. As this seemed physically unreasonable, we took as a worst case the value of β from the single particle fragmentation function. As with the E_t spectrum, the z threshold above which events were generated (namely, z=0.05) was chosen so as to not bias the observed z distribution above z=0.1.

E.3 Jet Energy Scale

To keep the arithmetic simple, the correction for the jet energy scale was taken to be $E' = 1.25E$ where E' denotes the corrected

jet energy. As discussed in Appendix C, this formula compares quite well with the full quadratic correction for the bulk of the jets used in this analysis, namely those with energies ranging from 20 to 50 GeV uncorrected.

E.4 Uncertainty in the Energy Scale

The uncertainty in the energy scale has been presented in Appendix C. Reading off the plot in section C.5, we find

Jet E_t	Uncertainty in jet E_t
20 GeV	14% of the jet E_t
25	13%
30	12%
40	10%
50	8.7%
60	7.8%
70	7.2%
80	6.9%
250	5.0%

E.5 Jet Energy Resolution

The jet energy resolution was parametrized according to the fit of Appendix D for uncorrected jet energies:

$$\delta E_t = 1.66 \sqrt{E_t} - 5.38.$$

We will henceforth refer to this resolution as δE_{t0}. A generous uncertainty of 20% (of the resolution itself) was assigned to the value of the resolution to take into account possible effects due to not knowing the "true" jet energy (recall, we used the mean E_t of the two jets) and effects due to initial- and final-state radiation.

APPENDIX F

A GLIMPSE AT CORRELATED ELECTRON-D^* PRODUCTION

We mentioned in the introduction that one of the motivations for studying D^* production in jets was to use the tools developed in such an analysis to search for correlated lepton-charm production as a way of identifying semileptonic b decays. In this appendix, we present the results of a quick search for D^* production in a sample of events from the 1988-1989 run containing one or more central electrons. We emphasize that this is just for fun. We are merely running the same software as developed in this thesis on a new and different set of data and seeing what comes out. A full analysis of correlated electron-charm production (e.g. e-D^0 production) is being performed by other members of the CDF collaboration.

F.1 Event Selection

The data were collected during the 1988-1989 collider run during which an integrated luminosity of approximately 4.65 pb^{-1} was recorded. This analysis is based on events collected with an inclusive central electron trigger requiring an electromagnetic (EM) cluster with E_t > 12 GeV together with a track with p_t > 6 GeV/c matching the cluster in the ϕ coordinate.

In the offline analysis, the events were required to have one or more electron candidates passing the following cuts:

1) $|\eta|$ < 0.8.

2) The ratio of hadronic to EM energy less than 0.055 + 0.045·E/100 where E is in GeV. The second term parametrizes the leakage out of the back of the EM calorimeter for high-energy electrons.

3) $E_t > 15$ GeV.

4) The ratio of the cluster energy to track momentum (E/p) in the range $0.8 < E/p < 1.2$.

5) A lateral shower profile in the EM calorimeter consistent with that of an electron. (For those familiar with CDF, the exact cut was LSHR < 0.2.)

6) An energy profile in the strip chamber (proportional chambers embedded in the EM calorimeter; see Chapter 2) consistent with that of an electron in both the r-ϕ and z projections. (The exact cuts were strip $\chi^2 < 15$ and wire $\chi^2 < 15$, again for those familiar with CDF.)

7) A match between the position of the shower in the strip chamber and the extrapolated position of the track. In the r-ϕ projection, the two were required to match within 1.5 cm; in the z projection, the cut was at 3 cm.

Electrons from photon conversions were rejected by looking for either 1) electron candidates without a matching track in the VTPC, or 2) candidates with an oppositely charged track in the CTC, close to the electron track and forming a low invariant mass combination. In order to select non-isolated electron candidates typical of b-quark decays, the E_t summed over the calorimeter towers immediately adjacent to the electron cluster (including diagonal neighbors) was required to be greater than 2 GeV. Finally, a cut was placed requiring the z-position of the vertex to be within 60 cm of the center of the detector. A total of 3900 events passed these requirements. 97% of these events contain a single electron; the remaining events have two electrons per event.

F.2 Analysis

We looked for the decay sequence

$$b \rightarrow c \ e^- \ \bar{\nu}_e$$
$$c \rightarrow D^{*+} \rightarrow D^0 \ \pi^+$$
$$D^0 \rightarrow K^- \ \pi^+$$

as well as the charge conjugate modes. As before, the sign of the two pions is the same. In addition, the charge of the kaon is the same as that of the electron, both of which are opposite to the sign of the pions. The analysis was performed in almost exactly the same way as described in Chapter 4. K-π and K-π-π combinations satisfying the above charge requirements were formed by looping over all tracks (excluding the electron) which passed the same selection cuts as in Chapter 4. The following cuts were then applied:

1) The momentum vector of the K-π-π system was required to be within a cone of radius $\Delta R = 1.0$ with respect to the electron.

2) The K-π mass was required to be in the range $1.83 < M_{K\pi} < 1.90$ GeV/c^2.

3) The helicity angle was required to have $|\cos\theta_H| < 0.8$.

The vertex-constrained track fitting had not yet been applied when this analysis was performed.

The mass difference distribution after all the cuts is shown in Figure 90a. A control sample was formed by looking for the wrong-sign combinations $e^\mp K^\pm \pi^\mp \pi^\mp$ instead of $e^\mp K^\mp \pi^\pm \pi^\pm$ (Figure 90b). There is a small accumulation of events in the D^* signal bin, $144.5 < \Delta M < 146.5$ MeV/c^2, for the right-sign combinations which is absent in the control sample. Taking the background to be 1 event, the probability that 1 event fluctuates to greater than equal to 6 is $5.9 \cdot 10^{-4}$, a 3.2σ
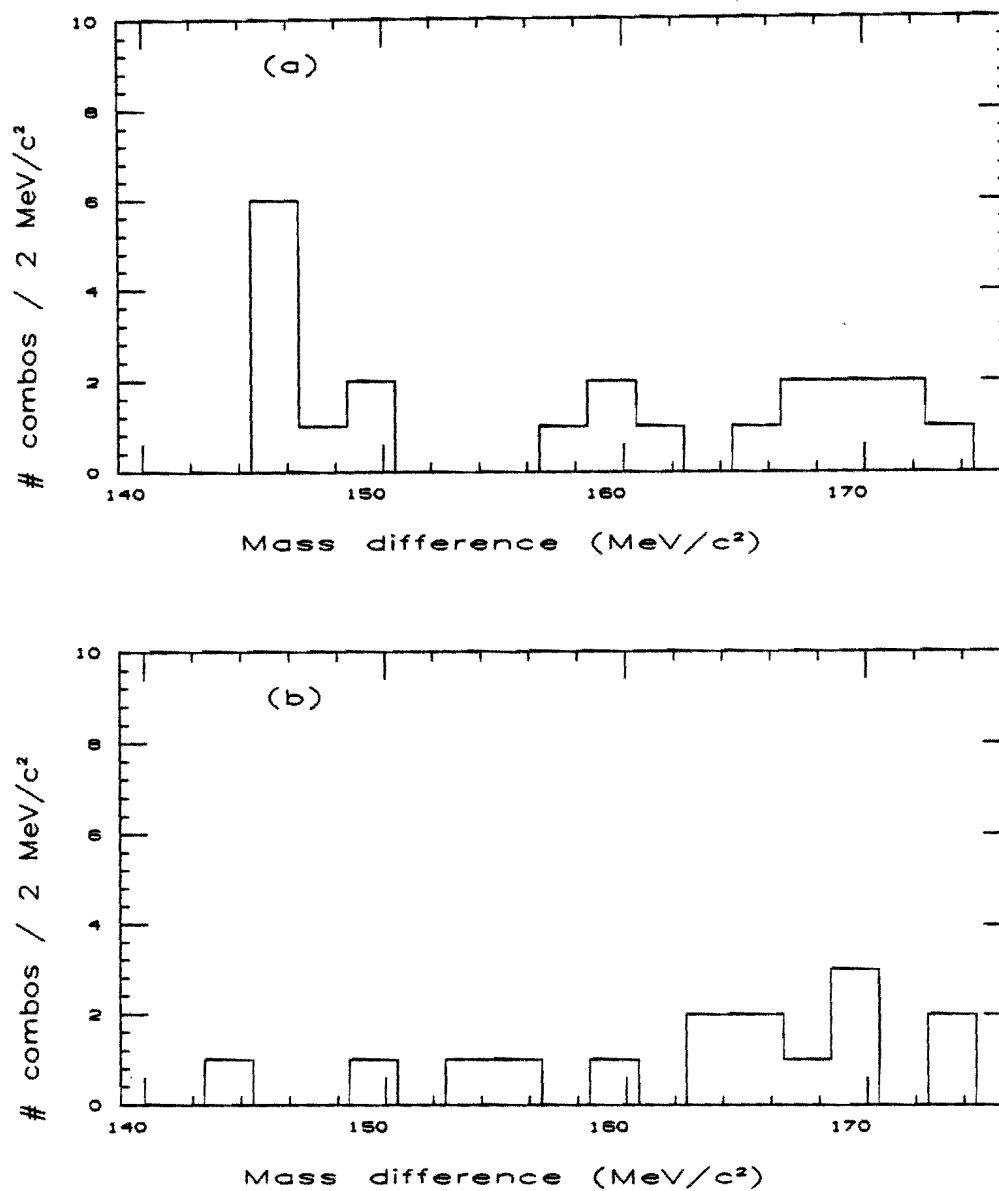
Figure 90. The mass difference distribution in events containing a central electron. (a) This plot is for the right-sign track combinations, where the charge of the kaon is the same as the charge of the electron. (b) The mass difference distribution in electron events for the wrong-sign track combinations.

effect. It would be interesting to study this in a larger sample of events.

Without knowing the efficiency for D^*s in this sample, it is difficult to estimate how many D^*s we expect to see. Denoting the unknown efficiency by ϵ, we have

$$N(D^{*+} + D^{*-}) = N(b \rightarrow ce\nu) \cdot P(c \rightarrow D^{*+} \text{ or } D^{*-}) \cdot BR(D^{*+} \rightarrow K\pi\pi) \cdot \epsilon$$

where

$N(b \rightarrow ce\nu)$ = the number of semileptonic b decays
   $\sim$ 3900, assuming all of the events in our sample come
   from b decays

$P(c \rightarrow D^{*+} \text{ or } D^{*-})$ = the probability that a charm quark materializes
   as a charged D^*
   $\sim$ 0.375

$BR(D^{*+} \rightarrow K\pi\pi)$ = 0.024.

Putting the numbers together, we come up with $N(D^{*+} + D^{*-}) = 35.1 \cdot \epsilon$. We will not hazard a guess here as to the value of ϵ.

As we mentioned earlier, a full analysis of correlated electron-charm production is currently being pursued by other members of the CDF Collaboration using a different sample of data with better statistics than the sample used here. Preliminary results are very encouraging,[106] and we expect this to be an area of active study in the coming years.

REFERENCES

1. See, for example, R.K. Ellis, Fermilab-Conf-89/168-T, to be published in the Proceedings of the 17th SLAC Summer Institute, Stanford, California, July 1989.

2. F. Abe et al., Fermilab-PUB-89/212-E (submitted to Physical Review Letters).

3. J.C. Collins, D.E. Soper, and G. Sterman, Nucl. Phys. B263, 37 (1986).

4. P. Nason, S. Dawson, and R.K. Ellis, Nucl. Phys. B303, 607 (1988).

5. For a review, see S.P.K. Tavernier, Rep. Prog. Phys. 50, 1439 (1987).

6. See, for example, M.G. Catanesi et al., Phys. Lett. 202B, 453 (1988); P. Bordalo et al., Z. Phys. C39, 7 (1988); C. Albajar et al., Z. Phys. C37, 505 (1988); C. Albajar et al., Phys. Lett. B213, 405 (1988); L. Cifarelli et al., Nucl. Phys. B1 (Proc. Suppl.), 55 (1988).

7. G. Feldman et al., SLAC-PUB-4838 (1989), CLNS 89/884 (1989), or LBL-26790 (1989).

8. This estimate is based on a lowest order calculation by E.L. Berger, ANL-HEP-PIC-87-90. The estimated cross section for $b\bar{b}$ pairs produced with rapidity $|y| < 2$ at $\sqrt{s} = 2$ TeV is 10μb. The Fermilab

collider is now running at a "luminosity" which produces events with a 1μb cross section at a rate of one per second.

9. C. Albajar et al., Phys. Lett. 186B, 237 (1987); C. Albajar et al., Phys. Lett. 186B, 247 (1987).

10. Particle Data Group, Phys. Lett. 204B, 1 (1988).

11. J.C. Anjos et al., Phys. Rev. Lett. 60, 1239 (1988).

12. The D^{*} meson is a spin-1 bound state of a charm quark and one of the light quarks, u or d. The quark content of the D^{*} mesons is as follows: $D^{*+} = c\bar{d}$, $D^{*0} = c\bar{u}$, $\bar{D}^{*0} = \bar{c}u$, $D^{*-} = \bar{c}d$.

13. See Appendix A for a listing of the members of the CDF Collaboration.

14. W. Bacino et al., Phys Rev. Lett. 43, 1073 (1979); R. Schindler et al., Phys. Rev. D24, 78 (1981); J. Green et al., Phys. Rev. Lett. 51, 347 (1983); A Chen et al., Phys. Rev. Lett. 52, 1084 (1984); S.E. Csorna et al., Phys. Rev. Lett. 54, 1894 (1985); R. Baltrusaitis et al., Phys. Rev. Lett. 54, 1976 (1985).

15. A.H. Mueller and P. Nason, Nucl. Phys. B266, 265 (1986).

16. For a review, see A. Bassetto, M. Ciafaloni, and G. Marchesini, Phys. Rep. 100, 201 (1983).

17. Note, however, that the growth of the hadron multiplicity with jet energy can be calculated because it is controlled by the growth of the parton shower itself, which is calculable.

18. G. Altarelli and G. Parisi, Nucl. Phys. B126, 298 (1977).

19. A. Kernan and G. Van Dalen, Phys. Rep. 106C, 297 (1984).

20. For example, S.J. Brodsky et al., Phys. Lett. 93B, 451 (1980); S.J. Brodsky, C. Peterson, and N. Sakai, Phys. Rev. D23, 2745 (1981); B.L. Combridge, Nucl. Phys. B151, 429 (1979); V. Barger, F. Halzen, and W.Y. Keung, Phys. Rev. D25, 112 (1979); P.D.B. Collins and T.P. Spiller, J. Phys, G10, 1667 (1984).

21. Unfortunately this production mechanism, i.e. charm quarks as jet fragments, accounts for a relatively small part of the total cross section, $p\bar{p} \rightarrow$ charm + anything, so that the question of non-perturbative contributions to the total charm cross section is still open.

22. G. Arnison et al., Phys. Lett. 147B, 222 (1984).

23. V. Barger and R.J.N. Phillips, Phys. Rev. D31, 215 (1985); G. Kopp, J.H. Kuhn and P.M. Zerwas, Phys. Lett. 153B, 315 (1985); A. Ali and G. Ingelman, Phys. Lett. 156B, 111 (1985).

24. The transverse energy is the jet energy multiplied by the sine of the angle made by the jet with respect to the incoming beams.

25. Throughout this thesis, one charged mode will be used to refer to both modes.

26. M. Della Negra (UA1 Collaboration), Proceedings of the 6th Topical Workshop on Proton-Antiproton Collider Physics, Aachen, W. Germany, edited by K. Eggert, H. Faissner, and E. Radermacher, (World Scientific, 1986).

27. A. Kernan, private communication.

28. For details on the UA1 estimates, see R. Frey, Ph.D. Thesis, U.C. Riverside (1984).

29. C. Albajar et al., Phys. Lett. 186B, 237 and 247 (1987); C. Albajar et al., Phys. Lett. 200B, 380 (1988); C. Albajar et al., Phys. Lett. 209B 397 (1988); C. Albajar et al., Z. Phys. C37, 489 (1988).

30. S.D. Drell and T.M. Yan, Phys. Rev. Lett. 25, 316 (1970).

31. The price one has to pay is in the branching ratio. For example, the semileptonic decay $B^0 \rightarrow D^{*+}\mu\nu$ followed by $D^{*+} \rightarrow D^0\pi^+$ and $D^0 \rightarrow K^-\pi^+$ has a branching ratio of $(0.07)(0.49)(0.038) = 1.3 * 10^{-3}$. The branching ratios have been obtained from Reference 10.

32. See F. Abe et al., Nucl. Inst. and Meth. A271, 387 (1988) for a general description of the detector as well as a full list of references for each of the detector subsystems.

33. For further details on the Tevatron, see for example, H. Edwards, Ann. Rev. Nucl. Sci. 35, 605 (1986) and J. Peoples, IEEE Trans. Nucl. Sci. 30, 1970 (1983).

34. T. Liss, CDF Internal Note 552 (unpublished).

35. Looking to the future, the rate anticipated for the Superconducting Super Collider is on the order of 10^8 Hz.

36. F. Abe et al., Nucl. Inst. and Meth. A271, 387 (1988).

37. F. Snider et al., Nucl. Inst. and Meth. A268, 75 (1988).

38. For example, the TPC built by the ALEPH Collaboration for the LEP Collider at CERN has a maximum drift length of 2.2 m.

39. F. Bedeschi et al., Nucl. Inst. and Meth. A268, 50 (1988).

40. G.W. Foster et al., Nucl. Inst. and Meth. A269, 93 (1988).

41. The typical resolution one obtains from charge division (when the drift electrons are collected in proportional mode) is 1% of the wire length, which in the case of the CTC would amount to 3 cm. It is possible to achieve a resolution of 0.1% of the wire length by operating in limited-streamer mode. This would give a resolution comparable to the stereo wires, but is much more difficult to implement.

42. L. Balka et al., Nucl. Inst. and Meth. A267, 272 (1988); S. Bertolucci et al., Nucl. Inst. and Meth. A267, 301 (1988); Y. Fukui et al., Nucl. Inst. and Meth. A267, 280 (1988); G. Brandenburg et al., Nucl. Inst. and Meth. A267, 257 (1988); S. Cihangir et al., Nucl. Inst. and Meth. A267, 249 (1988).

43. This just means that the signals which are recorded are taken from pads etched into the cathode planes of the chambers.

44. D. Amidei et al., Nucl. Inst. and Meth. A269, 51 (1988). The central track processor and the muon trigger were built elsewhere. See G.W. Foster et al., Nucl. Inst. and Meth. A269, 93 (1988) for details on the track processor. The muon trigger is described in G. Ascoli et al., Nucl. Inst. and Meth. A269, 63 (1988) and K. Byrum et al., Nucl. Inst. and Meth. A268, 46 (1988).

45. E. Barsotti et al., Nucl. Inst. and Meth. A269, 82 (1988).

46. There are 10 such components: Central EM and Hadron, plug EM and Hadron (one of each on each side of the interaction point), forward and backward EM and Hadron.

47. Since our analysis does not depend on this quantity, we will not describe how it was determined. The full details are described in T. Liss, CDF Internal Note 552 (unpublished).

48. R.D. St. Denis, Ph.D. Thesis, Harvard University (1988).

49. For details, see, for example, S. Cihangir et al., Proceedings of the IEEE Nuclear Science Symposium, Orlando, Florida (1988), or M.E.B. Franklin, Proceedings of the 7th Topical Workshop on Proton-Antiproton Collider Physics, Batavia, Illinois, edited by R. Raja, A. Tollestrup and J. Yoh (World Scientific, 1988).

50. D. Brown and A. Baden, CDF Internal Note 812 (unpublished).

51. A. Baden, CDF Internal Note 569 (unpublished).

52. S. Kuhlmann and J. Yoh, CDF Internal Note 548 (unpublished); G. Redlinger and Y.D. Tsai, CDF Internal Note 521 (unpublished).

53. The metric is defined as $R^2 = (\Delta \eta)^2 + (\Delta \phi)^2$, with ϕ expressed in radians.

54. For example, see J. Huth, Fermilab-Conf-89/117-E or D. Brown et al., CDF Internal Note 605 (unpublished). These tests are also described in Y.D. Tsai, Ph.D. Thesis, University of Chicago (1989).

55. G. Sterman and S. Weinberg, Phys. Rev. Lett. 39, 1436 (1977); S. Ellis, Z. Kunszt, and D. Soper, Phys. Rev. Lett. 62, 726 (1989).

56. P. Bagnaia et al., Phys. Lett. 138B, 430 (1984).

57. Y.D. Tsai, private communication; R.D. St. Denis, Ph.D. Thesis, Harvard University (1988).

58. F. Snider, Ph.D. Thesis, University of Chicago, 1989.

59. F. Snider, private communication.

60. P. Billoir, R. Frühwirth, and M. Regler, Nucl. Inst. and Meth. A241, 115 (1985).

61. J. Hauser, private communication.

62. S. Nussinov, Phys. Rev. Lett. 35, 1672 (1975). The method was first used successfully in the discovery of the D^{*+} meson by G.J. Feldman et al., Phys. Rev. Lett. 38, 1313 (1977).

63. For example, see M. Althoff et al., Phys. Lett. 126B, 493 (1983). The discovery of the effect is attributed to G. Goldhaber.

64. For the greater part of the run, the first quadrant of the outermost axial superlayer was turned off. In addition there were four cells (two at $\phi \sim 0°$ and two at $\phi \sim 210°$) in the third axial superlayer from the inside which were not operational. These four cells cover approximately $36°$.

65. We have also considered the possibility where the right-sign decay $D^{*+} \rightarrow D^0 \pi^+ \rightarrow K^- \pi^+ \pi^+$ occurs but where the K and π assignments for the D^0 have been switched. If the K-π mass still comes out to the D^0 mass, this would contribute to a D^* "signal" from the wrong-sign combination. A quick Monte Carlo calculation shows that this probability is negligible.

66. F. James and M. Roos, CERN Computer Centre Program Library D506. This is an updated version of the writeup in Computer Physics Communications 10, 343 (1975).

67. G. Arnison et al., Phys. Lett. 132B (1983) 223.

68. For those familiar with CDF, the dead cells which are taken into account are cells 1,2,43 and 44 in superlayer 4 and cells 0 through 29 in superlayer 8. (See Section 4.2.)

69. The dead cells in superlayer 4 cover roughly the first two bins in Figure 8 and the two bins starting at $\phi=207°$. The entire ϕ plot contains 18,018 entries in 40 bins. We would therefore expect to see 18,013/20 or 901 entries in two bins; we see 889 and 878 entries in the two dead regions, consistent with 901.

70. G. Arnison et al., Nucl. Phys. B276, 253 (1986).

71. One possible method is discussed in G. Lutz, Nucl. Inst. and Meth. A273, 349 (1988).

72. J. Adler et al., Phys. Lett. B208 (1988) 152.

73. J. Adler et al., Phys. Rev. Lett. 60 (1988) 89.

74. See References 22 and 26. Both of these analyses used the branching ratios: $BR(D^{*+} \rightarrow D^0 \pi^+) = 0.44 \pm 0.10$ and $BR(D^0 \rightarrow K^- \pi^+) = 0.049 \pm 0.009 \pm 0.005$. The difference between these branching ratios and those that we have used is small compared to other systematic uncertainties.

75. R.K. Ellis, private communication.

76. For the lowest-order calculation of the z distribution of charm quarks in gluon jets (equation 8.2), see R.K. Ellis, Fermilab-Conf-89/168-T, to be published in the Proceedings of the 17th SLAC Summer Institute, Stanford, California, July 1989. We will extend this calculation later in this chapter to describe the z distribution of D^*s.

77. C. Peterson et al., Phys. Rev. D27, 105 (1983).

78. CLEO: P. Avery et al., Phys Rev. Lett. 51, 1139 (1983); HRS: S. Ahlen et al., Phys. Rev. Lett. 51, 1147 (1983); DELCO: H. Yamamoto et al., Phys. Rev. Lett. 54, 522 (1985); TASSO: M. Althoff et al., Phys. Lett. 126B, 493 (1983).

79. See, for example, Reference 78. Other measurements include W. Bartel et al., Phys. Lett. 146B, 121 (1984); P. Baringer et al., Phys. Lett. 206B, 551 (1988).

80. F. Paige, S. Protopopescu, Proceedings of the 1986 Summer Study on the Physics of the Superconducting Supercollider, edited by R. Donaldson and J. Marx (1986). Version 5.2 of ISAJET was used.

81. The structure functions used were Set 1 from E. Eichten, K. Lane, I. Hinchliffe, and C. Quigg, Rev. Mod. Phys. 56, 579 (1984).

82. G. Marchesini and B.R. Webber, Nucl. Phys. B310, 461 (1988).

83. R. Ansari et al., Phys. Lett. 186B, 452 (1987).

84. We have recently learned that the statistical significance has been increased with an analysis of a new, large sample of data. The new results were reported at the 8th Topical Workshop on Proton-Antiproton Collider Physics, Castiglione, Italy, September 1989.

85. A. Byon, CDF Internal Note 572 (unpublished); M. Schub, CDF Internal Note 597 (unpublished).

86. The p_t cut is applied because a disproportionate fraction of tracks with large r-ϕ separation are low p_t tracks (which curl away from the core of the jet) and we wish to disentangle the

effect of the falling efficiency at low p_t from the (flat) behavior of the efficiency at large values of r-ϕ separation.

87. For example, see J. Huth, Fermilab-Conf-89/117-E or Y.D. Tsai, Ph.D. Thesis, University of Chicago (1989).

88. This is not strictly true in the sense that one can use events from $\bar{p}p$ collisions in which a jet recoils against a photon where the photon energy is well-determined. One problem with this, of course, is a lack of statistics at high jet energies.

89. L. Balka et al., Nucl. Instr. and Meth. A267, 272 (1988).

90. S. Bertolucci et al., Nucl. Instr. and Meth. A267, 301 (1988).

91. S. Hahn et al., Nucl. Instr. and Meth. A267, 351 (1988). Also see reference 90.

92. S. Behrends et al., CDF Internal Note 583 (unpublished).

93. See for example, C. Fabjan, Proceedings of the 1984 NATO Advanced Study Institute on Techniques and Concepts of High Energy Physics III, St. Croix, U.S.V.I., edited by T. Ferbel (Plenum Pub. Corp., 1985).

94. S. Behrends and S. Kuhlmann, CDF Internal Note 684 (unpublished).

95. R.D. Field and R.P. Feynman, Nucl. Phys. B136, 1 (1978).

96. B. Flaugher and S. Kuhlmann, CDF Internal Note 685 (unpublished).

97. S. Kuhlmann, CDF Internal Note 687 (unpublished).

98. S. Kuhlmann et al., CDF Internal Note 686 (unpublished).

99. R. Brandelik et al., Phys. Lett. 94B, 437 (1980).

100. P. Bagnaia et al., Phys. Lett. 144B, 283 (1984); for the details of the application of this method to CDF, see for example R.D. St. Denis, Ph.D. Thesis, Harvard University (1988) or Y.D. Tsai, Ph.D. Thesis, University of Chicago (1989).

101. This requires the angular resolution for jets to be good enough so that the K_η distribution reflects the intrinsic p_t and not the angular resolution. Studies by J. Huth, comparing the jet axis determined with tracking information to the axis determined with calorimeter information, show that the angular resolution at CDF is better than $\pm 3°$.

102. This is probably a reasonable assumption for initial-state radiation which we expect to be more-or-less independent of the hard collision since the hard collision occurs over a very short time-scale. The validity of the assumption is not so clear for final-state radiation which is probably correlated with the direction of the leading jets. We will shortly examine our sensitivity to this assumption.

103. F. Abe et al., Phys. Rev. Lett. 62, 613 (1989).

104. J. Huth and S. Behrends, CDF Internal Note 747 (unpublished). The argument is due to A. Para.

105. F. Abe et al., to be published in Physical Review Letters. The details are described in B. Hubbard, Ph.D. Thesis, Univ. of California at Berkeley, (1989).

106. For example, see the discussion by K. Ragan in the Proceedings of the 1989 SLAC Topical Conference, July 21-23, 1989, Stanford, CA (to be published).